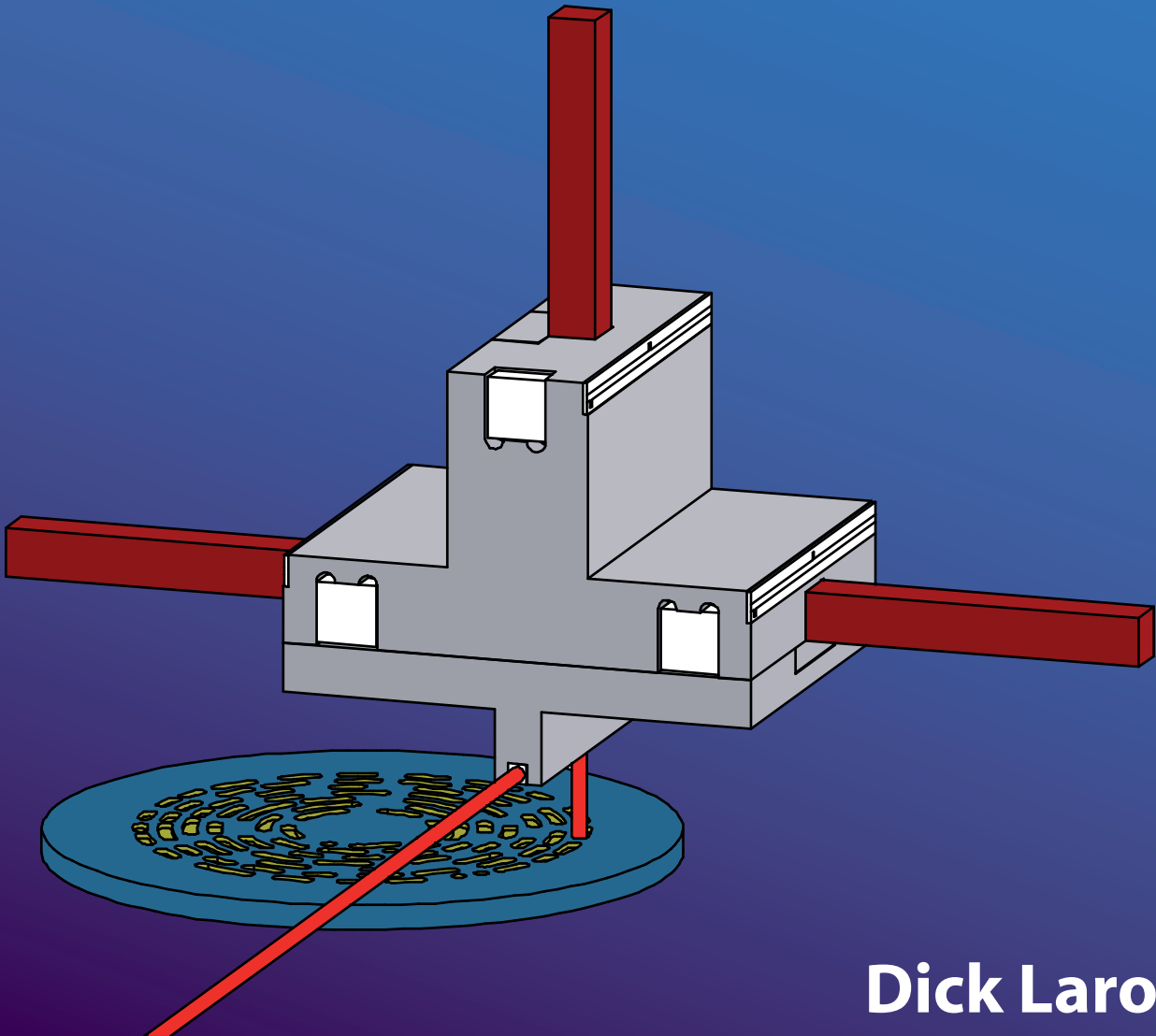


Mechatronic Design of an Electromagnetically Levitated Linear Positioning System using Novel Multi-DoF Actuators



Dick Laro

**Mechatronic Design of an Electromagnetically
Levitated Linear Positioning System
using Novel Multi-DoF Actuators**

PROEFSCHRIFT

ter verkrijging van de graad van doctor
aan de Technische Universiteit Delft,
op gezag van de Rector Magnificus prof.dr.ir. J.T. Fokkema,
voorzitter van het College van Promoties,
in het openbaar te verdedigen op maandag 18 mei 2009 om 15:00 uur
door

Dick Antonius Hendrikus LARO

werktuigkundig ingenieur
geboren te Roosendaal en Nispen.

Dit proefschrift is goedgekeurd door de promotor:

Prof.dr.ir. J. van Eijk

Copromotor: ir. J.W. Sprock

Samenstelling promotiecommissie:

Rector Magnificus	voorzitter
Prof.dr.ir. J. van Eijk	Technische Universiteit Delft, promotor
Ir. J.W. Spronck	Technische Universiteit Delft, copromotor
Prof.dr. E.A. Lomonova	Technische Universiteit Eindhoven
Prof.dr.ir. J. van Amerongen	Universiteit Twente
Prof.dr.ir. H. van Brussel	Katholieke Universiteit Leuven
Prof.dr.ir. P.M.J. Van den Hof	Technische Universiteit Delft
Dr.ir. A. Molenaar	SKF
Prof.dr. D.J. Rixen	Technische Universiteit Delft



This research was supported by STW.

ISBN 978-90-9024255-2

Copyright © 2009 by D.A.H. Laro

All rights reserved. No part of the material protected by this copyright notice may be reproduced or utilized in any form or by any means, electronic or mechanical, including photocopying, recording, or by any information storage and retrieval system, without written permission from Dick Laro.

Printed in the Netherlands.

Voorwoord

Zes jaar geleden begon ik met het onderzoek naar een nieuw type electromagnetische actuator en zijn integratie in een magnetische gelagerde slede, waarover u alles in dit proefschrift kunt lezen. Zelf moet ik nog een beetje aan het idee wennen, maar het proefschrift is nu toch echt klaar. Het proefschrift, waardoor ik de laatste tijd soms zo “ongezellig” was en geen tijd had om langs te komen, excuses hiervoor. Toen ik begon met het schrijven had ik ook niet gedacht dat het me zo veel tijd zou kosten. Het blijkt maar weer eens dat het schrijven van een proefschrift en werken niet de beste combinatie is. Gelukkig zijn er heel wat mensen die mij tijdens het onderzoek en het schrijven hebben geholpen, zonder jullie was het me niet gelukt. Nu is het tijd om jullie te bedanken.

Te beginnen met mijn promotor, Jan, je creatieve inzichten en scherpe opmerkingen hebben mij ontzettend geïnspireerd. Ik ben je ontzettend dankbaar voor de manier hoe je mij geholpen hebt om het proefschrift af te ronden. Jo, mijn copromotor, je stond altijd voor me klaar met goede adviezen en nieuwe ideeën. Door jou kregen wij, de promovendi, alle vrijheid onze wetenschappelijke en soms wat minder wetenschappelijke experimenten uit te voeren. Ik kijk daarom ook zeer positief terug naar mijn jaren als promovendus bij de vakgroep “Advanced Mechatronics” (nu “Mechatronic design”). Onder de studenten en promovendi heerste een zeer goede sfeer, zowel op de universiteit als daarbuiten. Zo was er altijd wel een reden om een BBQ te houden, van een promotie tot de eerste sneeuwvlokjes. Sander, Maarten, Marc, Warner, Peter, Leon, Hussein, Guido, Robin, en Jeroen bedankt voor de gezelligheid.

Ik heb een aantal studenten mogen begeleiden tijdens hun afstudeerwerk waarin zij een deelstuk van het onderzoek voor hun rekening namen. Zij hebben hiermee een belangrijke bijdrage geleverd aan het onderzoek naar de magnetische gelagerde slede. Stefan, Henry, Thomas, Jasper, en Coen, bedankt voor jullie inzet en de discussies die ik met jullie heb gehad. Met name Henry, Porck, en DJ-Jasper hebben naast het onderzoek een enorme bijdrage geleverd in de sfeer in en rond het mechatronica lab. Anton, mijn collega uit Eindhoven, bedankt voor je hulp met de electromagnetische simulaties en het toch wel enigszins ongezonde lijmen van de lamellen.

De begeleidingscommissie, ingesteld door de financier STW, heeft het onderzoek altijd met interesse gevolgd en hielp met praktische tips. Hiervoor mijn dank.

Tevens maakte de financiële steun van Philips Apptech en SKF het mogelijk om de apparatuur aan te schaffen, die nodig was voor het realiseren van sub-nanomater positionering. John Compter, Elena Lomonova, John, Eric, Thomas, Jasper, en Maarten bedankt voor het helpen met verbeteren van de kwaliteit van dit proefschrift.

Bedankt Thomas en Michiel, jullie zorgden er gelukkig voor dat ik me ook nog eens met wat anders bezig hield dan met de techniek. Zonder de hulp van mijn ouders en zus bij het opknappen van mijn huis, het bestrijden van lekkage, en het repareren van houtrot, had het afmaken van het proefschrift behoorlijk langer geduurd. Dank jullie! En tot slot, Rianne, bedankt voor je steun en hulp bij het afmaken van het proefschrift. Het samenleven met een promovendus is niet altijd even makkelijk. Eerst is hij altijd laat, omdat hij nog wat moet meten of uit moet zoeken. Als hij dan klaar is met het onderzoek is hij er wel, maar heeft hij zich opgesloten in zijn kamer en is hij bezig met typen. Nu het proefschrift is afgerond kan ik beginnen met klussen en weer nieuwe technische projectjes oppakken. Maar eerst ga ik met jullie allemaal een biertje drinken.

Contents

Nomenclature	ix
1 Introduction	1
1.1 Background	1
1.1.1 Optical disc mastering	1
1.1.2 A novel electromagnetic actuator: the IU-module	3
1.1.3 Mechatronic design approach for a magnetically suspended positioning system	5
1.2 Problem statement	6
1.3 Outline	6
2 Active magnetic levitation for linear high precision systems	9
2.1 Advantages of magnetic suspension in high precision systems . . .	9
2.2 Magnetism basics	11
2.2.1 Magnetic field description	12
2.2.2 Magnetic circuit description	12
2.2.3 Magnetostatic forces	13
2.3 Actuators for magnetically levitated positioning systems	15
2.3.1 Reluctance actuator	16
2.3.2 Lorentz force actuators	19
2.4 Precision positioning stages	20
2.5 Comparison between alternatives for the Slider applied in optical disc mastering	26
3 The IU-module	29
3.1 The 2-DoF IU-module	29
3.1.1 Actuation of the suspension direction	30
3.1.2 Actuation of propulsion x -direction	35
3.2 Design of the IU-module	37
3.2.1 Applied modelling methods	38
3.2.2 Design choices for the IU-module	40

3.3	Force measurement on 2-DoF IU-module	46
3.3.1	Force measurement setup	46
3.3.2	Results of force measurements on 2-DoF IU-modules	49
3.4	Comparison between model and measurements	53
3.5	Additional DoFs of the IU-module	56
3.5.1	Overview of actuation constants	59
3.6	Alternative designs	61
3.6.1	Short propulsion coils	61
3.6.2	UO-module	61
3.7	Conclusions and remarks	64
4	Design of 6-DoF electromagnetically suspended Slider	65
4.1	Dynamic Error Budget design methodology	65
4.1.1	Dynamic Error Budgeting analysis tool	66
4.2	Specifications for the Slider in optical disc mastering	72
4.2.1	Error in radial direction (x)	73
4.2.2	Error in tangential direction (y)	75
4.2.3	Error in axial Direction (z)	75
4.2.4	Additional requirements for the Slider	75
4.3	Conceptual design of the Slider	77
4.4	The Slider design	83
4.4.1	Actuator Configuration	83
4.4.2	Sensor configuration	84
4.4.3	Mechanical design of the Slider	87
4.4.4	Electronic design	92
4.5	Mechatronic design evaluation of the Slider	94
4.5.1	Model of the plant and controller	95
4.5.2	Models of the disturbances acting on the Slider	98
4.5.3	Results and design process illustration	102
4.5.4	Optimal test for suspension directions	104
4.5.5	Conclusions and remarks	105
5	Control and performance of 6-DoF electromagnetically suspended Slider	109
5.1	Practical aspects to realisation and start-up	110
5.1.1	Realisation of the Slider	110
5.1.2	First time levitation of the Slider	111
5.2	Control design for the Slider	112
5.2.1	Start-up controller and high performance control	112
5.2.2	Decoupling of the Slider	113
5.2.3	Stiffness compensation	119
5.2.4	Evaluation of decoupling	123
5.2.5	Position controllers	128

5.3	Performance of the Slider	130
5.3.1	Differences between modelled and actual system	130
5.3.2	Performance of Slider at standstill	131
5.3.3	Performance of the moving Slider	132
5.4	Performance of the IU-module Actuator	135
5.5	Conclusions and remarks	137
6	Improved positioning by use of over-actuation	141
6.1	Modal control basics	142
6.2	Mode decoupled actuation for the Slider	148
6.3	Conclusions and remarks	154
7	Conclusions and recommendations	157
7.1	Conclusions	157
7.2	Recommendations	163
A	Additional design information	167
A.1	Disturbances entering through the negative stiffness compensation	167
A.2	Electronic connection of the RPI-20 board	170
A.3	Amplifier transfers	171
B	Additional experimental results of the IU-module	173
B.1	The IU-demonstrator	173
B.1.1	Static force measurements on the IU-demonstrator	174
B.1.2	Dynamic results of the IU-demonstrator	178
B.2	The Baby-IU setup	181
B.2.1	Design of the dynamic Baby-IU setup	181
B.2.2	Dynamic measurement results of the 2-DoF Baby-IU	182
B.3	Modal control applied to the Baby-IU setup	188
C	Additional measurement results of the Slider	193
C.1	Position dependency of the eddy current sensor	193
C.2	Stiffness compensation: model and experiment	196
C.3	Additional servo-errors of the Slider	199
D	Construction drawings of the Slider	203
E	Photographs	215
	Curriculum Vitae	225
	Abstract	227

Nomenclature

Symbols

<i>Symbol</i>	<i>Description</i>	<i>Unit</i>
a_1	Inner actuation parameter on rigid body mode	[-]
a_i	Inner actuation parameter on flexible body mode, $i > 1$	[-]
b_1	Outer actuation parameter on rigid body mode	[-]
b_i	Inner actuation parameter on flexible body mode, $i > 1$	[-]
d	Damping	[Ns/m],[Nms/rad]
d_{crit}	Critical dimension	[m]
d_{tp}	Track pitch of optical disc	[m]
d_{short}	Shortest pit length on optical disc	[m]
f	frequency	[Hz]
f_{fund}	fundamental frequency of laser interferometer	[Hz]
f_N	Nyquist frequency	[Hz]
h	Actuator constant	[N/A], [Nm/A]
h_{xy}	Actuator constant, from actuation in y-direction to force in x-direction	[N/A]
e	Servo-error	[m]
e_x	Servo-error in x-direction	[m]
i	Current	[A]
i_x	Current for actuation of x-direction	[A]
j	Imaginary unit $j = \sqrt{-1}$	[-]
k	Stiffness	[N/m],[Nm/rad]
k_{xy}	Stiffness, resulting in a force in x-direction, due to y-displacement	[N/m]
k_1	Photoresist process related factor	[-]
l	Length	[m]
m	Mass	[kg]
n	Number of turns on a coil	[-]
ni	Interpolation factor	[-]
o	Application point	[-]
p	Probability density	[-]
u	Control output	[V], [A]

continued on next page...

... continued from previous page

<i>Symbol</i>	<i>Description</i>	<i>Unit</i>
u_x	Control output in x -direction	[V], [A]
u_G	Input to plant G	[V], [A]
w	Disturbance signal	[-]
r	Reference set-point to control loop	[m]
r_x	Reference set-point to control loop in x -direction	[m]
t	Time	[s]
t_{eddy}	Position transducer output of eddy current sensor	[m]
t_{cap}	Position transducer output of capacitive sensor	[m]
t_{las}	Position transducer output of laser interferometer	[m]
t_{linear}	Position transducer output of linear encoder	[m]
s	Number of bits	[-]
x	Coordinate or displacement in x -direction	[m]
x_X	x -CoG co-ordinate of body X	[m]
\vec{x}	Position vector $(x \ y \ z \ \varphi \ \gamma \ \theta)^T$	[m,rad]
y	coordinate or displacement in y -direction	[m]
y_X	y -CoG co-ordinate of body X	[m]
z	coordinate or displacement in z -direction	[m]
z_X	z -CoG co-ordinate of body X	[m]
z_{floor}	floor displacement in z -direction	[m]
s	Laplace operator	[-]
A	Area	[m ²]
\mathbf{A}_{ss}	State space matrix	[-]
B	Magnetic flux density	[T]
\mathbf{B}	Plant input matrix, Chapter 6	[-]
\mathbf{B}_{ss}	State space input matrix	[-]
\mathbf{C}	Plant output matrix	[-]
C_c	SISO controller	[-]
\mathbf{C}_c	MIMO controller	[-]
\mathbf{C}_{ss}	State space output matrix	[-]
$\text{CPS}(f)_w$	Cumulative Power Spectrum	[unit ²]
D	Electric displacement	[C/m ²]
\mathbf{D}	Damping matrix	[Ns/m], [Nms/rad]
E	Electric field	[V/m]
$\mathbf{E}(s)$	$\mathbf{G}_{diag}^{-1}(s) \cdot (\mathbf{G}(s) - \mathbf{G}_{diag}(s))$	[-]
F	Force	[N]
F_x	Force in x -direction	[N]
F_s	Suspension Force of Slider	[N]
F_S	Force on CoG of Slider	[N]
F_p	Propulsion Force of Slider	[N]
\vec{F}	Force vector $(F_x \ F_y \ F_z \ T_x \ T_y \ T_z)^T$	[N,Nm]
$G(s)$	SISO Plant	[-]
$\mathbf{G}(s)$	MIMO Plant	[-]

continued on next page...

... continued from previous page

<i>Symbol</i>	<i>Description</i>	<i>Unit</i>
H	Magnetic field strength	[A/m]
H_{PM}	Coercive force of permanent magnet	[A/m]
$H(s)$	Closed-loop transfer	[-]
I	Mass moment of inertia	[kgm ²]
I_x	Mass moment of inertia around x -axis	[kgm ²]
\mathcal{L}	Inductance	[H]
K_i	Integral gain of parallel integrator	[-]
K_d	Overall gain of controller	[-]
\mathbf{K}	Stiffness matrix	[N/m], [Nm/rad]
L	Open-loop transfer	[-]
M	Magnetisation	[A/m]
\mathbf{M}	Mass matrix	[kg], [kgm ²]
\mathcal{MMF}	Magneto motive force	[A-turns]
N	Transfer of inner actuator leg	[-]
N_c	Lead-lag filter parameter	[-]
O	Transfer of outer actuator leg	[-]
P	Probability	[-]
P_e	Perimeter	[m]
\mathbf{P}_1	Constant output matrix for dyadic decoupling	[-]
\mathbf{P}_2	Constant input matrix for dyadic decoupling	[-]
$\text{PSD}(f)_{2w}$	Power Spectral Density of w	[unit ² /Hz]
Q	Electric charge	[C]
Q_a	Quantisation interval	[-]
R	Resistance	[Ω]
\mathcal{R}	Reluctance	[Am ² /T]
$\mathbf{S}(s)$	Sensitivity function $(\mathbf{I} + \mathbf{L}(s))^{-1}$	[-]
S_e	Surface	[m ²]
$\mathbf{S}_{\text{svd}}(s)$	Matrix containing singular values	[-]
SNR	Signal to Noise Ratio	[-]
T	Torque	[Nm]
T_x	Torque around x -axis	[Nm]
\mathbf{T}	Transformation matrix	[-]
T_p	Period time	[s]
\mathbf{T}_U	Input decoupling transformation matrix	[-]
$\mathbf{T}_{U,s}$	Input decoupling matrix for suspension of Slider	[-]
$\mathbf{T}_{U,p}$	Input decoupling matrix for propulsion of Slider	[-]
$\mathbf{T}_s\text{tiff}, \mathbf{U}$	Input decoupling matrix for stiffness compensation	[-]
\mathbf{T}_Y	Output decoupling transformation matrix	[-]
$\mathbf{T}_s\text{tiff}, \mathbf{U}$	Output decoupling matrix for stiffness compensation	[-]
\mathbf{T}_Y,s	Output decoupling matrix for suspension of Slider	[-]
\mathbf{T}_Y,p	Output decoupling matrix for propulsion of Slider	[-]
$\mathbf{U}_{\text{svd}}(s)$	Matrix containing output singular vectors	[-]

continued on next page...

... continued from previous page

<i>Symbol</i>	<i>Description</i>	<i>Unit</i>
\mathbf{V}	Matrix containing eigenvectors, \vec{V}_i	[-]
\vec{V}_i	Eigenvector	[-]
$\mathbf{V}_{\text{svd}}(s)$	Matrix containing input singular vectors	[-]
Y	Young's modulus	[Pa]

Greek Symbols

<i>Symbol</i>	<i>Description</i>	<i>Unit</i>
δ_{tp}	Track pitch variation of optical disc	[m]
η	Gain compensation factor	[-]
ξ	Excitation ratio between flexible modes	[-]
λ	Wavelength	[m]
μ	Relative permeability	[-]
$\mu_{\text{Delta}c}$	Structured Singular value interaction measure	[-]
μ_0	Permeability of vacuum $4\pi \cdot 10^{-7} \text{ H/m}$	
Φ	Magnetic flux	[Tm ²]
γ	Angle around y-axis	[rad]
ω	frequency	[rad/s]
φ	Angle around x-axis	[rad]
ρ	density	[kg/m ³]
σ	Standard deviation	[unit]
σ_x	Standard deviation of x	[unit]
σ_{svd}	Singular value	[-]
τ_d	Coefficient of differentiator in lead lag-filter	[-]
θ	Angle around z-axis	[rad]
ζ	relative damping coefficient	[-]

Subscripts

<i>Subscript</i>	<i>Description</i>
<i>act</i>	Actuator
<i>b</i>	Bottom of IU-module
<i>back</i>	Back of IU-module
<i>bar</i>	Slider bar
<i>bias</i>	Bias
<i>cap</i>	Capacitive sensor
<i>clearance</i>	Stand-off between stator legs of the IU-module
<i>c</i>	Controller
<i>con</i>	Control flux
<i>coil</i>	Coil
<i>d</i>	Decoupled
<i>diag</i>	Diagonal

continued on next page...

... continued from previous page

<i>Subscript</i>	<i>Description</i>
<i>eddy</i>	Eddy current sensor
<i>F</i>	CoG of Force frame
<i>front</i>	Front of IU-module
<i>g</i>	CoG coordinates
<i>gap</i>	Airgap
<i>f_{enc}</i>	Free and enclosed
<i>I</i>	CoG of Intermediate reference frame
<i>l</i>	Left of IU-module
<i>linear</i>	Linear encoder
<i>p</i>	Propulsion
<i>q</i>	Modal coordinate
<i>PM</i>	Permanent magnet
<i>las</i>	Laser interferometer
<i>ms</i>	Magnetostatic
<i>r</i>	Right of IU-module
<i>R</i>	CoG of Reference frame
<i>s</i>	Suspension
<i>S</i>	CoG of Slider
<i>sens</i>	Sensor
<i>t</i>	Top of IU-module
<i>tp</i>	Track pitch

Operators

<i>Symbol</i>	<i>Description</i>
δ	Difference operator
d	Differential operator
\propto	Proportional to
$\text{diag}(\mathbf{X})$	Diagonal entries of \mathbf{X}
eig	Eigenvectors of
\bar{x}	Average of x
\dot{x}	$\frac{dx}{dt}$
\ddot{x}	$\frac{d^2x}{dt^2}$
\vec{x}	Vector x
\mathbf{X}^H	Complex conjugate transpose of \mathbf{X}
\mathbf{X}^T	Transpose of \mathbf{X}
\times	Schurr or Hadamard product
\cdot^{-1}	Matrix inverse
\sim	Estimated
$\ \cdot\ _{rms}$	RMS norm

Abbreviations and Acronyms

<i>Abbreviation</i>	<i>Description</i>
PID	Proportional-Integral-Derivative
PD	Proportional-Derivative
AD	Analog to Digital
CoG	Centre of Gravity
DA	Digital to Analog
DEB	Dynamic Error Budget
DoF	Degree of Freedom
NdFeB	Neodymium Iron Boron
DoF	Degree Of Freedom
FEM	Finite Element Method
FFT	Fast Fourier Transform
MEN	Magnetic Equivalent Network
MIMO	Multi Input, Multi Output
MDA	Mode Decoupled Actuation
NA	Numerical Aperture
P(I)D	Proportional, (Integral,) Derivative
SISO	Single Input, Single Output
ZOH	Zero Order Hold

Chapter 1

Introduction

1.1 Background

Precision manufacturing machines are used in the production of precision parts, such as optical discs and semiconductor chips. The feature size of these parts is constantly reduced to satisfy the demand for increased data storage and faster computer chips. Therefore, the accuracy in the precision machines and the positioning systems within them needs to be continuously improved. Current state of the art precision positioning systems attain positioning stability within several nanometres.

To increase performance, the positioning systems are isolated from disturbance sources originating from the environment. This has resulted in the application of contactless positioning systems, such as air bearings. A next generation of precision machines is expected to operate under vacuum conditions, to realise complete separation from the environment.

Operating in a vacuum environment poses new challenges on the precision positioning systems. Lubricated roller bearings and air bearings contaminate the vacuum environment, making them impractical. Thermal management in a vacuum environment is extremely important, due to the absence of convective cooling. Cables going to the moving stage in the vacuum environment often consist of vacuum incompatible materials. These moving wires will have to be shielded, adding complexity to the system. Active magnetic suspension technology, where the positioned object is contactlessly suspended using electromagnetic forces, promises to be capable of fulfilling the demands for a vacuum environment. One industry, where vacuum compatible positioning systems are studied, is the optical disc mastering industry [3].

1.1.1 Optical disc mastering

The information on an optical disc is written in the form of spiral shaped tracks consisting of pits and lands. This information is read contactlessly with a focused laser

beam. Initially, the optical disc, the CD, was developed for audio content. Currently, the third generation, the Blu-Ray disc, is capable of playing high definition movies. This trend has led to a significant increase of the data capacity of the optical disc. The data capacity is increased by reducing the track pitch and pit size on the disc. Figure 1.1 shows the increase of the information density over three generations of optical discs, the CD, the DVD and the Blu-Ray disc.

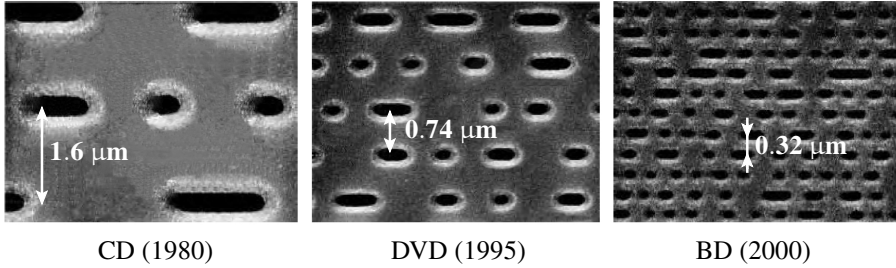


Figure 1.1: Atomic Force Microscope images of three generations of optical discs, the CD (650 MB), the DVD (4.7 GB), and the Blu-Ray disc (25 GB). The number of bits on the disc is proportional to the track pitch squared.

Optical discs are replicated by using an injection moulding machine. The basic mould is manufactured in an optical disc mastering machine. The optical disc mastering machine records the pits onto a photoresist-coated glass substrate using a pulsed laser beam. The glass substrate is rotated on a rotating platform, while a positioning system, making a linear motion over the substrate, points the laser beam towards the disc, as in Fig 1.2. The linear positioning system, referred to as the Slider, has the ability to make one linear motion of 50 mm, while the other 5 degrees of freedom (DoF) are constrained, currently using air bearings.

The smallest feature on the disc, capable of being written in the photoresist, is determined by the critical dimension of a focussed laser beam, Eq. 1.1. In this equation, the wavelength of the applied laser is λ_{light} , and the numerical aperture of the projection lens is NA. The factor, k_1 , is process related and determined by the applied photoresist, which is it is approximately 0.4 for optical disc mastering.

$$d_{crit} = k_1 \frac{\lambda_{light}}{NA}. \quad (1.1)$$

The pit size of the optical disc is decreased, by applying either a larger numerical aperture, NA, or by decreasing the wavelength of the applied light. One of the current solutions for Blu-Ray mastering [3], is deep ultraviolet mastering, using a liquid immersion lens to obtain higher NA values. For future generations of optical

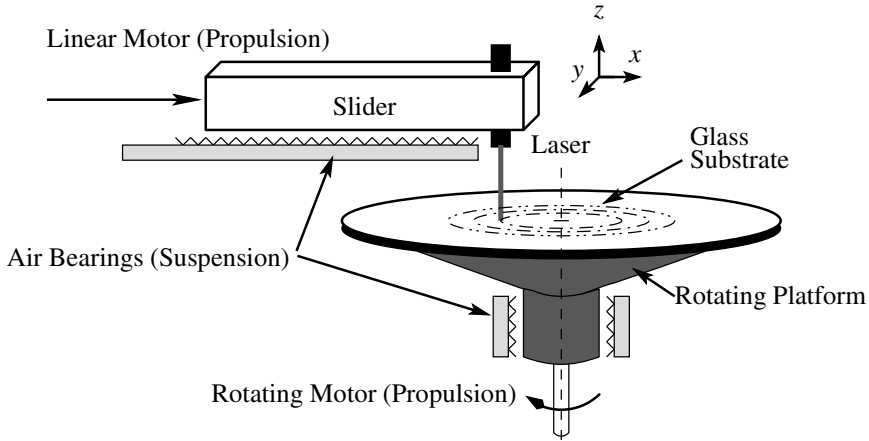


Figure 1.2: Schematic of a currently applied optical disc mastering system. The system consists of a Slider, pointing a pulsed laser beam towards a photoresist coated glass substrate, and a rotating platform spinning this glass substrate.

discs, even higher information densities are desired. Therefore, the application of extreme ultraviolet light or electron beams seems inevitable. Since electromagnetic waves at these wavelengths are absorbed by air, a vacuum environment is required. The vacuum environment introduces the need for vacuum compatible positioning systems, for which magnetic suspension is an option. Two projects were started at Delft University of Technology to demonstrate the capabilities of magnetic suspension technology for vacuum compatible high precision positioning systems, as the optical disc mastering system. These projects included the development of a rotating platform (funding provided by IOP [33]), while the second project entails the work of this thesis on an electromagnetically suspended Slider (funding provided by STW¹). This proposed Slider should have the positioning performance required for manufacturing modern optical discs such as the Blu-Ray disc. The electromagnetic actuator for this Slider is the IU-module.

1.1.2 A novel electromagnetic actuator: the IU-module

In active magnetic positioning systems, a body is held in position contactlessly through electromagnetic forces. The electromagnetic forces are generated using an active position feedback loop. Various research institutions have contributed to the development of electromagnetic positioning systems, also called stages. The

¹Stichting Toegepaste Wetenschappen

research conducted by [46] at Massachusetts Institute Technology shows that these magnetically levitated stages are capable of achieving positioning performance down to 0.05 nm. Research on linear magnetic suspended positioning systems is also conducted at Delft University of Technology in the Netherlands.

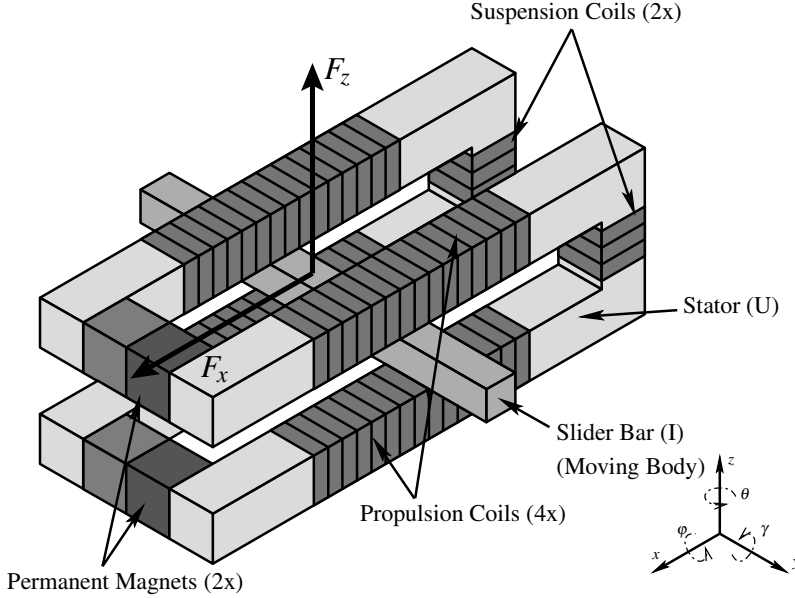


Figure 1.3: The IU-module showing the I-shaped Slider bar (the moving component) and the U-shaped stator, the propulsion force, F_x , and suspension force, F_z . (Electromagnetic details on the operation of the actuator are found in Chapter 3.)

Here, the research of Molenaar [50] resulted in the proposal for a novel active magnetic actuator, the IU-module. The IU-module, with the I-shaped Slider bar and U-shaped stator, is shown in Fig. 1.3. The IU-module is a multi-DoF actuator devised for generating a suspension force, F_z , and a propulsion force, F_x . The suspension force, F_z , is actuated by the suspension coils, while the propulsion coils actuate the propulsion force, F_x . The propulsion actuation uses the “moving iron” principle [50] and has a relatively long stroke. The suspension direction of the IU-module has a limited stroke and mainly functions as a bearing, constraining a specific DoF. In the suspension direction, the IU-module is capable of generating a static force for the compensation of a gravity load, using the permanent magnets. This force is generated by placing the Slider bar in an out of centre z -position in the airgap. No continuous current is required for the creation of this static force, minimising ohmic losses and heat generation within the coils. All coils of the IU-module are situated on the stator, removing the need for shielding moving wires in a vacuum

environment. Due to the lossless suspension force and wireless actuation, the IU-module promises to be an ideal actuator for vacuum applications. By combining three IU-modules, a magnetically levitated Slider for the optical disc mastering can be realised.

In addition to the suspension and propulsion forces, individual actuation of the coils, allows the generation of additional torques. It is uncertain whether these torques can be effectively applied. Molenaar's TU-shaped actuator design suffered from crosstalk between actuation directions. The IU-module resulted from an attempt to reduce this crosstalk.

The starting point for the research is the basic concept of the IU-module, where the IU-module acts as a 2-DoF actuator. The specifics of the actuator design, and the implications of integrating it into a nm-resolution linear positioning system, are still unknown.

1.1.3 Mechatronic design approach for a magnetically suspended positioning system

Active magnetically suspended systems require an active control loop to stabilise the system. This renders the magnetically levitated Slider, a complete mechatronic system comprising of mechanics, electronics, and control. The successful realisation of such a mechatronic positioning system requires an integrated design approach over a variety of disciplines. Mechatronics is the research field, dealing with the design of such complex systems. A graphical depiction of mechatronic positioning system is shown in Fig. 1.4.

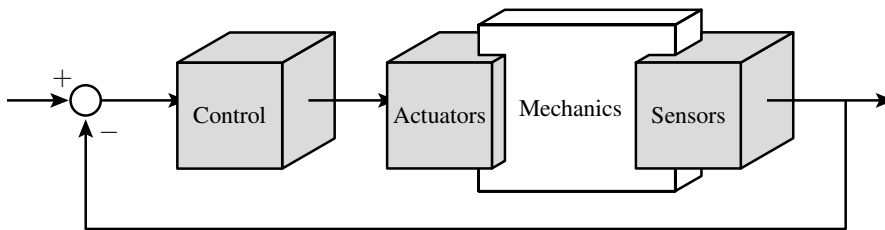


Figure 1.4: A mechatronic positioning system, consisting of mechanics, actuators, sensors and control.

Conventional design methods for precision machines rely on a static error budget to predict the positioning performance. This static error budget will not suffice for the design of a mechatronic system, since the performance is realised through a dynamic position control loop. Research on the development of a Dynamic Error Budget for mechatronic systems has been conducted, [69, 33]. These techniques allow a mechatronic design to be dynamically evaluated over the boundaries of the

various disciplines. The design of the magnetically levitated Slider is expected to benefit from these techniques.

1.2 Problem statement

The primary goal of this research is to determine whether the IU-module is capable of being applied as a 2-DoF actuator in a nm-resolution contactless linear positioning system. To answer this question, the IU-module is integrated into a linear positioning system for optical disc mastering, referred to as the Slider. This Slider is a good example of a contemporary complex precision machine, for which a vacuum compatible actuator might be required in the near future. The Slider has to attain a positioning performance required for manufacturing modern optical discs, such as the Blu-Ray disc. Therefore, the Slider requires a position stability of less than 1 nm (σ) over a stroke of 50 mm, while the other DoFs are held fixed within 5 nm (σ). The design, realisation, and evaluation of the Slider are all integral parts of this research.

The second goal of this research is to determine, how a balanced mechatronic design of the Slider with IU-modules can be achieved. The Slider is a mechatronic system, achieving its performance through an active control loop, consisting of a controller, actuators, mechanics and sensors. The mechatronic system is subjected to both external (e.g. floor vibrations) and internal (e.g. sensor noise, amplifier noise) disturbances. How and to what extent these disturbances influence the positioning performance is determined by the overall mechatronic design and not just by the applied actuator. To reach a position stability of better than 1 nm (σ), a balanced design over the involved disciplines is essential.

The third goal of the research is to establish whether the IU-module is capable of actuating additional DoFs in addition to the suspension and propulsion actuation, and to determine how these additional actuation capabilities can be applied. The IU-module contains 6 coils which can be individually actuated. This might allow the actuation of additional torques. It is not known whether these additional actuation capabilities can be effectively applied.

The optimisation of the IU-module's electromagnetic design is not part of this research. A second project, conducted at the EPE group of the Technical University of Eindhoven, aims at optimising the electromagnetic design for the IU-module [44].

1.3 Outline

This thesis is part of an ongoing research attempt to create an accurate electromagnetically suspended positioning systems. An overview of linear precision positioning systems is found in Chapter 2. Chapter 2 also contains an introduction to the

basic electromagnetic description applied in this thesis.

In Chapter 3, the IU-module is studied and developed. The applied design tools are discussed and compared to actual measurements on the actuator. The feasibility of actuating additional DoFs is experimentally determined. At the end of the chapter, alternatives to the IU-module are presented, which circumvent some of its limitations.

The design of the Slider starts out with the determination of the specifications in Chapter 4. The specifications lead to an initial conceptual design of the Slider. This conceptual design is expanded towards a detailed design. The design process is facilitated by the Dynamic Error Budget. The basics of this method are explained within this chapter.

The Slider for optical disc mastering with the IU-module actuators is realised. To levitate the electromagnetic Slider and realise nm-performance, a position controller has to be designed. The control design and the performance evaluation of the Slider are presented in Chapter 5.

From Chapter 3, it is clear that the IU-module has the capability to actuate on 4-DoF. The flexible modes present in the Slider, limit its performance. By using the additional DoFs of the IU-module, excitation of the flexible modes can be reduced. Chapter 6 demonstrates the use of the over-actuation, present in the Slider, to improve its positioning performance. This will establish the full potential of the IU-module.

Chapter 2

Active magnetic levitation for linear high precision systems

In an active magnetic levitation system, stable magnetic levitation is achieved by an active control loop, where the position is measured and the magnetic fields manipulated to suspend and position an object. These active magnetic levitation systems have found their applications mainly in rotary systems, like turbo-molecular pumps and flywheels¹. Due to their contactless nature and vacuum compatibility, active magnetic levitation promises to be a technology suitable for the next generation of vacuum compatible high precision positioning machines. This can be seen by the recent number of new patent applications for linear magnetically levitated positioning systems, [48, 36, 22, 29, 28, 72, 71, 74].

Section 2.1 defines these high precision systems and shows the advantages of magnetic levitation for high precision systems. The theoretical background of the magnetic levitation systems is covered in Section 2.2. The theoretical force equations show that two basic magnetostatic forces exist, the reluctance force and mutual force between permanent magnets and activated coils. Two actuators, using these forces, are discussed in Section 2.3. In Section 2.4 precision positioning systems, developed by research groups around the world, are summarised. Finally, a comparison is made between these existing systems and the new linear Slider, using the IU-module actuators, in Section 2.5.

2.1 Advantages of magnetic suspension in high precision systems

In precision positioning systems, one object is positioned with respect to another, i.e. the positioning between a tool and a workpiece. How well this positioning is

¹These systems are commercially supplied by the companies Mecos, S2M, and Revolve.

achieved, is a significant contributor to the quality of the end product. Two well known linear positioning systems are the ASML wafer stepper and the laser beam recorder from Singulus Mastering. According to Slocum [67], there are three measures of how well the positioning system performs:

- *Accuracy* The maximum translational or rotational error between any two points in the machine's volume work.
- *Repeatability* Repeatability is the error between a number of successive attempts to move the machine to the same position. The term repeatability is often expressed using its mean and the standard deviation (σ).
- *Resolution* Resolution is the smallest programmable step or the smallest mechanical step the machine can make during a point-to-point motion. Resolution gives a lower bound on the repeatability.

The definitions of accuracy, resolution, and repeatability are relatively simple, but measuring them at nm-level is often rather complicated. To determine these quantities, external references must be used, or a product made from which the quantities can be deduced. A quantity easily established in an actively controlled machine is the *servo-error*. The servo-error is the difference between the set-point placed on the controller and the measured position, using the sensors present in the positioning system. The difference between the *servo-error* and *accuracy* is primarily determined by the design, stability and calibration of the metrology system (low frequency errors). The focus in this thesis is on dynamic errors of the positioning system and thus the *servo-error* is used as a measure of performance. Current state of the art positioning machines have servo-errors in the order of a few nanometres (σ). These positioning stages are mainly built using air bearings and linear motors².

Precision positioning systems are often employed photolithographic processes. To decrease the feature size of these processes, extreme ultraviolet light (wavelength down to 10 nm) or electron beams will be used. Since these sources are absorbed by air and require a vacuum environment, the next generation of positioning systems must be vacuum compatible. Magnetic bearings in contrast to air bearings will not pollute a vacuum environment, because there is no air leakage, making them ideally suited for such an environment.

Improved accuracies in the manufactured features require better accuracies of the positioning systems. In passive air bearings, this accuracy is determined by the accuracy of the bearing surfaces and the bearing stiffness. To increase the bearing stiffness, the airgap can be reduced. However, this leads to higher costs, due to more stringent manufacturing tolerances on the bearing and the guideway.

In magnetic bearings, the final accuracy is achieved by the position control loop applied to stabilise the system. This means that the accuracy mainly is determined

²Suppliers of high precision positioning stages are for example Aerotech and Etel.

by the accuracy of the metrology system. Any remaining alignment or straightness errors of the metrology system can afterwards be compensated by calibration of the machine, and modifying the setpoint to the controller.

A magnetically levitated system uses all of the advantages present in an active control loop. Firstly, active magnetic bearings can theoretically have an infinite static stiffness, when an integrator is present in the control loop. Secondly, in an electromagnetically suspended machine, the force and the metrology loops can be completely separated, see Fig. 2.1. The positioning performance is attained between the metrology reference and the stage through the active control loop. The actuation forces of the stage are placed on a separate force frame, while the metrology reference is isolated from the world (using for example a vibration isolation system). This separated machine architecture has demonstrated being capable of achieving sub-nm stability in a rotating positioning system [33].

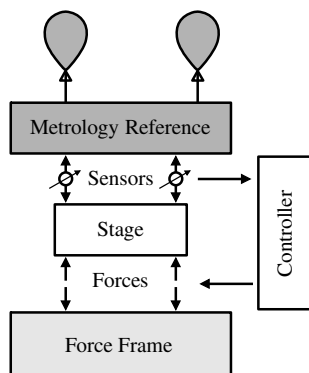


Figure 2.1: Separation between metrology and force loop: The performance of the system is achieved between the metrology reference and the stage, while actuation forces act on a separate force frame.

A complete summary of the advantages of magnetic bearings over air and roller bearings in precision machines is found in [58]. The conclusion from this paper and the previous discussion, is that magnetic levitation systems show potential for high precision vacuum compatible positioning systems.

2.2 Magnetism basics

This section gives a short introduction to magnetic field equations and the magnetostatic forces acting on a body. These magnetostatic forces are applied to levitate precision positioning stages. Electrodynamic levitation forces are not discussed in this section, since they are deemed impractical for high precision positioning sys-

tems [50, 34]. For more detailed information on electromagnetism the reader is referred to [25, 59, 79].

2.2.1 Magnetic field description

The magnetic field is described by the Maxwell equations. The Maxwell equations are given by Eq. 2.1-2.4 (Notation is as used in [25]).

$$\oint_{S_e} \vec{D} \cdot d\vec{A} = Q_{f_{enc}}, \quad (2.1)$$

$$\oint_{S_e} \vec{B} \cdot d\vec{A} = 0, \quad (2.2)$$

$$\oint_{P_e} \vec{E} \cdot d\vec{l} = -\frac{d}{dt} \int_{S_e} \vec{B} \cdot d\vec{A}, \quad (2.3)$$

$$\oint_{P_e} \vec{H} \cdot d\vec{l} = i_{f_{enc}} + \frac{d}{dt} \int_{S_e} \vec{D} \cdot d\vec{A}. \quad (2.4)$$

The electric field, \vec{E} , gives the force on a test charge of 1 C. The magnetic flux density, \vec{B} , represents the force on a current carrying wire, carrying 1 A of current. The symbols, \vec{D} and \vec{H} , represent the electric displacement field and magnetic field strength, respectively, which are intermediate fields for description purposes but are in themselves not directly related to electromagnetic forces. The free electric charge, $Q_{f_{enc}}$, and the free magnetic current density, $i_{f_{enc}}$, constitute the sources of the electromagnetic field. The perimeter, P_e , is any closed path that encircles surface, S_e . The surface element is denoted by $d\vec{A}$.

There are two sources of the magnetic field, \vec{B} , the free current, $i_{f_{enc}}$, and the magnetisation, \vec{M} , present in magnetic materials. The material relation is expressed by Eq. 2.5.

$$\vec{B} = \mu_0(\vec{H} + \vec{M}) \equiv \mu_0\mu_r\vec{H}. \quad (2.5)$$

The relative permeability μ_r is a material property and is often a non-linear functions of \vec{H} . While μ_0 is the permeability of free space.

2.2.2 Magnetic circuit description

The solutions to the Maxwell equations, Eq. 2.1-2.4, are often intricate. When a large part of the magnetic system consists of iron with relatively small airgaps, the magnetic field is aligned with the iron and a simplified description exists. This description is similar to the description of an electric circuit. Therefore, this analogy is called the Magnetic Equivalent Network (MEN) description. The MEN description

creates a better understanding and aids in the development of design rules. Although it is a common analogy [59], it is repeated here to introduce the terminology.

Only slowly varying magnetostatic fields are taken into account (changes much slower than the velocity of light), therefore the dynamic term in the fourth Maxwell equation, Eq. 2.4, is neglected. Assuming the magnetic field is aligned with the physical components, m , as shown in Fig. 2.2, Eq. 2.6 results, where n is the number of turns on the coil, and l_m the length of the component.

$$\sum_{m=1}^k H_m \cdot l_m = ni. \quad (2.6)$$

The material relation, Eq. 2.5, can be substituted in the loop equation, Eq. 2.6, resulting in Eq. 2.7. For the magnetic circuit, the Maxwell's second equation, Eq. 2.2, simplifies to Eq. 2.8.

$$\sum_{m=1}^k \mu_0 \mu_m B_m \cdot l_m = ni, \quad (2.7)$$

$$B_1 A_1 = B_2 A_2 = \dots = B_m A_m. \quad (2.8)$$

The magnetic field, integrated over a surface, is the magnetic flux, Φ . For the circuit, this is expressed as $\Phi = B_m A_m$, where A_m is the area. Combining Eq. 2.7 and Eq. 2.8, the network equation, Eq. 2.9, results.

$$\Phi = \frac{ni}{\sum_{m=1}^k \frac{l_m}{\mu_0 \mu_m A_m}} = \frac{\mathcal{MMF}}{\sum_{m=1}^k \mathcal{R}_m}. \quad (2.9)$$

The magnetic circuit, shown on the left side of Fig. 2.2, is transformed to a magnetic equivalent circuit, shown on the right side of Fig. 2.2. The reluctance, $\mathcal{R}_m = \frac{l_m}{\mu_0 \mu_m A_m}$, is the equivalent of electric resistance. The magnetic flux, Φ , is equivalent to the current and the Magneto Motive Force (\mathcal{MMF}) is the equivalent of voltage, see Tab. 2.1.

The MEN, shown in Fig. 2.2, can be extended to model complex systems and perform optimisation [45]. Non-linear effects like saturation and fringing can be included as is done by [39]. Eddy current losses are included in [15].

2.2.3 Magnetostatic forces

The magnetostatic force, F_{ms} , acting on a target in a magnetic circuit, containing a coil and a permanent magnet, is given by Eq. 2.10 [50].

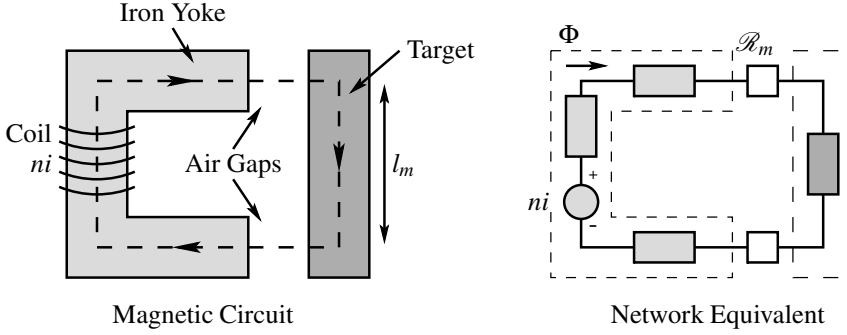


Figure 2.2: Transformation of a magnetic circuit to a Magnetic Equivalent Network (MEN).

Magnetic Circuit			Electric Circuit		
Magneto Motive Force	\mathcal{M}	[A-turns]	Electro Motive Force	\mathcal{E}	[V]
Magnetic flux	Φ	[Tm ²]	Current	i	[A]
Reluctance	\mathcal{R}	[Am ² /T]	Resistance	R	[Ω]

Table 2.1: Table showing analogies between the magnetic and electric network.

$$F_{ms} = \underbrace{\frac{1}{2}i^2 \frac{d\mathcal{L}_{coil}}{dx}}_1 - \underbrace{\frac{1}{2}\Phi_{PM}^2 \frac{d\mathcal{R}}{dx}}_2 + \underbrace{ni \frac{d\Phi_{PM,coil}}{dx}}_3. \quad (2.10)$$

The self inductance of the coil, \mathcal{L}_{coil} , is defined as $\mathcal{L}_{coil} = \frac{n\Phi_{coil}}{i}$, where Φ_{coil} is the flux linked to the coil, and n the number of turns. The displacement of the target is indicated by the x -parameter. Φ_{PM} is the flux generated by the permanent magnet and $\Phi_{PM,coil}$ the permanent magnet flux enclosed by the coil. The magneto-static force, Eq. 2.10, consists of the following three force components, which are illustrated in Fig. 2.3:

1. *Reluctance or magnetisation force generated by a current carrying coil in a magnetic circuit.* The force exerted on the target is proportional to the square of the current, and is therefore independent of its sign. The direction of the force is always such, that it tends to increase the inductance and hereby decreases the reluctance \mathcal{R} . The inductance is equal to $\mathcal{L}_{coil} = \frac{n^2}{\Sigma \mathcal{R}}$, see Eq. 2.9.
2. *Reluctance or magnetisation force generated by a permanent magnet.* The reluctance force generated by the permanent magnet always tends to decrease

the reluctance, \mathcal{R} , of the total circuit. This force is independent of the direction of the magnetic flux.

3. *Mutual force between the current carrying coil and permanent magnet flux.* A force is generated between a position dependent flux, enclosed by a coil, $\frac{d\Phi_{PM,coil}}{dx}$, and the current passed through this coil. The direction of the force is determined by the direction of the current and the flux in the coil. In [50] it is shown, that the mutual force term can be converted to a “conventional” Lorentz force equation, $F = Bil_{coil}$. Here, l_{coil} is the length the coil in the magnetic field, and B the field at the location of the current carrying wire.

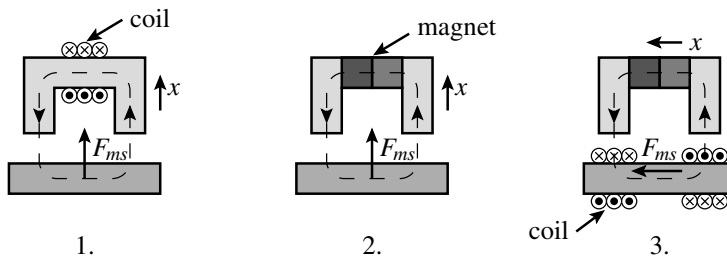


Figure 2.3: Illustration of the three types of magnetostatic force, described in Eq. 2.10.

The force equation, Eq. 2.10, gives rise to two basic magnetic actuators the reluctance and the mutual force actuator. Examples of these actuators are discussed in Section 2.3.

2.3 Actuators for magnetically levitated positioning systems

This section discusses some of the basic magnetic actuators elements, which are applied in the magnetically levitated precision positioning systems shown in Section 2.4. The reluctance actuator is often applied as an active magnetic bearing, to constrain a specific DoF. This type of actuator is discussed in Section 2.3.1. The Lorentz type actuators are mutual force actuators, Eq. 2.10. These actuators are often used in precision systems because of their linear force to current relationship and low stiffness, limiting the transfer of external disturbances. Examples of these Lorentz type actuators are discussed in Section 2.3.2.

2.3.1 Reluctance actuator

The schematic of a reluctance actuator and its control loop, is shown in Fig. 2.4. The actuator consists of a ferromagnetic stator and a rotor, where the rotor is the object to be suspended. It should be noted, that the term rotor is commonly applied in magnetically levitated systems for both linear and rotating systems. Around the central leg of the stator, a coil is wound through which a current is passed. This current generates a magnetic flux, Φ , and this flux creates a reluctance force, F_z , on the rotor. Due to the unstable nature of the electromagnetic forces, an active control loop is required to reach stable suspension. The input to the current amplifier is produced by a digital or analog controller. The input of the controller is formed by a position sensor measuring the position in the airgap. The force acting on the rotor is described by the Eq. 2.11 [33].

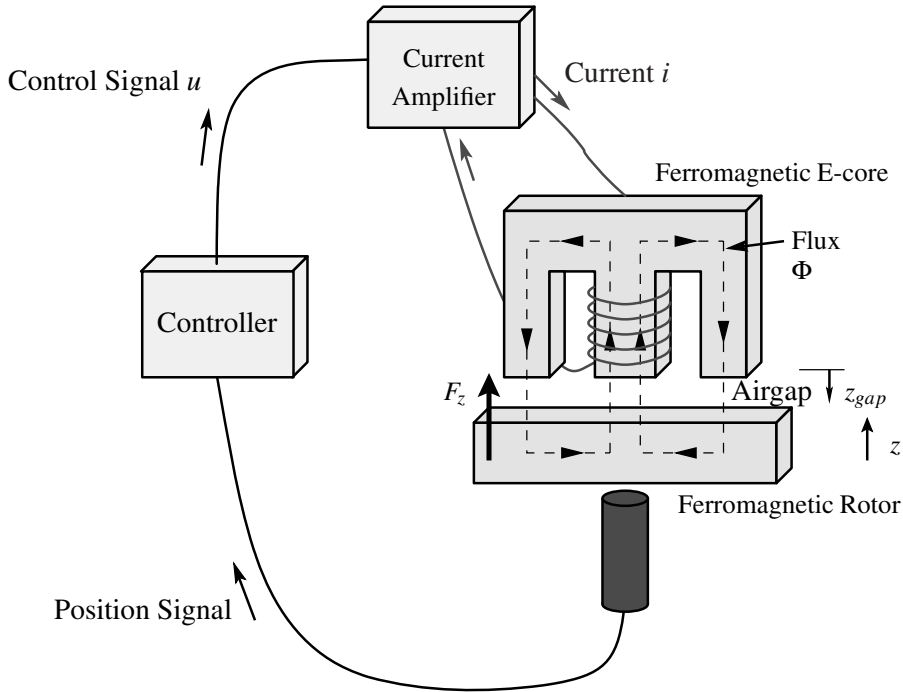


Figure 2.4: Magnetic reluctance actuator with peripheral components

$$F_z = \frac{1}{4} \mu_0 n^2 A_{gap} \cdot \frac{i^2}{z_{gap}^2}. \quad (2.11)$$

The suspension force, F_z , is quadratic dependent on actuation current, i , and inverse quadratic dependent on the airgap position, z_g . Where n is the number of

coil turns, and the area of the airgap is A_{gap} . This type of actuator is only capable of making an attractive force, due to the nature of the reluctance force, Eq. 2.11. To generate an active force in the opposite direction, a second actuator can be placed on the opposite side of the rotor.

Control of a reluctance actuator

An active controller needs to be applied to stabilise the magnetic bearing. To account for the non-linear force characteristic of Eq. 2.11, linearization is required. The basic linearization technique is called bias current linearization. A bias current, i_{bias} , is injected into the coil, which acts as a gravity compensator. Around this bias current, a current variation, the control current, i_{con} , is applied. Stabilisation is only achieved when the deviations of the displacement, z , and the control current are small. The bias current linearization process, at the nominal airgap position, z_0 and $z = 0$, is illustrated by Eq. 2.12-2.14, where $k_N = \frac{1}{4}\mu_0 n^2 A_{gap}$.

$$F_z = k_N \cdot \frac{i^2}{z_{gap}^2} = k_N \cdot \frac{(i_{bias} + i_{con})^2}{(z_0 - z)^2}, \quad (2.12)$$

$$F_z \approx F_0 + \left. \frac{\partial}{\partial z} F_z \right|_{i_{con}=0, z=0} z + \left. \frac{\partial}{\partial i_{con}} F_z \right|_{i_{con}=0, z=0} i_{con} + \dots, \quad (2.13)$$

$$F_z \approx F_0 + 2k_N \frac{i_{bias}^2}{z_0^3} z + 2k_N \frac{i_{bias}}{z_0^2} i_{con} = F_0 - k_{zz} z + h_{zz} i_{con}. \quad (2.14)$$

The constants, k_{zz} and h_{zz} , represent the bearing stiffness and actuation constant, respectively. It should be noted that the stiffness, k_{zz} , is negative and tends to destabilise the magnetic bearing. To stabilise this system, a linear controller with position and derivative feedback can be applied, a so called PD controller. The PD controller should have a high gain to suppress the negative stiffness. An overview of alternative linear control strategies, like voltage control, flux control and sensorless³ control is found in [8].

The bias current results in energy dissipation, due to ohmic losses within the coil. Such heat generation within nm-precision positioning systems is generally undesirable. A larger bias current also results in larger negative stiffness, making it more complex to control the instability [21]. To limit bias current and extend the range, non-linear controllers can be used. A feedback linearization scheme is presented in Fig. 2.5. In this scheme the square root is taken of the output of the linear controller and then multiplied by the actual airgap. In the research of [73] a comparison is made between this non-linear technique and the common linear control. Jabben [33] uses this non-linear control strategy to limit the negative stiffness in a rotating magnetic bearing to achieve nm-resolution.

³In sensorless magnetic bearings the inductance of the coil is used to estimate the position.

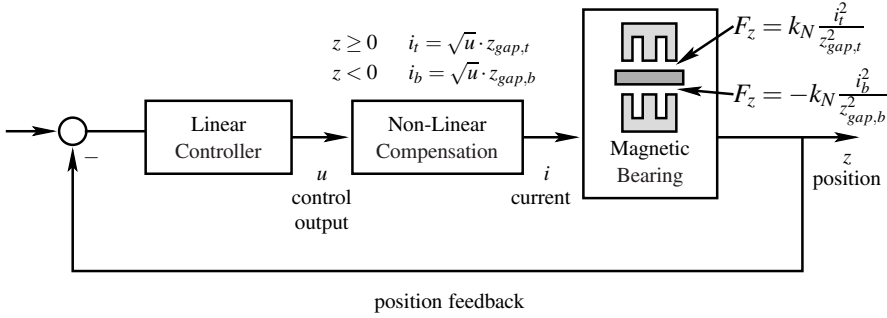


Figure 2.5: Schematic of feedback linearization non-linear control strategy for a 2 E-core system. The force on the rotor is indicated by F_z , while the subscript t indicates top E-core, and b indicates the bottom E-core. When the feedback linearization scheme is implemented, the force on the rotor is to $F_z = k_N u$. More information on this non-linear control method is found in [73, 33].

Permanent magnet integration

To limit heat generation within the active magnetic bearing, a permanent magnet can be integrated to generate a bias flux. Two basic layouts for a magnetic bearing with a permanent magnet exists, the series and parallel configuration, as shown in Fig. 2.6.

In the series structure, the flux from the coil passes through the permanent magnet. In the parallel structure, flux from the coil does not pass through the permanent magnet; only in the airgap the flux paths are combined. The reluctance experienced by the coil in the parallel configuration is less when compared to the series configuration, because the flux does not pass through the permanent magnet, which has a low permeability (NdFeB, $\mu_{PM} \approx 1.1$). This results in a lower control current, and thus lower dissipation in the coil. A second limitation to the series configuration is the risk of local saturation of the steel core, through which the control flux passes, which might lead to non-linearities in the actuator.

Conclusions on reluctance actuators

Large force densities can be obtained with reluctance actuators. According to [49], the maximum force of a reluctance actuator is given by Eq. 2.15.

$$F_{max} = \frac{\Phi_{max}^2}{2\mu_0 A_{gap}} = \frac{B_{sat}^2 A_{gap}}{2\mu_0}. \quad (2.15)$$

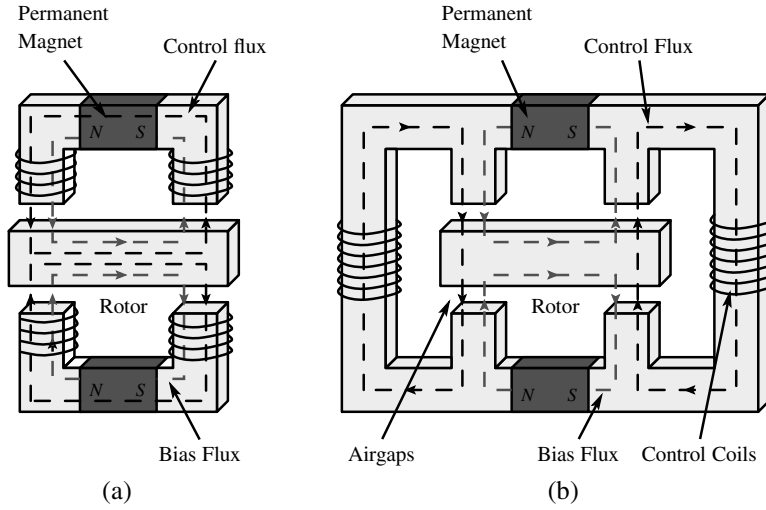


Figure 2.6: Magnetic bearing with permanent magnet to generate the bias, series configuration (a), and parallel configuration (b).

Where the maximum flux density, Φ_{max} , in the airgap is determined by the saturation flux density of the stator, assuming that the stator has the same area as the airgap. The magnetic saturation flux density, B_{sat} , is the maximum flux that can be attained in the ferromagnetic material. The maximum pressure of this reluctance actuator is then estimated to be $1 \cdot 10^6 \text{ N/m}^2$ ($B_{sat} = 1.6\text{T}$). By incorporating permanent magnets in the reluctance actuator, it is possible to attain these forces without any power consumption. Therefore, reluctance actuators are ideally suited for carrying the weight of a positioning stage. A drawback of reluctance actuators is the destabilising negative stiffness. Secondly, this type of reluctance actuator is often characterised by a limited stroke.

2.3.2 Lorentz force actuators

The Lorentz force, Eq. 2.16, is directly proportional to the current passed through the coil and the flux density at the location of the coil. In Eq. 2.16, the vector, \vec{l}_{coil} , denotes the length and direction of the current carrying wire.

$$\vec{F} = i \oint \left(d\vec{l}_{coil} \times \vec{B} \right). \quad (2.16)$$

An example of a Lorentz force actuator is the voice-coil motor, depicted in Fig. 2.7a. Due to a constant \vec{B} , it has a low to zero stiffness, $\frac{dF_x}{dx}$ and $\frac{dF_z}{dz}$. This minimises the connection to the outside world and eliminates the transfer of disturbances to the moving body, due to external perturbations. The control of the

voice-coil actuator is less complex than the control of a reluctance actuator, due to the linear to force-current relationship and the lack of a large negative stiffness. The Lorentz force actuator does require a current to generate a force, resulting in ohmic losses within the coil. For larger strokes, actuators with sinusoidal magnetic flux distributions and coils with commutated current, can be employed, see Fig. 2.7(b). The commutation of the currents will add to the complexity of the control loop. The actuator in Fig. 2.7(b) can be used to generate a propulsion as well as a suspension force [37]. The actuators of Fig. 2.7 are applied as “moving coil” or as “moving magnet”.

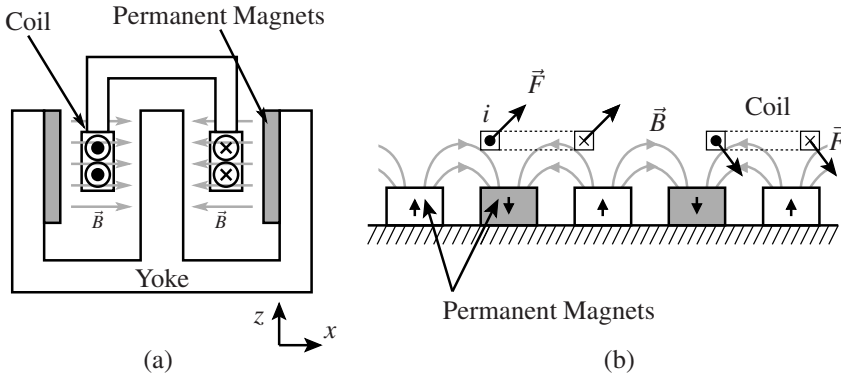


Figure 2.7: Voice-coil motor with a constant \vec{B} -field in the gap (a), Planar motor with permanent magnets and moving coils (b).

An alternative Lorentz force actuator to the “moving magnet” and “moving coil” is the “moving iron” principle of Molenaar [50], as shown in Fig. 2.8. In the “moving iron” principle, a moving piece of iron constitutes the change in enclosed flux by the coil. The “moving iron” has a linear force-current relationship similar to that of a voice-coil actuator. The “moving iron” principle is applied in the IU-module and further discussed in Section 3.1.

2.4 Precision positioning stages

Several research institutions and universities have been working on the development of high precision linear magnetically levitated positioning systems, sometimes referred to as magnetically levitated stages. These stages use the basic actuators, as presented in Section 2.3. An overview of these linear magnetically levitated stages is given in this section.

The first project, to the authors knowledge, in which nm-position stability combined with magnetic levitation was achieved, is the positioning stage developed by

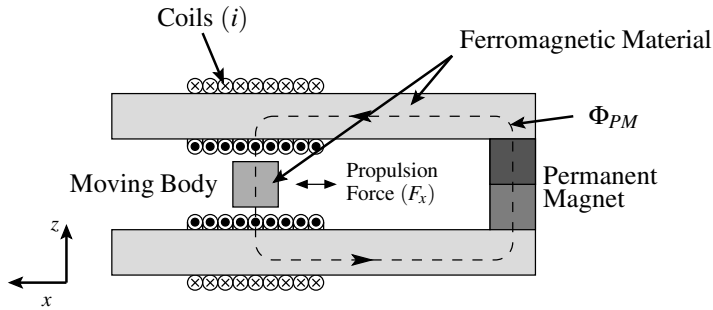


Figure 2.8: The “moving iron” principle [50] for propulsion, F_x , with stationary magnet and coil.

Trumper [70] at Massachusetts Institute of Technology in 1990⁴. The idea of the positioning stage grew out of the proposal of an Ångström Resolution Measuring Machine [20]. Trumper's stage is a 5-DoF actively controlled magnetically levitated linear Slider. The system reaches a peak to peak position stability of 5 nm and a stroke of 50 mm. Ideas developed by Trumper led to the development of several other positioning stages, discussed in the subsequent paragraphs.

In 1996, Ludwick, Trumper and Holmes [46] build the Ångström positioning stage with a resolution of 0.05 nm (σ). The application of this Ångström positioning stage is in Scanning Tunnelling Microscopy (STM), where an electrically charged tip is placed above a moving conductive sample. The resulting current between tip and sample is a measure for their relative distance. A picture of the sample surface was reconstructed with a resolution up to 0.2 nm [31]. The stroke of the system was 100 μm in the two planar directions, which was sufficient for the STM. The stage is actuated by E-core magnetic bearings. To obtain damping within the system, the stage is floated in oil. The advantages of mechanical contact damping over a digital controller damping are that it has no limited bandwidth and it does not introduce noise, since it is a passive component. The oil also serves as a gravity compensator and creates a high frequency stiffness coupling between the stage and the machine frame. The oil present in the Ångström stage forms an obstacle for introducing it into a vacuum environment. The control bandwidth of the stage is 5 Hz, although this is rather low, the positioning performance of the stage is remarkable.

In 1998, Kim and Trumper [37] developed the magnetic levitation stage shown in Fig. 2.9(a). For propulsion and suspension actuation of the stage, it uses a Halbach [27] magnet array with commutated stationary coils, similar to Fig. 2.7(b). The suspension and propulsion actuation of the stage is completely wireless, making it

⁴The years of publication are used in this section, because actual construction date is hard to establish.

extremely suitable for vacuum applications. The specifications for this stage are taken from a wafer stepper. In the wafer stepper, a silicon wafer is illuminated with a desired pattern to create an integrated circuit. The stage is capable of 50 mm x 50 mm stroke with a positioning error of 5 nm (σ). Kims stage is not submerged in oil and uses an active controller to create the required damping. The closed-loop bandwidth of the system is 50 Hz.

Holmes, Hocken and Trumper [30] developed the LOng Range Scanning Stage (LORS) positioning stage in 2000. The LORS is a follow up to the Ångström stage and has a stroke of 25 mm × 25 mm. The stage uses the ideas from Kims Halbach motor assembly for suspension and propulsion actuation. The stage has a positioning noise in horizontal direction of 0.2 nm (σ) and in vertical direction of 0.7 nm (σ). The system has a targeted positioning accuracy of 10 nm. The design of the LORS stage, uses a kinematically mounted metrology frame to measure the position of the stage on which the sample is placed. The LORS stage is submerged in oil like the Ångström stage.

In 2003 at Samsung, Kim et al. [35] developed a magnetic levitation stage using E-core magnetic bearings, as shown in Fig. 2.10. This stage is capable of obtaining 0.1 μ m suspension position accuracy and a 0.5 arc-seconds rotation accuracy for all rotations. The stage has a stroke in its propulsion direction of 100 mm. The stage uses reluctance actuators as bearings and uses a separate linear motor for propulsion. Offline straightness compensation is added to ensure straight motion of the stage.

De Klerk et al. [38] developed a linear magnetically levitated stage at Philips Applied Technologies, as shown in Fig. 2.11. The stage has a 1.1 nm (σ) position error over a 120 mm stroke. The stage uses E-core reluctance actuators for suspension and uses separate Lorentz force actuators for propulsion. A crucial factor in the design has been minimisation of leakage flux outside of the system, because it was designed for E-beam writer applications, where any magnetic field distorts the operation of the system. The change in the magnetic field outside the shielded part of the system is less than 1 mT.

Cho et al. [11] built a magnetically levitated stage using a 2-dimensional Halbach magnet array, see Fig. 2.12. The magnets are on the fixed world while the coils move. This configuration allows a larger planar stroke than the design by Kim et al. 2.9. The Cho et al. demonstrator is a proof of concept, without an attempt to achieve high accuracies.

Compter [13] built a “moving coil” stage in 2004 at Philips Applied Technologies. The stage is a 6-DoF actuated stage. It uses the Lorentz force for suspension and propulsion. A 2-dimensional Halbach magnet array is attached to fixed world. The stage is designed as a positioning stage for a wafer stepper. The positioning performance of this system is not known. The system is made to be completely vacuum compliant by shielding of the cables attached to the stage. At the Euspen 2006 conference, a “moving magnet” version of the stage was presented, removing the need of transferring wires to the moving system. At the Technical University of

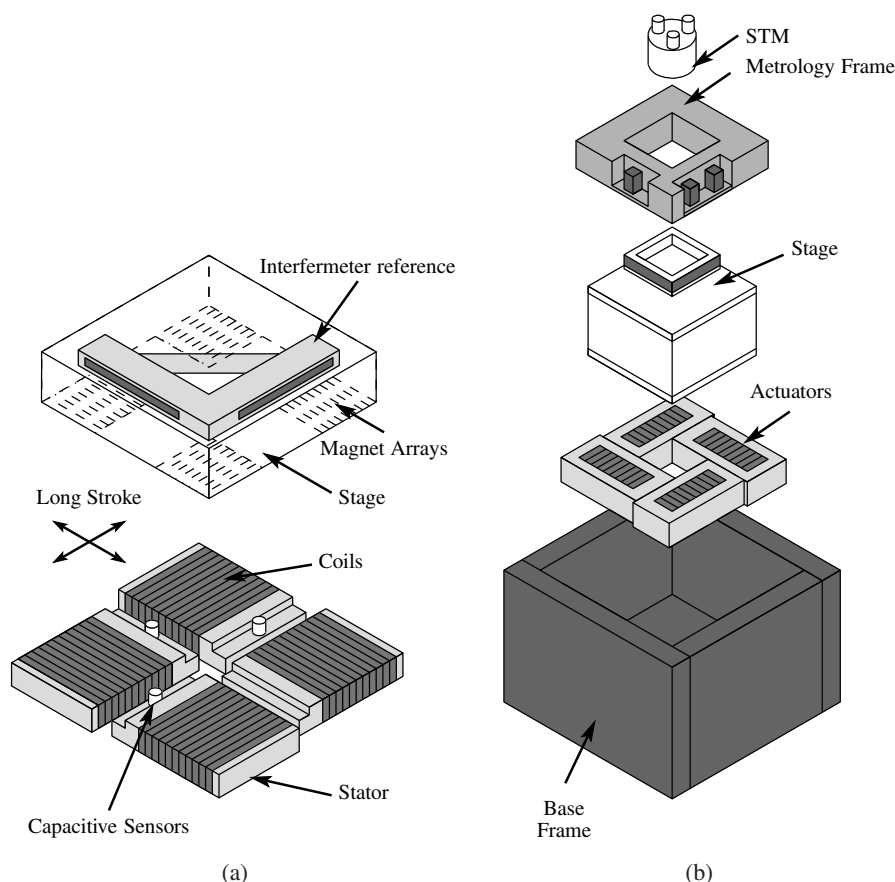


Figure 2.9: Positioning stages of Kim and Trumper [37] (a), and Holmes et al. [30] (b), both using a Halbach magnet array and stationary coils.

Eindhoven, an inverted planar motor was separately realised by Jansen [34]. This system has a servo-error of less than $0.5 \mu\text{m}$. The inverted planar motors are very promising vacuum compatible designs, because they allow a large stroke and the coils are situated on the stator, where they can easily be cooled.

Auer [4] built a positioning stage at the Microtechnology Laboratory in Delft (predecessor of the Advanced Mechatronics group) in 1990, see Fig.2.13. This stage uses a conventional 2 E-core current biased layout, while placing a secondary set of windings on the moving body to create a propulsion force, using the Lorentz force principle. The suspension uses the bias current linearization technique, of Section 2.3.1. The bias flux used in the suspension, is also used as the field on which the Lorentz force acts for activation of the propulsion. Auer's design proved that it

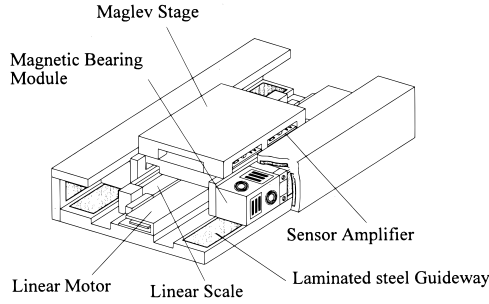


Figure 2.10: Linear positioning stage by Kim et al. at Samsung [35].

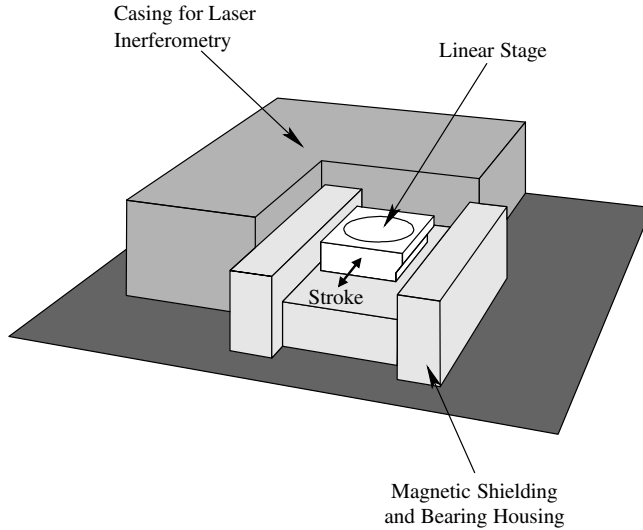


Figure 2.11: Linear stage by de Klerk et al. [38].

is possible to use the bias flux as a source for the Lorentz force without significant crosstalk. The stroke of the stage in the suspension directions is 1 mm, and in the propulsion directions 10 mm. The achieved position resolution is 0.3 μm . Control bandwidths of 100 Hz have been demonstrated.

The Planar Active Magnetic Bearing, the PAMB, was built at Delft University of Technology, as a follow up to Auers stage. The limitations of the PAMB led to development of the IU-module, the actuator researched in this thesis. Figure 2.14

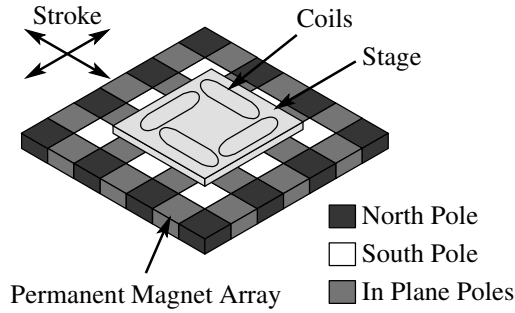


Figure 2.12: Two dimensional positioning stage suggested by Cho et al. [11].

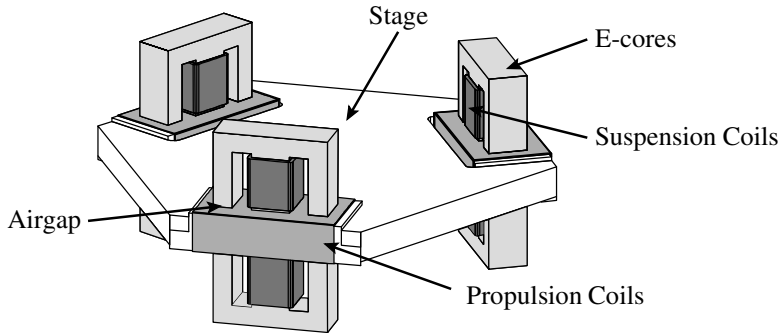


Figure 2.13: Auer's [4] planar positioning stage was built at Delft University of Technology.

shows the PAMB setup. The uniqueness of the PAMB setup is that the suspension and the propulsion do not require magnets nor wires on the moving stage. The weight of the stage is compensated using forces generated by the permanent magnets, resulting in a low power consumption for the suspension ($< 1\text{mW}$ was demonstrated). The performance of the PAMB are summarised in Tab. 2.2.

The positioning stability in propulsion was 37.5 nm . It was limited by a controller bandwidth of only 12 Hz . The open-loop bandwidth in suspension direction of 110 Hz is relatively good compared to the propulsion. The PAMB suffered from crosstalk between the different actuation directions. This coupling manifests itself at the following points:

- Electromagnetic coupling between the suspension directions, due to changing flux path lengths, which are dependent on propulsion and suspension positions.

Item	Performance
Suspended mass	3.37 kg
Propulsion stroke	+/- 50 mm
Suspension stroke	+/- 0.25 mm
Position stability suspension	37.5 nm (σ)
Position stability propulsion	37.5 nm (σ)
Open-loop bandwidth suspension	110 Hz
Open-loop bandwidth propulsion	12 Hz
Stiffness suspension	$1 \cdot 10^6$ N/m
Stiffness propulsion	50 N/m
Maximum force suspension	40 N (1 coil at 2 A)
Maximum force propulsion	6.5 N (2 coils at 4 A)

Table 2.2: Achieved results with the PAMB by Molenaar [50].

- A mechanical coupling exists in xy -plane, due to the changing application point of the propulsion force with respect to the CoG (centre of gravity) of the stage.

The controllers, present in the PAMB, are not able to compensate for the cross-talk, since Single Input Single Output controllers are applied. Still, the PAMB had an adequate performance, and showed the potential of multi-DoF electromagnetic actuators in precision systems. To obtain even better performance, an improved means of decoupling is required. Such decoupling can be reached through advanced control techniques or through a modified actuator design. An attempt was made to apply system identification techniques to improve the controller of the PAMB [63]. However, even in the centre position, it proved to be quite complex and no significant improvements were achieved. Molenaar advised modifying the design of the actuator, as he suggested the IU-module, which will be discussed in Chapter 3.

2.5 Comparison between alternatives for the Slider applied in optical disc mastering

In this section, a comparison is made between the systems, presented in Section 2.4, and the proposed Slider, using the IU-module actuators. The Slider for optical disc mastering must be vacuum compatible and has to obtain sub-nanometre resolution. One of the challenges in a vacuum environment is to have low power dissipation to minimise thermal deformation of the precision system. In addition to this, the amount of electrical connections to the Slider should be minimised to limit contamination of this vacuum environment and the transfer of disturbances. The Slider for

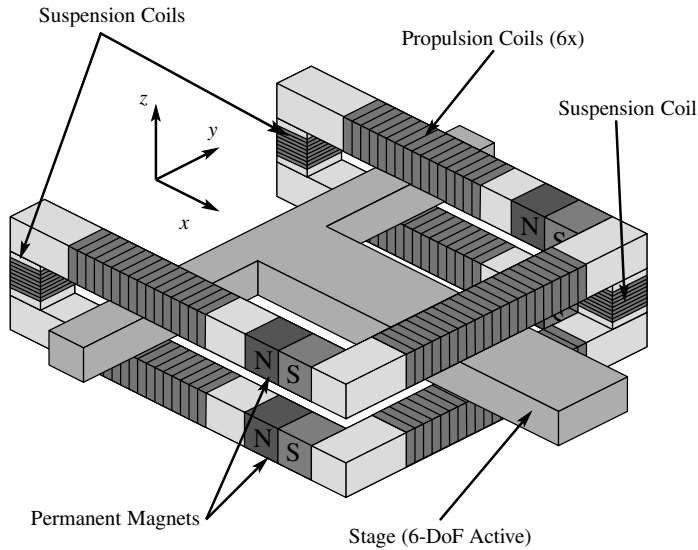


Figure 2.14: PAMB, TU shaped Planar Active Magnetic bearing by Molenaar.

the optical disc mastering process has its highest performance requirement in the propulsion direction.

The stages of de Klerk et al. [38] and Kim et al. [35] best resemble the vacuum compatibility and precision requirements for the Slider. Both systems use reluctance actuators to suspend the Slider, minimising the energy consumption. In the propulsion direction these Sliders use Lorentz force actuators for propulsion, minimising the transfer of disturbances. The actuators of both systems are attached to the moving body. This introduces the complexity of moving wires in a vacuum environment.

A Slider design using IU-modules, as proposed in the Chapter 1, eliminates the need for wires going to a moving body, since it allows wireless actuation. Secondly, a Slider using the IU-modules might lead to a more compact design, since motor and bearing functions are integrated. In Chapter 3, the IU-module is discussed in more detail. While Chapter 4 focusses on the integration of the IU-module in the Slider.

Chapter 3

The IU-module

The IU-module is originally devised as a 2-DoF (degrees of freedom) electromagnetic actuator for actuation of a suspension and a propulsion force. The actuation forces are generated without any wires connected to the moving part of the actuator. Due to its wireless capabilities and compact design, the IU-module has the potential to become a vacuum compatible modular actuator for use in a new generation of high precision systems. The suspension force is generated by a reluctance force, while the propulsion force uses the Lorentz force like “moving iron” concept. The original concept of the IU-module is devised by Molenaar [50]. To demonstrate the capabilities of the IU-module, it is used as a basic building block in the development of the nm-resolution electromagnetic levitated Slider, described in Chapter 4.

To realise a suitable IU-module for the Slider, an electromagnetic design is performed. This electromagnetic design of the IU-module is a joint effort with Anton Lebedev at Technical University of Eindhoven [44]. The basic operating principle and the design are presented in sections 3.1 and 3.2, respectively. Test setups are realised to evaluate performance of the designed actuator and the validity of the applied modelling methods. The design of the test setups and measurement results are found in Section 3.3.

During the course of the research on the basic 2-DoF IU-module, it became clear, that the IU-module is capable actuating 2 additional torques, next to the suspension and propulsion forces. These additional actuation capabilities are investigated in Section 3.5. Finally, in Section 3.6 alternative designs are presented, circumventing some of the limitations of the IU-module design.

3.1 The 2-DoF IU-module

Previous research [50] showed that a planar magnetic bearing with integrated propulsion actuation, is capable of reaching sub- μm positioning performance with low power consumption, which was discussed in Section 2.4. Molenaar’s PAMB (Pla-

nar Active Magnetic Bearing) suffered from magnetic and mechanical coupling between the DoFs. As a solution to these problems, Molenaar posed the idea of the IU-module. A schematic of the IU-module is shown in Fig. 3.1. The schematic shows an I-shaped Slider bar and U-shaped stator bars. The IU-module is capable of suspending the I-shaped bar in z -direction and propelling it in the propulsion x -direction. In the next 2 subsections, the basic principles of operation for the suspension and propulsion actuation are elaborated.

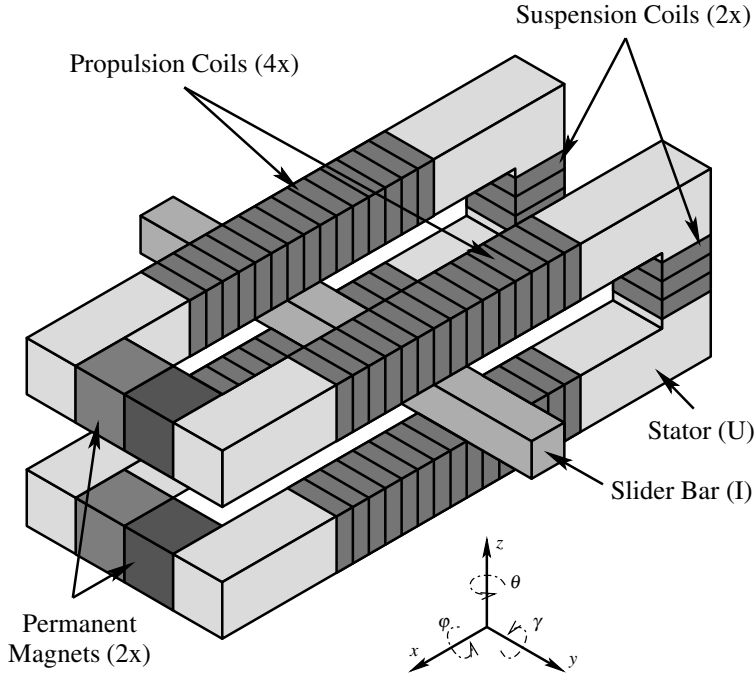


Figure 3.1: The IU-module showing all components. The IU-module is capable of generating a suspension force in z -direction, and a propulsion force in x -direction on the Slider bar. Both the Slider bar and stator are made from ferromagnetic materials.

3.1.1 Actuation of the suspension direction

The suspension is a magnetic bearing where the bias flux is generated by a permanent magnet, as described in Section 2.3.1. The suspension direction belongs to the formal class of the parallel switched flux machines. Figure 3.2 shows the nominal flux paths for generating a suspension force, F_z . The permanent magnet creates a bias flux, Φ_{bias} , through the stator bars, crossing through the airgaps, and into the Slider bar. The bias flux then passes along the length of the Slider bar and returns

through the stator bar on the opposite side of the IU-module. A similar flux path at the bottom side of the IU-module is generated by the lower permanent magnet. The current, i_z , through the suspension coils generates a control flux, Φ_{con} , at the back of the IU-module. This flux takes its path through the stator bars, crosses through the airgap into the Slider bar and then returns directly through the lower stator bar. This scheme places a surplus of flux in the upper airgap, $\Phi_{gap,t} = \Phi_{bias} + \Phi_{con}$, while creating a shortage of flux in the bottom airgap $\Phi_{gap,b} = \Phi_{bias} - \Phi_{con}$. The resulting force on each side of the Slider bar is approximately equal to $F_z = \frac{1}{2} \frac{\Phi_{gap,t}^2 - \Phi_{gap,b}^2}{\mu_0 A_{gap}}$, where A_{gap} is the area of the gap, and where μ_0 is the permeability of free space.

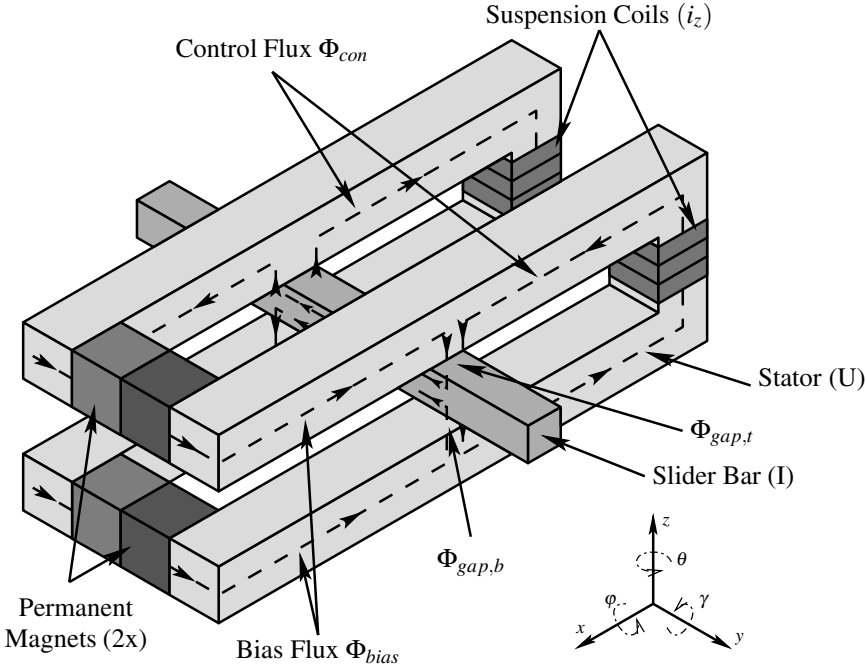


Figure 3.2: IU-module, showing simplified flux paths, contributing to the suspension force on the Slider bar. The Slider bar is at the centre airgap position, $z = 0$ and $x = 0$. Propulsion coils are not visible.

The bias flux locally linearizes the suspension force, F_z , with respect to the control current, i_z , and suspension z -position. The linearized force in suspension direction can be described by $F_z = -k_{zz} \cdot z + h_{zz} \cdot i_{zz}$, similar to Eq. 2.14. Here k_{zz} and h_{zz} are the stiffness and actuation constants, dependent on geometry and material properties. The negative stiffness, k_{zz} , together with a z -displacement of the Slider bar allows for compensation of a static load without energy consumption. The IU-module is capable of making a small stroke in z -direction of up to few millimetre

(depending on airgap size and magnetic design). The application point of the suspension force, F_z , moves along with the Slider bar as it moves in the propulsion x -direction.

1st-order approximation of the magnetic field in the suspension direction

The IU-module has a intricate magnetic structure. The circuit description of Section 2.2.2 is applied to magnetic flux paths, as indicated in Fig. 3.3. The following assumptions are made:

- Linear magnetic behaviour of the permanent magnet, and thus its permeability can be approximated by a constant.
- No loss of magnetisation in the permanent magnets, for example due to thermal effects.
- No leakage flux, outside of the circuit.

The bias flux generated by each of the permanent magnets, Φ_{bias} , splits up into 2 branches, one directly passes through the airgap into the Slider bar, while the other passes through the back of the IU-module and enters the IU-module through the airgap on the opposite side. In the centre $z = 0$ -position, the bias flux passing through the back of the IU-module cancels due to symmetry. The flux entering the Slider bar through the airgap at the right side is given by Eq.3.1-3.2. Definitions of subscripts: t - top, b - bottom, $front$ - front stator of IU-module near PM, $back$ - back stator of the IU-module, bar - Slider bar, $bias$ - bias flux from the permanent magnets and con - control flux path.

$$\Phi_{gap,tr} = \frac{\mathcal{R}_{gap,br} + \mathcal{R}_{back,br} + \mathcal{R}_{back,tr}}{\mathcal{R}_{gap,tr} + \mathcal{R}_{gap,br} + \mathcal{R}_{back,br} + \mathcal{R}_{back,tr}} \Phi_{bias,t} + \dots$$

$$\frac{\mathcal{R}_{gap,br}}{\mathcal{R}_{gap,tr} + \mathcal{R}_{gap,br} + \mathcal{R}_{back,br} + \mathcal{R}_{back,tr}} \Phi_{bias,b} + \Phi_{con,r}, \quad (3.1)$$

$$\Phi_{gap,br} = \frac{\mathcal{R}_{gap,tr}}{\mathcal{R}_{gap,tr} + \mathcal{R}_{gap,br} + \mathcal{R}_{back,br} + \mathcal{R}_{back,tr}} \Phi_{bias,t} + \dots$$

$$\frac{\mathcal{R}_{gap,tr} + \mathcal{R}_{back,br} + \mathcal{R}_{back,tr}}{\mathcal{R}_{gap,tr} + \mathcal{R}_{gap,br} + \mathcal{R}_{back,br} + \mathcal{R}_{back,tr}} \Phi_{bias,b} - \Phi_{con,r}. \quad (3.2)$$

The magnetic flux generated by each source is given by Eq. 3.3-3.4. Where n is the number of turns, H_{PM} is the coercive force of the permanent magnet, and l_{PM} the length of the permanent magnet.

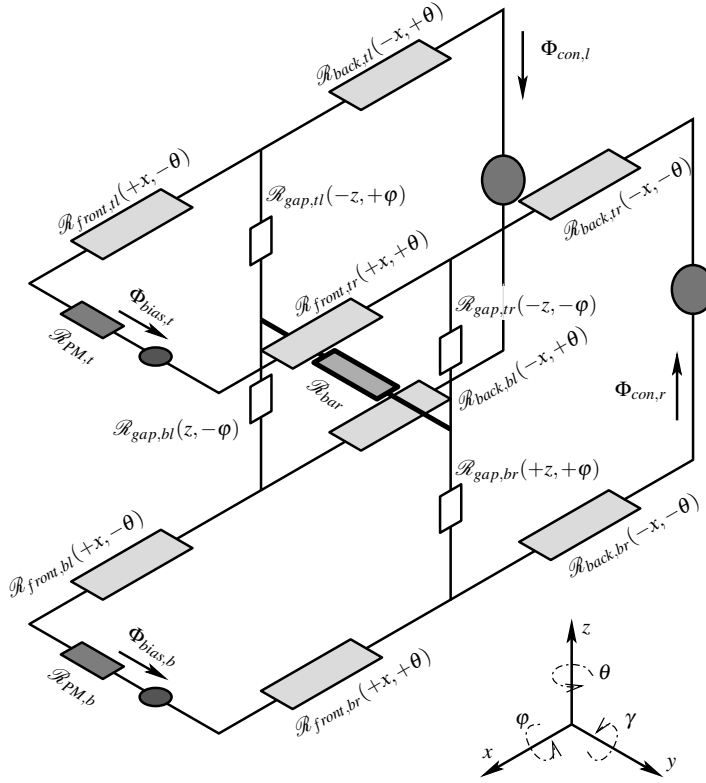


Figure 3.3: Magnetic equivalent network of IU-module, with geometric dependance of the reluctance $\mathcal{R}_m = \frac{l_m}{\mu_0 \mu_m A_m}$ indicated. (Definitions of subscripts: *t* - top, *b* - bottom, *front* - front stator of IU-module near PM, *back* - back stator of the IU-module, *bar* - Slider bar, *bias* - bias flux from the permanent magnets and *con* - control flux path).

$$\Phi_{bias,t} = \left(\frac{H_{PM,t} \cdot l_{PM,t}}{\mathcal{R}_{bias,t}} \right), \quad \Phi_{bias,b} = \left(\frac{H_{PM,b} \cdot l_{PM,b}}{\mathcal{R}_{bias,b}} \right), \quad (3.3)$$

$$\Phi_{con,r} = \frac{n \cdot i_z}{\mathcal{R}_{con,l}}, \quad \Phi_{con,l} = \frac{n \cdot i_z}{\mathcal{R}_{con,r}}. \quad (3.4)$$

The summed reluctance for each source is given by:

$$\mathcal{R}_{con,r} = \mathcal{R}_{back,tr} + \mathcal{R}_{gap,tr} + \mathcal{R}_{gap,br} + \mathcal{R}_{back,br}, \quad (3.5)$$

$$\mathcal{R}_{con,l} = \mathcal{R}_{back,bl} + \mathcal{R}_{gap,bl} + \mathcal{R}_{gap,tl} + \mathcal{R}_{back,tl}, \quad (3.6)$$

$$\begin{aligned} \mathcal{R}_{bias,b} = & \mathcal{R}_{front,br} + 1 / \left(\frac{1}{\mathcal{R}_{gap,br}} + \frac{1}{\mathcal{R}_{back,br} + \mathcal{R}_{back,tr} + \mathcal{R}_{gap,tr}} \right) + \mathcal{R}_{bar} \\ & + 1 / \left(\frac{1}{\mathcal{R}_{gap,bl}} + \frac{1}{\mathcal{R}_{gap,tl} + \mathcal{R}_{back,tl} + \mathcal{R}_{back,bl}} \right) + \mathcal{R}_{front,bl} + \mathcal{R}_{PM,b}, \end{aligned} \quad (3.7)$$

$$\begin{aligned} \mathcal{R}_{bias,t} = & \mathcal{R}_{front,tr} + 1 / \left(\frac{1}{\mathcal{R}_{gap,tr}} + \frac{1}{\mathcal{R}_{back,tr} + \mathcal{R}_{back,br} + \mathcal{R}_{gap,br}} \right) + \mathcal{R}_{bar} \\ & + 1 / \left(\frac{1}{\mathcal{R}_{gap,tl}} + \frac{1}{\mathcal{R}_{gap,bl} + \mathcal{R}_{back,bl} + \mathcal{R}_{back,tl}} \right) + \mathcal{R}_{front,tl} + \mathcal{R}_{PM,t}. \end{aligned} \quad (3.8)$$

From Fig. 3.3 and Eq. 3.5-3.8, it is clear that the angular DoFs, γ and θ , do not directly influence the total reluctance of the flux paths. Therefore, the angular DoFs, γ and θ , are only of a second order influence on the nominal flux paths. The angle, φ , does influence the bias flux paths directly due to the path at the back of the IU-module. The force on the right side of the Slider bar is equal to:

$$F_{z,r} = \frac{\Phi_{gap,tr}^2}{2\mu_0 A_{gap}} - \frac{\Phi_{gap,br}^2}{2\mu_0 A_{gap}}. \quad (3.9)$$

Equation 3.9 leads to the linearised equation, Eq. 3.10, if the following conditions are satisfied:

- The permanent magnets on the top and bottom side have an equal energy product (The permanent magnets have the same magnetic properties).
- The system is electromagnetically symmetrical in y-direction, allowing the force to be multiplied by a factor of 2.
- The reluctance of the iron stator parts in the control flux path, Φ_{con} , can be neglected. This is valid as long as the control flux only passes through non-saturated iron parts.

$$\begin{aligned} F_z \approx & F_0|_{z=0,i=0} + \frac{dF_z}{dz} \cdot z + \frac{dF_z}{di} \cdot i, \\ \approx & -k_{zz} \cdot z + h_{zi} \cdot i, \\ k_{zz} = & -4 \frac{\mu_0 A_{gap} H_{PM}^2 l_{PM}^2 h_{gap}}{\left(-h_{gap}^2 - \left(\frac{l_{bar} A_{gap} h_{gap}}{\mu_{bar} A_{bar}} \right) - \left(\frac{l_{PM} A_{gap} h_{gap}}{\mu_{PM} A_{PM}} \right) \right)^2}, \\ h_{zz} = & 2 \frac{n \mu_0 A_{gap} H_{PM} l_{PM}}{\left(h_{gap}^2 + \left(\frac{l_{bar} A_{gap} h_{gap}}{\mu_{bar} A_{bar}} \right) + \left(\frac{l_{PM} A_{gap} h_{gap}}{\mu_{PM} A_{PM}} \right) \right)}. \end{aligned} \quad (3.10)$$

The permeability of the Slider bar, μ_{bar} , is dependent on the design conditions of the IU-module, which are:

- The Slider bar is saturated, $B_{bar} > B_{sat}$, and the permeability μ_{bar} is equal to one. When the Slider bar is in saturation, the magnetic flux passing through the Slider bar is approximately constant, $\Phi_{bias,t} + \Phi_{bias,b} \approx B_{sat}A_{bar}$.
- The Slider bar is below the material saturation levels and the permeability of the Slider bar $\mu_{bar} \gg 1$. The reluctance of Slider bar \mathcal{R}_{bar} can then again be neglected in comparisons to the reluctance of the airgap \mathcal{R}_{gap} .

The design of the PAMB already showed that saturation of the Slider bar does not degrade non-linearity, as long as the control flux, Φ_{con} , does not pass through the saturated part [50], and that in some cases, it might even be beneficial. The relatively large airgap in the IU-module leads to extended leakage and fringing flux. Therefore, especially in the case of a saturated Slider bar, the 1st-order approximation has a limited validity, and more advanced modelling tools are essential. These more advanced modelling tools are presented Section 3.2.

3.1.2 Actuation of propulsion x -direction

The actuation in the propulsion direction uses the “moving iron” principle [50], discussed in Section 2.3.2. The “moving iron” principle uses the change of enclosed flux, from Eq. 2.10, in a special way. In this principle, neither the coil nor the permanent magnet moves, the change in flux linkage is realised by the movement of the ferromagnetic Slider bar. As the Slider bar displaces in positive x -direction, more of the bias flux is enclosed by the propulsion coils, as shown in Fig. 3.4.

The flux travelling into the Slider bar is locally independent of the x -position. The change in the enclosed flux of the coil is then expressed by $\delta\Phi_{bias,coil,x} = B_{gap}l_{coil} \cdot \delta x$. Taking the limit gives $\frac{d\Phi_{bias,coil,x}}{dx} = B_{gap} \cdot l_{coil}$. Substituting this in the third force component of Eq. 2.10, results in the “basic” Lorentz force equation, $F_x = n_{gap}i_x B_{gap}l_{coil}$. In this equation, l_{coil} is the length of the coil in y -direction, n_{gap} is the amount of turns in the airgap, B_{gap} is the flux density in the airgap. The total propulsion force, F_x , for the 4 propulsion coils is equal to $F_x = 4n_{gap}i_x B_{gap}l_{coil}$.

The stiffness in the propulsion direction, $\frac{F_x}{dx}$, is negligible. There is no position dependent reluctance force, since the change in reluctance change is limited to \mathcal{R}_{front} and \mathcal{R}_{back} , which have negligible reluctance compared to the airgap ($\mu_{iron} > 1000$). The low stiffness in the x -direction and the wireless propulsion reduces transfer of disturbances from the outside world to the suspended body. Irrespective of Slider bar’s position, the propulsion force, F_x , is theoretically linear with respect to the propulsion current, i_x , making the actuator ideal for control.

The influence of the suspension control flux, Φ_{con} , on the propulsion force is negligible. The control flux is much smaller than the bias flux and any flux added to top side of the Slider bar airgap is subtracted from bottom airgap and vice versa.

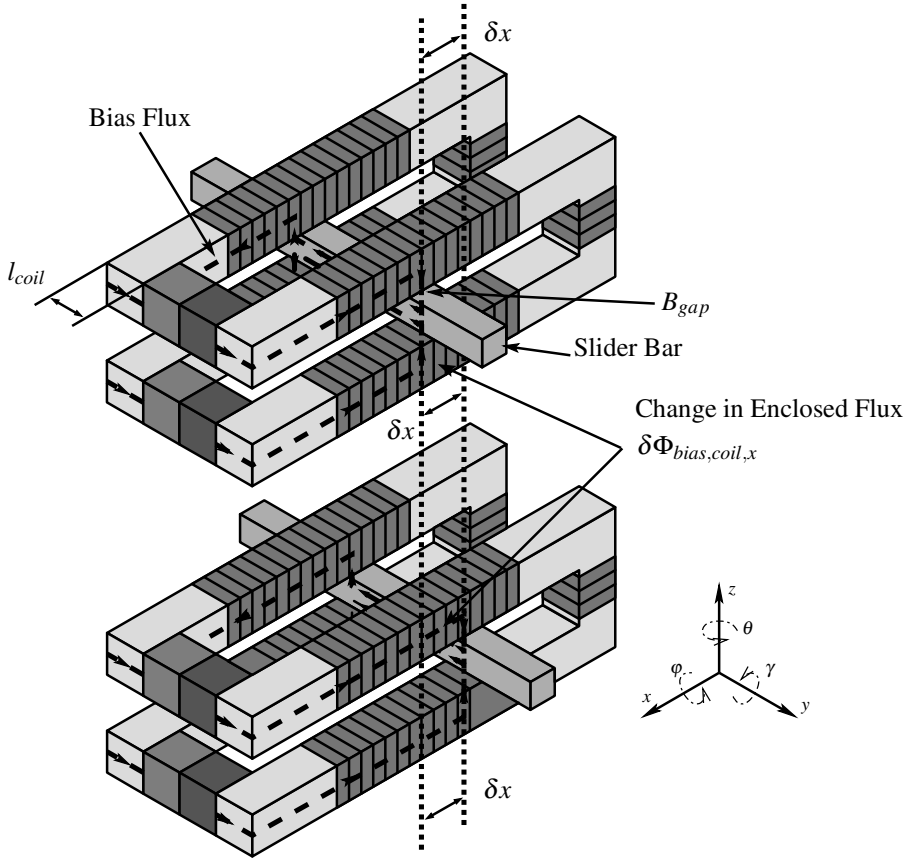


Figure 3.4: IU-module and displaced IU-module, along distance, δx . The change in flux enclosed by the propulsion coils is indicated by $\delta\Phi_{PM,coil,x}$.

A relatively long stroke can be realised depending on the actuator geometry and propulsion coil length. A longer propulsion coil has three drawbacks:

- A longer coil will have a larger inductance than a shorter coil, requiring a larger supply voltage for the current amplifier.
- The effective portion of the propulsion coil resides in the airgap above the Slider bar. In the case of a longer propulsion coil the ratio between produced forced and effective coil turns drops, reducing efficiency of the coil.
- A longer propulsion coil will influence the bias flux, Φ_{bias} , resulting in cross-talk between the suspension and propulsion force. Generally, the magneto motive force of the permanent magnet should be much larger than that of the propulsion coils, $H_{PM} \cdot l_{PM} \gg n \cdot i_x$, to minimise crosstalk from the propulsion to the suspension. A more detailed analysis on crosstalk is found in Section 3.2.

3.2 Design of the IU-module

The previous section demonstrated that the IU-module is capable of generating a suspension and propulsion force. In this section, the IU-module actuator used for the Slider is synthesised. To determine the geometry the basic 1st-order approximation are augmented with 2 additional modelling methods, a Magnetic Equivalent Network model and a Finite Element Method model, Section 3.2.1. The design choices leading to the final geometry are given in Section 3.2.2.

Table 3.1 gives an overview of the specifications required for the actuator of the linear Slider. More details on the specifications of the Slider itself are found in Chapter 4. The lower bound on the negative stiffness is determined, by the requirement that the IU-module should compensate the weight of its load in 0.05 mm (one tenth of the stroke) using the permanent magnets. The negative stiffness should not be larger than $-5 \cdot 10^4$ N/m, otherwise the transfer of disturbances from the environment to the Slider will become too large, see Section 4. A large negative stiffness is also more difficult to suppress by the controller [21]. The phase lag between current passed through the coil and the force acting on the Slider bar should be minimised at 300 Hz to facilitate a control bandwidth with considerable phase margin ($> 30^\circ$). Therefore, the goal is to keep the phase lag below 5° . Phase lag in the actuator is caused by electromagnetic losses, such as eddy current losses and hysteresis losses. The suspension actuation force should be large enough to compensate the force created by the negative stiffness, k_{zz} , and the displaced Slider bar when it is attached to the stator, otherwise the Slider bar cannot be retracted from its rest position.

Suspension	
Stroke	0.5 mm
Negative stiffness	$1 \cdot 10^4 < k_{zz} < 5 \cdot 10^4$ N/m
Phase lag at 200 Hz between F_x and i_x	$< 5^\circ$
Actuation Force	Enough to compensate $k_{zz} \cdot z_{gap}$
Crosstalk to propulsion	$< 1\%$ N/m
Propulsion	
Stroke	60 mm
Actuation Force	4 N
Stiffness	< 500 N/m
Crosstalk to suspension	$< 20\%$ N/m
Phase lag at 300 Hz between F_x and i_x	$< 5^\circ$
General	
Internal mechanical resonances	> 1200 Hz

Table 3.1: Requirements for the IU-module to be used in the Slider designed in Chapter 4.

3.2.1 Applied modelling methods

The development of the IU-module for the Slider is done using 2 basic modelling techniques, a magnetic equivalent network model (MEN) and the finite element method model (FEM). The MEN model is used to establish basic dimensions, while the FEM model is then used to improve the design and establish absolute values of the force. The modelling of the IU-module is performed in co-operation with EPE group of Technical University of Eindhoven [45]. Later on, the EPE group continued with optimisation of the IU-module, while the AM group in Delft focussed on the integration of IU-module in the Slider.

MEN model

The MEN model was initially built by Stoutjesdijk [68], during his MSc project. The network model is an extension to the 1st-order model with additional reluctances, \mathcal{R} . The layout of the used network model is shown in Fig. 3.5. The model is numerically implemented in Matlab.

The MEN model gives more accurate results than the 1st-order approximation in Section 3.1. The network includes elements for the leakage flux. The behaviour of a non-linear BH -curve is implemented, taking saturation into account. To estimate the effective area of the airgap, analytical expressions, found in [5], are applied. By splitting the propulsion coils in separate sources, the effect of position dependent crosstalk between propulsion and suspension directions can be investigated. The model allowed determination of the basic dimensions as depicted in Fig. 3.7.

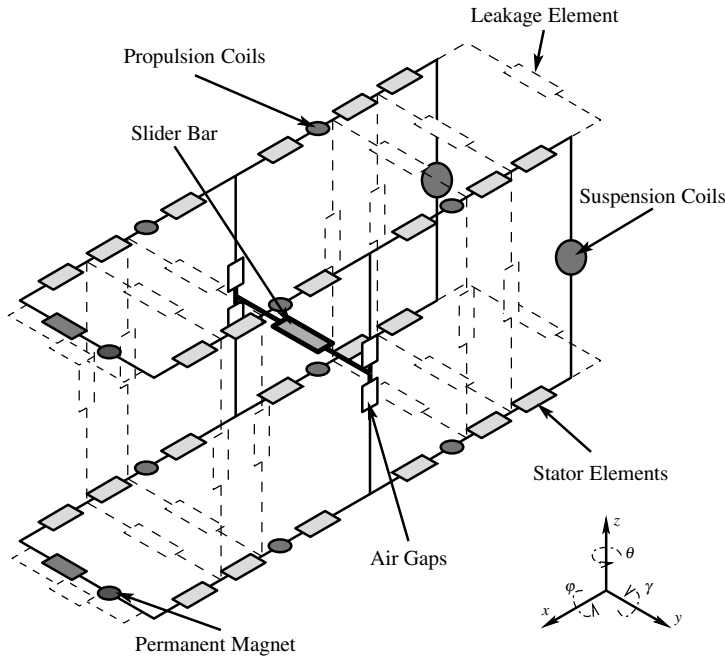


Figure 3.5: Magnetic equivalent network model of IU-module.

FEM model

The FEM model is more accurate than the MEN model, but also more complex and computationally intensive. At the Advanced Mechatronics Laboratory in Delft, the Ansys finite element software is used to analyse the characteristics of the IU-module. The EPE group developed a finite element model using the Maxwell software; this allowed comparison and verification of both FEM models.

In the Ansys finite element simulation, the resulting forces on the Slider bar were heavily dependent on the mesh. To minimise the mesh dependency, the Slider bar and airgaps were manually meshed using hexahedral elements instead of an automated mesh with tetrahedral elements. The forces are computed using the virtual work principle. The flux distribution of the IU-module, with dimensions as depicted in Fig. 3.7, is shown in Fig. 3.6.

Optimisation of the IU-module

The IU-modules presented in this chapter are not optimised from an electromagnetic or thermal point of view. Lebedev [45] performed an optimisation to achieve an optimal actuator from the viewpoint of electromagnetic energy efficiency. An extensive study is also conducted evaluating different magnetic materials for the

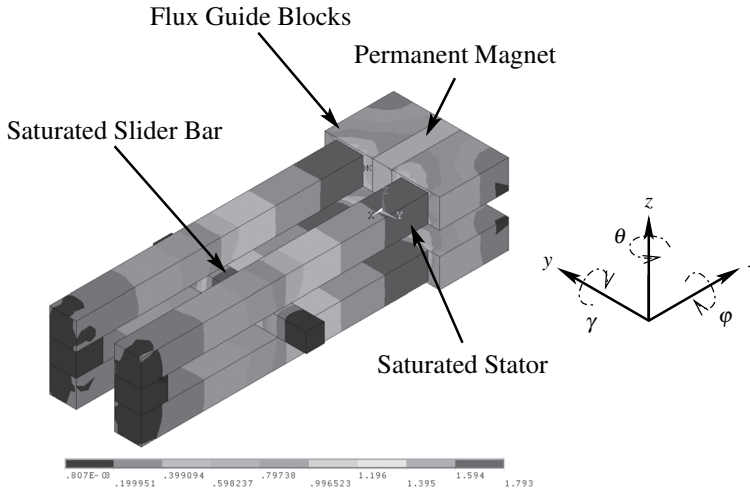


Figure 3.6: Flux distribution of the IU-module, computed using Ansys, with the Slider bar in the centre position at $z = 0$, $x = 0$ without any actuation current. The centre of the Slider Bar is saturated.

design. The interested reader is referred to Lebedev's thesis [44].

3.2.2 Design choices for the IU-module

In this section the design choices are presented, which led to the IU-module for the Slider in Chapter 4.

Permanent magnet material

The permanent magnets in the IU-module are made from NdFeB and are supplied by Bakker Magnetics (type BM35). NdFeB magnets are the magnet type with the highest energy product. This makes this permanent magnet ideal for providing a high flux density in a small volume. A drawback of this magnet type is the relatively low demagnetisation temperature. For the BM35 magnets the maximum operating temperature is 80°C . In the IU-module this is not a issue, because the permanent magnets are separated from the coils and the temperature is not expected to rise more than 10°C at the location of the permanent magnets.

Stator and Slider bar material

The stator and Slider bar materials have a significant influence on the performance. Aspects determining the choice for the magnetic materials, to be used in the stator and Slider bars, are:

- **Saturation flux density** A larger saturation flux density means that larger actuation forces can be generated within the same volume.
- **Initial permeability** The initial permeability determines the effectiveness of the magnetic material and will directly influence the actuation constants and stiffness constants.
- **Eddy current losses** The eddy current losses are ohmic losses, due to induced currents caused by changing magnetic fields in a conductor. The eddy current losses introduce phase lag between the control current, i_z , and the control flux, Φ_{con} , and therefore also between, i_z , and the force, F_z .
- **Hysteresis** The hysteresis of the magnetic material should be low to avoid non-linearities and phase lag between actuation current, i_z , and force on the Slider bar.
- **Availability** A lot of magnetic materials are available, but only a few are available in low volume batches.
- **Manufacturability** Preferably, the materials are easily machined into the shapes required for the IU-module.

The choice is made to use laminated steel. Laminated steel has a low level of eddy currents, because the conductive sheets are isolated with respect to each other and have a reduced conductivity, by the addition of a small percentage of silicon. The laminated steel sheets have little hysteresis, because the steel sheets are optimised for electromagnetic applications. Two setups were realised from 2 different laminated materials. The Baby-IU¹ is constructed from PowerCore C 130-27 transformer steel, while the Slider-IU is constructed from M35 motor grade steel. The PowerCore is obtained through Smit Transformatoren and the M35 through Paulides BV. Figure 3.7 shows the orientation of the laminations. The suspension coils generate varying magnetic fields, for which eddy currents are to be minimised. Therefore, the laminations in the stator and Slider are aligned with the control flux, Φ_{con} .

Three ways were tested to manufacture the Slider and stator bars from the laminated steel sheets:

- In the first test setup the sheets were mechanically cut. The separate strips were then glued and afterwards machined to obtain the desired accuracy. The glue was an epoxy donated by Smit Transformatoren. The machining causes electrical shortcuts between the different strips, enabling eddy currents. To remove this electrical connection, the laminated bars were etched afterwards.

¹The name originates from the fact that it is small experimental version.

In addition to removing electrical connections, the etching process damages the glue between the laminated sheets, breaking some of the bars, [76].

- By changing the glue to Loctite 326, the resulting layer of glue was much thinner (0.05 mm), and the drying time decreased. The glue allowed better positioning of the strips in the glue mold. This resulted in bars, 14 mm wide, which did not require an additional machining step. The glueing process caused additional tolerances on the Slider bar of 0.2 mm in all directions.
- In the final version of the IU-module, the laminations were cut using spark erosion and were afterwards glued with Loctite 326. The spark erosion allowed L-shaped bars to be manufactured and higher tolerances to be achieved on the individual strips.

The glue mould is limiting the accuracy of the manufactured bars. More attention should be paid to this in future designs. Another option might be to grind the stator bars on one side. This allows only limited eddy currents, while a high degree of flatness is achievable.

An alternative for the Slider bar material is to use solid magnetic stainless steel or soft magnetic composite materials. The changing flux path, through the Slider bar, is relatively small, so this will have little influence on the eddy current losses. A Sandvik 1802 (magnetic stainless steel) Slider was implemented and levitated using the Baby-IU setup, describe in Appendix B.2.

Dimensioning of the magnetic circuit

Figure 3.7 shows the IU-module with the general dimensions of the magnetic circuit. The minimum cross-section of the Slider bars are determined by their clamped natural frequency. The Slider bars transfer the actuation forces to the suspended body. For a stable control loop, the natural frequency should be sufficiently larger (>3 times) than the required bandwidth of the closed-loop system (300-400 Hz), see Chapter 4. The first bending natural frequency of a beam (representing the Slider bar), which is clamped on one side and free on the other side is, according to [32]:

$$f_n = \frac{1}{2\pi} \left(\frac{1.8751}{l_{beam}} \right)^2 \cdot \sqrt{\frac{YI}{\rho A}}. \quad (3.11)$$

Where, l_{beam} is the length of the beam, Y is modulus of elasticity, ρ is the material density, I is the cross sectional area moment of the beam, and A is the area of cross section of the beam. A steel beam, with a cross section of 10 x 10 mm and a length of 75 mm, has its natural frequency at 1500 Hz. The Slider bar is manufactured out of glued steel sheets, therefore the actual eigen-frequency will be slightly lower. From

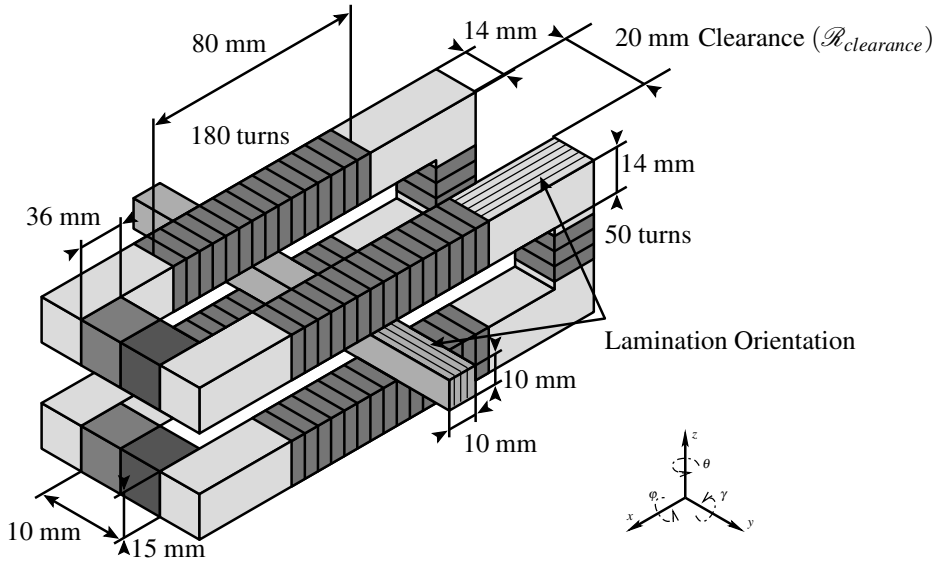


Figure 3.7: IU-module with dimensions and indication of the lamination orientation.

a magnetic point of view for achieving the minimum required negative stiffness, a smaller cross section of the Slider bar suffices, Eq. 3.10.

The airgaps in the IU-modules are 1 mm on each side of the Slider bar. This is relatively large for magnetic bearings, normally airgaps are in the order of 0.5 mm to reduce reluctance and fringing. A larger airgap reduces the sensitivity of the setup with respect to mechanical construction tolerances of the stator and Slider bars. A second reason for the large airgap is that the propulsion coils of the IU-module occupy a large portion of the airgap. Windings of 0.4 mm easily occupy 0.5 mm in the air-gap, due to a layer of insulation underneath the coil. On top of the propulsion coils a protective layer of 0.2 mm is taped, to prevent the Slider bar from damaging the coils. With an airgap on both sides of 1 mm, the propulsion coils and its protection leave 0.6 mm for movement, approximately the desired value.

The applied permanent magnets are 10 mm x 15 mm x 36 mm NdFeB magnets. They are chosen because of their availability and the capability to easily saturate the Slider bar. The size of the stator bar is 14 mm x 14 mm to decrease the reluctance of the stator bars compared to the Slider bars.

The suspension coils have 50 windings. This is enough to retract the Slider bar with 4 A of current from the stator bar and keep the coil inductions acceptable. The diameter of the wire is 0.4 mm. The length of the propulsion coil is taken 30 mm longer than the desired stroke, to make sure the IU-module does not suffer from edge effects.

The stator legs are spaced apart with a clearance of 20 mm. The stator leg spacing is a tradeoff between a slim mechanical construction and a better magnetic circuit layout to limit leakage. The application points of the suspension force, F_z , and propulsion force, F_x , are on the Slider bar at the location of the airgaps. It is desired to have these points close to each other, since then the actuation force acts as a point source. A secondary advantage of a smaller stator clearance is a shorter Slider bar, resulting in a higher eigenfrequency, Eq. 3.11. However, a small clearance leads to a low reluctance between the stator legs, resulting in a large part of the bias flux crossing directly the legs without passing through the Slider bar. The reluctance of the path through air between the stator legs in y -direction is equal to $\mathcal{R}_{clearance} = \frac{l_{clearance}}{A_{clearance} \cdot \mu_0}$ and the reluctance of the desired path is to $\mathcal{R}_{bar} + 2\mathcal{R}_{gap} = \frac{l_{bar}}{A_{bar} \cdot \mu_0 \mu_{sat}} + \frac{2l_{gap}}{A_{gap} \cdot \mu_0}$. Contemplating that μ_{sat} approaches 1 for a saturated Slider bar, and that the total surface between the stator legs, is $A_{clearance} \approx 30 \cdot A_{gap}$, it is clear that the reluctance $\mathcal{R}_{clearance}$ is of considerable influence.

Slider bar saturation

The Slider bar is chosen to operate in a state where its centre is magnetically saturated. In the research of [50], it is shown that magnetic saturation at the centre of the Slider bars does not degrade force linearity in suspension direction, as long as the ends of the Slider bars, through which the control flux passes, are not saturated. Figure 3.8 shows the simulated suspension force, F_z , and flux density, B_{bar} , at the centre of the Slider bar versus z -position for different permanent magnet strengths. In the saturated case, $H_{PM} = 892$ kA/m, the suspension force, F_z , versus z -position behaves linear and flux density at the centre, B_{bar} , remains constant. The saturated IU-module achieves a larger force density within the same volume than the unsaturated Slider bars. The z -position range over which the stiffness, k_{zz} , is constant, is even larger than in the unsaturated situations ($H_{PM} = 200$ kA/m and $H_{PM} = 400$ kA/m). The suspension force, F_z , versus current, i_z , for the saturated Slider bar is linear for different z -positions, see Fig. 3.9.

Figure 3.10 shows the propulsion force, F_x , versus propulsion current, i_x , when the Slider bar is at $x = +20$ mm and $z = 0$ mm from the centre of the IU-module. With a stronger permanent magnet and a saturated Slider, a better linearity and a higher actuation constant, h_{xx} , are achieved in the propulsion direction. Summarising, a saturated Slider bar allows high force densities to be achieved with a more linear response to the applied propulsion current than the same geometric design with unsaturated Slider bars.

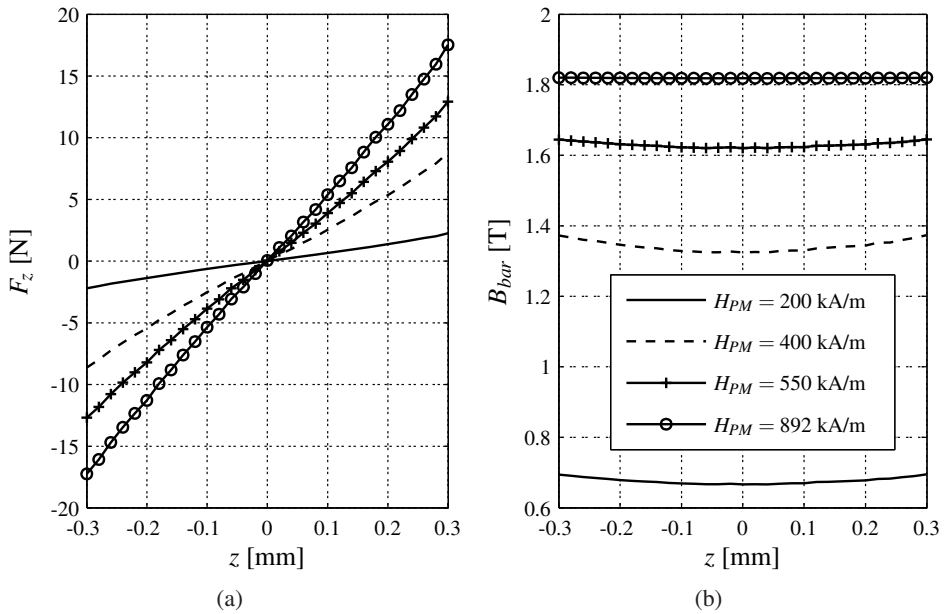


Figure 3.8: Suspension force, F_z , versus suspension z -displacement of the Slider bar for several magnets of different coercive force, H_{PM} (a). Flux density in the Slider bar, B_{bar} , versus z -position (b) for several magnets with different coercive force, H_{PM} (Ansys FEM simulations).

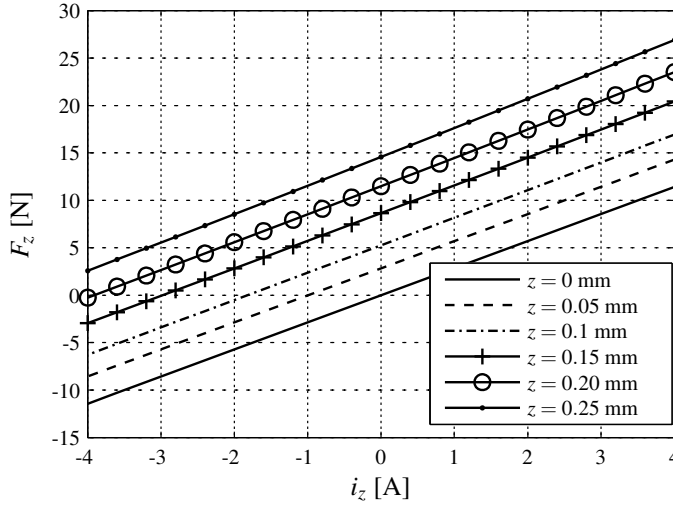


Figure 3.9: Suspension force, F_z , versus suspension current, i_z , for several z -positions ($H_{PM} = 892000$ A/m). The Slider bar is at the centre of the IU-module, the $x = 0$ position. The suspension coils have 50 turns. On the opposite side of the airgap the response is symmetrical (Ansyz FEM simulations).

3.3 Force measurement on 2-DoF IU-module

A static force measurement setup is constructed to evaluate the forces acting on the Slider bar of the designed IU-modules. This setup verifies the designed actuator and the applied modelling methods, leading to the design. Two versions of the IU-module with similar dimensions, as described in Section 3.2, are measured in the setup. The Baby-IU was manufactured from laminated transformer steel. While the Slider-IU steel was manufactured from motor grade steel. The Baby-IU has 100 turns on the suspension coil, while the Slider-IU has 50 turns. The Baby-IU has a 190 turn propulsion coil with a total length of 65 mm, while the Slider IU-has a 180 turn propulsion coil with a length of 80 mm. Table 3.2 gives a summary of the differences between both IU-modules. The Baby-IU setup is used in a dynamic test setup for testing the dynamic positioning capabilities of a single IU-module, see Appendix B.2. The Slider-IU is the follow up of the Baby-IU and is used in the 6-DoF electromagnetically levitated Slider of Chapter 4.

3.3.1 Force measurement setup

To validate the models and to predict the performance of the IU-module, it is desired to measure forces on the Slider bar in all 5-directions in which forces and torques

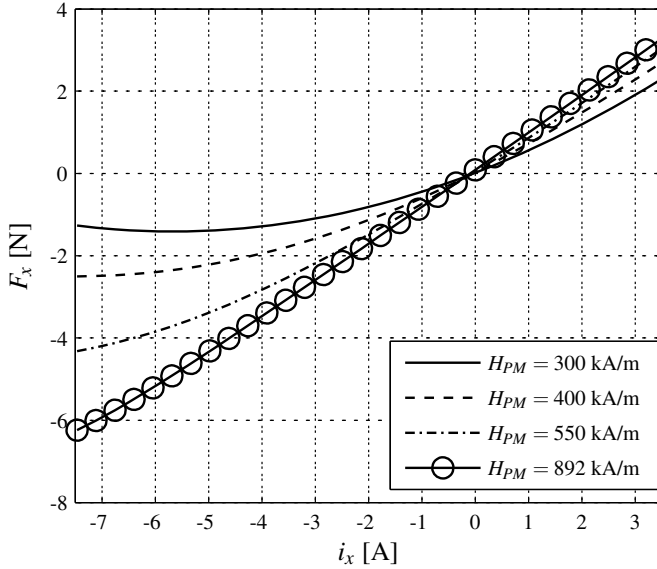


Figure 3.10: Propulsion force, F_x , for permanent magnets with different coercive force, H_{PM} (Ansys FEM simulations). The Slider bar is situated at $x = +20$ mm and $z = 0$ mm from the centre of the IU-module. The number of turns on the propulsion coil is 180.

	Slider-IU	Baby-IU
Lamination material	M35 motor grade	PowerCore C 130-27
Suspension coil turns	50	100
Propulsion coil turns	180	190
Propulsion coil length	80 mm	65 mm
Overall stator length	155 mm	130 mm

Table 3.2: Differences between the Baby-IU and Slider-IU, the other dimensions are the same as shown in Fig. 3.7.

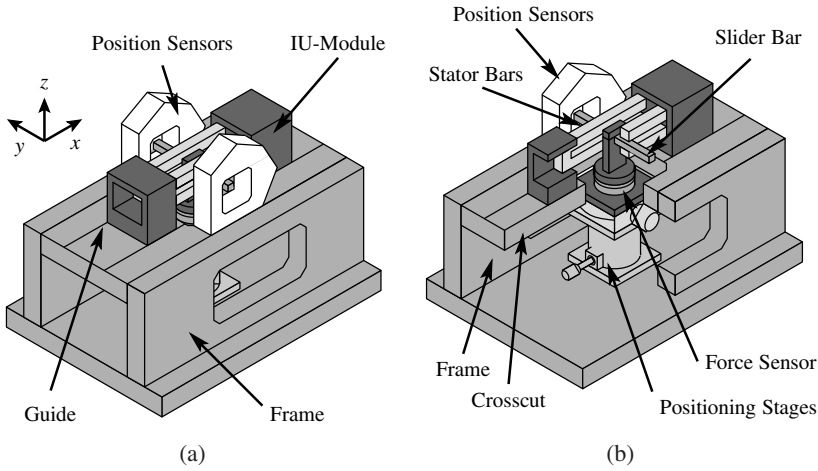


Figure 3.11: Static force measurement setup for the IU-modules [77]. System overview (a), and section view of the setup (b).

are exerted $(x, z, \varphi, \theta, \gamma)$. For his MSc project, Wesselingh [77] designed and built a 5-DoF force measurement setup. The setup is capable of simultaneously measuring forces and displacements of the Slider bar in 5-DoF, see Fig. 3.11.

To measure the forces, a Schunk Mini 40 strain gage force sensor is used. The sensor measures forces in 6-DoF, $(F_x, F_y, F_z, T_x, T_y, T_z)$. A clamp holds the Slider bar on top of the force sensor, fixing it in place. To orient the Slider bar in the airgap in the z , φ , θ and γ -directions, commercial manual positioning stages are used. The positioning stages are situated underneath the force sensor within the frame. The suspension z -position stage can be combined with a rotation stage to form a combined movement. To facilitate a motion in the x -direction of 50 mm, the IU-modules are mounted on a carriage, which slides through a guide in the frame.

To accurately determine the stiffness of the Slider bar, position measurement of the Slider bar is required. The position of the Slider bar is measured in 5-DoF using a newly developed Position Sensitive Device (PSD) based sensor. A compact commercial 5-DoF sensor was not available, therefore a custom sensor is developed. The position sensors consist of a laser sources, a reflective mirrors positioned on the Slider bar, and 2-dimensional PSDs. These PSDs measure the location the reflected laser beams targeted at their surfaces in 2 dimensions. Using 4 PSDs the global displacement of the Slider bar can be reconstructed, see Fig. 3.12. More details on the sensor design are found in [77].

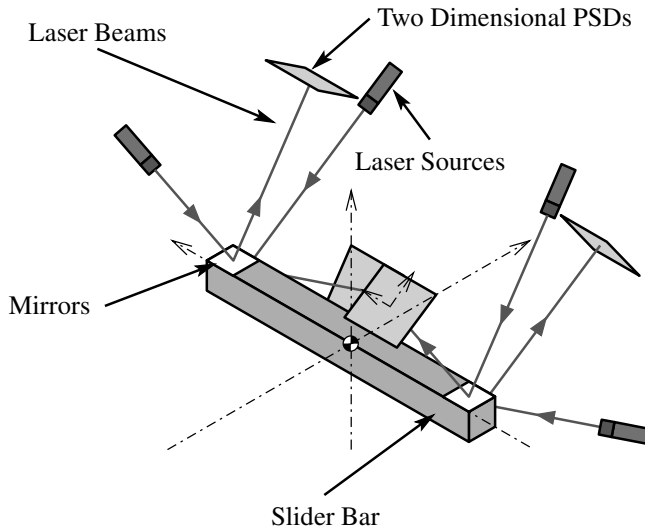


Figure 3.12: Layout of the 5-DoF position sensor using 2-dimensional PSDs, developed in [77]. The laser beams reflect off the Slider bar with the reflection mirrors attached. The location of the laser spots on the PSDs (Position Sensitive Device) determine the position of the Slider bar.

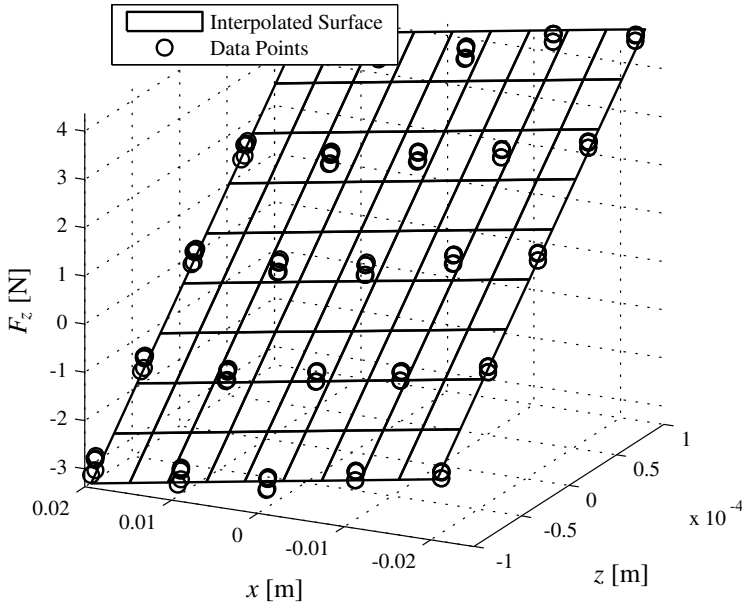
3.3.2 Results of force measurements on 2-DoF IU-modules

The static force measurements of the forces acting on the 2-DoF IU-module are presented in this section.

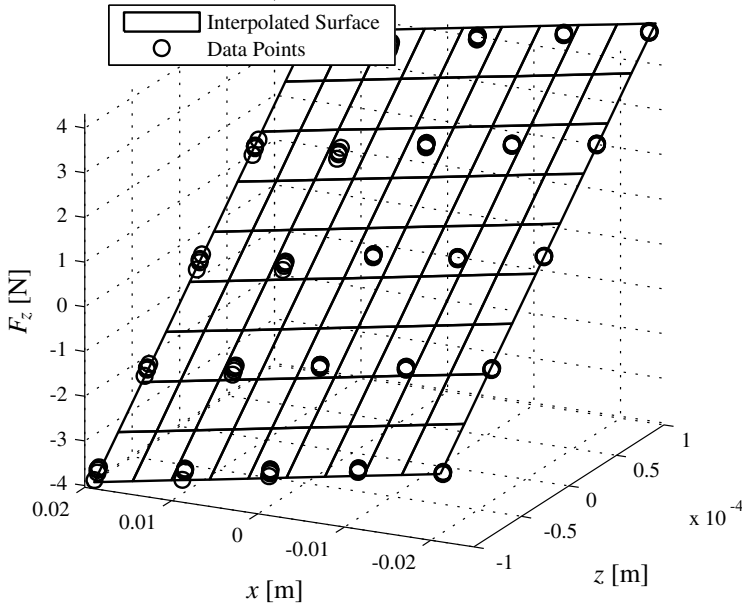
Force in suspension z -direction

Figure 3.13 shows the suspension force, F_z , on the Slider bar versus z -position of the Slider-IU and Baby-IU. The suspension force, F_z , is linear with respect to the z -position. The stiffness, k_{zz} , is $-30 \cdot 10^3$ N/m for both IU-modules. A 30 N/m stiffness, k_{zx} , is measured. This stiffness, most likely originates from a measurement error, caused by misalignment in the force measurement setup and crosstalk in the force sensor, specified by the manufacturer at 5% of the nominal force.

Figure 3.14 shows the actuation of the Slider bar at various suspension positions. It is clear, that over a $200 \mu\text{m}$ z -displacement, the actuation constant, h_{zz} , is constant. The actuation constant, h_{zz} , of the Baby-IU is 1.7 times that of the Slider-IU with twice the amount of suspension turns, while the negative stiffness, k_{zz} , is the same. In Section 3.4, the measurements are compared to simulations of the 2 IU-modules.



(a) Slider-IU



(b) Baby-IU

Figure 3.13: Force measurements of F_z , of the Slider-IU (a) and Baby-IU (b), versus x and z -position. The slope of the surface determines the stiffness, k_{zz} .

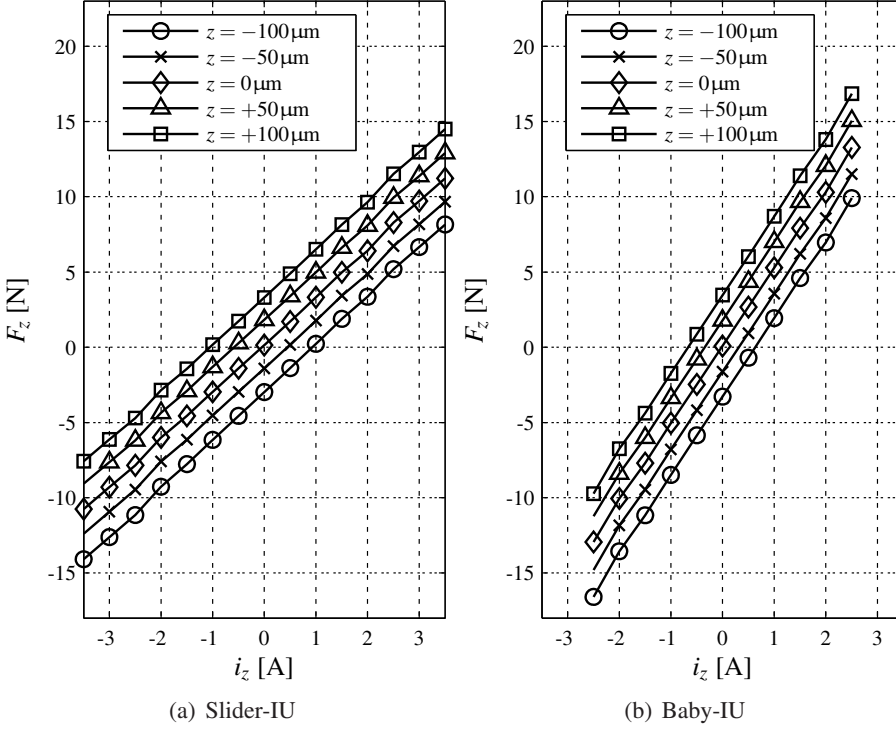


Figure 3.14: Measurements of suspension force, F_z , versus actuation current, i_z , for the Slider-IU (a) and the Baby-IU (b).

Force in propulsion x -direction

A constant force of approximately, $F_x = 0.2$ N, attracts the Slider bar towards the permanent magnets. The actuation in the propulsion direction is shown in Fig. 3.15. The propulsion force, F_x , is only linear with respect to propulsion current over all x -positions up to $i_x = \pm 1$ A. For higher currents, the actuation constant, h_{xx} , drops. At the $x = +20$ mm position, the effect is significant. This non-linearity is less in the Baby-IU module, especially if one looks at the obtained force. The non-linearity renders the actuator not applicable in situations, where large propulsion forces, F_x , are required. The drop in propulsion force occurs at much lower propulsion currents, i_x , than is simulated for the saturated Slider bar, as shown in Fig. 3.10. This indicates that the Slider bar is not completely saturated.

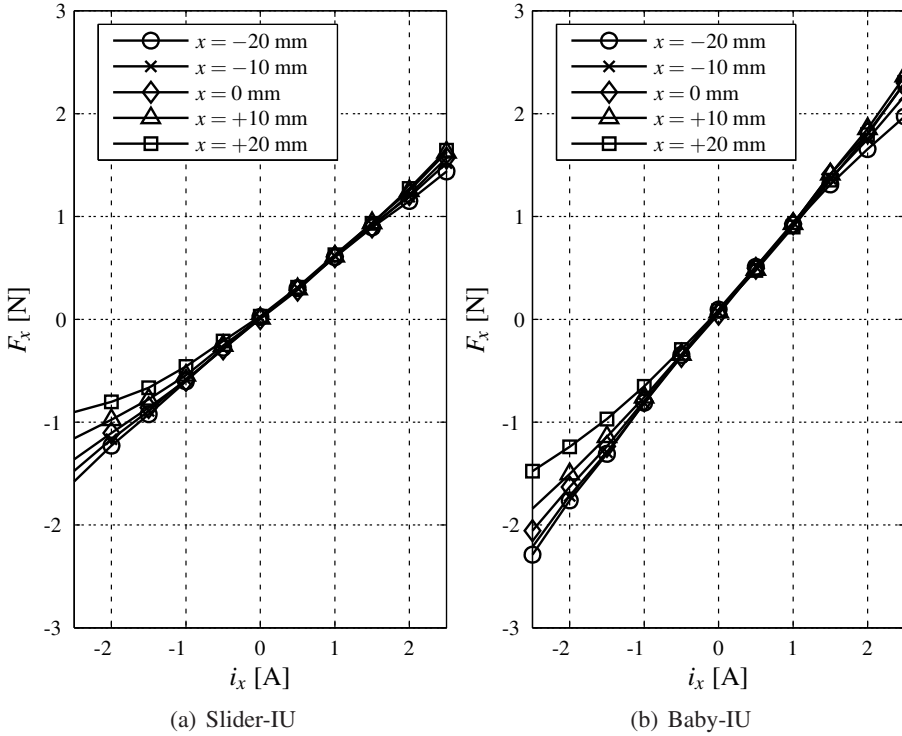


Figure 3.15: Measurement of propulsion force, F_x , versus propulsion actuation, i_x , Slider-IU (a), and Baby-IU (b).

Crosstalk between propulsion and suspension force

The magnitude of the interaction between propulsion and suspension is determined by measurements on various x and z -positions. The measured interaction from suspension current, i_z , to propulsion force, F_x , is negligible and was $h_{xz} < 0.1\text{N/A}$ over all x and z -positions.

An x and z -position dependent interaction exists from the propulsion current, i_x , to the suspension force, F_z . The suspension force, F_z , has a linear response to the propulsion current when the Slider bar is not in the centre z -position. The actuation constant, $\frac{F_z}{i_x}$, is shown in Fig. 3.16. Figures 3.15-3.16 show the ratio between the suspension and propulsion force, $\frac{F_z}{F_x} \approx 1$ at $x = 20\text{ mm}$ and $z = 0.1\text{ mm}$. The cause of this significant interaction lies in the influence of the propulsion coils on the flux density in the Slider bar and the airgaps. This is illustrated in Fig. 3.17, which shows simulated flux densities in the airgaps and Slider bar versus propulsion current, i_x , at $x = 20\text{ mm}$ and $z = 0.1\text{ mm}$ for 2 magnets with different, H_{PM} . Figure 3.17 shows that the relative influence on the airgap flux level and force is minimised,

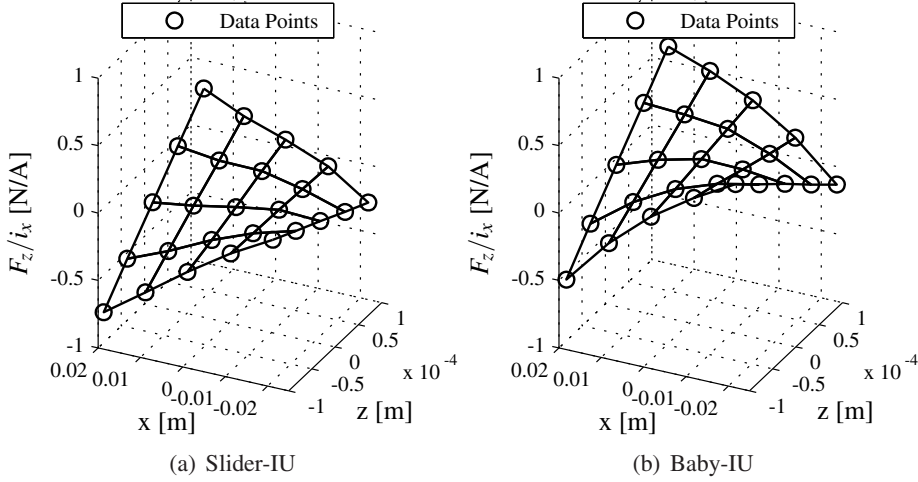


Figure 3.16: Measured coupling from propulsion actuation to suspension force, $\frac{F_z}{i_x}$, versus x and z -position, Slider-IU (a), and Baby-IU (b).

when the Slider bar is saturated ($H_{PM} = 892000 \text{ A/m}$). The interaction present in the measured IU-modules indicates the Slider bars are not fully saturated as was designed.

The crosstalk between i_x and F_z is minimal when the IU-module operates close to the centre position, $z = 0$. Future designs of the IU-module should be in such a way, that the nominal operating position (the position where the weight of the load is compensated by the permanent magnets) is close to the $z = 0$ position, while regarding the maximum allowed negative stiffness of the actuator.

3.4 Comparison between model and measurements

In this section, the modelling methods presented in Section 3.2.1 are compared to the measurements. The measurements of the interaction and propulsion force (Section 3.3.2) already indicated that the predicted saturation flux density in the Slider bar is not reached. In Tab. 3.3 the stiffness and actuation constants of the IU-module for the modelled and measured actuator are shown.

The models differ significantly from the measured values. In the 1st-order approximation, flux leakage is neglected resulting in a too high flux density in the Slider bar. Specifically, the leakage flux between the stator clearance (Fig. 3.7) has a significant influence. The MEN model is closer to the measured situation, but the stiffness and actuation constants are larger than measured. In the MEN model the

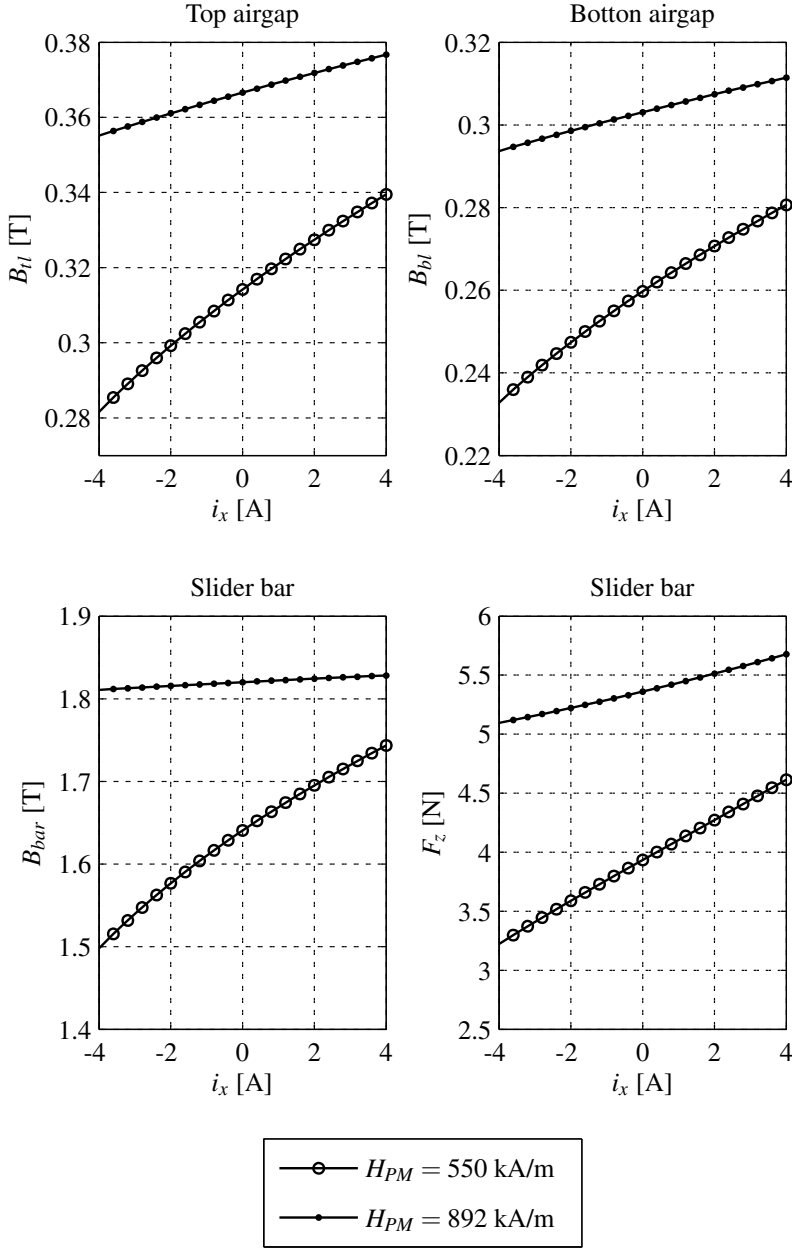


Figure 3.17: Flux density in the top airgap (top-left), bottom airgap (top-right), the Slider Bar (bottom-left), and suspension force, F_z (bottom-right) at $x = 20$ mm and $z = 0.1$ mm versus propulsion current, i_x (FEM Simulation Results).

	Slider-IU			Baby-IU		
	$k_{zz} \left[\frac{N}{m} \right]$	$h_{zz} \left[\frac{N}{A} \right]$	$h_{xx} \left[\frac{N}{A} \right]$	$k_{zz} \left[\frac{N}{m} \right]$	$h_{zz} \left[\frac{N}{A} \right]$	$h_{xx} \left[\frac{N}{A} \right]$
Measured data	$-3.0 \cdot 10^4$	3.1	0.56	$-3.0 \cdot 10^4$	5.2	0.85
1 st -order approx.	$-47 \cdot 10^4$	17	5.7	$-48 \cdot 10^4$	34	7.5
MEN model	$-10 \cdot 10^4$	8.2	0.53	$-13 \cdot 10^4$	17.3	0.74
Ansys model	$-5.6 \cdot 10^4$	2.9	0.94	$-6.8 \cdot 10^4$	6.2	1.3

Table 3.3: Comparison between the modelled and measured forces on the IU-modules.

effect of fringing flux is assumed to be constant and independent of the z -position. Secondly, the reluctance of the Slider bar in the control flux path is assumed to be negligible, leading to a too large actuation constant, h_{zz} .

The FEM predictions are closest to the actual measurements but the stiffness, k_{zz} , is still a factor of 2 larger than the measured values. Explanations for this difference are:

- The stator and Slider bars consist of laminated material, while the FEM model assumes the bars to be solid. The filling factor is 0.85, which means 15% less ferromagnetic material is present than was modelled.
- The Ansys software allows only *one* non-linear BH -curve to be implemented. The iron flux guide blocks, connecting the permanent magnets to the stator bars, and permanent magnets also have different non-linear BH -curves.
- Different nominal airgap size. The Slider bars are manufactured from laminated bars with 0.2 mm geometrical tolerances. This results in airgap deviations in the centre position of 0.1 mm on the nominal gap of 1 mm.
- Unmodelled airgaps exist between the different components of the IU-module. These airgaps are created, because of manufacturing tolerances in the laminated Slider bars. These gaps are easily 0.2 mm, which is significant with respect to a nominal airgap of 1 mm.
- Modelled material properties might be different from actual material properties. The Slider-IU is manufactured using a spark erosion process, which causes material properties to change locally. These local material changes increase the effective airgap.

Lebedev [44] studies the differences between the modelled and measured data of IU-module more thoroughly. The Ansoft Maxwell 3D software, available at the EPE group in Eindhoven, is specialised for these electromagnetic problems and overcomes many of the limitations present in Ansys.

3.5 Additional DoFs of the IU-module

Until now, the discussion has been on a 2-DoF IU-module. The IU-module has in total 6 coils, 4 propulsion coils and 2 suspension coils. These additional inputs can be used to generate additional torques around the x and z -axes. These additional DoFs can be used to decrease the number of required actuators in a system, reducing the costs. Secondly, these additional DoF allow stiffening or damping of flexible modes [61]. This section discusses how to actuate the torques, T_x and T_z . At the end of this section, a discussion is held why T_y cannot be actuated.

Actuation of Torque, T_x

The actuation of the torque, T_x , is shown in Fig. 3.18. The torque is achieved by reversing the direction of the current in one of the suspension coils with respect to conventional suspension actuation. Figure 3.19 shows the measurement of the torque, T_x , for the Baby-IU and the Slider-IU. The stiffness and the actuation constants are $k_{\varphi\varphi} = -8.95 \text{ Nm/rad}$ and $h_{\varphi\varphi} = 57.6 \cdot 10^{-3} \text{ Nm/A}$. From Fig. 3.19, it is clear the IU-module is capable of generating the torque, T_x , and its response is linear with respect to i_φ . The observed crosstalk between actuation of torque, T_x , and the other directions is smaller than could be reliably measured with the 6-DoF force sensor.

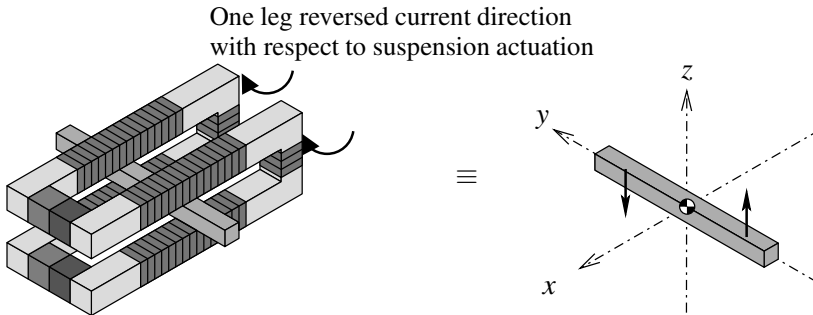


Figure 3.18: Actuation of torque, T_x .

Actuation of torque, T_z

Actuation of the torque, T_z , is performed by reversing the direction of the current through one side of the propulsion coils (left/right) with respect to the normal propulsion currents for F_x , see Fig. 3.20. The actuation constant is $h_{\theta\theta} = 11.9 \cdot 10^{-3} \text{ Nm/A}$, see Fig. 3.21.

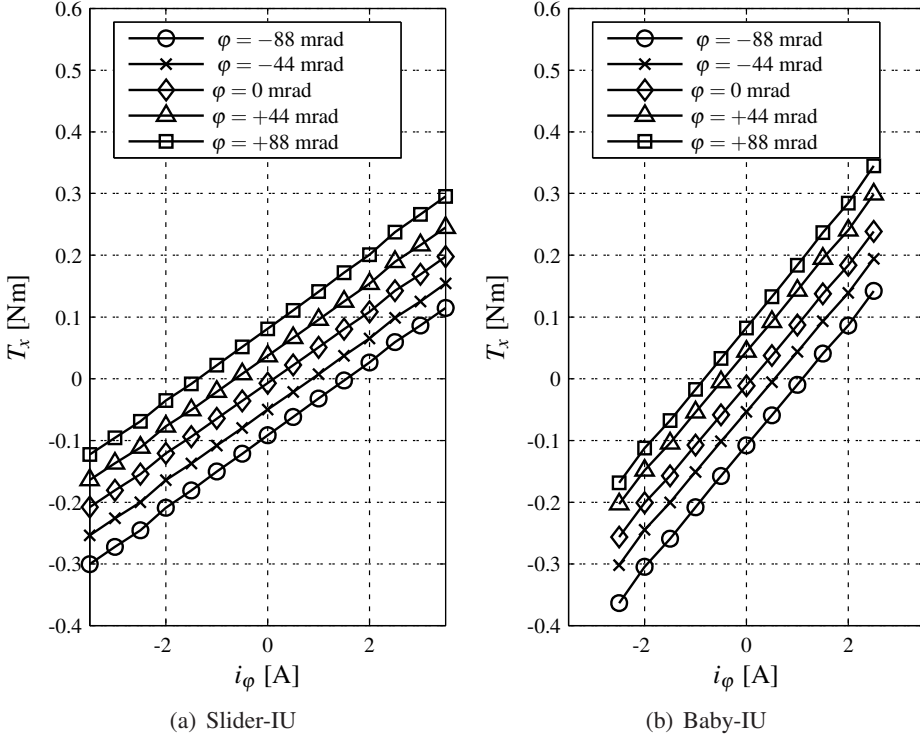


Figure 3.19: Measurement of torque, T_x , versus torque actuation, i_ϕ .

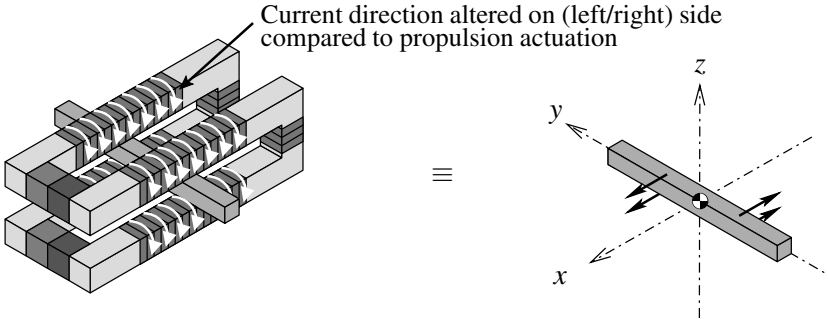


Figure 3.20: Actuation of torque T_z .

The actuation of torque, T_z , see Fig. 3.21, does not portray the non-linearities present in the actuation of the propulsion force, F_x , see Fig. 3.15. The polarity of the magnetic poles of the propulsion coils has changed compared to propulsion actuation, see Fig. 3.20. The generated fluxes now cancel each other with respect

to the permanent magnet, see Fig. 3.20. Therefore, there is no interaction between actuation of torque, T_z , and the force in suspension direction, F_z .

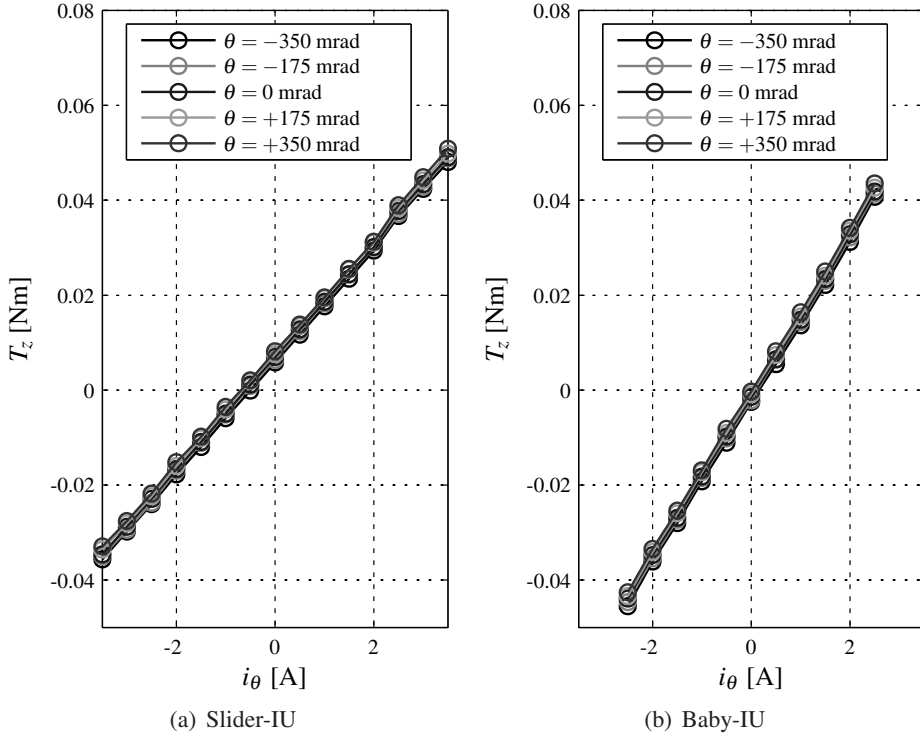


Figure 3.21: Measurement of torque, T_z , versus torque actuation current, i_θ .

Actuation of torque, T_y

The torque, T_y , cannot be actuated by changing the direction of the current in the bottom propulsion coils in comparison with making a force in F_x . Firstly, the change in enclosed flux within the propulsion coils, due to an angle, γ , is extremely small. Secondly, actuation of this torque results in large suspension forces. The propulsion coils now generate flux in the same direction as the suspensions coils. This generation of flux also introduces a large mutual induction between the propulsion and suspension coils as indicated by Fig. 3.22.

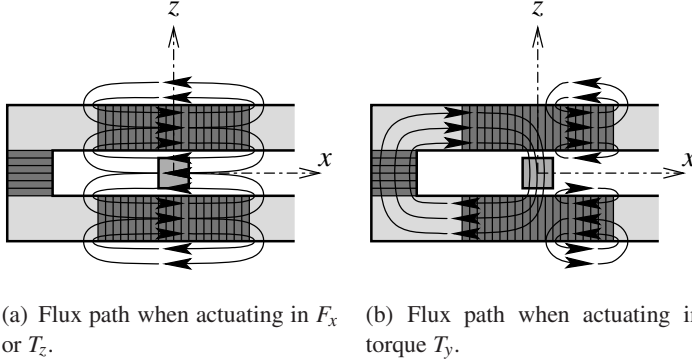


Figure 3.22: The flux produced in the actuation of torque, T_y , leads to mutual induction between the suspension and propulsion coils. The generated flux for the actuation a torque, T_y , also creates a significant suspension force, F_z . In contrast to the actuation of the propulsion force, F_x , or torque, T_z , which result in a balancing flux at the location of the suspension coil.

3.5.1 Overview of actuation constants

The measurement results of the actuation are combined in a 6-DoF stiffness and actuation model for the IU-module. The model is constructed using a linear least squares fit on the measured data. The resulting model is described as:

$$\vec{F} = -\mathbf{K}_{act} \cdot \vec{x} + \mathbf{H}_{act} \cdot \vec{i}, \quad (3.12)$$

$$\vec{F} = \begin{bmatrix} F_x \\ F_y \\ F_z \\ T_x \\ T_y \\ T_z \end{bmatrix}, \quad \mathbf{K}_{act} = \begin{bmatrix} k_{xx} & k_{xy} & k_{xz} & k_{x\varphi} & k_{x\gamma} & k_{x\theta} \\ k_{yx} & k_{yy} & k_{yz} & k_{y\varphi} & k_{y\gamma} & k_{y\theta} \\ k_{zx} & k_{zy} & k_{zz} & k_{z\varphi} & k_{z\gamma} & k_{z\theta} \\ k_{\varphi x} & k_{\varphi y} & k_{\varphi z} & k_{\varphi\varphi} & k_{\varphi\gamma} & k_{\varphi\theta} \\ k_{\gamma x} & k_{\gamma y} & k_{\gamma z} & k_{\gamma\varphi} & k_{\gamma\gamma} & k_{\gamma\theta} \\ k_{\theta x} & k_{\theta y} & k_{\theta z} & k_{\theta\varphi} & k_{\theta\gamma} & k_{\theta\theta} \end{bmatrix}, \quad (3.13)$$

$$\vec{x} = \begin{bmatrix} x \\ y \\ z \\ \varphi \\ \gamma \\ \theta \end{bmatrix}, \quad \mathbf{H}_{act} = \begin{bmatrix} h_{xx} & h_{xy} & h_{xz} & h_{x\varphi} & h_{x\gamma} & h_{x\theta} \\ h_{yx} & h_{yy} & h_{yz} & h_{y\varphi} & h_{y\gamma} & h_{y\theta} \\ h_{zx} & h_{zy} & h_{zz} & h_{z\varphi} & h_{z\gamma} & h_{z\theta} \\ h_{\varphi x} & h_{\varphi y} & h_{\varphi z} & h_{\varphi\varphi} & h_{\varphi\gamma} & h_{\varphi\theta} \\ h_{\gamma x} & h_{\gamma y} & h_{\gamma z} & h_{\gamma\varphi} & h_{\gamma\gamma} & h_{\gamma\theta} \\ h_{\theta x} & h_{\theta y} & h_{\theta z} & h_{\theta\varphi} & h_{\theta\gamma} & h_{\theta\theta} \end{bmatrix}, \quad \vec{i} = \begin{bmatrix} i_x \\ i_y \\ i_z \\ i_\varphi \\ i_\gamma \\ i_\theta \end{bmatrix}. \quad (3.14)$$

The significant stiffness and actuation constants are shown in Tab. 3.4-3.5, respectively. Significant cross-stiffness terms are defined as terms larger than 5% of the dominant force, when the matrix, \mathbf{K}_{act} , is multiplied with the maximum displacement vector. Significant cross-actuation terms are defined as terms larger than 5% of the dominant force, when the matrix, \mathbf{H}_{act} , is multiplied with the maximum actuation vector. The tables show that the stiffness is reasonably well decoupled. The largest crosstalk between different actuation directions is h_{zx} , which is x and z -position dependent.

DoF	Slider-IU		Baby-IU		Remark
k_{xx}	0	N/m	0	N/m	see section 3.3.2
k_{yy}	—	N/m	—	N/m	-
k_{zz}	$-29.5 \cdot 10^3$	N/m	$-29.9 \cdot 10^3$	N/m	see section 3.5
$k_{\phi\phi}$	-8.95	Nm/rad	-9.62	Nm/rad	see section 3.3.2
$k_{\gamma\gamma}$	-0.27	Nm/rad	-0.30	Nm/rad	see section 3.5
$k_{\theta\theta}$	0	Nm/rad	0	Nm/rad	see section 3.5
k_{zx}	33.4	N/m	34.2	N/m	see section 3.3.2
$k_{z\phi}$	35.4	N/rad	58.3	N/rad	^a
$k_{z\gamma}$	-40.9	N/rad	-35.0	N/rad	^a
$k_{z\theta}$	48.1	N/rad	45.4	N/rad	^a
$k_{\phi x}$	0.82	Nm/m	0.16	Nm/m	^b

Table 3.4: Stiffness resulting from a linear fit for both IU-modules, only the significant terms are shown.

^aMost likely due to second order terms from position sensor giving very small displacements in z -directions when rotating, since force remains nearly constant.

^bLikely due to slanted geometry in the frame of IU-Module, as in k_{zx} .

DoF	Slider-IU		Baby-IU		Remark
h_{xx}	0.56	N/A	0.85	N/A	see section 3.3.2
h_{yy}	—	N/A	—	N/A	-
h_{zz}	3.13	N/A	5.16	N/A	see section 3.3.2
$h_{\phi\phi}$	$57.6 \cdot 10^{-3}$	Nm/A	$84.0 \cdot 10^{-3}$	Nm/A	see section 3.5
$h_{\gamma\gamma}$	0	Nm/A	0	Nm/A	see section 3.5
$h_{\theta\theta}$	$11.9 \cdot 10^{-3}$	Nm/A	$16.8 \cdot 10^{-3}$	Nm/A	see section 3.5
h_{zx}	-0.20	N/A	0.10	N/A	see section 3.5

Table 3.5: Actuation constants resulting from linear fit for both IU-modules, only significant terms are shown.

Summarising, the IU-module is applicable as a 4-DoF actuator. It is capable of actuating F_x , F_z , T_x and T_z . The actuation of the torque, T_z , introduces less crosstalk than the actuation of the propulsion force, F_x . When actuation of these addi-

tional DoFs has an advantage, there is no reason not to use them. Applications of these additional DoFs are found in Chapter 6 and Appendix B.3. In Chapter 4, the IU-module is regarded as a 2-DoF actuator. In the next section, alternatives are discussed to overcome some of the IU-module's limitations.

3.6 Alternative designs

The IU-module is capable of acting as an actuator for suspension and propulsion, however in the out of centre position crosstalk exists. When longer strokes or higher propulsion forces are required, alternative configurations should be considered. Two alternative configurations are presented here. In Section 3.6.1, an IU-module with short propulsion coils is presented. In Section 3.6.2, an alternative actuator layout is shown. These alternative configurations are not studied further in this thesis.

3.6.1 Short propulsion coils

An option to reduce the interaction between the propulsion and suspension is to use multiple commutated short propulsion coils. By applying shorter propulsion coils, the ratio between force producing and ineffective coils is improved, which leads to lower power dissipation. Figures 3.23 and 3.24 show the resulting forces, F_x and F_z , for 4 displaced short propulsion coils of 15 mm. The propulsion force, F_x , is maximal as the coil is centred above the Slider bar, while interaction between the suspension force, F_z , is minimal. This shows that coils with commutated current are an option, if larger strokes or higher propulsion forces are required. However, research needs to be conducted on the placement and length of the coils, and the shape of the commutated current within these coils.

3.6.2 UO-module

The UO-module is an alternative to the IU-module for making a suspension and a propulsion force, F_z and F_x , as shown in Fig. 3.25. The idea of the UO-module is inspired by the fact that the generation of torque, T_z , in the IU-module does not influence the suspension force. By rotating one of the stator legs over 180° , the flux mechanism for actuating torque, T_z , is applied to the actuation of a propulsion force. Therefore, the UO-module might be able to propel the Slider bar with less crosstalk than the IU-module. In addition to the suspension and propulsion force, the UO-module is capable of generating torque, T_y . The potential advantages of the UO-module were discovered at the end of the project, and were not studied further.

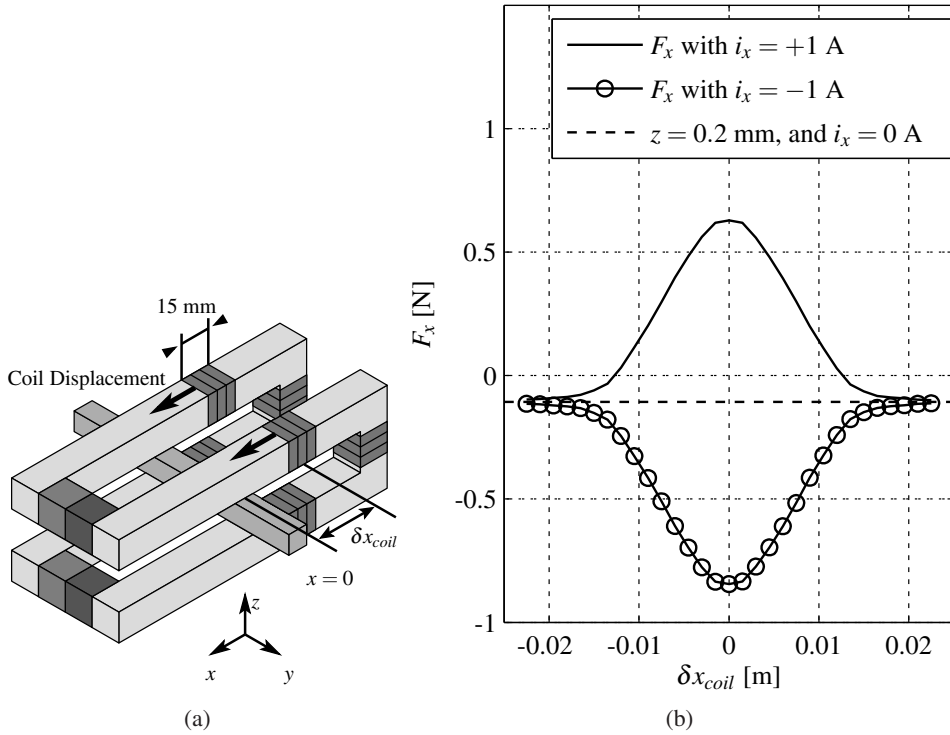


Figure 3.23: Simulation schematic, where 4 short propulsion coils are displaced, δx_{coil} , while the Slider bar is kept at the centre position ($x = 0, z = 0$) (a). Propulsion force, F_x , versus short coil displacement, δx_{coil} (b). The graph shows that maximum propulsion force, F_x , is achieved when the coils are centred above the Slider bar. In this centred position crosstalk is minimal, see Fig. 3.24.

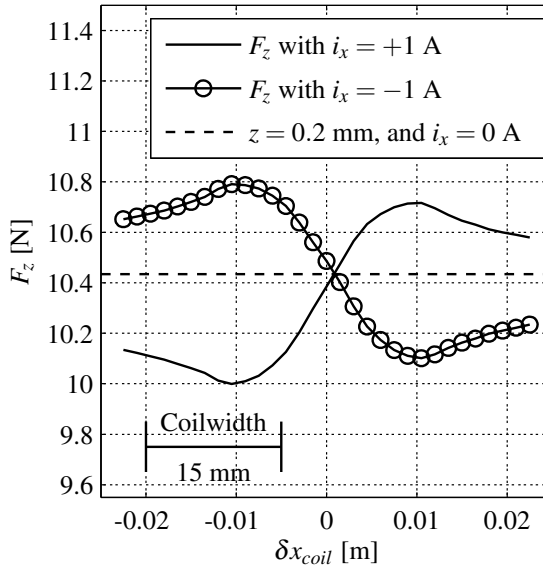


Figure 3.24: Suspension force, F_z , for displaced short propulsion coils, δx_{coil} , at $z = 0.2$ mm. The graph shows that the interaction between the propulsion and suspension is minimal when the propulsion coils are centred on the Slider bar.

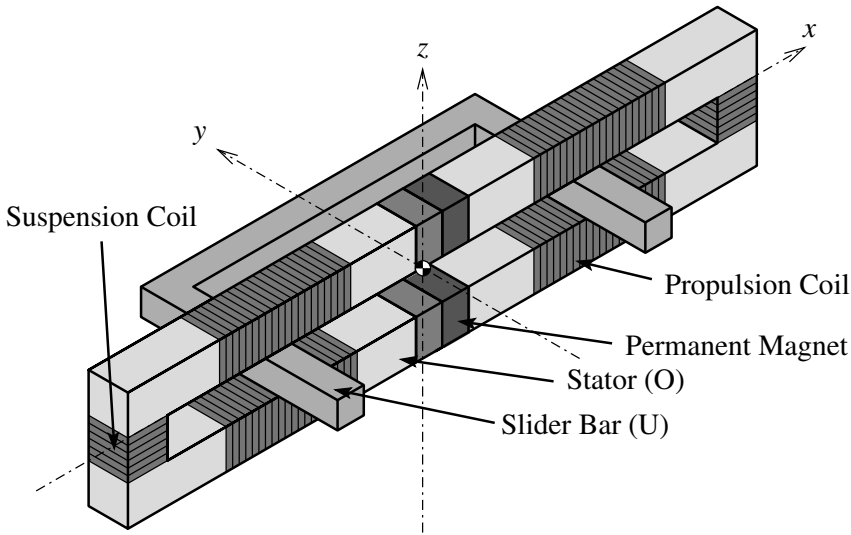


Figure 3.25: UO-module, capable generating propulsion force, F_x , suspension force, F_z , and torque, T_y .

3.7 Conclusions and remarks

This chapter demonstrates that the IU-module can be applied as a 2-DoF actuator for precision systems where the highest requirement is in the propulsion x -direction. Due to position dependent crosstalk, from propulsion actuation to the suspension force, the actuator is limited in maximum force and stroke. Secondly, the interaction between the propulsion and suspension limits applicability of the IU-module as a modular building block. To minimise the interactions the IU-module should be operated close to its centre z -position. In Chapter 4, an IU-module, actuated in 2-DoF, is integrated in the design for a Slider for optical disc mastering.

The applied modelling methods are not able to fully predict the behaviour of the IU-module, therefore in [44] improvements to the applied models and alternative modelling methods are researched.

In addition to generating the suspension and propulsion forces, the IU-module is capable of generating 2 torques, T_x and T_z . Since these torques can be actuated without any significant crosstalk, they can be applied when desired. In Chapter 6, these additional degrees of actuation are applied for modal control of the magnetically levitated Slider.

Chapter 4

Design of 6-DoF electromagnetically suspended Slider

The IU-module, presented in Chapter 3, is applied to the design of a Slider for an optical disc mastering (ODM) machine. In the ODM machine, the Slider translates over a separately rotating platform, while pointing a laser beam towards it. The ODM machine requires nm-resolution positioning, and therefore a careful design of its mechatronic components.

The ODM system is a mechatronic system, where disturbances from the electrical and mechanical domain influence performance. To take all these disturbances into account during the design, the Dynamic Error Budgeting (DEB) technique [69, 33] is used. In Section 4.1 this design methodology and its mathematics are explained. The design of any precision machine starts with an overview of the specifications. Herefore, in Section 4.2 the specifications for the ODM Slider are illuminated. The design of the Slider is split in a conceptual design and a component level design. The conceptual design choices are presented in Section 4.3. The design on component level is discussed in Section 4.4. The evaluation of the design, using the DEB technique, is performed in Section 4.5.

4.1 Dynamic Error Budget design methodology

The Slider for optical disc mastering is a mechatronic system, which achieves its performance through a balanced combination of mechanics, electronics and control engineering. The evaluation and optimisation over the different domains is not a straightforward task. Optimisation tools like finite element methods and optimal controller synthesis lead to optimisation in the separate domains. A solution to this is found in the DEB method [33].

Figure 4.1 graphically illustrates the applied design methodology of the Slider, with DEB at the centre. The design phase starts with an overview of the required specifications. Using these specifications a conceptual design is chosen. This conceptual design leads to initial specifications for the various components, like for the sensors and the actuators. These component level specifications result in an initial design. This design is then analysed using the DEB technique. If the specifications are met, a prototype can be manufactured. If not, the DEB technique indicates how performance can be improved, and a next design iteration is performed. In Section 4.1.1 the basics of the DEB technique are presented.

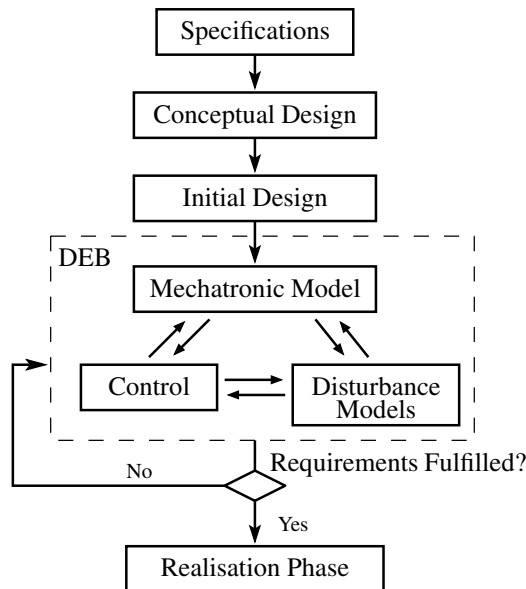


Figure 4.1: Design methodology with the Dynamic Error Budgeting (DEB) tool [33]. Design iterations are performed until the specifications are met. When the performance is satisfactory, the realisation phase is initiated, which consists of making detailed design drawings and the realisation of the prototype itself.

4.1.1 Dynamic Error Budgeting analysis tool

In DEB the disturbances acting on the system are assumed to be random stationary signals. The propagation of each of these disturbances to the output of a linear time invariant system is computed using linear system theory [55]. A short summary of the mathematical tools used in DEB is given here; a complete overview of the mathematical theory can be found in [33]. First, an introduction of random signals

in the time domain and frequency domain is given. Finally, the propagation of these disturbances through a linear system is discussed.

Time domain classification of stationary random signals

A disturbance signal, $w_n(t)$, is one of many realisations of the stochastic process, $w(t)$. The properties of this stochastic process, $w(t)$, are determined by taking the average of infinitely many realisations of $w(t)$, referred to as the ensemble average. If this ensemble average remains constant over time, the random process is called stationary. If the mean, \bar{w} , and variance, σ_w , defined by Eq. 4.1 and Eq. 4.2, of a single sufficiently long realisation of $w(t)$, are identical to that of the ensemble average of $w(t)$, the signal is called ergodic. In this thesis all disturbance signals are assumed to be stationary and ergodic.

$$\bar{w} = \lim_{T_p \rightarrow \infty} \frac{1}{2T_p} \int_{-T_p}^{T_p} w(t) dt, \quad (4.1)$$

$$\sigma_w^2 = \lim_{T_p \rightarrow \infty} \frac{1}{2T_p} \int_{-T_p}^{T_p} (w(t) - \bar{w})^2 dt. \quad (4.2)$$

The average power of a signal, $\|w\|_{rms}^2$, defined by Eq. 4.3, is related to the standard deviation by $\sigma_w^2 = \|w - \bar{w}\|_{rms}^2 = \|w\|_{rms}^2 - \bar{w}^2$.

$$\|w\|_{rms}^2 = \lim_{T_p \rightarrow \infty} \frac{1}{2T_p} \int_{-T_p}^{T_p} w(t)^2 dt. \quad (4.3)$$

Stochastic signals are described by their probability density function, $p(w)$, which expresses the probability, P , that a stochastic variable, w , lies in a certain interval, Eq. 4.4.

$$P(a \leq w(t_0) \leq b) = \int_a^b p(w) dw. \quad (4.4)$$

The shape of the probability density function, $p(w)$, characterises the random process. Common distributions for mechatronic systems are the *Uniform* and the *Gaussian* distribution. The uniform distribution (also called rectangular distribution), p_U , described by Eq. 4.5, characterises quantisation noise, caused for example by rounding of an analog observation to a digital number.

$$p_U(w) = \begin{cases} \frac{1}{b-a} & \text{if } a \leq w \leq b, \\ 0 & \text{if } w < a \text{ or } w > b. \end{cases} \quad (4.5)$$

The Gaussian distribution, p_G , described by Eq. 4.6, is often encountered in engineering. The *central limit theorem* [52] states that when a random process results

from infinitely many random elements (like often in a mechatronic system), it tends to have a Gaussian distribution.

$$p_G(w) = \frac{1}{\sigma_w \sqrt{2\pi}} \cdot e^{-(w-\bar{w})^2 / (2\sigma_w^2)}. \quad (4.6)$$

The Gaussian distribution is completely defined by its standard deviation, σ_w , and its mean, \bar{w} . In Fig. 4.2, a realisation of a Gaussian process is shown with a graph depicting the probability density function, $p_G(w)$. For a Gaussian distribution, the drawn values of the stochastic variable are for 68% are within σ , for 95% within 2σ , and for 99.7% within 3σ , from the mean. The servo-error and repeatability of a mechatronic system, defined in Section 2.1, are often Gaussian distributions, since they are the result of numerous disturbance sources.

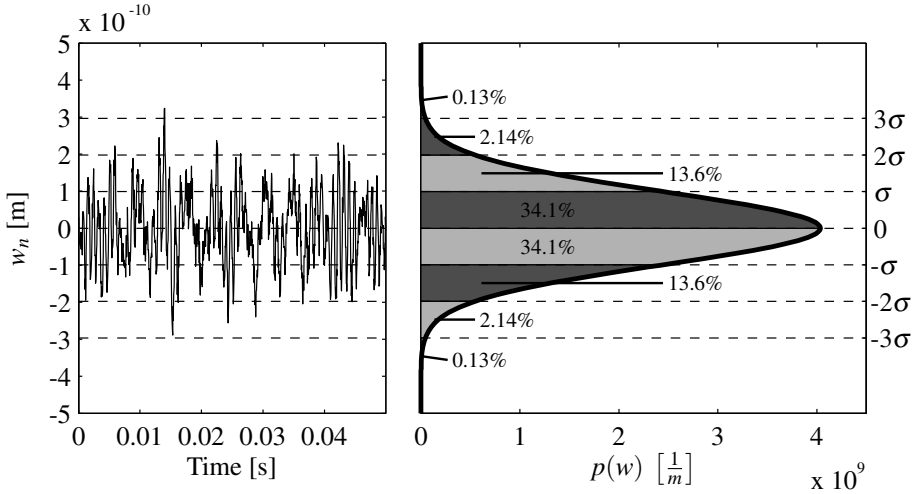


Figure 4.2: A realisation, $w_n(t)$, of a Gaussian distributed random process with zero mean (left) and a graph displaying its probability density, $p(w)$ (right). The percentage indicates the probability that w lies within the interval.

Frequency domain classification of stationary random signals

The power spectral density, $\text{PSD}_{2w}(f)$, represents the power density distribution over frequency of a random process $w(t)$. The power spectral density, $\text{PSD}_{2w}(f)$, is given by Eq. 4.7, where R_{ww} is the auto-correlation function.

$$\text{PSD}_{2w}(f) = \int_{-\infty}^{+\infty} R_{ww}(\tau) e^{i2\pi f\tau} \cdot d\tau, \quad (4.7)$$

$$R_{ww}(\tau) = \lim_{T_p \rightarrow \infty} \frac{1}{2T} \int_{-T_p}^{+T_p} (w(t - \tau) \cdot w(t)) \cdot d\tau. \quad (4.8)$$

The integral of the PSD is equal to the total power of the signal, Eq. 4.9. This equation is also known as *Parsevals equation*.

$$\|w\|_{rms}^2 = \int_{-\infty}^{\infty} \text{PSD}_{2w}(f) df. \quad (4.9)$$

The power spectrum density $\text{PSD}_{2w}(f)$ is an even function. Therefore, the one sided power spectrum, $\text{PSD}_w(f)$, is introduced to simplify representation, Eq. 4.10.

$$\text{PSD}_w(f) = \begin{cases} \text{PSD}_{2w}(0) & \text{for } f = 0, \\ 2 \cdot \text{PSD}_{2w}(f) & \text{for } f > 0. \end{cases} \quad (4.10)$$

The Dynamic Error Budget only deals with dynamic errors. Static error components or a non-zero mean, can be eliminated in a control loop by applying integral gain or by inserting an offset. Therefore, disturbances are assumed to have zero mean and the power is equal to the standard deviation squared, $\|w\|_{rms}^2 = \sigma_w^2$.

A graph containing the one sided power spectral density, PSD_w , gives the distribution over frequency, however the total power is not directly clear from the PSD_w -graph. Its cumulative sum is directly related to the power, $\|w\|_{rms}^2$, and standard deviation, σ^2 , in time domain. Therefore, the Cumulative Power Spectrum, $\text{CPS}_w(f)$, and the Cumulative Amplitude Spectrum, $\text{CAS}_w(f)$, are introduced, Eq. 4.11-4.12. The assumption is made that there are no DC components in the spectra.

$$\text{CPS}_w(f) = \int_0^f \text{PSD}_w(f) df, \quad f \geq 0, \quad (4.11)$$

$$\text{CAS}_w(f) = \sqrt{\text{CPS}_w(f)}. \quad (4.12)$$

Figure 4.3, shows the PSD_w , the $\text{CPS}_w(f)$ and the $\text{CAS}_w(f)$ of a time signal. The advantage of the $\text{CAS}_w(f)$ over the $\text{CPS}_w(f)$ is that it sums up to the variance, σ , and is in the same units as the actual measurement. Its drawback is that it is a non-linear function over frequency and emphasises low frequent contributions.

Disturbance propagation through linear time invariant systems

Figure 4.4 depicts a linear time invariant closed-loop system, subjected to various *uncorrelated* disturbance sources, w . The system consists of a linear time invariant

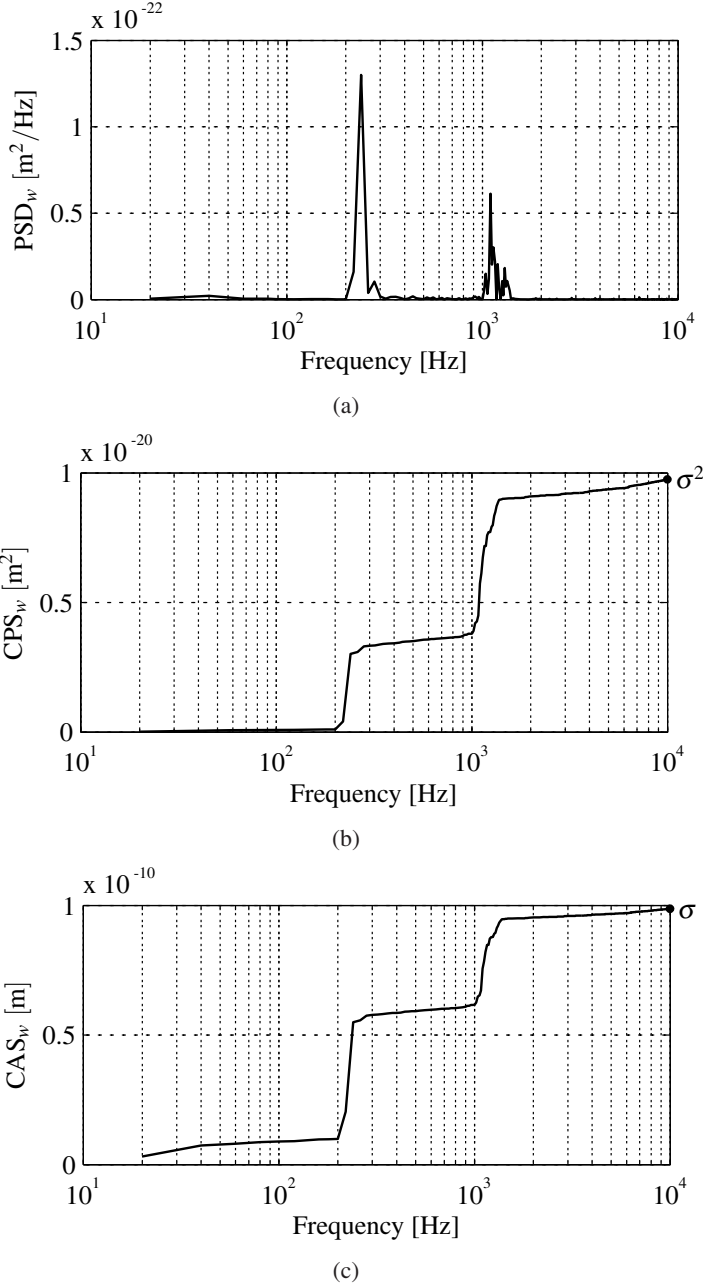


Figure 4.3: One sided Power spectral density (a), Cumulative Power Spectrum (b) and Cumulative Amplitude Spectrum (c) of the stochastic signal of Fig. 4.2.

plant, $\mathbf{G}(s)$, and a controller, $\mathbf{C}_c(s)$. The disturbance sources, w , lead to a position error, y . A closed-loop transfer function $H_w(s)$, of the linear time invariant mecha-tronic plant, is constructed from each disturbance source, w , to the output location, y . Using this transfer, the propagation of each *uncorrelated* stochastic disturbance source w_n can be computed using Eq. 4.13.

$$\text{PSD}_y(f) = \sum_{n=1}^N |H_{w_n}(f)|^2 \cdot \text{PSD}_{w_n}(f). \quad (4.13)$$

Assuming zero mean, the standard deviation of the closed-loop system, σ_y , can then be established with Eq. 4.14 and compared to the requirements for the design.

$$\sigma_y^2 = \int_0^\infty \text{PSD}_y(f) \cdot df = \int_0^\infty \sum_{n=1}^N |H_{w_n}(f)|^2 \cdot \text{PSD}_{w_n}(f) \cdot df. \quad (4.14)$$

If the specifications are not met, the most dominant disturbance source is easily singled out, since $\sigma_y^2 = \sigma_{y1}^2 + \sigma_{y2}^2 + \dots + \sigma_{yN}^2$. By displaying Cumulative Amplitude Spectra, the most critical frequency range indicates how the plant or controller is best improved. Modifications to the design of the plant, $\mathbf{G}(s)$, and/or controller, $\mathbf{C}_c(s)$, can then made to reduce the influence of the most dominant disturbances. These design iterations are pursued until the requirements of the design are obtained.

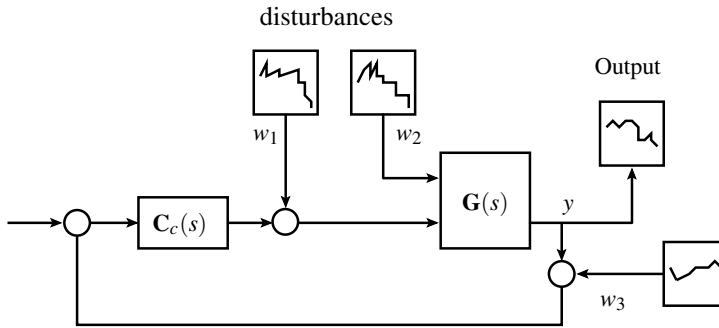


Figure 4.4: A closed-loop system with $\mathbf{C}_c(s)$ - controller, $\mathbf{G}(s)$ - plant, w - disturbances, and y - output.

4.2 Specifications for the Slider in optical disc mastering

Around 1983, Philips and Sony launched the Compact audio Disc, the CD. The CD was the first optical disc to be a commercial success. The information on the optical disc is imprinted in the form of bumps and pits in the shape of spiral grooves. The information is read contactlessly, using a laser beam focused on the optical disc. The desire to have higher information densities for the optical disc resulted in the DVD in 1998 and the Blu-Ray Disc in 2003. This higher information density led to decreased track pitch and pit sizes, as shown in Tab. 4.1.

	CD	DVD	Blu-Ray
Capacity [GB]	0.67	4.7	25
Laser Wavelength [nm]	780	650	405
Numerical Aperture	0.45	0.65	0.85
Track pitch [μm] (d_{tp})	1.6	0.74	0.32
Scanning Velocity [m/s] ($1\times v_{lin}$)	1.3	3.49	4.92
Shortest Pit Length (3T) [nm] (d_{short})	830	400	149
Radial Runout [μm] (d_{rr})	140	100	75
Radial Servo Error [nm]	70	22	9
Axial Servo Error [nm]	1000	230	45

Table 4.1: Specifications for Optical Discs and the read-out servo, information obtained from [17, 18, 3].

Optical discs are replicated using a stamper (the mould) in an injecting moulding machine. The manufacturing of this stamper is performed with the ODM machine. The ODM machine consists of two main parts, a rotating platform and a Slider, see Fig. 4.5. The rotating platform spins a glass substrate coated with photo resist. The Slider moves over the substrate, pointing a laser beam onto it, exposing the photo resist. This glass substrate forms the basis for the stamper in the injection moulding machine. The current state of the art ODM machines use air-bearings to achieve the required accuracy.

The smaller dimensions of the optical features on the Blu-Ray disc place more stringent demands on the ODM machine and its recording source. To record future generations of discs, Extreme Ultraviolet Violet and Electron Beam Recording can be applied. However, these sources require vacuum conditions. Pioneer [3] built an E-beam recording machine for optical disc mastering. This machine has a leadscrew to drive the Slider. Lubrication of such a system leads to contamination of the vacuum environment. Such problems could be eliminated if magnetic bearings are applied.

The full specifications of the Blu-Ray disc are not publicly available. However, the specifications of the DVD and CD are available [17, 18]. Together with a white

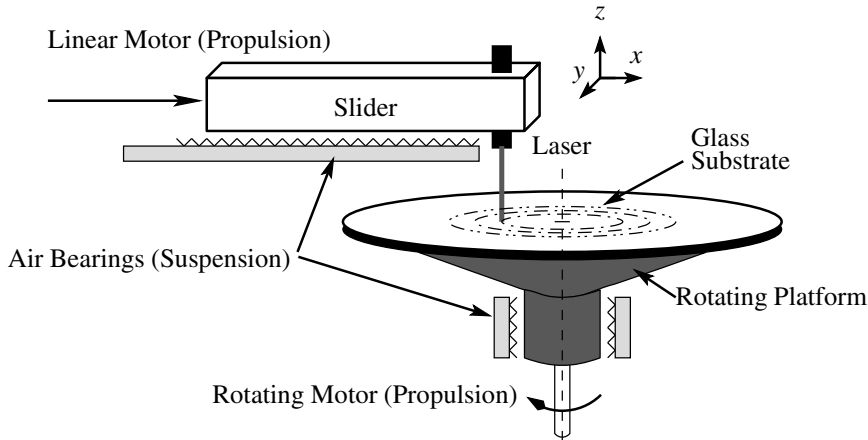


Figure 4.5: Current State of the Art Optical Disc Mastering Machine

paper [3] educated guesses can be made on the specifications of the disc and the Optical Disc Mastering machine.

The error in the optical disc is split up in three directions: the radial, the tangential and axial direction, see Fig. 4.6. The radial direction is influenced by the x -position of the Slider. The tangential and axial directions are influenced by the suspension y -position, and horizontal z -position from Fig. 4.5.

4.2.1 Error in radial direction (x)

The errors in the radial direction on the optical disc are split up between two parts: the asynchronous and the synchronous error. The synchronous error is repetitive with each full cycle of rotation, while the asynchronous error is a stochastic variation on top of the synchronous error. According to the specifications the radial runout of the optical disc, containing both the synchronous and asynchronous error, should be less than $75\text{ }\mu\text{m}$, see Tab. 4.1. The specifications on the asynchronous error are much tighter than on synchronous error. The reason for this is that the synchronous error forms a low frequency repetitive disturbance on the read-out servo-system in the optical disc player, which can be suppressed by this servo-system. The synchronous error contribution of the Slider in the mastering process is mainly caused by low frequency disturbances, like sensor drift, thermal drift and alignment errors. These low frequent effects are out of the scope of this research.

The asynchronous error, also called track pitch variation, δ_{tp} , is the error between two successive tracks, see Fig. 4.6. Jabben [33] deduces that the maximum allowed track pitch variation for the Blu-Ray Disc is $\pm 7\text{ nm}$ ($\pm 3\sigma$) using the specifications from the DVD and CD. The allowed standard deviation for the track pitch

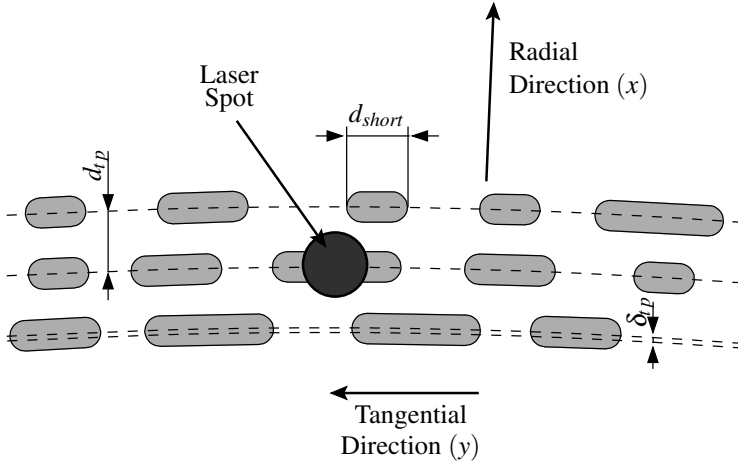


Figure 4.6: Magnified optical disc with pit pattern and dimensions of the track pitch d_{tp} , track pitch variation δ_{tp} , and shortest pit length d_{short} .

variation, σ_{tp} , then becomes $2.3 \text{ nm}(\sigma)$.

The track pitch variation, δ_{tp} , is caused by:

- Perturbations of the alignment optics, delivering the laser beam to the Slider.
- Position errors of the Slider in x -direction.
- Tilt and position errors of the focus optics.
- Radial error motions of the rotating platform.

When these 4 error sources contribute an equal amount, the allowed standard deviation for the Slider in the x -direction is $\sigma_x = \sqrt{\frac{\sigma_{tp}^2}{4}} = 1.15 \approx 1 \text{ nm}$. The stroke in the propulsion direction should be larger than the data area of the disc (60-24 mm). At nominal recording speed of the Blu-Ray disc, the rotational speed varies between 13 Hz at outer radius, to 32 Hz on inner radius. Disturbances below half the rotation frequency, $< 6.5 \text{ Hz}$, do not directly influence the track pitch variation, δ_{tp} , since they are distributed over several tracks. While taking a considerable safety margin into account, it is assumed that errors below 1 Hz are not contributing to the asynchronous error. Errors below 1 Hz will not be accounted for within the Dynamic Error Budget.

4.2.2 Error in tangential direction (y)

Tangential errors or pit length variations, cause timing variations in the read-out signal of the optical disc, which are called jitter. Blu-Ray players correct for such timing variations up to 9 kHz; only length variations above this frequency contribute to the jitter. The mass of the Slider acts as a natural filter for any disturbances above 9 kHz. Therefore, the specifications in the tangential direction are less tight than in the radial direction.

To limit spillover from the tangential direction to the radial direction, the specifications for the tangential direction are allowed to be 5 times that of the radial specification, $\sigma_y = 5$ nm.

4.2.3 Error in axial Direction (z)

The laser for writing the pits has to be kept in focus on the substrate. The main disturbances on the focus are the alignment of the surface and the roughness of the glass substrate. The substrate introduces disturbances up to a few kHz, since the disc is already rotating at speeds up to 30 Hz. The current optical disc mastering systems have a light (< 100 g) voice-coil focus actuator for suppression of these disturbances up to 4 kHz. A very light actuator with low phase lag is required for such a system. It is assumed that a separate focus will have to be added to the Slider in the future to make optical discs. However, this actuator is not part of the current design. To allow a focus actuator to be added afterwards, the Slider should have significant mass and for the design 1 kg is chosen.

The specification of the servo-error in the axial direction of the CD, DVD and Blu-Ray players are a factor of 5 to 10 times less stringent than in the radial direction. Therefore, the servo-error in suspension direction is specified at $\sigma_x = 5$ nm (σ), 5 times the radial direction.

4.2.4 Additional requirements for the Slider

Just after introduction, the initial recording speeds of the optical discs in the ODM machine were equal to the nominal read speeds. In the following years, this recording speed was increased, resulting in a production time of about 15 min. To make sure the Slider is capable of achieving any future demand, it should be capable of making Blu-Ray discs in 15 min, resulting in a radial translation velocity of $55 \mu\text{m/s}$.

The Slider is built using the IU-modules presented in Chapter 3. The IU-module is capable of suspending the Slider completely contactless and with close to zero energy dissipation. To make full use of the IU-modules, the design should have no additional wires connected to the Slider. This reduces coupling of any mechanical vibrations to the Slider. The gravity forces should be compensated by the permanent magnets, minimising energy consumption and thermal effects on the Slider. The

Stroke	Propulsion (x) Suspension (z)	50 mm 0.5 mm
Servo-Error	Propulsion (x) Suspension (z) Horizontal (y)	$< 1 \text{ nm } (\sigma)$ $< 5 \text{ nm } (\sigma)$ $< 5 \text{ nm } (\sigma)$
Absolute error	Propulsion	$75 \text{ }\mu\text{m}$
Slider Mass		1 kg
Actuator		IU-module
Sensors		On fixed world
Reference velocity	Propulsion (x)	$55 \text{ }\mu\text{m/s}$

Table 4.2: Main design specifications for the Slider.

Slider will not be tested in a vacuum environment. However, the Slider should only use components which are vacuum compatible. The sensitivity of the optical recording to angular errors is very dependent on the design of the optical path and this goes beyond the scope of this thesis. The specifications on the angular errors, φ , γ , and θ , are not treated in detail. The displacements on the Slider, caused by the angles, are aimed to be in the same order of magnitude as x , y and z -errors. Table 4.2 gives an overview of the main design specifications.

Specifications of the Singulus Mastering AM266

At the end of the research a brochure was obtained from Singulus mastering, the largest manufacturer of Optical Disc Mastering equipment. Its AM266 production system, capable of mastering Blu-Ray discs, has a radial relative position error in its translation stage of $2.5 \text{ nm } (\sigma)$. This is comparable to the assumed specification in the x -direction of $1 \text{ nm } (\sigma)$, showing that the used specifications of Tab. 4.2 are close to those of a modern ODM machine.

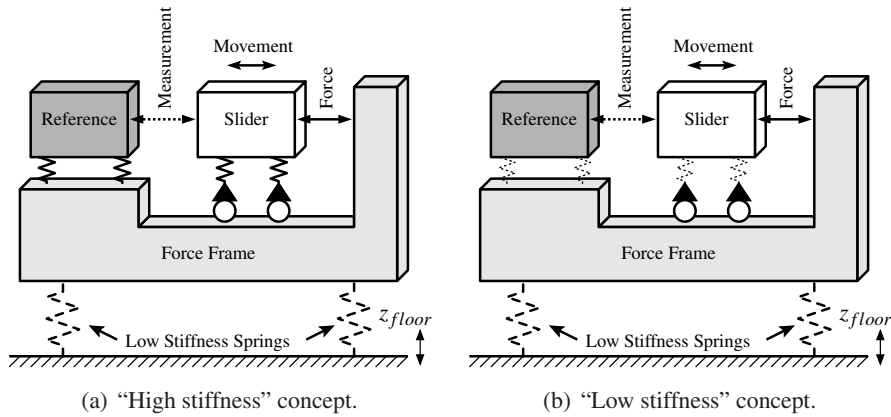


Figure 4.7: The "high" and "low" stiffness design concepts.

4.3 Conceptual design of the Slider

The Slider in an optical disc mastering system aims to realise nm-position stability between the Slider and the rotating platform over a stroke of 50 mm. The rotating platform is not part of project described in this thesis. Therefore, the goal is to reach the position stability between a separate reference frame and the Slider. The illumination process of the glass substrate, does not introduce any process forces and is therefore not a source of disturbance. The main dynamic external disturbances acting on the Slider are floor vibrations. Reproducible errors, caused by unbalance of the rotating platform, are not taken into account in the dynamic error budget. Such reproducible errors can for example be compensated by "conventional" feed-forward control or by "learning" feed-forward control [16].

Two conceptual choices are available for the design of the Slider, the "high" and "low" stiffness concept, depicted in Fig. 4.7.

The "high stiffness" concept

The "high stiffness" concept is most commonly used in precision engineering. In the "high stiffness" concept, a vibration isolation system separates the machine frame from its surroundings, while all high accuracy components are referenced to each other through high stiffness connections to the force frame.

The "low stiffness" concept

In the "low stiffness concept", all high accuracy components are connected to the frame with a low stiffness. The accurate components are then referenced to each-

other through a high stiffness control loop. The actuation forces are guided to the force frame, but not through the high accuracy components themselves. This separation of control and performance location is made possible by active control. This situation is similar to the situation of Fig. 2.1.

Comparison of Design Concepts

A lumped mass-spring model is used to compare both design concepts and test their applicability to the Slider for the ODM machine. The IU-modules have close to zero stiffness in the propulsion direction, making them ideally suited for the “low stiffness” concept in this direction. In the suspension the IU-module has a high negative stiffness, making it less ideal for the “low stiffness” concept. Therefore, to obtain a fair comparison and to determine the implications of the negative stiffness, the comparison is made in the suspension direction.

A graphical representation of the model, used for the comparison, is shown in Fig. 4.8. The performance measure of the system is the position error between the Slider and the reference, $z_S - z_R$. To obtain the required performance, a PID controller closes a position loop between the servo-error, $e = z_S - z_R$, and the actuation force F_S . The suspension frequency of the reference, f_R , is taken as 4 Hz and 500 Hz. The 4 Hz represents a “low stiffness” system, while the 500 Hz represents a “high stiffness” configuration. The entire system is placed on a vibration isolation platform with a suspension frequency of $f_F = 20$ Hz. Ground vibrations enter the system through z_{floor} . Internal disturbances, due to for example electronic noise, enter the system through the actuation force, F_S . The mass and stiffness properties of the model are representative for the Slider using IU-modules in the optical disc mastering application.

Figures 4.9 and 4.10 show the plant and open-loop transfer of the system. The plant transfer, $G(s)$, shows a flat response up to 70 Hz and rolls off with a -2 (-40 dB per decade) slope. The flat response is caused by the negative stiffness connection between the Slider and the force frame. The transfer to position, z_S , for a mass, m_S , connected with a negative spring constant, k_{zz} , subjected to a force, F_S , is described by Eq. 4.15.

$$\frac{z_S(s)}{F_S(s)} = \frac{1}{m_S \cdot s^2 + k_{zz}}. \quad (4.15)$$

Transfer function, Eq. 4.15, resembles that of a conventional mass-spring system, except for the negative spring constant. The Bode diagram of such a system has a flat response until $f_S = \frac{1}{2\pi} \sqrt{\frac{k_n}{m}}$ and then rolls off with the -2 slope. The Bode diagram does not show a resonance peak at f_S , which would be present in the case of a conventional mass-spring system with positive stiffness.

Figure 4.10 shows the open-loop transfer, $L(s)$. The open-loop 0 dB crossing, lies at 300 Hz. The transfer function of the PID controller is given by Eq. 4.16, with

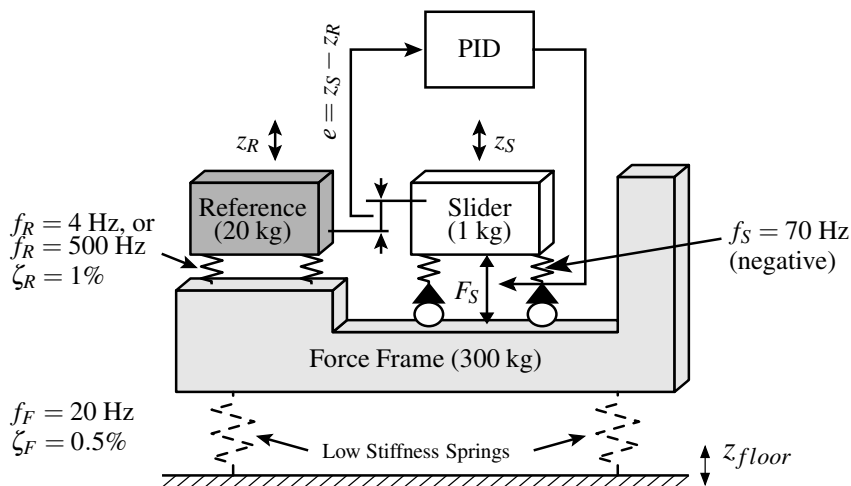


Figure 4.8: Lumped mass-spring model for the “low” and “high” stiffness concept comparison. With subscripts, S - Slider, F - force frame and R - reference frame.

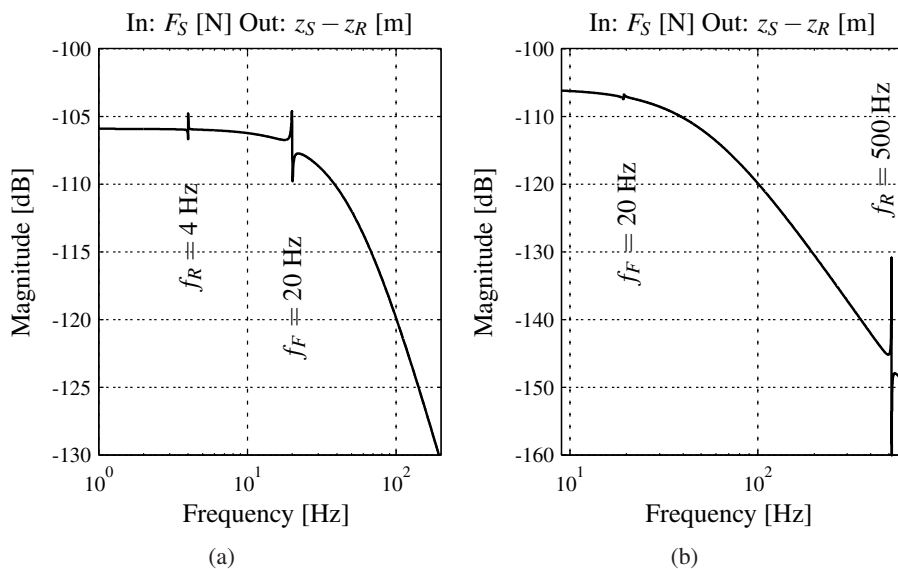


Figure 4.9: Plant transfer, $G(s)$, from input force F_S to position error, $z_S - z_R$, with $f_R = 4$ Hz (a), and $f_R = 500$ Hz (b).

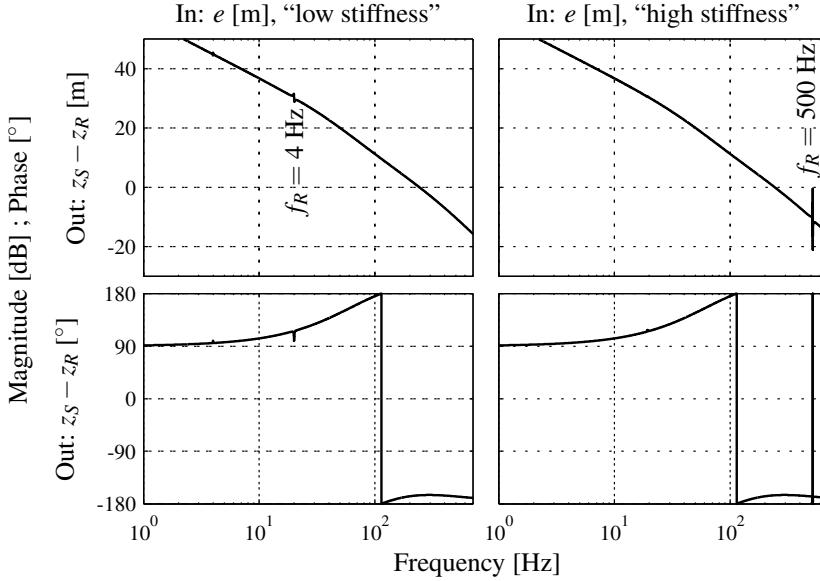


Figure 4.10: Open-loop transfer from controller input e , to measured position error, $z_S - z_R$, for $f_R = 4$ Hz and $f_R = 500$ Hz. In “low stiffness” concept, $f_R = 4$ Hz, the flexible modes, do not threaten stability margins.

$\tau_d = 100$ Hz, $N = 3$, $K_i = 60$ Hz and $P_d = 1.2 \cdot 10^6$. In the “low stiffness” concept, the modes at f_R and f_F are mildly excited by actuation force F_S . These modes are not a threat to stability. In the “high” stiffness concept, the mode at 500 Hz directly limits the stability margins of the control loop.

$$\frac{F_S(s)}{e(s)} = K_d \cdot \frac{s + K_i}{s} \cdot \frac{(1 + \tau_d s)}{(1 + N_c \cdot \tau_d s)}. \quad (4.16)$$

The effect of the internal disturbances entering through the actuation force, F_S , is shown in Fig. 4.11. The graph shows the transfer of the closed-loop system for both the “high” and “low stiffness” concept. The low frequency modes of the “low stiffness” system, depicted in Fig. 4.9, are not visible in the closed-loop of Fig. 4.11. In the “high stiffness” concept, the mode at 500 Hz is excited. This mode degrades performance significantly, since it directly influences the asynchronous error. It might be argued that, through careful design, the resonance frequency at $f_R = 500$ Hz can be increased, reducing the excitation of the resonance. However, one has to realise that the entire internal flexibility of the force frame is represented by f_R . A very good design of the force frame will be required to make this much higher than 500 Hz.

Figure 4.12 shows the closed-loop transfer of floor vibrations, z_{floor} , to the position error between the Slider and reference, $z_S - z_R$. The “high stiffness” concept has the best performance in the low frequency region up to 60 Hz. Specifically at 20 Hz the performance of the “low stiffness” concept is poor, resulting in amplification of the floor disturbances. However, in the range above 50 Hz, the “low stiffness” outperforms the “high stiffness” concept.

The poor performance of the “low” stiffness concept at frequencies below 60 Hz is caused by the negative stiffness of the IU-module actuators. This negative stiffness causes force frame displacements, z_F , to perturb the Slider. An effective way of improving the performance of the “low stiffness” concept is by reducing or compensating the negative stiffness. Compensation is performed by a separate feedback loop, from the position difference between the Slider and the force frame, to the force acting on the Slider, $F_{S,comp} = k_{comp}(z_S - z_F)$. Where k_{comp} opposes the negative stiffness of the IU-modules. The negative stiffness was compensated by 90%, the improved transfer from floor vibrations to the position error is now shown in Fig. 4.13. It is clear that this stiffness compensated “low stiffness” concept outperforms the “high stiffness” concept in most of the critical frequency range above 6.5 Hz.

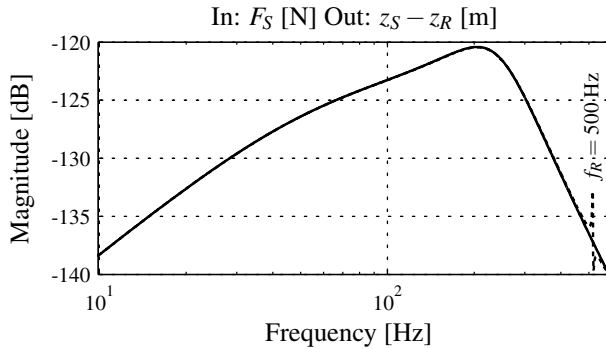


Figure 4.11: Transfer from disturbance force, F_S , to position error $z_S - z_R$ for $f_R = 4$ Hz (—), and $f_R = 500$ Hz (---).

For the design of the prototype Slider, the “low” stiffness conceptual design is chosen. The “low stiffness” concept is less sensitive to disturbances by ground vibrations and internal excitations in the frequency range of interest. In addition to these advantages, the “low stiffness” is less sensitive to any unmodelled modes present in the force frame, since the reference frame is decoupled from the force frame. The bandwidth of the controller for the “low stiffness” concept can generally be lower, since a higher degree of isolation to external disturbances is achieved by the mechanical design.

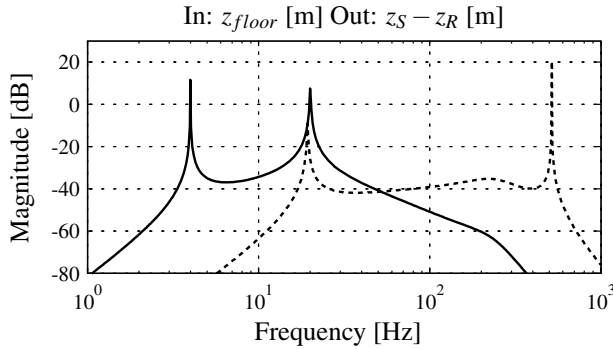


Figure 4.12: Transfer from floor vibrations, z_{floor} , to position error, $z_S - z_R$, for $f_R = 4$ Hz (—), and $f_R = 500$ Hz (---).

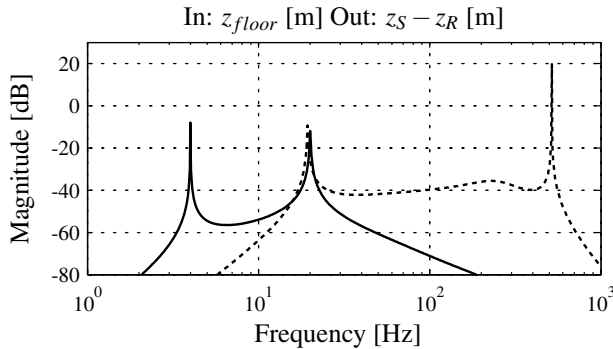


Figure 4.13: Transfer from floor vibrations, z_{floor} , to position error, $z_S - z_R$, with *stiffness compensation* for $f_R = 4$ Hz (—), and $f_R = 500$ Hz (---). The stiffness compensated “low stiffness” concept outperforms the “high stiffness” concept for disturbance frequencies above 15 Hz. The optical disc is less tolerant to high frequent disturbances. Therefore, the stiffness compensated “low stiffness” concept is applied to the design of the Slider.

4.4 The Slider design

The “low stiffness” design concept is chosen during the conceptual design in Section 4.3. Since the Slider is a mechatronic system, the design is a combination of actuator design, mechanical design, sensor design and electrical design. Each of these components are discussed in the following subsections.

4.4.1 Actuator Configuration

The design of the IU-module actuator for the magnetically levitated Slider was described in Chapter 3. A non-optimised, but sufficient version of the IU-module is used for the Slider. A more optimised design of the IU-module is presented in [44].

In the Slider design, the IU-modules are used as 2-DoF actuators. The IU-module has one long stroke of 50 mm, and a short stroke of 0.5 mm. The stiffness layout of the IU-module exactly meets the requirements for the ODM machine in combination with the “low stiffness” design concept. The long stroke has zero stiffness in the x -direction and is aligned with the highest specifications in radial direction. In the short stroke z -direction, the negative stiffness can be used to compensate the weight of the Slider. The specifications in the z and y -directions are less critical, rendering the system more tolerant in these directions to disturbances being transferred through the negative stiffness of the IU-module.

Geometric actuator configuration

The body of the Slider has in total 6-DoF: x , y , z , φ , γ and θ . To control these 6-DoF, three separate 2-DoF IU-modules are required (each creating a suspension and propulsion force). The 2 main configurations for placing the IU-module around the Slider are the 90-degree and 120-degree configuration, as shown in Fig. 4.14.

Both configurations can be controlled with decentralised PD control loops, between actuation force on the Slider bar F_{act} , and a local position measurement on each bar. However, in the 120-degree setup, a displacement in y or z -direction, will result in a restoring force F_y and F_z , without any parasitic torque around the centre of gravity. In the 90-degree configuration, a displacement of the CoG in y -direction results in a restoring force, F_y , and a parasitic torque, T_x . To counter this, a centralised controller with an actuator decoupling can be applied, resulting in a more complex controller.

In spite of the control complexity, the 90-degree setup is chosen, because of geometrical advantages. In the actual optical disc mastering system, there is little space between the Slider and the rotating disc (less than 100 μm) and the 90-degree setup uses the least amount of space underneath the Slider.

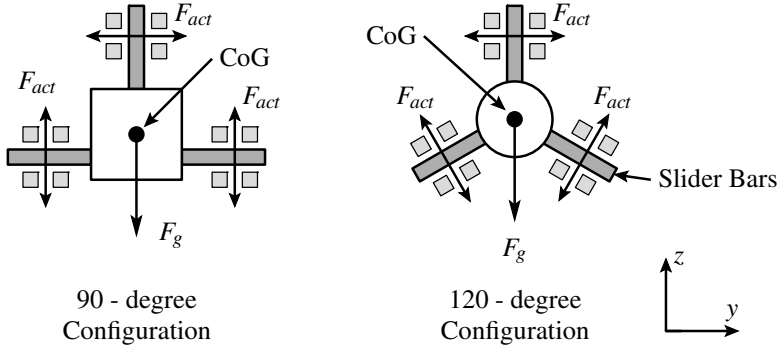


Figure 4.14: Actuator layouts for the Slider in suspension direction with respect to the centre of gravity (CoG), showing the actuation forces, F_{act} .

4.4.2 Sensor configuration

To determine the position of the Slider with respect to the reference, 6-DoF must be measured: 3 short stroke measurements giving the suspension positions, y , z , and, φ , and 3 long stroke measurements giving the propulsion positions, x , γ , and θ .

The negative stiffnesses of the IU-modules act between the Slider and the force frame in the suspension directions, y , z and φ . To compensate the stiffness, position measurement of the Slider in these 3 directions with respect to the force frame is required. Before start-up, the Slider is stuck to the force frame in an undefined position. In this position, the Slider might not be in range of the sensors on the reference frame. Therefore, to facilitate a smooth start-up, the propulsion directions with respect to the force frame are measured as well. Summarising, the Slider is designed to have 6 sensors measuring with respect to the force frame and 6 sensors measuring with respect to the reference frame.

Frame sensors and their layout

Figure 4.15 shows the Slider with the position sensors, which are attached to the force frame. To simplify initial start-up of the Slider, the sensors of the Slider are located close to the actuators, allowing near-collocated control [61]. The sensors are placed on the top side of the Slider, so the reference frame sensors can be placed near the rotating platform where the highest accuracy is required, see Fig. 4.15.

In the suspension directions, y , z and φ , the Micro Epsilon NCDT 3700, eddy current sensors are used. An eddy current sensor measures the change of inductance, caused by the presence of eddy currents induced in a conducting aluminium target. The eddy current sensor NCDT 3700 was chosen, because of its high resolution.

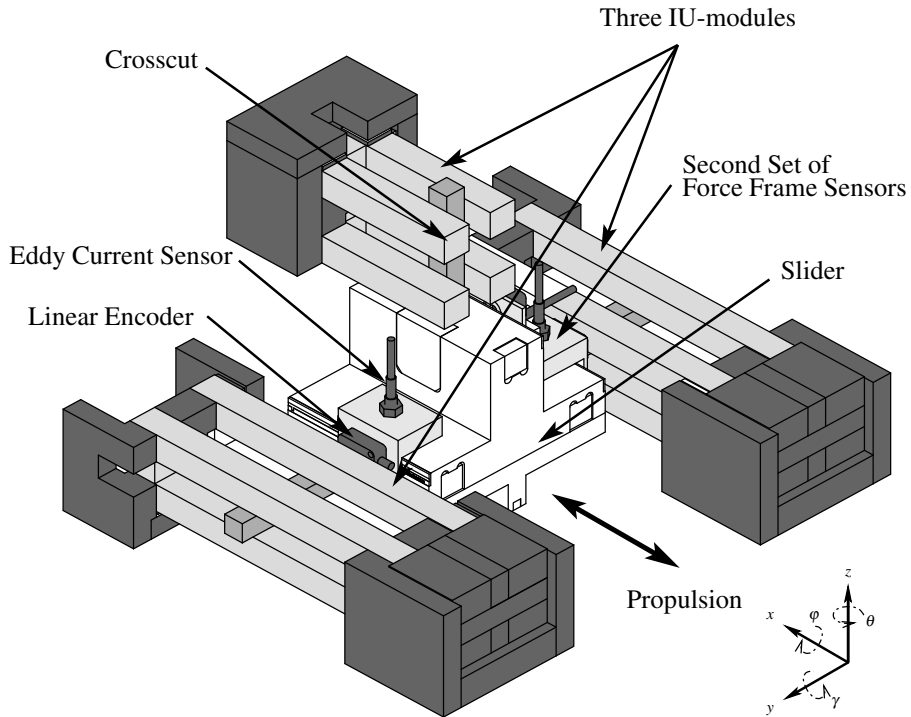


Figure 4.15: Slider with three IU-modules and force frame sensors, with top IU-module cut for clarity. Note that the positive x -direction differs from Chapter 3.

The drawback of this sensor is limited linearity, see Tab. 4.3.

For the long stroke directions, an optical linear encoder, the MicroE M3000, is chosen. The choice for this encoder is made, because it is one of the smallest of its kind, and it is relatively tolerant to parasitic rotations and translations. The parasitic rotations and translations are required during the start-up phase, because at start-up these sensors are not aligned with a fixed reference.

Reference sensors and their layout

Capacitive sensors manufactured by ADE are chosen to perform the measurement of the suspension positions. Laser interferometers are used for the propulsion directions, x , γ and θ .

The ADE 4810 capacitive sensors are applied, because of a good previous experience in the rotating optical disc mastering project [33]. The Ångström stage [46], which demonstrated extraordinary performance, also used similar capacitive sensors. Table 4.5 gives the specifications of these sensors. The drawback of capacitive

Stroke	1 mm
Resolution (0-1000 Hz)	1.3 nm (σ)
Accuracy	6% of the Stroke
Output	0-10 V
Target	Aluminium, minimum thickness 0.5 mm
Price	$\approx 2000\text{€}$
Cutoff Frequency	10 kHz

Table 4.3: Specifications of the Micro Epsilon eddy current sensor, NCDT 3700.

Stroke (x)	50 mm (Grating Dependent)
Stroke (y)	± 0.15 mm
Stroke (z)	± 0.2 mm
Allowed rotation angle φ	1°
Allowed rotation angle γ and θ	2°
Resolution	20 nm
Accuracy	$\pm 3\text{ }\mu\text{m}$ over one metre
Output	RS422 quadrature
Target	ruler grating
Price	$\approx 1000\text{ €}$
Maximum Speed at 20nm resolution	576 mm/s

Table 4.4: Specifications of the MicroE M3000 optical linear encoder used in the Slider. x is the measurement direction, y planar direction perpendicular to x , z is the standoff between the sensor head and the grating.

Stroke	100 μm
Resolution (0-1000 Hz)	1.3 nm (σ)
Accuracy	0.02% of the Stroke
Output	$\pm 10\text{ V}$
Target	Any Grounded Conductive Surface
Price	$\approx 3000\text{ €}$
Cut Off Frequency	10 kHz

Table 4.5: Specifications of the ADE 4810 capacitive sensor.

sensors is that they require a grounded target. To ground the Slider, wires can be connected, violating the demand for wireless propulsion. According to the manufacturer, it is possible to ground the target contactlessly using capacitive grounding. Capacitive grounding is non-trivial and a separate study on this subject is conducted by Overschie [56], at the Advanced Mechatronics group in Delft.

The Renishaw RLE10 laser interferometers with RPI-20 read-out boards, measure the propulsion directions with respect to the reference frame. The specifications of the Renishaw RLE10 are given in Tab. 4.6. A laser interferometer can measure translations very accurately, while the moving body is still capable of making perpendicular motions. The drawback of the interferometer is the sensitivity to low frequency environmental disturbances, like air pressure and air temperature variations. A full overview of disturbances, acting on laser interferometers, is found in [14]. The choice for the Renishaw laser is made, because it is easily aligned and it has a relatively low price, compared to other laser interferometers. The ease of alignment comes from the fact that all optical components with adjustments are contained within one unit. The laser interferometer provides only relative measurement. Therefore, the index marks of the linear encoders are used as the fixed reference for starting the measurements.

The Slider with the reference sensors is shown in Fig. 4.16. The sensors are placed on the exterior of the Slider, so that the angles, φ , γ and θ , are measured with similar resolutions as the translations.

4.4.3 Mechanical design of the Slider

Figure 4.17 shows the layout of the mechanical system as a whole. This full system consists of the Slider, the reference frame and the force frame. The mechanical design of each of these components is discussed in the subsequent subsections.

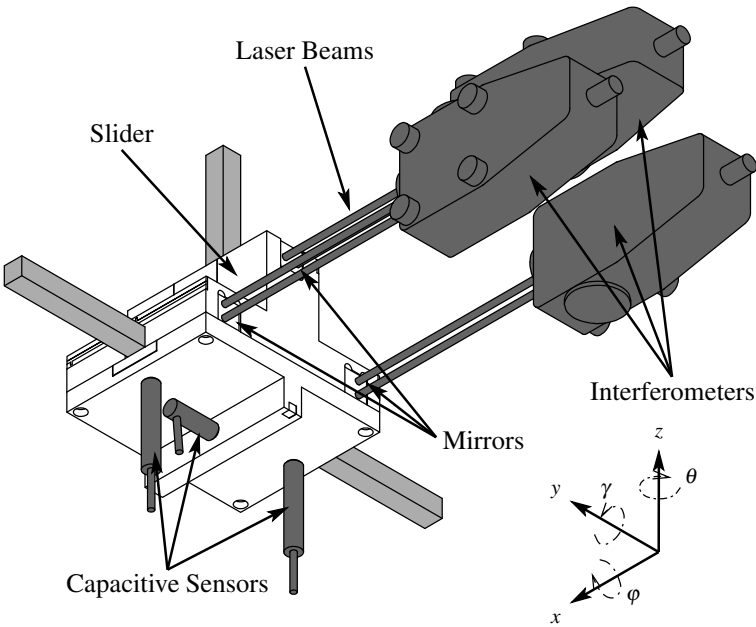


Figure 4.16: Slider with high accuracy sensors, which are attached to the reference frame. The viewpoint is from underneath the Slider.

Maximum Stroke	3 m
Resolution with RPI-20	38.6 pm (σ)
Electrical Noise	0.5 nm
Angular alignment	<1 mrad
Target	plane mirror ($\frac{\lambda}{10}$)
Price for 2 axes	$\approx 17000 \text{ €}$
Maximum velocity	1 m/s

Table 4.6: Specifications of the Renishaw laser interferometer RLE10.

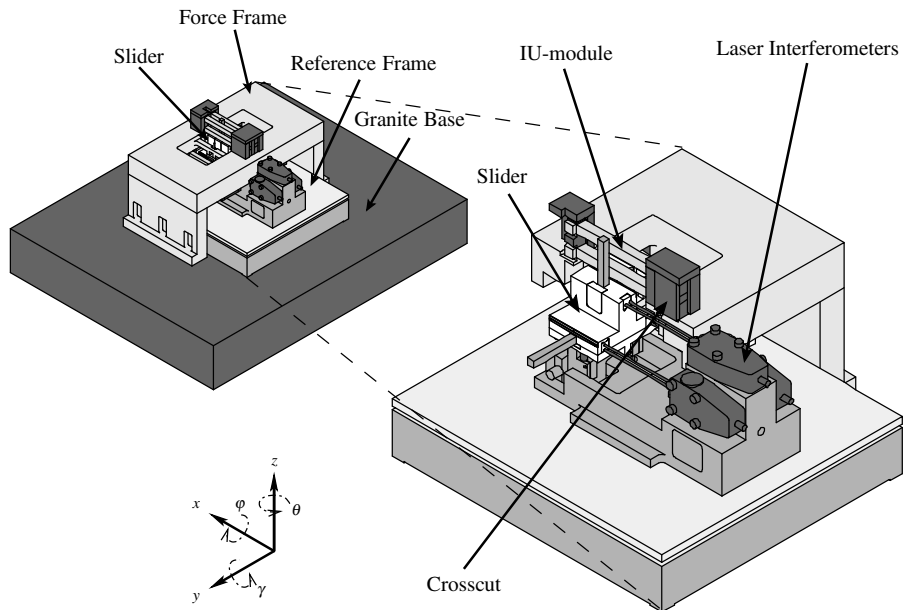


Figure 4.17: Overview of the Slider with force and reference frame. The drawing on the right side shows a cross-section of Slider system, with the force frame cut in half.

Slider construction

Figure 4.18 shows an exploded view of the Slider. The moving body has its central part made out of aluminium. The Slider bars, consist of laminated iron, and are clamped to this body at a 90° orientation. The top part of the aluminium body is the target surface for the eddy current sensors, while the bottom part acts as the target for the capacitive sensors. Placing the eddy current sensors and capacitive sensors too close to each other might lead to undesired crosstalk. The sensors of the Slider are placed on the fixed world. Therefore, the target surface for the eddy current and the capacitive sensors should be long enough to facilitate the movement of the Slider, resulting in a length of 80 mm. The side Slider bars are placed close to the CoG of the Slider in the z -direction, allowing actuation near to the CoG.

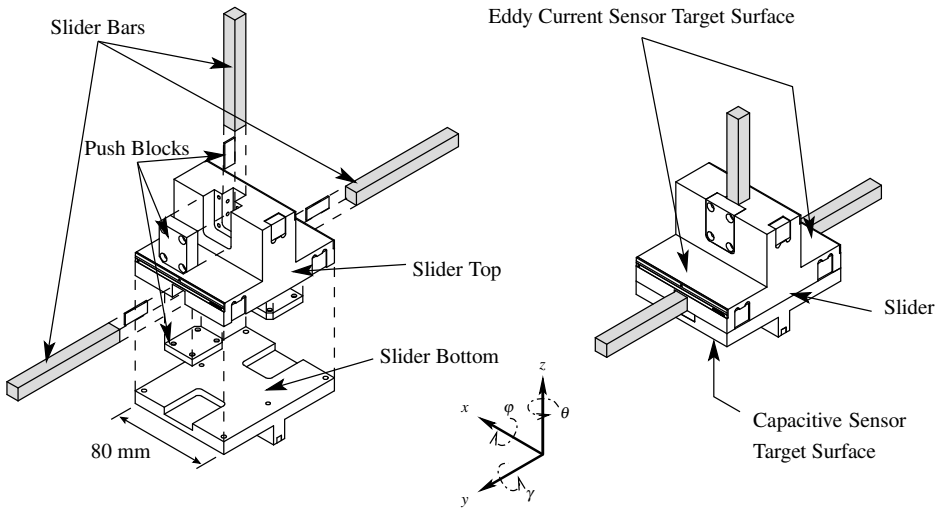


Figure 4.18: Exploded view of the Slider.

Because the 90-degree setup is chosen, a decoupling control strategy has to be implemented to achieve optimal performance. The decoupling strategy relies on the fact that the Slider behaves as a rigid body. Therefore, all internal resonance frequencies should be significantly higher than the estimated bandwidth of 300 Hz. A mode shape analysis, using the finite element software Ansys, is conducted on the Slider body. In the analysis, the Slider body is approximated as one flexible block. Figure 4.19 shows the first 6 flexible modes. The lowest mode is at 1400 Hz, which is significantly higher than the estimated bandwidth. The mode shapes are essentially the basic bending Slider bars.

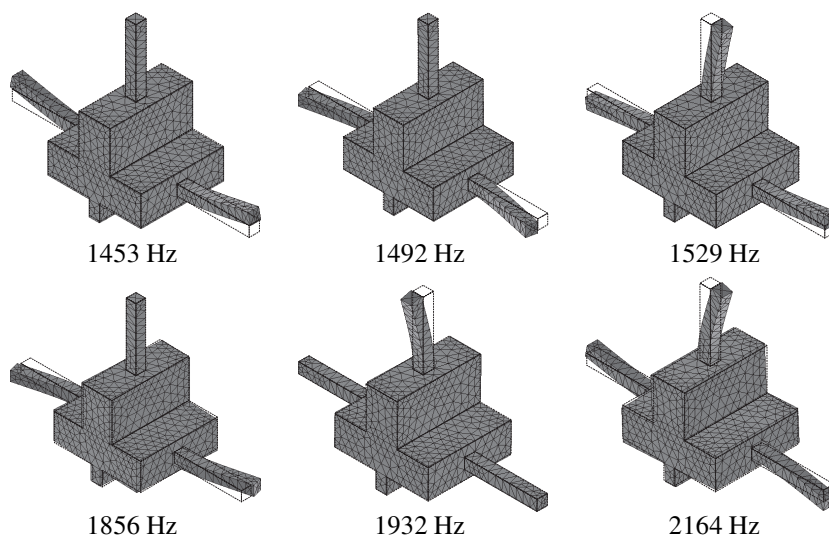


Figure 4.19: First 6 flexible modes, computed with Ansys.

Force frame

The force frame, containing the U-shaped stator bars, is placed above the Slider body, as shown in Fig. 4.20. All driving and suspension forces on the Slider react to the force frame. The force frame is built up from a number of aluminium blocks. The main component of the force frame consists of a thick force plate. All components, like the IU-modules and the sensors are directly connected to this plate. In an optical disc mastering system the space underneath the Slider is reserved for the rotating platform. Therefore, the Slider hangs underneath the frame, while the frame is elevated. The force frame is mounted on a passive granite vibration isolation table, which was already present in the Advanced Mechatronics laboratory. This table has a mass of 300 kg and has a suspension frequency of 7 Hz.

The start-up and stiffness compensation of the Slider are performed with respect to the force frame. The mode shapes present in the frame, therefore should allow the start-up and the stiffness compensation. The negative stiffnesses of the IU-modules, influence the open-loop transfer up to about 50 Hz. To overcome the negative stiffness, the start-up control loop should have a bandwidth of at least 100 Hz. The resonances in the frame should be 3 to 4 times higher than the required bandwidth (rule of thumb). A finite element simulation showed that the lowest resonance of significance is located at 900 Hz.

Reference frame

The reference frame holds the high precision sensors, measuring the position of the Slider with respect to itself. In a full optical disc mastering machine, consisting of a Slider and a rotating platform, the reference frame will serve as an intermediate reference, between both these parts, as shown Fig. 4.5. The reference frame consists of two parts, a vibration isolation system and the block for mounting all sensors to, see Fig. 4.21.

The granite table on which the Slider is placed has a resonance frequency of 7 Hz and to make the most effective use of the “low stiffness concept” the suspension frequency of the reference should be less than this 7 Hz. The Table Stable 150 is an active vibration isolation table, with a passive vibration isolation at a suspension frequency of 11 Hz and an active suspension frequency of 0.7 Hz. Additional information on such active vibration isolation systems is found in [7]. The 0.7 Hz is well below half of the lowest rotation frequency, which is 13 Hz. The reference frame is placed on top of this vibration isolation table, as in Fig. 4.21, while the reference frame holds both the capacitive sensors and the laser interferometers.

4.4.4 Electronic design

The electronic design is crucial in the design of a mechatronic system. The electronic disturbances propagate through the control loop and directly influence positioning performance. The components discussed in this section, are the digital controller, the current amplifier, and the signal conditioning.

Digital controller

The digital controller should allow the decoupling strategies for the sensor and actuators Multi Input Multi Output (MIMO) controller. This limits the amount of available controllers significantly. Most commercial controllers are built for Single Input Single Outputs (SISO) loops, where one sensor is directly coupled to one output. Therefore, the dSPACE DS-1005 card is chosen, which is programmable using the high level programming language of Matlab/Simulink. The goal is to reach a sampling frequency of 20 kHz to limit phase lag in frequencies up to the bandwidth.

Current amplifiers

Low noise current amplifiers for the IU-modules were designed by M.H. El-Husseini, see Fig. 4.22. The amplifiers are capable of delivering 3.6 A of continuous current to the coils of the IU-modules. A differential input to the current amplifier, formed by the Analog Devices AD620, minimises sensitivity to external electrical disturbances. The current amplifiers are fed with low noise switched mode power supplies

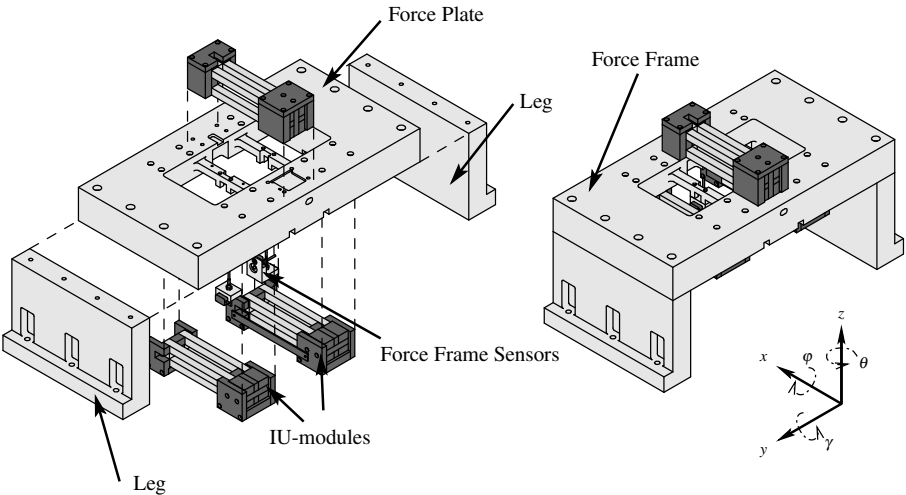


Figure 4.20: Force frame of the Slider, showing the mounting of IU-modules.

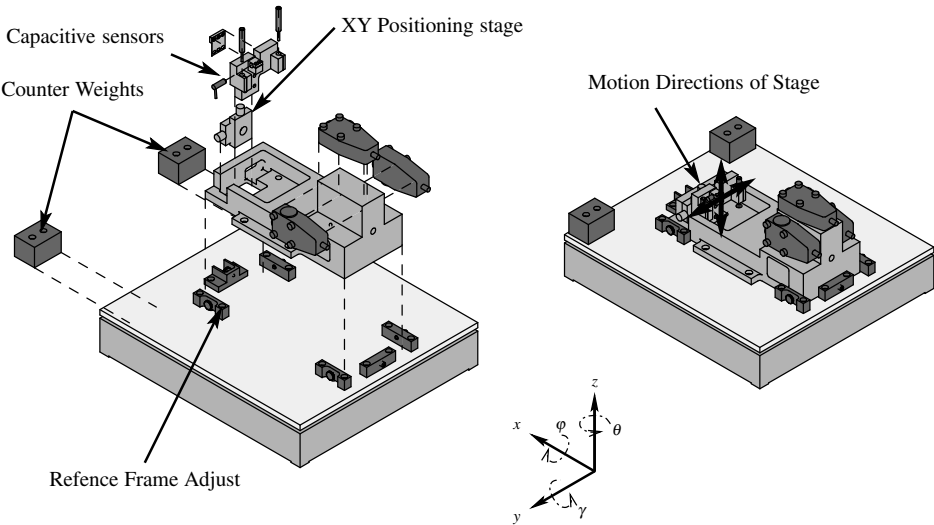


Figure 4.21: Reference frame of the Slider.

(Delta Electronics 240 S 24). The frequency response of the amplifiers is found in Appendix A.3.

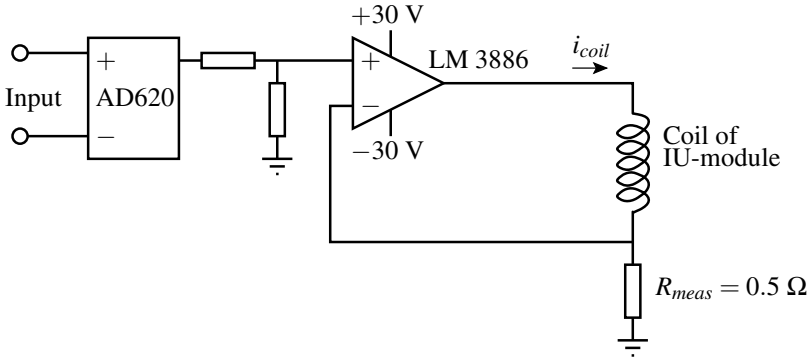


Figure 4.22: Current amplifier for the IU-module, where i_{coil} is the current through the coil, R_{meas} is the measurement resistance, the AD620 forms the differential input and the LM3886 is the high power operational amplifier.

Signal conditioning

On each of the eddy current sensors analog filtering is applied to eliminate aliasing. Each of the channels has a 5 kHz third-order low-pass filter. The capacitive sensors have sufficient filtering at 10 kHz by themselves. The laser interferometers are read out using the Renishaw RPI-20 digital parallel interface, without any additional signal conditioning. The interfacing of the RPI-20 board to the dSPACE controller is discussed in Appendix A.2.

4.5 Mechatronic design evaluation of the Slider

The design, presented in Section 4.4, is the result of several design iterations, using the Dynamic Error Budgeting technique. In this section, the models applied during the DEB design process, are treated. Section 4.5.1 presents the model of the plant. Section 4.5.2 enumerates the different disturbance sources. The models predict the position error of the Slider and indicate where the design is to be improved. In Section 4.5.3, the design process is illustrated and the predicted performance is given.

4.5.1 Model of the plant and controller

The Slider system is modelled as a mass-spring systems with 4 rigid bodies, each having 6-DoF. The 4 modelled rigid bodies are the force frame (\mathbf{M}_F), the Slider (\mathbf{M}_S), the reference (\mathbf{M}_R) and the internal reference frame (\mathbf{M}_I). The internal reference frame is part of the force frame and holds the force frame sensors from Section 4.4.2. The internal reference frame is added, to incorporate the effects of a flexible force frame. A schematic of the model is depicted in Fig. 4.23.

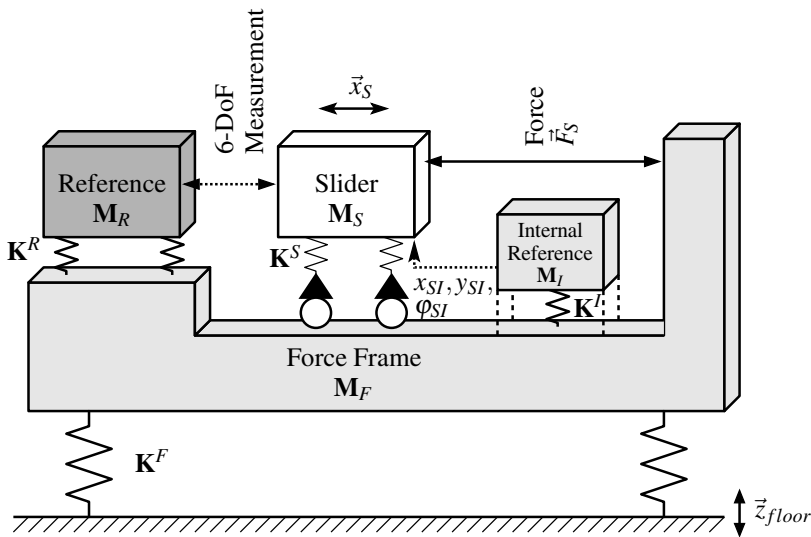


Figure 4.23: Schematic of the model used for DEB. The matrix \mathbf{K} is the stiffness matrix, while the superscript denotes origin of the spring (I - Internal frame reference, F - Force frame, R - Reference, S - Slider). The measurements for the stiffness compensation loop are given by x_{SI} , y_{SI} and ϕ_{SI} .

The mechanical model is built up in a finite element like way [32] and implemented in Matlab. First, nodes define the geometry. Masses, springs, sensors or actuators are then attached to these nodes. The matrices for the model, Eq. 4.17-4.20, are then automatically built up, this allows design changes to be implemented quickly. The model itself is implemented in Matlab, as a linear state space model, with state space matrices \mathbf{A}_{ss} - state matrix, \mathbf{B}_{ss} - input matrix, \mathbf{C}_{ss} - output matrix.

$$\mathbf{M}_g \ddot{\vec{x}}_g + \mathbf{D}_g \cdot \dot{\vec{x}}_g + \mathbf{K}_g \cdot \vec{x}_g = \mathbf{F}_g, \quad (4.17)$$

$$\ddot{\vec{x}}_{ss} = \mathbf{A}_{ss} \vec{x}_{ss} + \mathbf{B}_{ss} \vec{u}, \quad (4.18)$$

$$\vec{y} = \mathbf{C}_{ss} \vec{x}_{ss}, \quad (4.19)$$

$$\mathbf{A}_{ss} = \begin{bmatrix} 0 & \mathbf{I} \\ \mathbf{M}_g^{-1} \mathbf{K}_g & \mathbf{M}_g^{-1} \mathbf{D}_g \end{bmatrix}, \quad \mathbf{B}_{ss} = \mathbf{M}_g^{-1} \mathbf{F}_g. \quad (4.20)$$

The vectors \vec{y} and \vec{u} are the plant output and input vectors, while \vec{x}_{ss} is the state vector. The matrices and vectors in Eq. 4.20 are given by Eq. 4.21-4.25. In Eq. 4.22 and 4.23, the superscript index indicates the origin of the stiffness matrix, \mathbf{K} or damping matrix \mathbf{D} , while the subscript denotes the targeted body (I - Internal frame reference, F - Force frame, R - Reference, S - Slider). The coordinates in the state vector, \vec{x}_{ss} are the CoG coordinates, of each individual component and their derivatives, Eq. 4.24. The subscript g indicates that the equation of motion, Eq. 4.17, is written down in global CoG coordinates.

$$\mathbf{M}_g = \begin{bmatrix} \mathbf{M}_F & 0 & 0 & 0 \\ 0 & \mathbf{M}_S & 0 & 0 \\ 0 & 0 & \mathbf{M}_R & 0 \\ 0 & 0 & 0 & \mathbf{M}_I \end{bmatrix}, \quad (4.21)$$

$$\mathbf{K}_g = \begin{bmatrix} \mathbf{K}_F^F + \mathbf{K}_F^S + \mathbf{K}_F^R + \mathbf{K}_F^I & -\mathbf{K}_{FS}^S & -\mathbf{K}_{FR}^R & -\mathbf{K}_{FI}^I \\ -\mathbf{K}_{SF}^S & \mathbf{K}_S^S & 0 & 0 \\ -\mathbf{K}_{RF}^R & 0 & \mathbf{K}_R^R & 0 \\ -\mathbf{K}_{IF}^I & 0 & 0 & \mathbf{K}_I^I \end{bmatrix}, \quad (4.22)$$

$$\mathbf{D}_g = \begin{bmatrix} \mathbf{D}_F^F + \mathbf{D}_F^S + \mathbf{D}_F^R + \mathbf{D}_F^I & -\mathbf{D}_{FS}^S & -\mathbf{D}_{FR}^R & -\mathbf{D}_{FI}^I \\ -\mathbf{D}_{SF}^S & \mathbf{D}_S^S & 0 & 0 \\ -\mathbf{D}_{RF}^R & 0 & \mathbf{D}_R^R & 0 \\ -\mathbf{D}_{IF}^I & 0 & 0 & \mathbf{D}_I^I \end{bmatrix}, \quad (4.23)$$

$$\vec{x}_{ss} = [\vec{x}_F \quad \vec{x}_S \quad \vec{x}_R \quad \vec{x}_I \quad \dot{\vec{x}}_F \quad \dot{\vec{x}}_S \quad \dot{\vec{x}}_R \quad \dot{\vec{x}}_I]^T, \quad (4.24)$$

$$\mathbf{F}_g = \begin{bmatrix} -\mathbf{F}_S & \mathbf{K}_F^F \cdot \vec{z}_{floor} \\ \mathbf{F}_S & 0 \\ 0 & 0 \\ 0 & 0 \end{bmatrix}. \quad (4.25)$$

Mass		
\mathbf{M}_F	6-DoF Mass	300 kg
\mathbf{M}_S	6-DoF Mass	1 kg
\mathbf{M}_I	6-DoF Mass	0.5 kg
\mathbf{M}_R	6-DoF Mass	20 kg
Stiffness		
\mathbf{K}^F	6-DoF diagonal	7 Hz, $\zeta = 0.1$
\mathbf{K}^S	3-DoF coupled (y, z, φ)	50 Hz, Negative, $\zeta = 0$
\mathbf{K}^I	6-DoF diagonal	600 Hz, $\zeta = 0.001$
\mathbf{K}^R	6-DoF diagonal	2 Hz, $\zeta = 0.1$
Sensors		
Frame to Slider	3-DoF ($x_{SI}, \gamma_{SI}, \theta_{SI}$)	Linear encoders
	3-DoF ($y_{SI}, z_{SI}, \varphi_{SI}$)	Eddy current sensors
Reference to Slider	3-DoF ($x_{SR}, \gamma_{SR}, \theta_{SR}$)	Laser interferometers
	3 DoF ($y_{SR}, z_{SR}, \varphi_{SR}$)	Capacitive sensors
Forces		
\mathbf{F}_S	3-DoF (F_x, T_y, T_z)	Propulsion forces
	3-DoF (F_y, F_z, T_z)	Suspension forces

Table 4.7: Physical parameters of modelled Slider, where ζ is the relative damping co-efficient.

Table 4.7 gives the modelled parameters of the components. The assumption is made that the CoGs of the force frame and the reference frame coincide. The stiffness matrices, \mathbf{K}_F^F and \mathbf{K}_R^R , and their respective damping matrices are diagonal. The CoG of the Slider and reference frame are situated 130 mm above the CoG of the force frame.

The IU-module and the amplifiers are modelled as static gains, while the sensors are represented as low-pass filters. The model of this mechatronic system is combined with the model of the controller, see Fig. 4.24. The vectors, \vec{y}_{SR} and \vec{y}_{SI} , represent the measured position with respect to the reference frame and internal reference. The control structure of the Slider consists of two components: the stiffness compensation with respect to the force frame and the high accuracy position loop with respect to the reference frame. The high stiffness control loop consist of 6 diagonal PI²D controllers. The controllers act on the CoG coordinates of the Slider and the decoupling matrices, $\mathbf{T}_{Y,SI}$ and $\mathbf{T}_{Y,SR}$, are formed by the inverses of the output matrices, $\mathbf{C}_{Y,SI}$ and $\mathbf{C}_{Y,SR}$. The suspension controllers have an open-loop 0 dB crossings at 230 Hz and for the propulsion controllers these are at 300 Hz. The initial estimates for the open-loop 0 dB crossing are made using the experience gained with the Baby-IU setup, which is described in Appendix B.2.

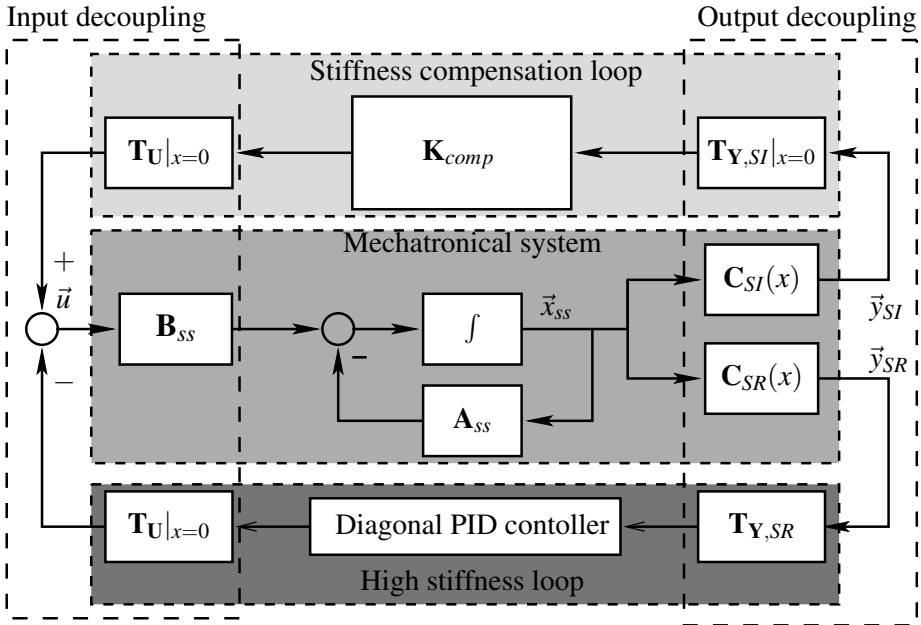


Figure 4.24: Control structure and model used for Dynamic Error Budget.

The stiffness compensation control loop, dealing with the negative stiffness of the suspension, is implemented in global coordinates using the global stiffness information. The stiffness compensation matrix, K_{comp} , is easily obtained from the model and in the ideal case is equal to stiffness matrix of the Slider, K_S . In the actual Slider this matrix is unknown; the solution to this is covered in Section 5.2.2. The stiffness is assumed to be compensated for 90% ($K_{comp} = 0.9 \cdot K_S$).

4.5.2 Models of the disturbances acting on the Slider

Figure 4.25 shows a block diagram of the Slider with noise sources and their application points. The noise sources will be described as power spectral densities, using data provided by the supplier or by measured data. The power of each of the disturbance signals is assumed to be distributed between 1 Hz and half the sampling frequency. Inside the digital model, any energy content at frequencies higher than half the sampling frequency will be wrapped back into that frequency range due to aliasing.

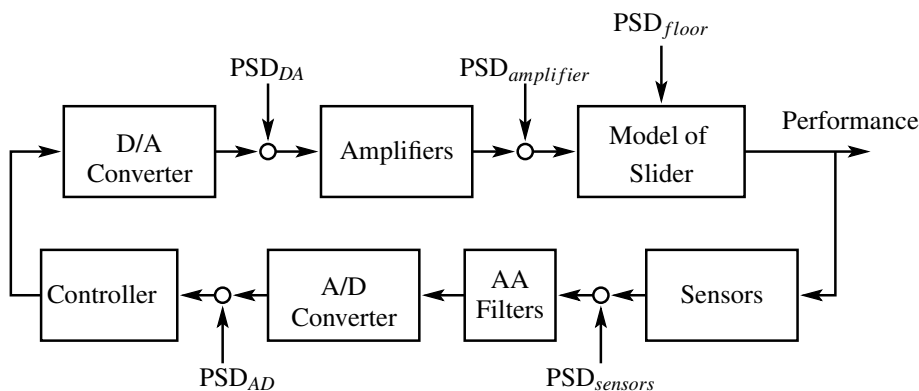


Figure 4.25: Disturbance sources acting on the Slider with their application points in the physical loop.

Ground Vibrations

Ground vibrations are a significant source of disturbance on nm-precision machines [62]. For the design of the Slider the ASML floor specifications are taken as a reference, see Fig. 4.26(a). With these specifications ASML determines whether a floor is suitable for their wafer stepper, the PAS5500 [69].

The Slider setup will be placed in the Advanced Mechatronics laboratory at the TU Delft. This laboratory is situated on the first floor in a hanging construction. This makes the floor extremely sensitive to people walking around. A measurement of the floor vibrations is performed at the Advanced Mechatronics laboratory, during a quiet period, see Fig. 4.26(a). The floor vibrations are below the ASML floor specifications. However, this is only the case during a quiet time. Although in reality the floor vibrations are correlated, the floor vibrations in the different directions are assumed to be uncorrelated. The floor vibrations in the x and y -directions, are presumed to be of the same magnitude.

Amplifier noise

The noise of the developed power amplifier, presented in section 4.4.4, is measured. The output and input of the amplifier were short circuited, while the current noise was measured, using a current probe. Figure 4.26 shows the resulting PSD of the measurement. The current amplifier shows significant spikes at 50 and 150 Hz. In course of the research, it turned out that these spikes could be reduced by improving the grounding of the amplifier design.

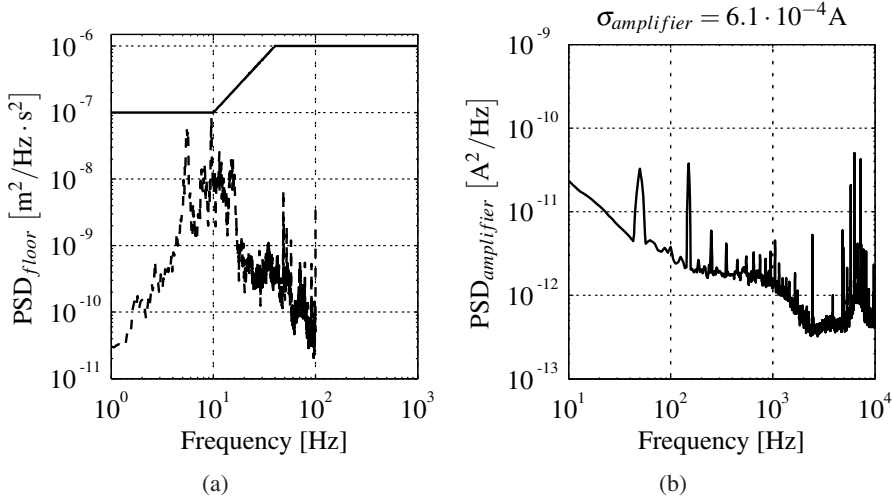


Figure 4.26: Power Spectral Densities, representing the ground vibrations, ASML floor Spec (—), Floor of AM Laboratory during quiet Period (---) (a). PSD of the applied current amplifier (b).

DA conversion noise

The noise from a Digital to Analog (DA) converter is governed by the quantisation noise which can be modelled as uniform distributed white noise, Eq. 4.26 [69]. In Eq. 4.26, f_N is the Nyquist frequency (half the sampling frequency). The quantisation interval, Q_a , is determined by the converter range and its bits, s , Eq. 4.27.

$$\text{PSD}_{DA} = \frac{Q_a^2}{12 \cdot f_N}, \quad (4.26)$$

$$Q_a = \frac{\text{range}}{2^s}. \quad (4.27)$$

AD conversion noise

The noise in an AD converter consists of two parts, the electronic noise and the quantisation noise. The PSD of the quantisation noise is established using Eq. 4.26. The electrical noise, originating in the electrical components of the AD converter, is often larger than the quantisation noise. The dSPACE AD-board has a signal to noise ratio of at least 80 dB. The signal to noise ratio, SNR, is the ratio between the power of the signal and the power of the noise. The assumption is made that the maximum signal is a sine with peak value 10 V (A_{signal}) and that the PSD_{AD}

can be modelled as white noise. Equation 4.28 gives the noise spectrum for the AD-converter.

$$\text{PSD}_{AD} = \left(\frac{1}{2} \sqrt{2} \frac{A_{\text{signal}}}{\text{SNR}} \right)^2. \quad (4.28)$$

Sensor noise

Capacitive sensors The specifications for the resolution for these sensors are 0.11 nm till 10 Hz, 0.15 nm till 100 Hz, 0.3 nm till 1 kHz and 1.6 nm till 10 kHz. Assuming, that the noise is spread out equally within these frequency intervals, the PSD can be computed. The PSD_{cap} is depicted in Fig. 4.27(a).

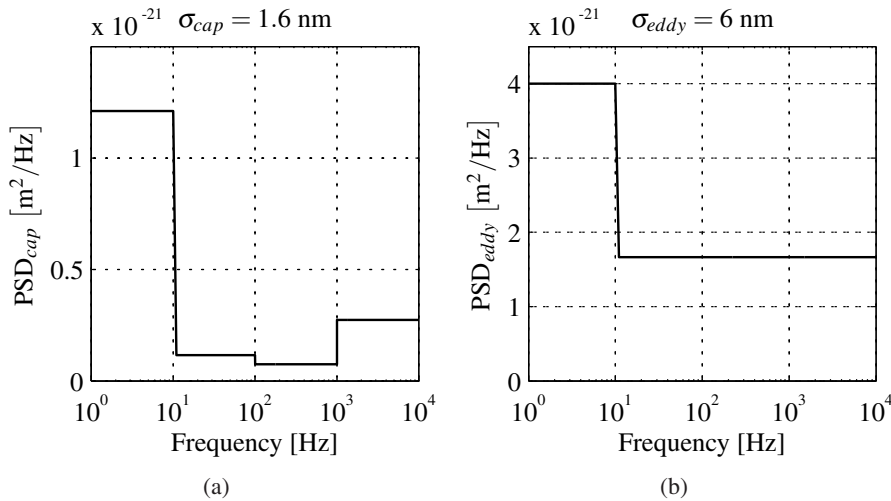


Figure 4.27: Power Spectral Densities for the capacitive sensor (a), and the eddy current sensor (b).

Eddy current sensors The eddy current sensor has noise specifications for two filtered signal settings. Assuming that the noise is uniformly distributed within these intervals, the resulting PSD_{eddy} is depicted in Fig. 4.27(b).

Linear encoder The linear encoder has a digital quadrature output. The pitch of encoder grating, p_{linear} , is 20 μm . The exact electrical noise of the interpolator and the sensor is not known. The interpolator is capable of interpolating the signal 4000 times, while in the Slider the sensor is only interpolated 400 times, n_i (due to limited input speed of the encoder counter boards). There-

fore, it is safe to assume the main source of error is the quantisation noise, Eq. 4.29, with $p_{linear} = 20 \cdot 10^{-6}$ m.

$$\text{PSD}_{linear} = \frac{p_{linear}^2}{12 \cdot n_i^2 \cdot f_N}. \quad (4.29)$$

Laser interferometers The laser interferometers and theirs electronics are vital components for achieving the most critical performance in the x -direction, and therefore their noise level is measured in the laboratory. The measurement is performed on a vibration isolation table, the Table Stable TS 150. The laser and the reflection mirror are placed directly next to each-other, hereby minimising the influence of environmental disturbances, like pressure and temperature variations. Figure 4.28 shows the results, PSD_{las} .

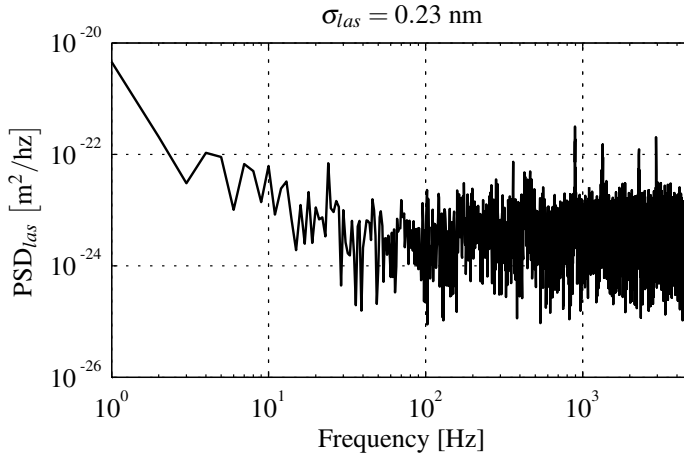


Figure 4.28: Measured Power Spectral Density of laser interferometer noise, PSD_{las} .

4.5.3 Results and design process illustration

The position error of the Slider is the displacement between the Slider and reference. Using the models from Sections 4.5.1 and 4.5.2, the position error at the output is computed. Figure 4.29 shows the CAS of the position error in propulsion direction, $x_S - x_R$, and suspension direction, $z_S - z_R$. The specifications of 1 nm (σ) and 5 nm (σ) are achieved in both directions. The error in suspension z -direction is mainly dominated by AD conversion noise. The capacitive sensors contribute to the error, $z_S - z_R$, for only a small amount indicating that worse resolution sensors could have been applied. The capacitive sensors are left in the design, because no

cheaper sensor could be found which could attain the performance. In propulsion x -direction, the error is dominated by the noise of the amplifier and the noise of the laser interferometer sensors.

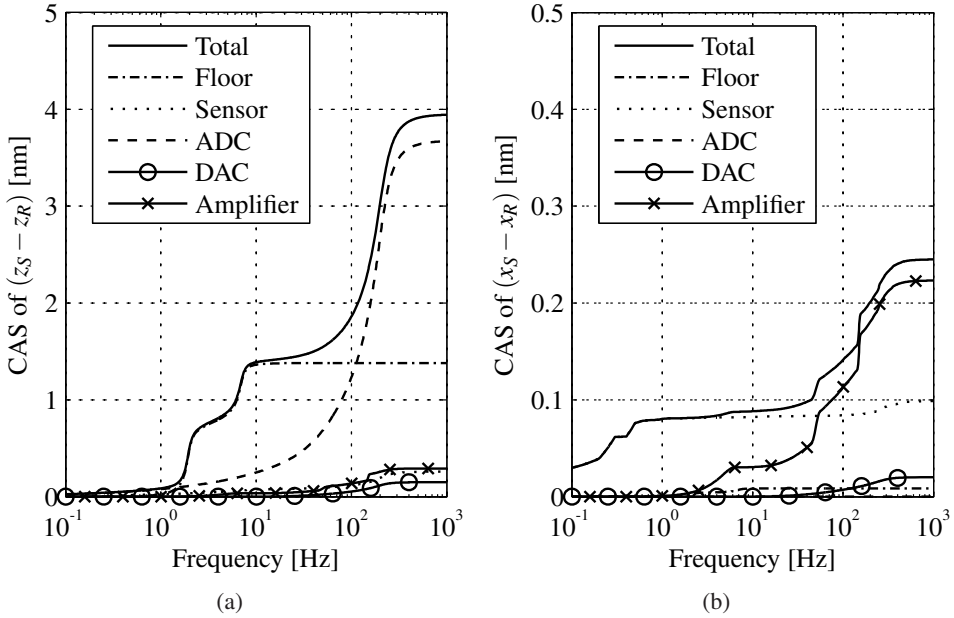


Figure 4.29: Cumulative Amplitude Spectrum of $z_S - s_R$ (a) and $x_S - x_R$ (b). The CAS of the individual contributions consist of the contributions of all components with this specific label. For example, the sensor contribution contains the error contributions of the eddy current sensors, the capacitive sensors, and the laser interferometers.

Figure 4.30 shows the error in the suspension y -direction. The resulting error, $y_S - y_R$, is over 5 nm (σ). The main cause of this error is the AD conversion noise, as shown Fig. 4.30. Three options were considered for decreasing the influence of this disturbance:

- Electronically amplifying the sensor signal
- Oversampling the sensor signal
- Applying an alternative AD-converter

Fortunately, an improved AD board, the DS-20004, became available for the dSPACE controller. This board has a signal to noise ratio of 85 dB, where the original board had a 80 dB SNR. This new board helped to improve performance in

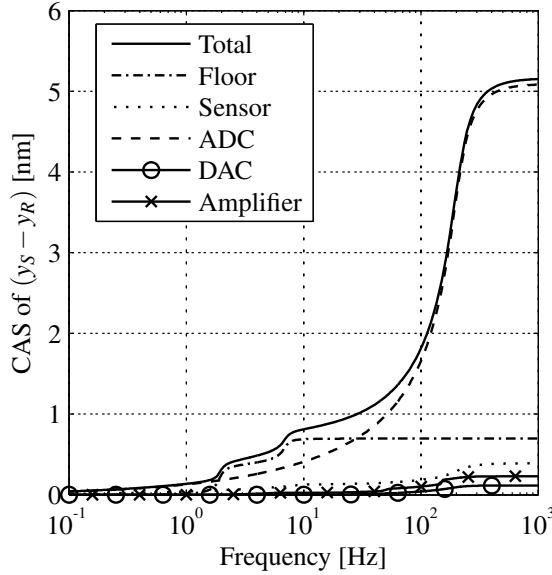


Figure 4.30: Cumulative Amplitude Spectrum error $y_S - y_R$ with the dSPACE 80 dB SNR AD-converters.

both the y and z -directions. The resulting error, $y_S - y_R$, becomes 2.6 nm (σ), see Fig. 4.31. The specification for the y -direction is now also met.

With this example, the DEB method indicated that the Slider initially did not meet its performance specifications. The DEB method identified the source of the error, allowing improvements to be made. This is an illustration of many design steps which were made to achieve the final performance.

4.5.4 Optimal test for suspension directions

The performance in the suspension directions is within a factor of 2 of its specifications. To determine if the performance of the closed-loop system can be improved by modifying the controller, a so called \mathcal{H}_2 optimisation is applied for the suspension y and z -directions in [60]. The same strategy is employed by Jabben [33]. In this method the norm $\|e\|_{rms}^2 + \alpha \|u\|_{rms}^2$ is minimised, where e is the position error, and u the controller output. The factor α scales the influence of the control effort in the optimisation function. The factor α is adjusted until the control effort, $\|u\|_{rms}^2$, of the optimal controller is equal to the control effort PI²D controller. This allows both controllers to be directly compared and makes sure that the resulting optimal controller does not create excessive gains.

The results for the Slider in suspension y and z -directions are shown in Fig. 4.32. The optimal controller reduces the error in both y and z -directions to below 2 nm

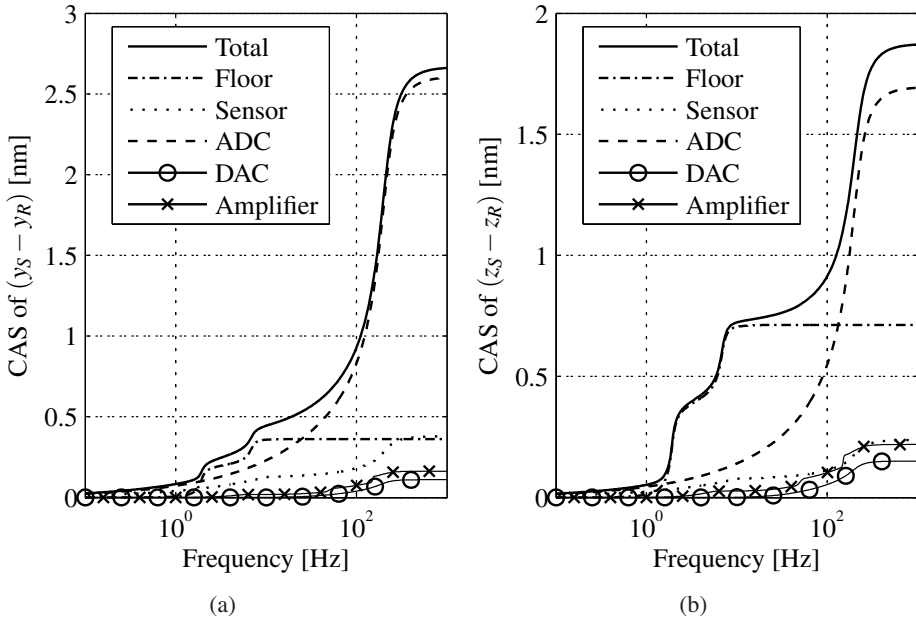


Figure 4.31: CAS of y -direction position error, $y_S - y_R$, with a 85 dB signal to noise ratio AD-converter (a). CAS of z -direction position error, $z_S - z_R$, with a 85 dB signal to noise ratio AD-converter (b).

(σ). The controller generated by the \mathcal{H}_2 optimisation algorithm is of equal order to the plant, combined with the order of the weighting functions of the disturbances. This results in high order controllers, often deemed impractical for implementation. A comparison between the two controllers in z -direction is shown in Fig. 4.33. It is clear the \mathcal{H}_2 controller places more control effort on the resonances present in the low frequency region caused by the granite table and the suspension of the reference frame. The low frequency gain of the \mathcal{H}_2 controller can be mimicked in a loop shaping method by placing inverse notches at the low frequency resonances.

4.5.5 Conclusions and remarks

A design is presented for an optical disc mastering Slider, using the IU-modules as actuators. The Slider requires a position error in the propulsion x -direction of 1 nm (σ). The suspension directions of the Slider are more tolerant to errors, and have specifications of 5 nm (σ). Using the Dynamics Error Budgeting technique, it is estimated that the Slider is capable of fulfilling these dynamic specifications.

The Slider is based on the “low stiffness” design concept, where the high accuracy components are isolated from the environment using low stiffness connections.

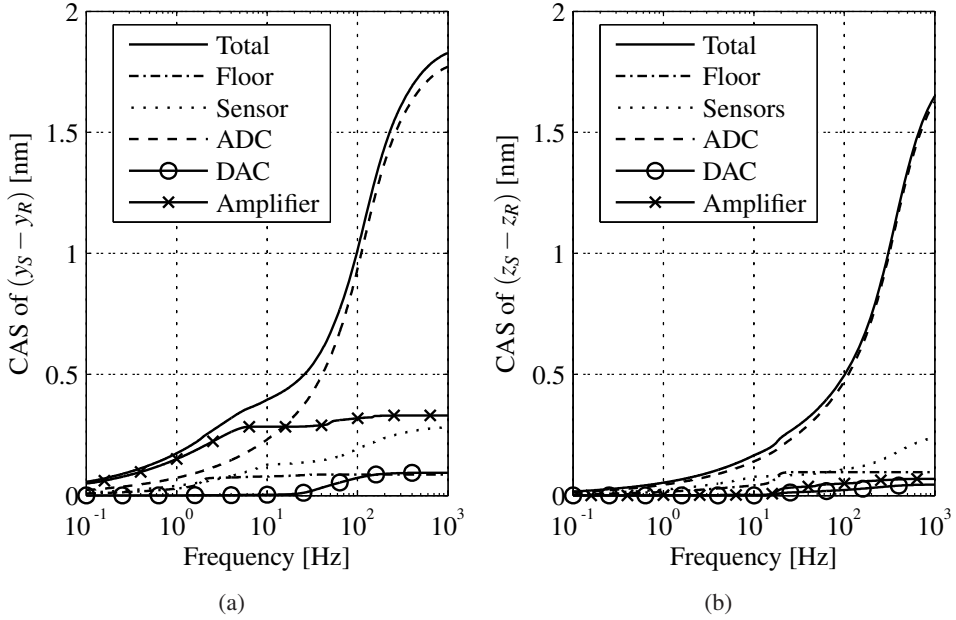


Figure 4.32: CAS of the error in y (a) and z (b) with \mathcal{H}_2 optimal controller.

The actuation forces generated within the system are placed on a separate force frame. The positioning performance is achieved through a control loop between the Slider and the isolated reference frame.

In the suspension directions, a stiffness compensation is required to reduce the transfer of disturbances through the negative stiffness of the IU-modules. Although this compensation performs well, it has its limitations. Therefore in Appendix A.1, a discussion is held on the limits of the negative stiffness compensation. The Slider has been realised, and the most important construction drawing are shown in Appendix E. The control and performance of the realised Slider are discussed in the next chapter.

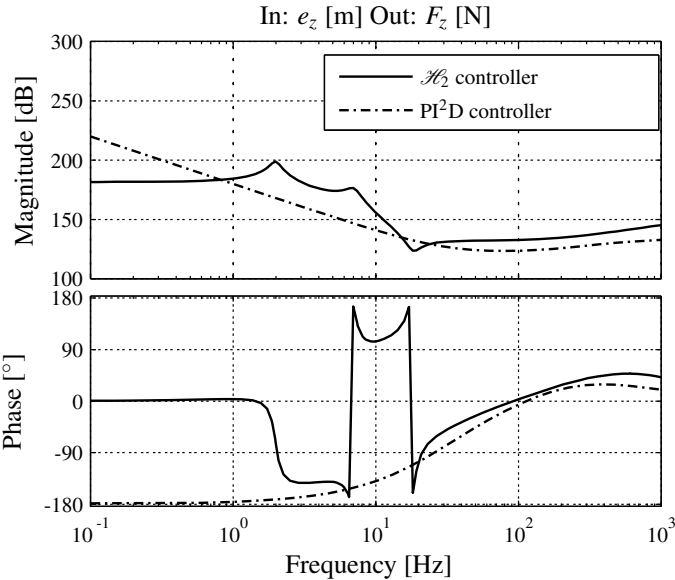


Figure 4.33: Bode diagrams of \mathcal{H}_2 and PI²D controller for suspension z -direction.

Chapter 5

Control and performance of 6-DoF electromagnetically suspended Slider

Pictures of the magnetically levitated Slider are shown in Fig. 5.1. A servo-error of 0.12 nm (σ), in the propulsion direction between Slider and reference frame, is realised. This chapter explains how this result is achieved with the IU-module acting as a 2-DoF actuator. The result was published in [40, 41].

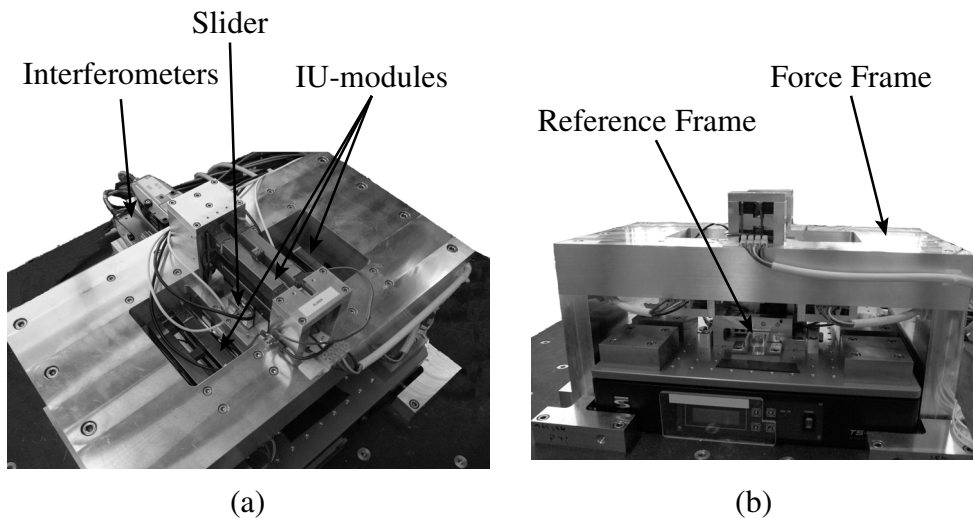


Figure 5.1: Realised Slider setup, top view (a), front view (b).

Before the performance of any positioning system can be demonstrated, it has to

be built and activated. Section 5.1 discusses the mechanical realisation and the first-time start-up of the Slider. To achieve the required positioning performance, a high performance position controller has to be designed. The design of this controller is presented in Section 5.2. The final performance of the Slider is dependent on the initial design, presented in Chapter 4, as well as the final implementation of this design. The achieved performance of the Slider and the boundary conditions are discussed in Section 5.3. The IU-modules, presented in Chapter 3, are an integral part of the design. In Section 5.4, the influence of the IU-modules on the Sliders performance, is studied.

5.1 Practical aspects to realisation and start-up

This section discusses the practical aspects encountered during the realisation and start-up of the Slider. The mechanical aspects to building up a nm-resolution linear Slider are discussed in Section 5.1.1. The difficulty in achieving stable levitation of the Slider, comes from the fact that all DoF of a rigid body must be simultaneously controlled, without the ability to measure open-loop frequency responses beforehand. The steps taken to reach initial stable levitation are discussed in Section 5.1.2.

5.1.1 Realisation of the Slider

The Slider is designed by the author and manufactured at the central workshop at Delft University of Technology. The body of the Slider, the force frame and the reference frame, shown in Fig. 4.17, are the most accurate parts. The construction drawings of these parts are found in Appendix E. The manufacturing and assembly of the mechanical components of the Slider proceeded without serious complications.

The most tedious task in the construction of the linear Slider is the manufacturing of the laminated stator and Slider bars for the IU-modules. The laminations of the bars are spark eroded to achieve the desired shape. The laminations had to be cleaned, individually glued, and placed in a glue mold, to create the Slider and stator bars. It took 2 PhD students one full week to manufacture the stator and Slider bars for the Slider. To make the IU-modules more economically attractive, an alternative means of manufacturing of the laminated sheets should be applied, or different materials not requiring lamination should be used. The research of [44], investigates the possibility of applying alternative materials for the IU-module.

The laser interferometers require an accurate alignment between the mirrors on the Slider and the laser heads on the reference frame. Although manual alignment facilities exist, the angular alignment of the laser interferometers with the mirrors on the rear side of the Slider body, was one of the most critical tasks. The manual

alignment process of all laser interferometers took a full day, without achieving optimal signal levels on all laser interferometers simultaneously. This is caused by the angular tolerances on each of the individual mirrors and their mounting. It is advised to apply mirrors manufactured out of a single piece or pre-aligned mirrors, to create a more accurate reference in a future design.

5.1.2 First time levitation of the Slider

The closing of the control loop in an active positioning system is often preceded by measuring an open-loop reponse frequency function (FRF). From this FRF initial controller settings can be deduced. Due to the negative stiffness, present in the suspension direction of the IU-modules, it is not possible to measure an open-loop FRF, representing the behaviour of the levitated Slider. Because all 6-DoF of the Slider have to be stabilised simultaneously and the amount of variables in the controller is extensive, a structured approach to reach stable suspension is required. This section explains how initial suspension of the Slider is reached.

The mechanical design of the Slider allows collocated SISO control with respect to the force frame. The Slider was initially levitated using these local control loops. The stability of these local control loops was first checked using a rigid body model of the Slider. The rigid body model uses the information gathered from the test setups of the IU-modules. More information on these test setups is found in Section 3.3.2 and Appendix B.2. The model showed the Slider is capable of stable suspension, using these local control loops.

To verify, whether the Slider satisfies the rigid body description, a modal analysis is performed on the assembled Slider. This is done using an impact hammer and accelerometers. The Slider is placed on a piece of soft foam, mimicking free suspension. The accelerometers are placed near the measurement locations on the Slider body, while the impact hammer applies the force near the actuation locations. The first flexible mode of the Slider is at approximately 1090 Hz and is the bending mode of the clamped Slider bars. Since, the first flexible mode is at a much higher frequency than the bandwidth of the start-up control loop (aimed at 120 Hz), the rigid body assumption is justified. The modal measurement results are found in the appendix of [60].

The electrical connections of the Slider are thoroughly checked, making sure the directionality of the sensors and actuators, is the same as was modelled. The directionality of each of the position sensors is checked by manually displacing the Slider body and determining the direction. On the actuator side, the individual FRFs of each current amplifier and its load are measured using a current probe. To determine direction of the generated forces, a current is sent through each actuator, while the position sensors monitored the direction of the displacement.

To simplify the start-up of the system, paper sheets are placed underneath the Slider bringing the Slider closer to the centre position in the air gap. The modelled

SISO loops were then closed between the IU-modules and local actuators. The controllers were implemented as a lead-lag filters with a proportional gain. The lead and lag frequencies were kept fixed and were determined using the model and the experience gained with the Baby-IU setup. The proportional gain was adjusted until satisfactory levitation was achieved. Upon the initially suspended Slider closed-loop FRFs can be measured. From the measured FRFs the open-loop plant FRFs are reconstructed as described in Appendix B.2. The open-loop FRF is used as a basis for the design of more advanced control, discussed in Section 5.2.

5.2 Control design for the Slider

The position control loops stabilise the Slider, and bring about the desired positioning performance between the reference frame and the Slider. In Section 5.2.1, the steps during a normal start-up procedure are presented. The Slider is a multivariable control system. The Slider has 6 inputs, consisting of the 3 suspension currents and the 3 propulsion currents. It has 12 outputs, 6 position measurements with respect to the force frame, and 6 position measurements with respect to the reference frame. These in- and outputs are coupled, meaning that one input influences multiple outputs. To deal with this coupling, a decoupling strategy is applied. Upon the decoupled coordinates, position controllers can be independently designed. The applied decoupling strategy is discussed in Section 5.2.2.

The negative stiffness of the IU-modules transfers disturbances from the environment to the Slider, as described in Section 4.3. Next to this, the negative stiffness reduces the effectiveness of the decoupling method of Section 5.2.2. The procedure, applied to compensate the negative stiffness in the multivariable plant, is discussed in Section 5.2.3. In Section 5.2.4, the effectiveness of the applied decoupling method is evaluated by comparing it to alternative decoupling methods found in literature. The design of the position controllers is discussed in Section 5.2.5.

5.2.1 Start-up controller and high performance control

Two control loops are used to control the Slider. The start-up control loop and the high performance control loop. The start-up control loop suspends the Slider with respect to the force frame and brings it in range of the high precision sensors. The high performance control loop then couples the Slider to the reference frame to achieve nm-performance. The sensors with respect to the force frame remain active for compensation of the stiffness present in the IU-modules.

Both the start-up and high performance control loop rely on a decoupling method for their controller design. The start-up control loop has a similar architecture as the high performance control loop with lesser performance requirements. Therefore, only the decoupling in the high performance control loop is discussed. The applied decoupling methods are discussed in Section 5.2.2.

To facilitate a smooth transition between the control loops, the position before the switch is measured using the laser interferometers and the capacitive sensors. This position is then set as the reference position for the high performance control loop. Secondly, the actuation currents of a sample before the switch are added to the high bandwidth control loop as an offset or starting value.

5.2.2 Decoupling of the Slider

The Slider is a coupled Multi Input Multi Output (MIMO) plant. Two main strategies exist for dealing with the interactions of a multivariable plant. The first method is decoupling the plant, using a decoupling method, and then applying SISO design methods to the decoupled system. The second method is applying model based optimal control synthesis [66], like \mathcal{H}_∞ or LQG control. The choice is made to apply the decoupling control strategy to control the Slider, because:

- *Straightforwardness of the individual SISO design*

The SISO control design techniques are straightforward and well known. If the DoFs are decoupled, these techniques can be directly applied. This reduces complexity and allows straightforward improvement of the controller, if performance is not achieved in a certain direction.

- *Simple implementation on a digital computer*

The automated design procedures, like \mathcal{H}_2 and \mathcal{H}_∞ methods, generate high order controllers. These high order controllers increase the required computation time in a digital computer. A shorter computation time due to a simpler digital controller, allows enhancements like averaging and tracing of signals.

- *Less accurate model of the Slider is required*

The automated control design procedures require an accurate model of the plant. The identification procedure of a complex system as the Slider is quite extensive and time consuming.

The general layout of a MIMO plant with decoupling is shown in Fig. 5.2. The coupled in- and outputs of the plant, \vec{u}_G and \vec{y}_G , are decoupled using the matrices, $\mathbf{T}_U(s)$ and $\mathbf{T}_Y(s)$, into decoupled coordinates, \vec{u}_d and \vec{y}_d . Upon the decoupled coordinates, \vec{u}_d and \vec{y}_d , multiple SISO controllers, $\mathbf{C}_{c,diag}(s)$, can be independently designed to achieve the desired performance.

As a decoupled set of coordinates for the Slider, the CoG coordinates of the Slider body are chosen. The CoG coordinates of a non-rotating free rigid body, as the Slider, are physically decoupled. The CoG coordinates directly reflect the specifications of Section 4.2. This decoupling method is referred to as CoG-decoupling.

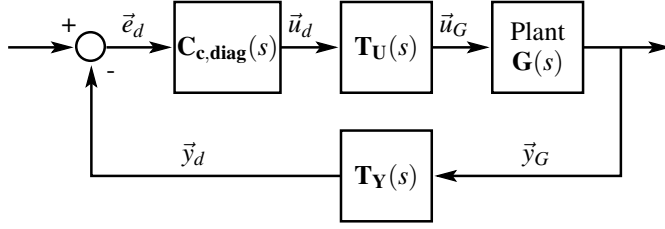


Figure 5.2: Generic decoupling scheme for a MIMO Plant.

The layout of the IU-module actuators creates a natural decoupling between the propulsion and suspension directions. Therefore, the decoupling of the propulsion (x_S, γ_S, θ_S) and suspension (y_S, z_S, φ_S) directions are treated separately in the next subsections. Afterwards, a remaining geometric coupling between the two directions, due to a propulsion x -position dependency, is treated.

Propulsion decoupling

The propulsion positions for the high bandwidth control loop are measured using the Renishaw laser interferometers, positioned on the reference frame.

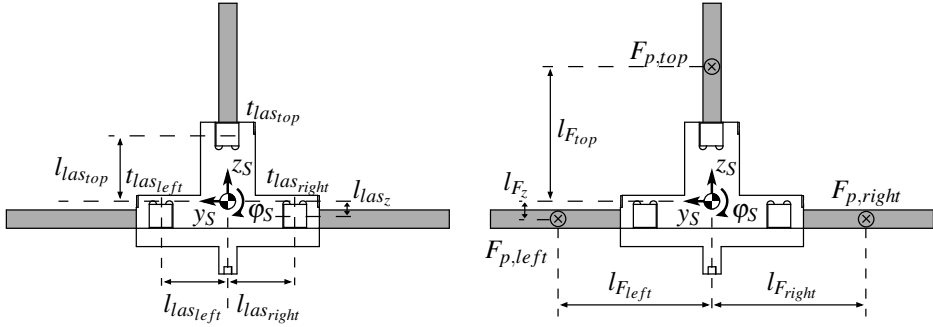


Figure 5.3: Front view of the Slider showing laser interferometer transducer outputs ($t_{las,left}, t_{las,right}, t_{las,top}$), and propulsion actuation forces ($F_{p,top}, F_{p,left}, F_{p,right}$). (Positive direction for x , measurement and force, pointing into the paper.)

Figure 5.3 shows the locations of the reflection mirrors and application points of the actuator forces on the Slider body with respect to its CoG. The measurements of the propulsion directions with respect to the CoG are x -position invariant. Equation 5.1 relates the global CoG coordinates to the local coordinates of the Slider. In Eq. 5.1 the assumption, $\sin(\theta) \approx \theta, \cos(\theta) \approx 1$, is made. In Eq. 5.2 the local ac-

tuator forces, $F_{p,top}$, $F_{p,left}$, and $F_{p,right}$, are transferred to forces and torques acting on the CoG, F_x , T_y , T_z . Since the exact location of the CoG is not known, the CoG location was computed using a CAD program.

$$\begin{bmatrix} t_{las_{top}} \\ t_{las_{left}} \\ t_{las_{right}} \end{bmatrix} = \mathbf{T}_{sens,p} \cdot \begin{bmatrix} x_S \\ \gamma_S \\ \theta_S \end{bmatrix} = \begin{bmatrix} 1 & l_{las_{top}} & 0 \\ 1 & -l_{las_z} & -l_{las_{left}} \\ 1 & -l_{las_z} & l_{las_{right}} \end{bmatrix} \begin{bmatrix} x_S \\ \gamma_S \\ \theta_S \end{bmatrix}, \quad (5.1)$$

$$\begin{bmatrix} F_x \\ T_y \\ T_z \end{bmatrix} = \mathbf{T}_{act,p} \cdot \begin{bmatrix} F_{p,top} \\ F_{p,left} \\ F_{p,right} \end{bmatrix} = \begin{bmatrix} 1 & 1 & 1 \\ l_{F_{top}} & -l_{F_z} & -l_{F_z} \\ 0 & -l_{F_{left}} & l_{F_{right}} \end{bmatrix} \begin{bmatrix} F_{p,top} \\ F_{p,left} \\ F_{p,right} \end{bmatrix}. \quad (5.2)$$

The decoupling matrices in the propulsion direction are formed by taking the inverse of $\mathbf{T}_{U,p} = \mathbf{T}_{act,p}^{-1}$ and $\mathbf{T}_{Y,p} = \mathbf{T}_{sens,p}^{-1}$. Figure 5.4 shows a Bode diagram of the decoupled plant in the propulsion directions. The performance of this decoupling is evaluated in Section 5.2.4. The following boundary conditions should apply, when this CoG-decoupling method is used:

Small angles The angles of the Slider should remain small, so the approximation $\sin(\theta) \approx \theta$, $\cos(\theta) \approx 1$ remains valid.

Unactuated metrology The position measurement is a relative measurement between the reference frame and the Slider body. The decoupling scheme assumes, that only the Slider is excited by the actuators and that the reference frame remains undisturbed. This is ensured by the mass of the force frame and the low stiffness connection of the reference frame to the force frame.

Small y_S and z_S -displacements The y_S and z_S -displacement should remain much smaller than the arms, l , of the various components.

The lack of a coupled stiffness A coupled stiffness matrix acting on a rigid body, introduces a coupling, which the CoG-decoupling will not be able to compensate.

Rigid body behaviour The Slider body should behave as a rigid body and flexible modes of the Slider should not be present in the cross-over region of the open-loop.

Suspension decoupling

Figure 5.5 depicts the suspension forces, $F_{s,bot}$, $F_{s,left}$, and $F_{s,right}$, and the measurement locations of the capacitive sensors, t_{cap} . The negative stiffness of the IU-modules is represented by k_{zz} . The geometric sensor and actuator matrices in the suspension directions on the $x_S = 0$ -position, are:

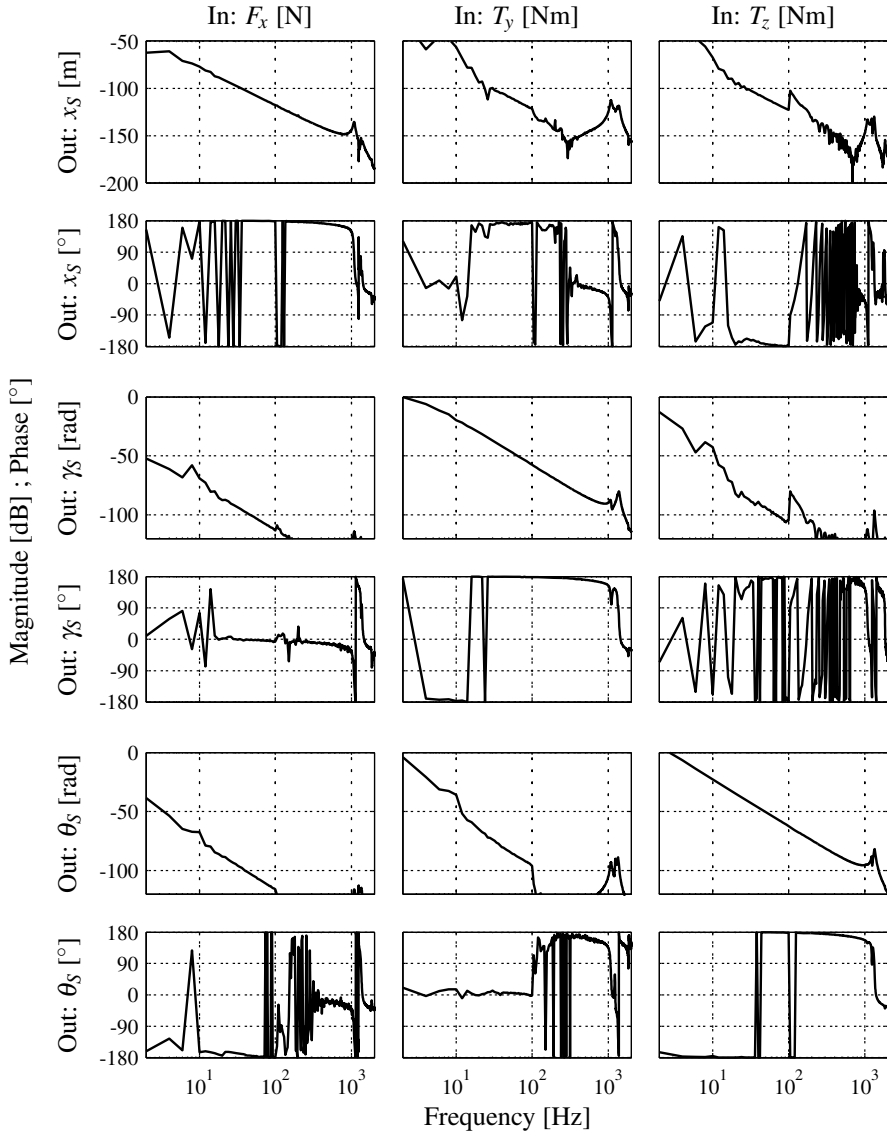


Figure 5.4: Bode diagram of the decoupled plant $G_{d,p}(s)$ in the propulsion directions (x_S, γ_S, θ_S). The position is measured with respect to the reference frame.

$$\begin{bmatrix} t_{cap_{bot}} \\ t_{cap_{left}} \\ t_{cap_{right}} \end{bmatrix} = \mathbf{T}_{sens,s} \cdot \begin{bmatrix} y_S \\ z_S \\ \phi_S \end{bmatrix} = \begin{bmatrix} -1 & 0 & -l_{cap_{bot}} \\ 0 & 1 & l_{cap_{left}} \\ 0 & 1 & -l_{cap_{right}} \end{bmatrix} \begin{bmatrix} y_S \\ z_S \\ \phi_S \end{bmatrix}, \quad (5.3)$$

$$\begin{bmatrix} F_y \\ F_z \\ T_x \end{bmatrix} = \mathbf{T}_{act,s} \cdot \begin{bmatrix} F_{s,top} \\ F_{s,left} \\ F_{s,right} \end{bmatrix} = \begin{bmatrix} 1 & 0 & 0 \\ 0 & 1 & 1 \\ -l_{F_{top}} & l_{F_{left}} & -l_{F_{right}} \end{bmatrix} \begin{bmatrix} F_{s,top} \\ F_{s,left} \\ F_{s,right} \end{bmatrix}. \quad (5.4)$$

The suspension decoupling matrices are formed by taking the inverse, $\mathbf{T}_{U,s} = \mathbf{T}_{act,s}^{-1}$ and $\mathbf{T}_{Y,p} = \mathbf{T}_{sens,s}^{-1}$.

Figure 5.6 shows the CoG-decoupled plant. Although Eq. 5.3 and Eq. 5.4 geometrically decouple the plant, the plant remains coupled through the negative spring stiffness. The compensation of the negative stiffness is discussed in Section 5.2.3. In the next part, a geometric position dependent coupling between the propulsion and suspension directions is discussed.

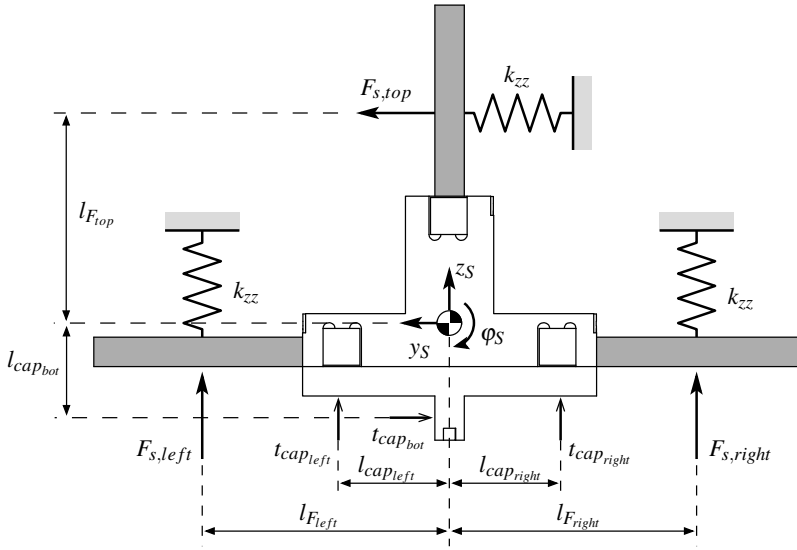


Figure 5.5: Front view of the Slider with locations of the capacitive sensors, t_{cap} , and suspension forces, F_s , given with respect to the CoG.

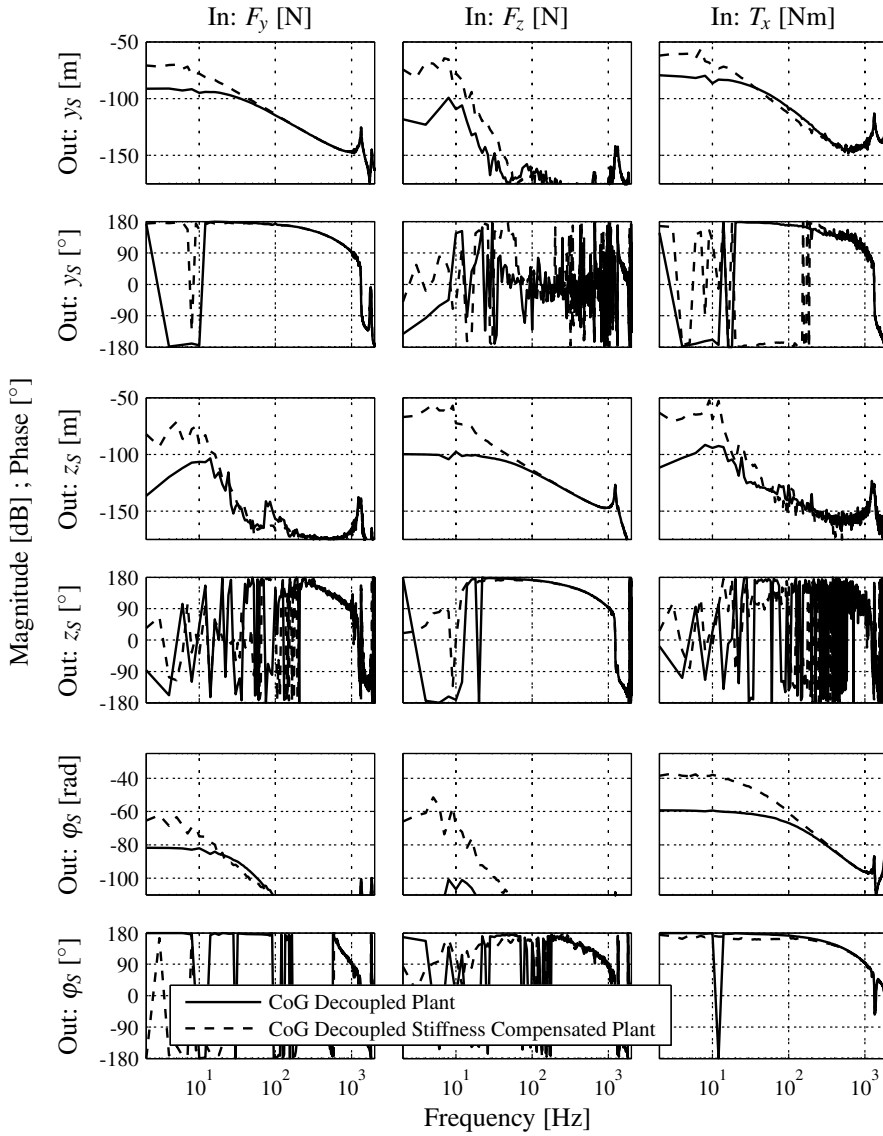


Figure 5.6: Measured open-loop transfer function of the decoupled plant in the suspension directions, $\mathbf{G}_{d,s}(s)$, between Slider body and the reference frame. The Bode diagram depicts the system with and without stiffness compensation.

Coupling between propulsion and suspension directions

A geometric coupling exists between the propulsion and suspension directions as the Slider displaces in the x -direction. The CoG position of the Slider changes with respect to the measurement location of the capacitive sensors. This is caused by the fact, that the capacitive sensors are connected to the fixed world. The coupling is visualised in Fig. 5.7. The coupling causes the reconstruction of the x_S and y_S -coordinates to be biased with displacements equal to $\gamma_S \cdot x_{pos}$ and $-\theta_S \cdot x_{pos}$.

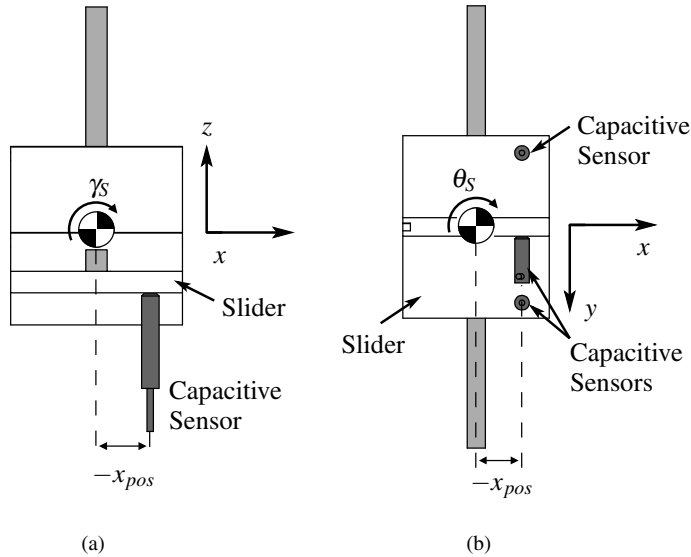


Figure 5.7: Side (a) and bottom (b) view indicating dependency of z_S and y_S -coordinates on x -position (x_{pos}) and angles γ_S and θ_S of the Slider.

The reconstruction of the angles, γ_S and θ_S , are independent of the x_S -position. Therefore, y_S and z_S -coordinates are easily corrected as a function of x_S -position as depicted in Fig. 5.8. The x -position dependency is visible in the transfer $\frac{y_S}{T_z}$. The transfer $\frac{y_S}{T_z}$ is distorted by the term $\theta_S \cdot x$, when x -dependency is left uncompensated. Figure 5.9 shows the measured position transfer $\frac{y_S}{T_z}$ for the situation with and without the compensation. From Fig. 5.9, it is clear that the coupling is reduced by using the decoupling scheme of Fig. 5.8.

5.2.3 Stiffness compensation

The stiffness compensation is conceptually discussed in Section 4.3 and is required for the Slider to properly function in a “low stiffness” design concept. The stiff-

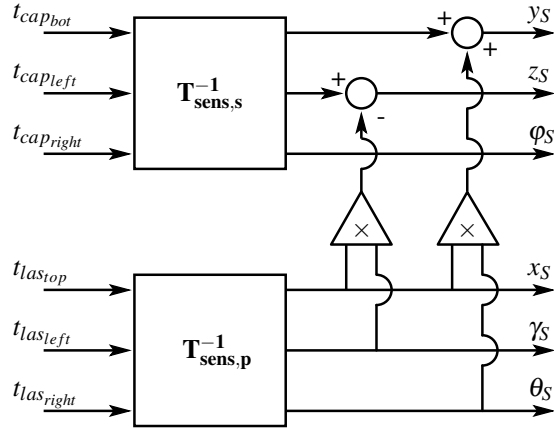


Figure 5.8: Reconstruction of the suspension (y_s, z_s, ϕ_s) coordinates with x -dependency compensation.

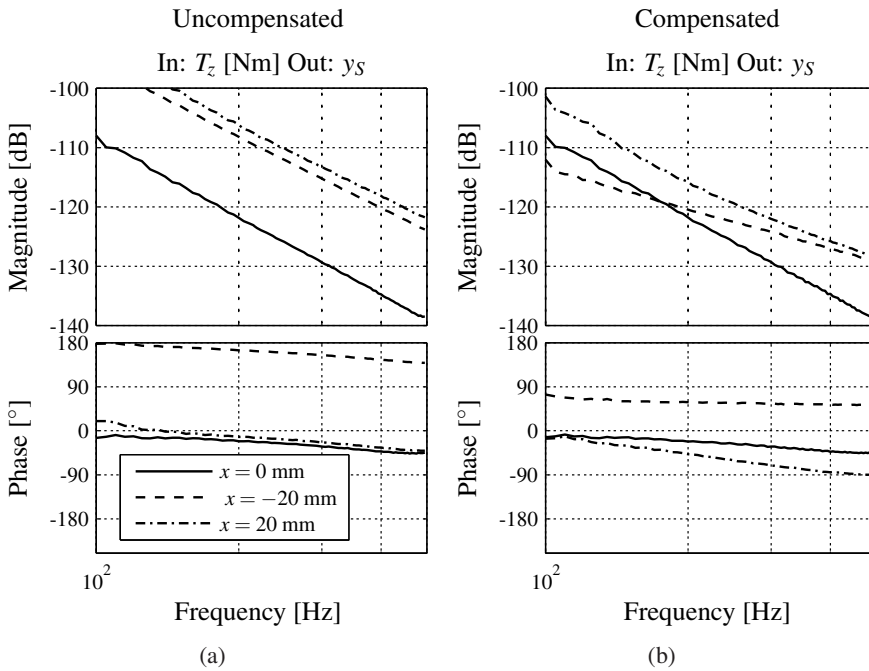


Figure 5.9: Measured transfer $\frac{y_s}{T_z}$ at positions $x = -20, 0, 20$ mm, un-compensated for geometric x -position dependency (a), and compensated for geometric x -position dependency (b) as depicted in Fig. 5.7.

ness compensation reduces the transfer of disturbances from the surroundings to the Slider body. Figure 5.5 gives an overview of the Slider relative to its CoG, together with the negative spring stiffness, k_{zz} , introduced by the IU-modules. The negative stiffness of the IU-modules couple the y and φ -DoF. For example, a y -displacement of the CoG results in a torque, T_x , caused by the negative springs. Therefore, the negative stiffness of the actuators reduces the effectiveness of a CoG-decoupling of the previous subsection. Summarising, the stiffness compensation scheme aims to improve the decoupling and to decrease the transfer of disturbances.

The idea behind the negative stiffness compensation is straightforward. The negative stiffness, k_{zz} , places a force proportional to the displacement from the centre position in the air gap, $F_z = k_{zz} \cdot z$, on the Slider bars. To compensate the force, the displacement of the Slider bars is measured, multiplied with a positive spring constant and fed back to the actuator force, F_{act} . Ideally this results in zero stiffness. In Fig. 5.10 the stiffness compensation scheme is illustrated for a 1-DoF rigid body. The negative stiffness, k_{zz} , and actuation constant, h_{zz} , of the IU-module remain constant over the all propulsion and suspension positions of the Slider, see Section 3.3.2. The stiffness compensation has to occur with respect to the force frame, since the stiffness acts between the Slider and the force frame.

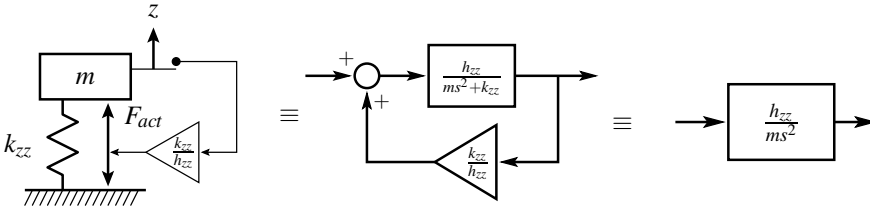


Figure 5.10: Stiffness compensation of a 1-DoF mass-spring system.

To apply the scheme of Fig. 5.10 to the Slider, a decoupled set of coordinates representing the stiffness must be found. Therefore, the theory of modal analysis and dyadic transfer function matrices [57] is employed. The behaviour of the Slider, in CoG coordinates, is described by Eq. 5.5. The mass matrix, \mathbf{M}_g , is decoupled, while the stiffness matrix, \mathbf{K}_g , is coupled, due to the layout of negative stiffness in the IU-modules.

$$\mathbf{M}_g \cdot \ddot{\vec{z}}_g + \mathbf{K}_g \cdot \vec{z}_g = \vec{F}_g. \quad (5.5)$$

Equation 5.5 is a conventional description for a linear dynamic system without damping. Such a linear mechanical system can be transformed to modal/principal coordinates \vec{q} , where the modal mass \mathbf{M}_q and stiffness matrix \mathbf{K}_q are decoupled [23].

Upon these modal decoupled coordinates the stiffness compensation of Fig. 5.10, can easily be applied.

$$\mathbf{M}_q \cdot \ddot{\vec{q}} + \mathbf{K}_q \cdot \vec{q} = \vec{F}_q. \quad (5.6)$$

To find the transformation matrices decoupling the system in modal coordinates, the theory of dyadic transfer functions is used. Owens [57] introduced the term dyadic transformation matrix:

Definition 1 *An $m \times m$ transfer-function matrix $\mathbf{G}(s)$ is said to be dyadic, if and only if $\det(\mathbf{G}(s)) \neq 0$ and there exist constant matrices \mathbf{P}_1 , \mathbf{P}_2 and transfer functions $g_1(s), \dots, g_m(s)$ such that:*

$$\mathbf{G}(s) = \mathbf{P}_1 \cdot \text{diag}\{g_1(s) \dots g_m(s)\} \cdot \mathbf{P}_2. \quad (5.7)$$

A linear mechanical system of Eq. 5.6, which can be transformed to modal coordinates is a dyadic transfer function, [2, 9]. For a dyadic system, static decoupling matrices are found by $\mathbf{T}_{U,\text{stiff}} = \text{eig}(\mathbf{G}^{-1}(\omega_1) \mathbf{G}(\omega_2))$ and by $\mathbf{T}_{Y,\text{stiff}} = \text{eig}(\mathbf{G}(\omega_2) \mathbf{G}^{-1}(\omega_1))$, according to [57]. The dyadic decoupling matrices, $\mathbf{T}_{U,\text{stiff}}$ and $\mathbf{T}_{Y,\text{stiff}}$, decouple the plant in the modal coordinates. Upon these modal coordinates, the stiffness compensation is applied.

The stiffness parameters in the decoupled DoFs, required for the stiffness compensation, still need to be determined. Second order transfer functions, described by Eq. 5.8, are fitted, on the dyadic decoupled plant. The fit is performed in the frequency domain and obtains the ratios $\frac{k_{zz}}{h_{zz}}$ and $\frac{m}{h_{zz}}$. The ratio $\frac{k_{zz}}{h_{zz}}$ is used in the stiffness compensation of Fig. 5.10. Figure 5.11 shows the schematic of the applied dyadic decoupling scheme and stiffness compensation for the MIMO Slider.

$$g(s) = \frac{1}{\frac{m}{h_{zz}} \cdot s^2 + \frac{k_{zz}}{h_{zz}}}. \quad (5.8)$$

In Fig. 5.6, the results of the stiffness compensation for the suspension directions of the plant are displayed. A perfect stiffness compensation results in -2 slopes on the diagonal. The stiffness compensation performs best in the y and z -direction, here a -2 -slope down to 10 Hz is attained. The stiffness in the φ -direction is not fully compensated. After investigation it was discovered, that a non-linearity is present in the suspension directions. This non-linearity might cause the limited effectiveness of the stiffness compensation. The cause of this non-linearity is most probably non-linear behaviour of the eddy current sensors. This non-linearity is further evaluated in Appendix C.1. To improve the performance of the stiffness compensation, it is first advised to separately calibrate the eddy current sensors and compensate for their non-linearity.

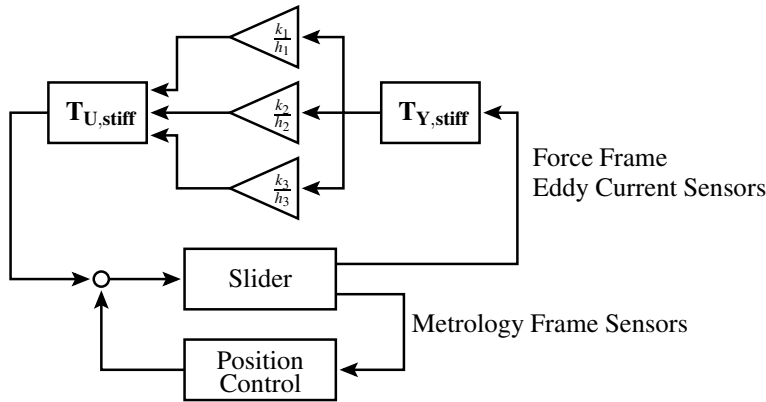


Figure 5.11: Stiffness compensation scheme applied to the Slider. The matrices, $\mathbf{T}_{U,\text{stiff}}$ and $\mathbf{T}_{Y,\text{stiff}}$, are the dyadic decoupling matrices decoupling the plant with respect to the force frame.

5.2.4 Evaluation of decoupling

In this section the performance of the CoG-decoupling method is evaluated. The performance of the decoupling is qualified using two decoupling measures: The Relative Gain Array [66] and the μ -interaction measure by Grosdidier and Morari [26]. At the end of this subsection, a theoretical comparison is made between the CoG-decoupling and alternative decoupling schemes found in literature.

The Relative Gain Array is often applied to evaluate interaction, because of its computational simplicity and the possibility to visualise, where coupling is present [66]. The relative gain array is defined as:

$$\text{RGA}(\mathbf{G}) = \mathbf{G} \times (\mathbf{G}^{-1})^T. \quad (5.9)$$

In Eq. 5.9 the product \times is the element-by-element multiplication, the so called Hadamard or Schur product. The closer the Relative Gain Array of the plant is to the identity matrix, the better decoupled it is. Figure 5.12 shows the RGA of the decoupled Slider. The relative gain arrays shows that a good degree decoupling is achieved up to 1000 Hz. The decoupling fails when the flexible modes, present above > 1000 Hz, are excited. A limitation to the Relative Gain Array is that it is insensitive to one way interaction [75] and therefore, gives only a limited indication of performance.

The μ -interaction measure by Grosdidier and Morari [26] is defined by Eq. 5.10.

$$\mu_{\Delta_C}(\mathbf{E}(s)) = \mu_{\Delta_C}(\mathbf{G}_{\text{diag}}^{-1}(s) \cdot (\mathbf{G}(s) - \mathbf{G}_{\text{diag}}(s))). \quad (5.10)$$

Here, μ_{Δ_C} is the structured singular value [66], with Δ_C the structured block diagonal uncertainty. $\mathbf{G}_{\text{diag}}(s)$ are the diagonal entries of the plant. The μ -uncertainty

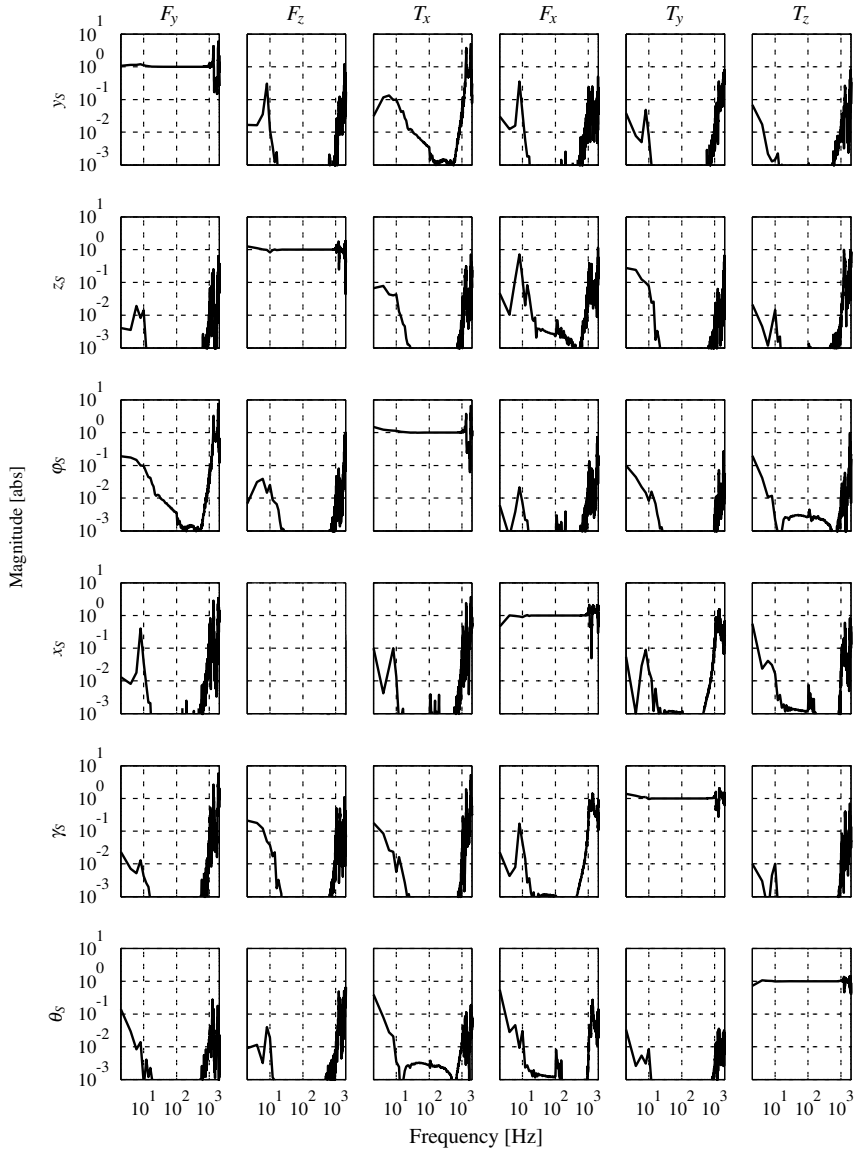


Figure 5.12: Relative Gain Array of the plant $G_d(s)$.

measure forms an upper bound, established by the interaction present in the plant, on the gain of the complementary sensitivity of the individual SISO loops. Where it is assumed that the individual SISO loops of the diagonal system, $\mathbf{G}_{diag}(s)$, are stabilisable. A closed-loop MIMO system is stabilisable, when the μ -interaction measure is less than 1 and its reciprocal $\mu_{\Delta_C}^{-1} > 1$. Figure 5.13 displays the μ -interaction measure, for the coupled plant, and the decoupled plant with and without stiffness compensation. Because the computation of the structured singular value is still an open scientific question, the reciprocal of upper bound on μ is shown in Fig. 5.13. (The reciprocal of the lower bound on μ was also plotted, but visually there was no difference between the lines on the applied scale).

The original coupled plant cannot be effectively controlled with 6 diagonal controllers, because the μ -interaction measure's reciprocal is always less than 1. The μ -interaction measure's reciprocal for the decoupled plants in the region from 100 to 300 Hz is more than 20 dB, so a considerable overshoot is allowed in the complementary sensitivity and little attention has to be paid to the interaction. The stiffness compensated plant performs better than the uncompensated plant in the frequency region below 100 Hz.

Both decoupling measures indicate that decoupling of the plant is successful and that the decoupled plant can be stabilised with a diagonal controller. In Section 5.2.5, the controllers are designed as if the plant is a set of SISO plants.

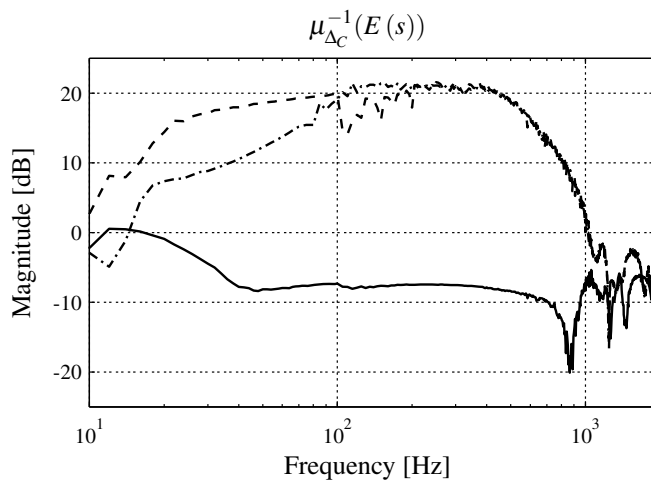


Figure 5.13: The μ -interaction measure's reciprocal for the original coupled plant (—), the decoupled plant with stiffness compensation (---) and the decoupled plant without stiffness compensation (·—).

Comparison to alternative decoupling schemes

In literature, alternative decoupling schemes to the CoG-decoupling method are found. An overview of these decoupling schemes is found in Vaes [75]. These techniques are compared to the CoG-decoupling to verify, if alternative static decoupling methods can realise a significantly better performance. The evaluation is a theoretical study on the measured FRF of the Slider. The decoupling methods are not implemented on the actual Slider.

Figure 5.2 shows the general layout of a decoupled plant and controller. The static pre- and postcompensator \mathbf{T}_Y and \mathbf{T}_U can be determined using methods described in [75]. A short summary of the tested static decoupling strategies is given here, a full overview of these methods is found in [75].

- *Approximate commutative controller* The basis for this decoupling is the eigenvalue decomposition of the plant, here $\mathbf{G}(s) = \Lambda^{-1}(s) \Delta(s) \Lambda(s)$. The matrix Λ contains the eigen-vectors of the plant. While Δ is a diagonal frequency response matrix containing the eigenvalues. The pre-compensator is chosen as $\mathbf{T}_U \approx \Lambda^{-1}(\omega_o)$ and post-compensator $\mathbf{T}_Y \approx \Lambda(\omega_o)$. Here, ω_o is the frequency at which Λ is evaluated. ω_o is selected to be 230 Hz, since this frequency is close to the desired open-loop bandwidth where the best decoupling is required [66]. The ALIGN-algorithm [19] is then used to find the best real approximation to the complex eigenvectors.
- *Inverse based pre-compensator* A static precompensator to the plant $\mathbf{T}_U \approx \mathbf{G}(\omega_o)^{-1}$ is applied ($\omega_o = 230$ Hz). The inverse of the plant is again a complex matrix and the real approximation is found by using the ALIGN algorithm [19].
- *Approximate reversed frame normalisation* The singular value decomposition, defined as $\mathbf{G}(s) = \mathbf{U}_{\text{svd}}(s) \mathbf{S}_{\text{svd}}(s) \mathbf{V}_{\text{svd}}(s)^H$, is the basis for the static approximate reversed frame normalisation. The singular values, contained in $\mathbf{S}_{\text{svd}}(s)$, form a diagonal matrix without phase information. The input and output singular vectors $\mathbf{U}_{\text{svd}}(s)$ and $\mathbf{V}_{\text{svd}}(s)$ are unitary matrices. First, the phase is transferred to the matrix containing the singular values, using the following minimisation:

$$\Gamma = \arg \min_{\gamma} \bar{\sigma}_{\text{svd}} \left(\mathbf{U}_{\text{svd}}^H(s) \mathbf{Y}(s) - \text{diag} \left(e^{j\gamma} \right) \right). \quad (5.11)$$

The decoupling matrices are then $\mathbf{T}_U = \Theta(\omega_o) \mathbf{U}_{\text{svd}}(\omega_o)^H$ and $\mathbf{T}_Y = \mathbf{V}_{\text{svd}}(\omega_o)$, with $\omega_o = 230$ Hz and with matrix $\Theta(\omega_o) = \text{diag} \left(e^{j\Gamma} \right)$.

- *Dyadic decoupling* The dyadic decoupling scheme, presented in Section 5.2.2, is also applied to the plant, $\mathbf{G}(s)$. \mathbf{T}_U is formed by the eigenvectors of $\mathbf{G}^{-1}(\omega_1)\mathbf{G}(\omega_2)$ and \mathbf{T}_Y by the eigenvectors of $\mathbf{G}(\omega_2)\mathbf{G}^{-1}(\omega_1)$. The choice of ω_1 and ω_2 close to the cross over frequency leads to a poorly decoupled system, indicating the plant does not have dyadic properties at these frequencies. With the choice of $\omega_1 = 10$ Hz and $\omega_2 = 20$ Hz good performance is achieved.

Figure 5.14 shows the μ -interaction measure's reciprocal in case of the CoG-decoupling and the alternative decoupling methods. None of the alternative schemes outperform the CoG-decoupling over the entire frequency range. The dyadic decoupling performs better in the frequency region below 100 Hz, while the inverse based controller performs better in the high frequency region. Since the CoG-decoupling is directly related to the performance specifications and none of the alternatives outperforms the CoG-decoupling, no further attempts were made to implement these alternative decoupling schemes on the Slider.

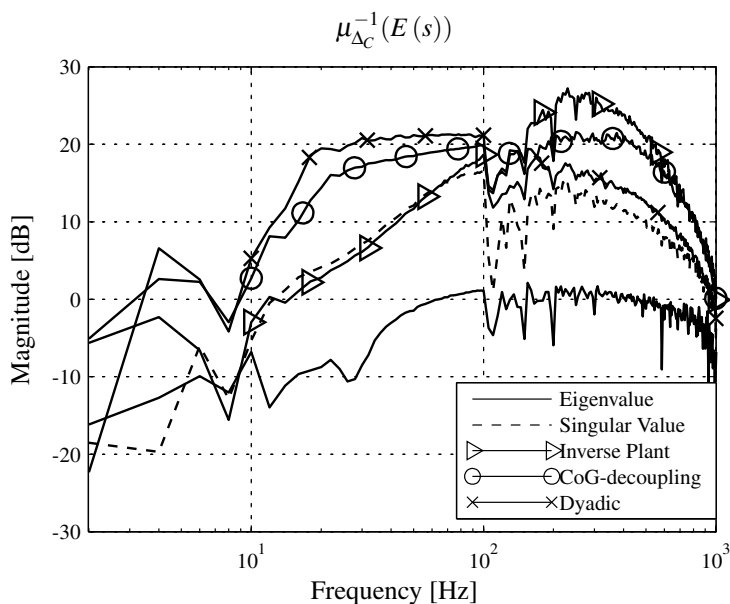


Figure 5.14: Comparison of various static decoupling schemes using the μ -interaction measure's reciprocal.

5.2.5 Position controllers

The position controller largely determines the final performance of the electromagnetically levitated linear Slider. This subsection discusses the design choices made for the controller. Section 5.2.2 and 5.2.4 show that plant, $\mathbf{G}_d(s)$, is decoupled using the CoG-decoupling scheme.

Figures 5.15-5.16 show the measured open-loop FRF and the designed controllers. The controllers are designed through an iterative procedure. At first, PD controllers were designed using Ziegler-Nichols tuning rules, the servo-error was then traced at standstill. From these error traces, CAS and power spectra were constructed. Then the controller was iteratively improved in the region where the error build-up was the most significant.

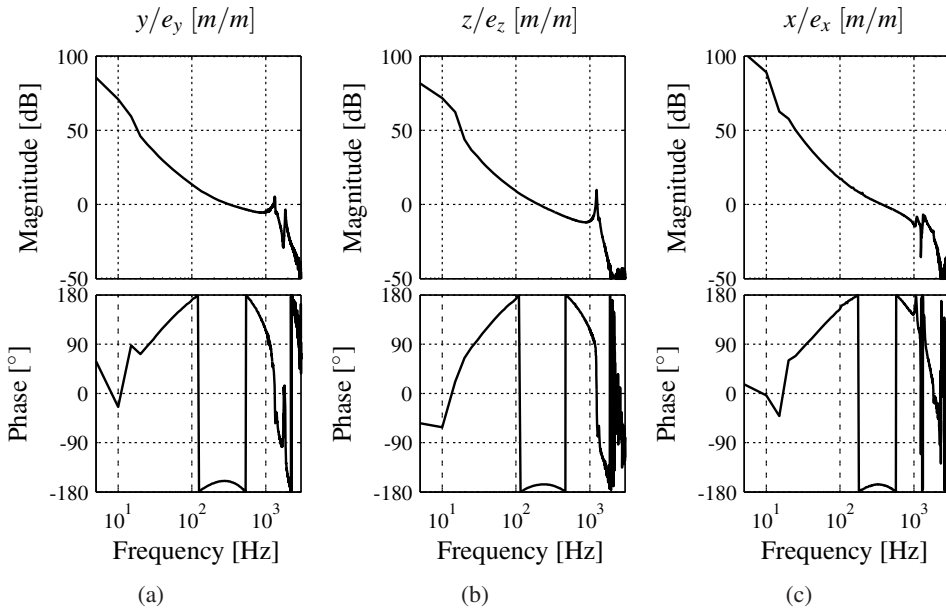


Figure 5.15: Measured open-loop FRF from controller input (e_y, e_z, e_x) to plant output (y_s, z_s, x_s) .

The propulsion x -direction has the highest performance specifications. The controller is designed to create an open-loop 0 dB crossing of 400 Hz. A notch is placed at 1090 Hz to suppress dynamics of the flexible Slider bars. In the low frequency region, a series connection of two integrators is placed, with a stop frequency of 41 Hz. This was done to suppress low frequency disturbances like floor vibrations passing through the vibration isolation. The series connection of two integrators (referred to by I^2), allows higher attenuation at low frequencies with less phase lag

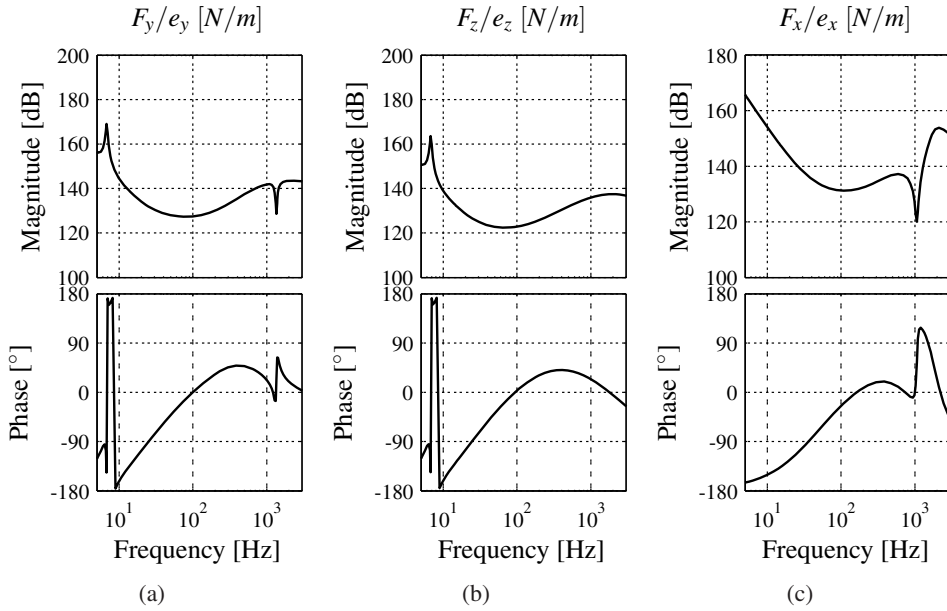


Figure 5.16: Bode diagram of the controllers, from controller input (e_y, e_z, e_x) to actuation force (F_y, F_z, F_x) .

at the cross-over region, than a single integrator would.

The suspension loops, y/F_y and z/F_z , suffer from phase lag of about 25° at 400 Hz, see Fig. 5.6. This phase lag is caused by the sum of the sampling delay, the eddy currents losses in the IU-module, and the phase lag in the position sensors. Section 5.4 shows the full decomposition of this phase lag.

Above 1000 hertz, all suspension loops suffer from mechanical resonances, caused by the Slider bars. In z -direction a normal PD controller with high frequency roll-off sufficed. In the y -direction the resonance at 1200 Hz was too heavily excited and a notch was implemented to reduce its excitation. This notch causes additional phase lag at the cross-over frequency, therefore an additional differential controller is added in series.

The error in the suspension loops had a large error build-up in the frequency region below 20 Hz. Therefore, two series integrators are implemented with integral gain up to 25 Hz. A main source of error was the resonance of the granite base at 7 Hz, which was not sufficiently reduced by the 2 integrators. The error is eliminated by implementing an inverse notch to increase the gain specifically at this frequency. The \mathcal{H}_2 controller of Section 4.5.4 also places additional attenuation at this frequency. In the next section the performance of the Slider is evaluated.

5.3 Performance of the Slider

This section evaluates the achieved performance of the Slider and compares it to the designed performance. First, a summary of the differences between the actual system and the designed system are given in Section 5.3.1. Section 5.3.2 shows the performance of the Slider at standstill, while Section 5.3.3 shows the performance of the Slider, moving at constant velocity.

5.3.1 Differences between modelled and actual system

This subsection discusses the differences between the Slider designed in Chapter 4 and the actual Slider. Some of these differences are due to gradual improvements, while others are model mismatches or imperfections in supplied components. The main differences between the modelled and actual Slider are:

- *Passive suspension frequency of the vibration isolation table*

The active part of the reference frame vibration isolation, introduces noise around 400 Hz. These frequency components directly contribute to the asynchronous error of the optical disc. Secondly, the active part of the vibration isolation table uses a noisy pulse width modulated amplifier, disturbing the measurements of the capacitive sensors. Therefore, the vibration isolation table is kept passive at an 11 Hz resonance frequency.

- *Lower negative stiffness of IU-modules than modelled in the Dynamic Error Budget*

The negative stiffness of the IU-modules, used in the DEB, was $-5 \cdot 10^4$ N/m, while in the actual system the negative stiffness is only $-3 \cdot 10^4$ N/m. The negative stiffness still has to be compensated, but to a lesser degree than in the model of Section 4.5. Appendix A.1 discusses the influence of the negative stiffness and stiffness compensation on the Slider's performance.

- *Averaging of sensor signals*

The eddy current sensors, the capacitive sensors, and the laser interferometers, produce analog signals. These signals are converted to digital signals by an AD-converter. To improve the signal to noise ratio of the converted sensor signals, averaging is applied to the AD-conversions. The averaging is made possible by the fact that only 22 μ s are used for the basic control loop, while the sampling frequency of the digital controller was 20 kHz (sampling period of 50 μ s). Instead of increasing the sampling frequency, the most critical sensor signals are averaged during the remainder of the sampling period.

The averaging is performed by oversampling the sensor signal within the sample period of 20 kHz. These samples are then summed, divided by their num-

ber and transferred to the controller running at 20 kHz. This averaging reduces the power of the noise of the AD-conversion by a factor $\frac{1}{\sqrt{n}}$, where n is the number of averages. The capacitive sensors and the eddy current sensors are averaged 5 times using the burst conversion on the dSPACE DS-2004 board. The laser interferometer signals are averaged 10 times, using the electronics presented in Appendix A.2.

- *High frequency components in the capacitive sensors*

The sensor signals of the capacitive sensors contained high frequency components, when the Slider body is left ungrounded. The origin most probably lies in the fact that the measurements of the separate capacitive sensors are influencing each-other. When a single capacitive sensor was applied, the noise is eliminated. The only way to keep these high frequency components low, was to ground the Slider body with a wire. This of course, violates the principle of “wireless” propulsion. An alternative might be, to apply a capacitive ground to the Slider. However, capacitive grounding of a magnetically levitated positioning system is non-trivial. More information on the grounding of capacitive sensors in conjunction with magnetically suspended systems will be found in [56].

- *Non-linearity in the eddy current sensors*

The eddy current sensors suffer from non-linear behaviour, see Appendix C.1. This is expected to limit the effectiveness of the stiffness compensation.

5.3.2 Performance of Slider at standstill

In this section, the performance of the linear Slider is evaluated by analysing the servo-error. The servo-error is a measure of performance, however it is not exactly the same as the repeatability of the Slider. Measurement drift below the bandwidth of the control loop is not part of the servo-error, but will result in a displacement of the Slider. Sensor noise above the bandwidth is present in the servo-error, but is not part of the displacement of the Slider.

Figure 5.17 shows the CAS of the servo-errors, e_x , e_y , and e_z , of the Slider. The standard deviation in the propulsion direction is less than 0.3 nm on all x -positions. The servo-errors in the y and x -directions are less than 3 nm. The Slider meets the design specifications from Section 4.2.

In the $x_S = 0$ -position the performance is even better. The standard deviation of the servo-error is 0.12 nm in the x -direction, 1.2 nm in the y -direction, and 0.8 nm in the z -direction. In the $x_S = 0$ -position the error build-up is smooth over frequency, while in the out of centre position the servo-error increases in the frequency range from 7 Hz to 20 Hz. The cause of this increased error lies in the transfer of low frequency disturbances to the Slider and the reference frame. As is indicated

in Section 5.3.1, the vibration isolation is left inactive resulting in a suspension frequency of 11 Hz. This higher suspension frequency allows transfer of disturbances from the force frame to the reference frame. Secondly, the stiffness compensation is designed at the $x_S = 0$ -position. Due to the non-linearity in the eddy current sensors (Appendix C.1), it is less effective at the outer positions. In the subsequent part, the effects of the stiffness compensation and the suspension frequency of the vibration isolation are investigated separately.

Performance of the stiffness compensation

Figure 5.18 shows the performance of the Slider with and without stiffness compensation at $x_S = 0$ -position. The servo-error, e_z , reduces from 16 nm to 1 nm (σ), when the stiffness compensation is switched on. The stiffness compensation is sufficient and necessary to obtain the specifications of Section 4.2. In propulsion direction the change in performance is negligible, showing that the x_S -coordinate is well decoupled from the suspension directions.

The active vibration isolation table

Figure 5.19 shows the servo-error with and without active vibration isolation at the $x_S = 0$ -position. The error in the low frequency region is significantly reduced, when the vibration isolation was switched on. However, the total servo-error is close to that of the passive isolation. The active vibration isolation reduces the low frequency components, but introduces noise at 400 Hz.

The frequency content of this noise directly influences the asynchronous errors on the optical disc. Therefore, it was decided not to use the vibration isolation. The error-reduction at the lower frequencies in x -direction shows that a significant performance increase can be achieved, when a better vibration isolation is used for the reference frame.

5.3.3 Performance of the moving Slider

In production, the Slider moves at near constant velocity. As a reference, a velocity of 55 $\mu\text{m/s}$ is chosen (approximately 1 disc in 15 min). Figure 5.20 shows the CAS of the servo error at two velocities, the production velocity of 55 $\mu\text{m/s}$ and a faster move of 500 $\mu\text{m/s}$. Both CAS show large periodic disturbances, at 174 Hz and 348 Hz for the 55 $\mu\text{m/s}$ -move, and at 1580 Hz and 3160 Hz for the 500 $\mu\text{m/s}$ -move. The standard deviation at the production velocity is larger than 1 nm (σ), exceeding the specifications. At the production velocity, the periodic error also transfers to the y and z -directions.

The position of the Slider is determined by interpolating two sinusoidal signals coming from the laser interferometer. If these sinusoidal signals are not perfectly

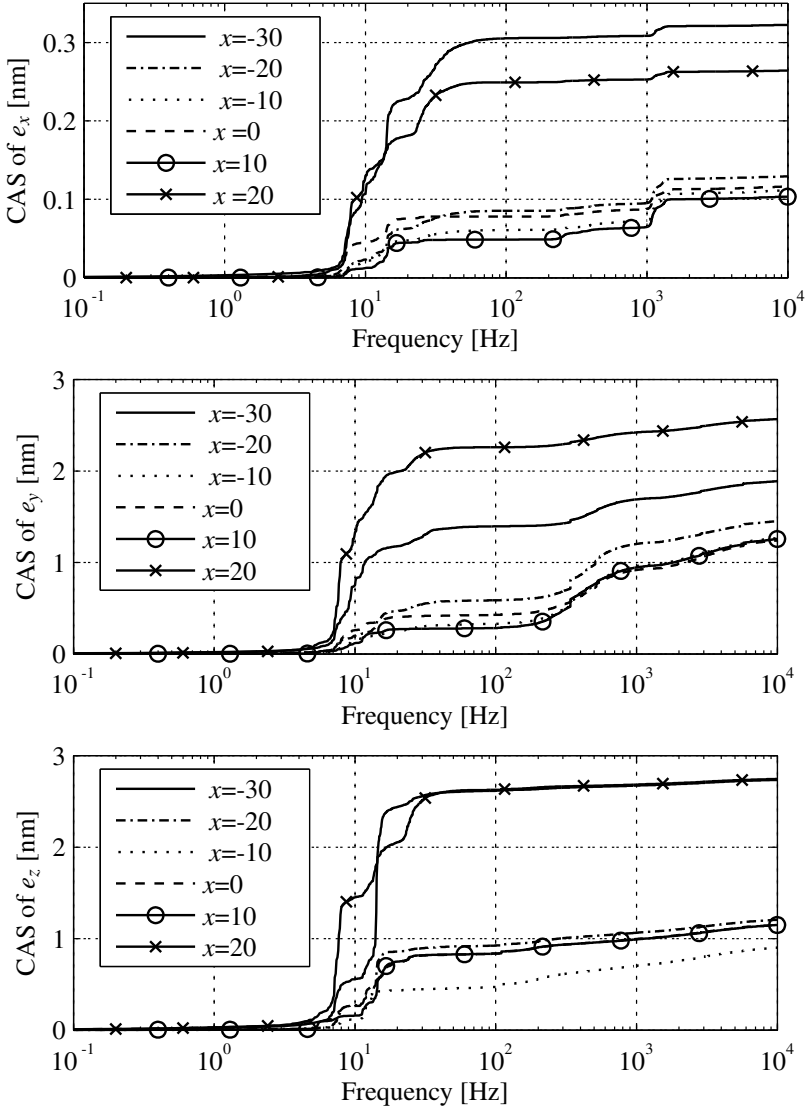


Figure 5.17: Cumulative Amplitude Spectra of servo-errors, e_x , e_y and e_z , at stand-still on different x -positions along the stroke, x -positions are given in [mm] from the centre position.

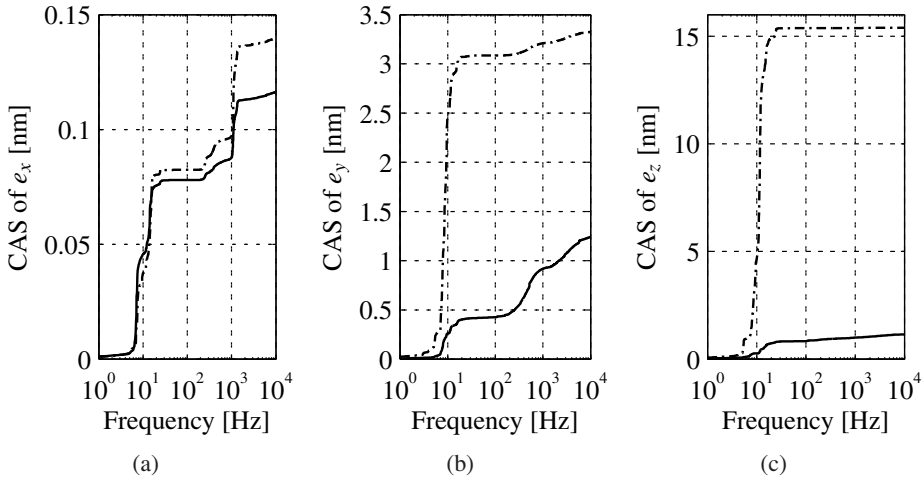


Figure 5.18: Servo-error, e_x , e_y and e_z with stiffness compensation switched on (—) and off (---).

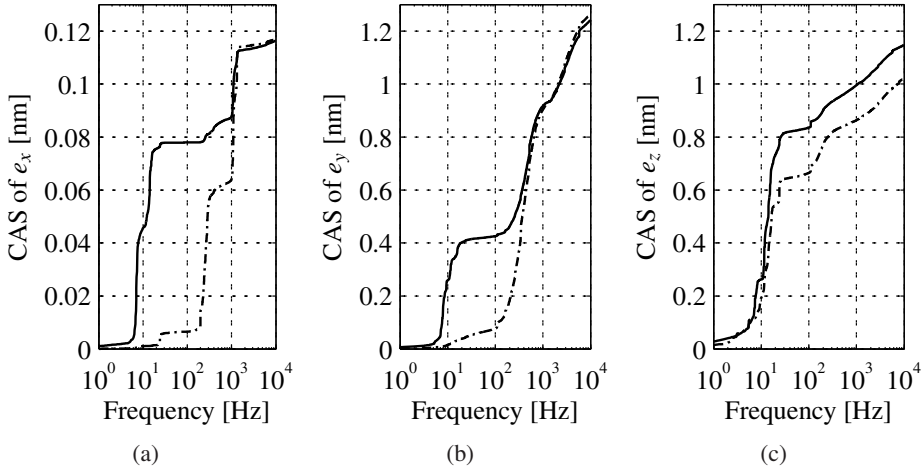


Figure 5.19: Comparison between active 1 Hz(---) and passive 11 Hz(—) vibration isolation.

sinusoidal or have DC offsets, interpolation errors occur. The first frequency of the interpolation error, f_1 , is equal to the Sliders velocity, \dot{x}_S , divided by half the laser wavelength, ($f_1 = \frac{\dot{x}_S}{0.5\lambda}$), with $\lambda = 633 \text{ nm}$; the second frequency is equal to ($f_2 = \frac{\dot{x}_S}{0.25\lambda}$).

The influence of these interpolation errors on the servo-error is determined by the bandwidth of the control system. At low frequencies, the controller suppresses any error signals in the measurement signal (resulting in an erroneous position on the Slider). At frequencies higher than the bandwidth, the controller will not suppress these errors, and the errors are not transferred to the Slider. At frequencies around the bandwidth, the error is amplified, as is the case for the production move.

Since the interpolation errors are repetitive with respect to the position reported by the interpolation board, they can be compensated. First, the servo-errors of the Slider moving at a velocity of $500 \mu\text{m/s}$ are recorded. The first periodic disturbance then occurs at 780 Hz , at this frequency the influence of the controller can be neglected. Three sinusoidal functions of position are fitted on the position error, at frequencies of ($f_1 = \frac{2\dot{x}_S}{\lambda}$), ($f_2 = \frac{4\dot{x}_S}{\lambda}$), and ($f_3 = \frac{8\dot{x}_S}{\lambda}$). These sinusoidal functions are then added as a compensation signal to the position of the laser interferometer. The result of the interpolation error compensated move at $55 \mu\text{m/s}$ is shown in Fig. 5.21. The specification of 1 nm (σ) is met once more.

The compensation performed well over a period of about 45 minutes and then started to loose performance. Environmental influences, like temperature are likely to influence the measurement and the interpolation. Control technical compensations for suppressing known periodic disturbances are found in literature [51, 65]. These techniques can be used to online compensate for these slow varying periodic disturbances. Methods for compensating periodic errors in laser interferometers themselves, are found in [14].

The compensation/calibration of periodic errors in laser interferometers might be a potential “new” application for the magnetically levitated Slider.

5.4 Performance of the IU-module Actuator

The IU-modules are an integral part of the design of the Slider. One of the limitations of the IU-modules is the crosstalk from the propulsion actuation to the suspension force, as presented in Section 3.3.2. In Section 5.2.5, the control loops are designed as if each loop is independent. The crosstalk, originating in the IU-module, degrades the performance of the decoupling and the Slider. The effect of the crosstalk on the Slider is visualised in the Bode diagram of the input sensitivity shown in Fig. 5.22. A set-point, r_x , with frequency content between 100 and 500 Hz has a significant influence on the servo-error in the z and y -direction. The Slider for optical disc mastering only uses set-points of near constant velocity. However when faster set-points with large accelerations are required, the interaction should

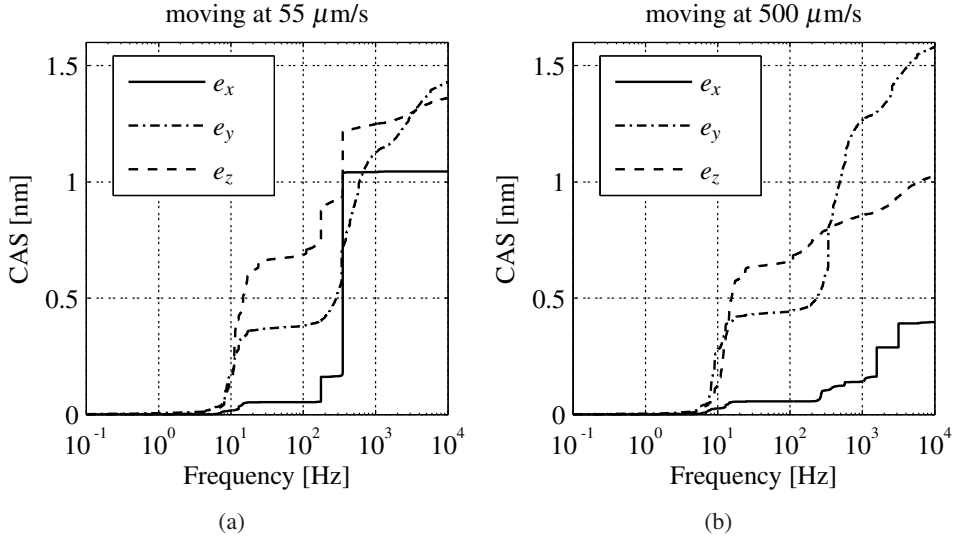


Figure 5.20: Servo-errors of moving slider, at 55 $\mu\text{m/s}$ (a), and at 500 $\mu\text{m/s}$ (b). The periodic errors are caused by interpolation errors of the laser interferometers.

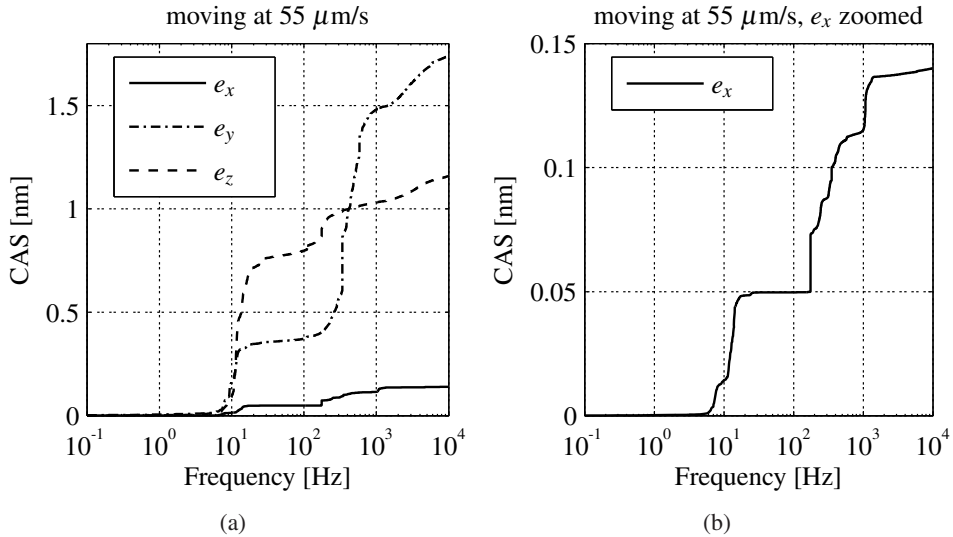


Figure 5.21: Servo-errors of the moving Slider at 55 $\mu\text{m/s}$, with a compensation for interpolation errors of the laser interferometers.

be dealt with or an alternative actuator should be applied.

A relatively large phase lag is present in the suspension directions, as indicated in Section 5.2.5. Non-linearities present in the IU-module, like eddy currents and hysteresis, can introduce phase lag between actuation current and the generated force. The phase lag of the IU-module cannot be directly measured on the Slider. However, by subtracting the known phase lags of each loop component from the total open-loop phase lag, the phase lag of the actuator can be estimated. Figure 5.23 shows the reconstruction of the phase lag in suspension direction of an IU-module. The analysis is performed on the high bandwidth loop, because the filtering present in the capacitive sensors is exactly known. The capacitive sensors have a 2-pole Butterworth filter at 10 kHz and a 5-pole Butterworth filter at 14 kHz. The phase lag of the current amplifiers and anti-aliasing filters was separately measured. The phase lag of the controller is approximated by a sample delay with a sampling frequency of 20 kHz. The resulting phase lag of the actuator is 10° at 400 Hz and is the largest contributor to the phase lag, closely followed by the capacitive sensor. The phase lag is slightly dependent on the x -position of the Slider. At the $x_S = -30$ mm position the phase lag is 2° less than at the $x_S = 20$ mm position (close to the permanent magnets), determined at 400 Hz. A more detailed study on the influence of magnetic materials and eddy currents on the performance of the IU-module is done by Lebedev [44].

Using the same methods, the phase lag in the propulsion direction is established. The propulsion actuation of the IU-module has less than 1° of phase lag at 500 Hz. The phase lag analysis shows, that the IU-module is generally capable of achieving a higher control bandwidth in the propulsion direction, than in its suspension direction.

5.5 Conclusions and remarks

The Slider, using the 2-DoF IU-module actuators, attains the specifications for the optical disc mastering application as specified in Chapter 4. At the centre position, the Slider is capable of achieving a servo-error at standstill of 0.12 nm (σ) in x -direction. During motion, a servo-error of 0.15 nm (σ) is achieved. In the y and z -directions the standard deviation of the servo-error remains below 3 nm over all x -positions. The achieved performance level demonstrates the capabilities of the IU-module, presented in Chapter 3, together with the “low stiffness” design concept and analysis techniques described in Chapter 4.

The behaviour of IU-module fits the application well. In the x -direction the requirements of the Slider are more stringent than in the suspension directions. The crosstalk from propulsion to suspension, present in the actuator, favours the performance in the propulsion direction. The IU-module has less phase lag in the propulsion direction, due to lower sensitivity to electromagnetic losses. This allows

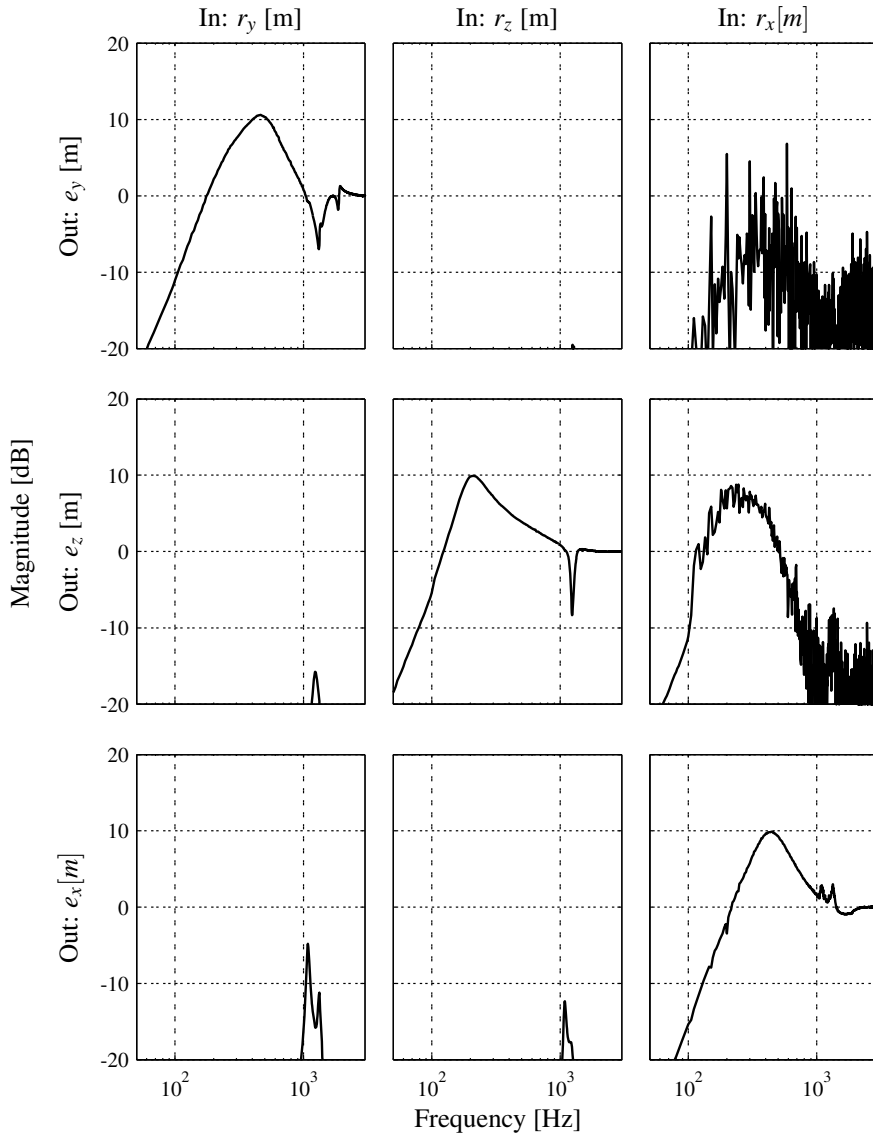


Figure 5.22: Input sensitivity of the Slider between reference set-point (r_x, r_y, r_z) and servo-error (e_x, e_y, e_z). The coupling introduced by the IU-modules is visible in $\frac{e_y}{r_x}$ and $\frac{e_z}{r_x}$.

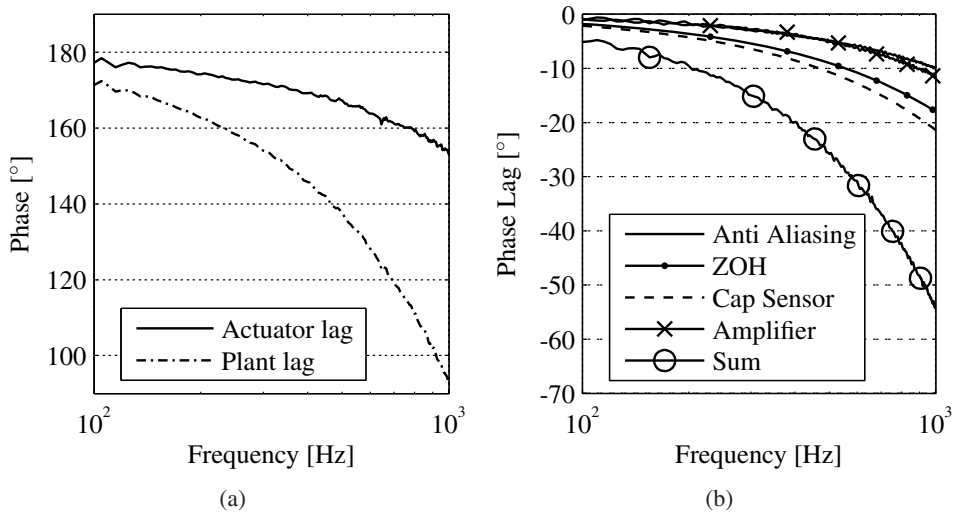


Figure 5.23: Phase lag of the open-loop suspension FRF, F_z/z , and estimated phase lag of the actuator (a), the phase lag of all known components and their sum (b). ZOH is the phase lag of the zero order hold introduced by the controller.

a larger control bandwidth in the propulsion direction of the IU-module. In addition to this, the IU-module does not have a negative stiffness in the propulsion direction, resulting in a minimal transfer of disturbances.

The error has been analysed by evaluating the servo-error. Low frequent drift is not present in the servo-error. The optical disc mastering system, itself, is tolerant to low frequent errors. By including static design principles, such as temperature compensation and calibration of the measurement system, the servo-error can be extended towards accuracy required for the Slider. Details on static design principles can be found in [64].

Chapter 6

Improved positioning by use of over-actuation

In systems where the CoG-decoupling is applied, flexible modes often form a barrier to achieving higher levels of performance. Modal control is a research field, dealing with the control of these flexible modes. The control of flexible modes, requires additional inputs to the plant. From the measurements of Section 3.5, it is clear that the IU-module is capable of generating torques around the x and z -axis, next to the suspension and propulsion forces. These additional degrees of actuation can be applied to suppress the excitation of the flexible modes of the Slider.

It is well known in mechatronics, that by placing position sensors or actuators in the node of a flexible mode, they can be rendered unobservable or uncontrollable [54]. The additional degrees of actuation of the IU-modules are not located in the nodes of the flexible modes of the Slider. However, by combining the additional actuation capabilities, a similar effect to actuation in the node of a mode can be achieved. This allows specific modes not to be excited by the controller, rendering them uncontrollable. In this thesis, this actuation method is referred to: mode decoupled actuation, MDA.

Figure 6.1 shows the Cumulative Power Spectrum of the servo-error, e_x . The CPS shows 2 distinct regions in which the error is built up. Low frequency errors enter between 10 and 20 Hz, and high frequency errors enter around 1100 Hz. The 1100 Hz contribution is just as significant as the low frequency build-up. The 1100 Hz contribution is caused by the excitation of a flexible mode of the Slider. By applying mode decoupled actuation, the flexible mode is not excited by the controller. Since the flexible mode is now uncontrollable, it is removed from the control loop. This allows controller improvements, not just in the frequency range of the flexible modes, but also at lower frequencies, due to increased stability margins. In Fig. 6.1, the effect on the CPS of the servo-error, e_x , due to the elimination of the flexible mode and an improved position controller, is shown. The servo-error,

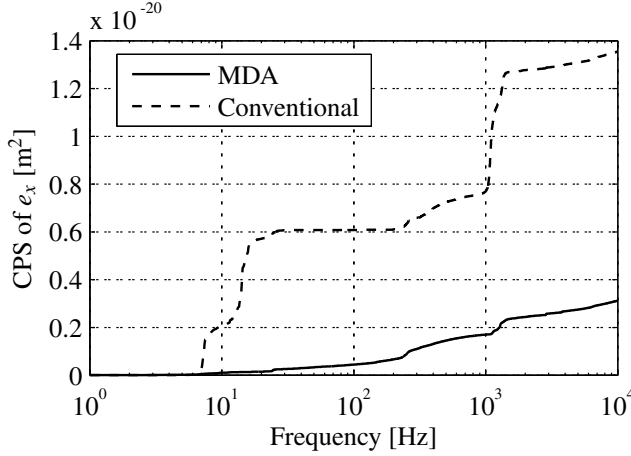


Figure 6.1: Cumulative Power Spectrum of the servo-error, e_x , in the $x = 0$ -position, using the CoG-decoupled controller of Chapter 5 (—), and CPS of servo-error, e_x , when the flexible mode is not excited and the position controller improved.

e_x , decreases by a factor of 2, to 58 pm (a factor 4 in power). These results were published in [43, 77].

In Section 6.1, the theoretical basis of MDA is explained. Special attention is paid to the rendering flexible modes uncontrollable and unobservable. The implementation of the MDA on the Slider is presented in Section 6.2.

6.1 Modal control basics

A conventional linear mechanical system is described by Eq. 6.1. Such a conventional mechanical system can be transformed to modal coordinates, using the modal eigenvectors [32].

$$\mathbf{M}_g \ddot{\vec{x}}_g + \mathbf{K}_g \vec{x}_g = \vec{F}_g. \quad (6.1)$$

The modal eigenvectors and eigenfrequencies are obtained through the generalised eigenvalue problem of Eq. 6.2.

$$\mathbf{K}_g \cdot \vec{V}_i = \omega_i^2 \cdot \mathbf{M}_g \cdot \vec{V}_i. \quad (6.2)$$

The eigenvector, \vec{V}_i , is i 'th real eigenvector with an eigenfrequency of ω_i . The eigenvectors decouple the coupled equations of motion, Eq. 6.1, into the decoupled modal equations, Eq. 6.3.

$$\mathbf{M}_q \cdot \ddot{\vec{q}} + \mathbf{K}_q \cdot \vec{q} = \vec{F}_q. \quad (6.3)$$

Both the modal mass matrix, \mathbf{M}_q , and modal stiffness matrix, \mathbf{K}_q , are diagonal and are given by $\mathbf{V}^T \mathbf{M}_g \mathbf{V} = \text{diag}(m_q) = \mathbf{M}_q$, $\mathbf{V}^T \mathbf{K}_g \mathbf{V} = \text{diag}(k_q) = \mathbf{K}_q$. The matrix, \mathbf{V} , contains the eigen-vectors, \vec{V}_i . The modal force vector is given by $\vec{F}_q = \mathbf{V}^T \cdot \vec{F}_g$ and modal coordinates by $\vec{q} = \mathbf{V}^{-1} \vec{x}_g$.

A linear system having proportional damping ($\mathbf{M}_g \ddot{\vec{x}}_g + \mathbf{D}_g \dot{\vec{x}}_g + \mathbf{K}_g \vec{x}_g = \vec{F}_g$) is also decoupled in modal coordinates using real eigenvectors. Proportional damping is defined as $\mathbf{D}_g = \alpha \mathbf{M}_g + \beta \mathbf{K}_g$, where α and β are non-negative scalars. Mechanical structures with low damping can often be described by proportional damping. Figure 6.2 graphically illustrates the modal decomposition of a mechanical structure.

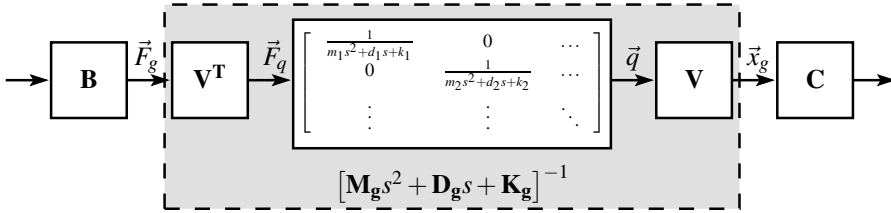


Figure 6.2: Conventional mechanical system of the form, $\mathbf{M}_g \ddot{\vec{x}}_g + \mathbf{D}_g \dot{\vec{x}}_g + \mathbf{K}_g \vec{x}_g = \vec{F}_g$, and its modal representation. With \mathbf{B} the input matrix, \mathbf{C} the output matrix, and \mathbf{V} the matrix containing the modal eigen-vectors, \vec{V}_i .

The modal coordinates are decoupled, making them an ideal basis for decoupled controller design. To realise this decoupling, the input decoupling matrix of Fig. 5.2, can be taken as $\mathbf{T}_U = (\mathbf{V}^T \mathbf{B})^{-1}$ and output decoupling matrix as $\mathbf{T}_Y = (\mathbf{C} \mathbf{V})^{-1}$. Of course, both combinations should be invertible. This type of control is referred to as modal control, an overview is found in [23].

A continuous parameter system, such as the Slider, has an infinite number of modes, and the eigenvectors, \vec{V}_i , are in fact continuous functions. Since the amount of computing power, actuators and sensors is limited, a selection must be made of the modes which to actuate, observe and control, Balas [6] states: “*The fundamental problem of controlling very flexible systems is to control a large dimensional system with a much smaller dimensional controller*”. The actuator matrix, \mathbf{B} , and sensor matrix, \mathbf{C} , determine which modes are controllable and observable. Only the properties, like stiffness and damping, of the controllable and observable modes can be altered using modal control, as described in [23, 61].

It is well known in mechatronics, that the actuator and sensor placement have significant impact on the dynamics of a system. The effect of sensor and actuator placement is illustrated with an example of a clamped Euler-Bernoulli beam with varying displacement sensor position, t_o , and actuator position, F_o . Figure 6.3 shows the first three mode shapes of this beam, where o is the application point for the actuation force or displacement measurement. The beam is discretized using a 20 node finite element model [32], and it has the same dimensions as the Slider bars of the Slider.

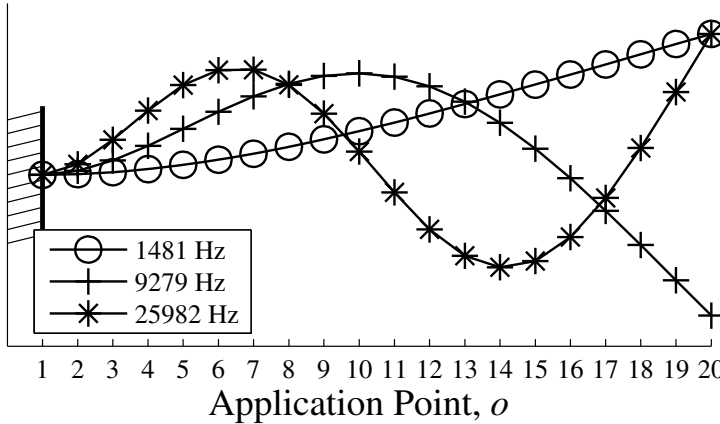


Figure 6.3: The first three mode shapes of a clamped beam with the application points, o , indicated. At these application points, a force, F_o , or a measurement, t_o , can be administered.

Observation of Modes By modifying the location of the position sensors t_o , the output matrix, \mathbf{C} , is altered. By doing so, certain modes can be made observable/unobservable [54]. The output of a mode is constructed by: $\mathbf{C}\mathbf{V}$. If a sensor is placed at the node of the i 'th flexible mode, where $V_{oi} = 0$, this mode will be unobservable. For example, the second mode at 9279 Hz is unobservable in the transfer $\frac{t_{16}}{F_{20}}(s)$, shown in Fig. 6.4(a), where the displacement sensor, t_o , is placed near application point 16 in the node of the second mode, see Fig. 6.3.

Actuation of modes The modes, which are acted upon by the actuators, are determined by $\mathbf{V}^T \cdot \mathbf{B}$. If actuation, F_o , occurs at a node of the i 'th flexible mode, where $V_{oi}^T = 0$, this mode will not be excited. The mode is rendered uncontrollable [54]. Figure 6.4(b) shows the difference in the transfer between actuation at the tip, $\frac{t_{20}}{F_{20}}(s)$, and actuation at the node of third mode near application point 10, $\frac{t_{20}}{F_{10}}(s)$.

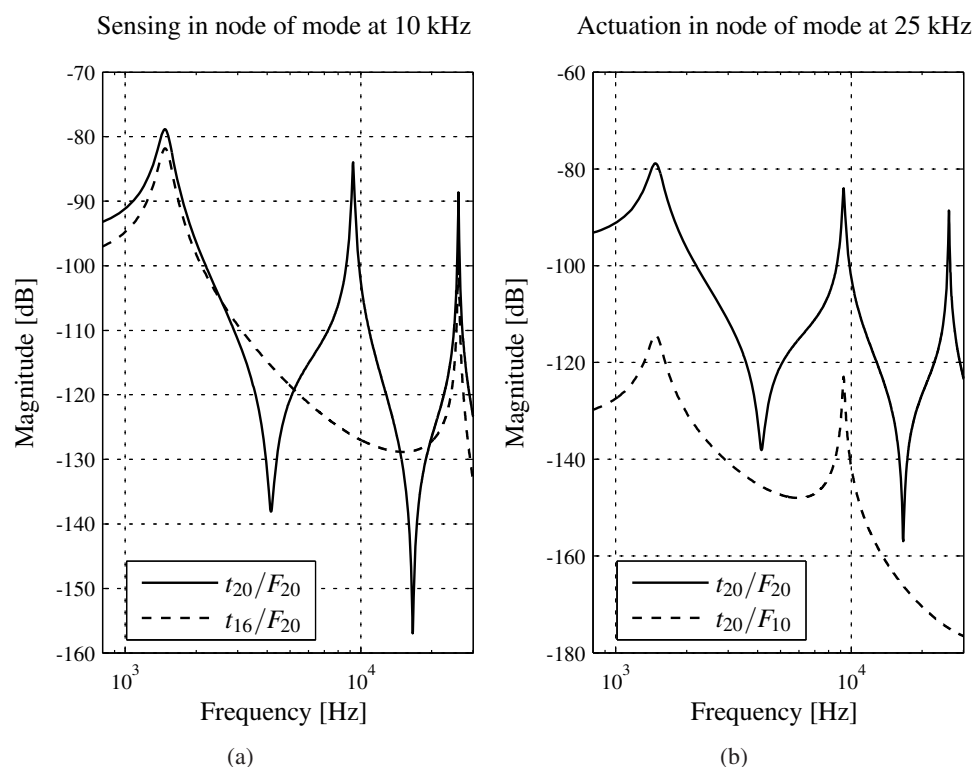


Figure 6.4: Effect of sensor location, t_o , on the observability of flexible modes (a), and the effect of actuator location, F_o , on the controllability of modes (b). The application points and mode shapes are found in Fig. 6.3.

The additional degrees of actuation, present in the IU-module, do not allow individual modal actuation, as described in [24]. However, the additional actuation capabilities do allow the exclusion of a specific mode, similar to that of actuating in the node of a flexible mode. The combination of $\mathbf{V}^T \mathbf{B}$ determines, which modes are excited. If $\vec{V}_i \cdot \vec{B} = 0$, the i 'th mode is not excited. Additional degrees of actuation present in the actuation, allow direct modification of the actuation vector \vec{B} .

For example, if the forces, F_{15} and F_{19} , at application point 15 and 19, are available for actuation, a simple scheme can be devised to exclude the second mode at 9297 Hz from the transfer, using Eq. 6.4.

$$\begin{aligned} \vec{V}_2 \cdot \vec{B} &= [V_{2,1} \quad \cdots \quad V_{2,14} \quad \cdots \quad V_{2,19} \quad V_{2,20}] \cdot \begin{bmatrix} 0 \\ F_{15} \\ 0 \\ \vdots \\ F_{19} \\ 0 \end{bmatrix} = \dots \\ &= V_{2,15} \cdot F_{15} + V_{2,19} \cdot F_{19} = 0, \\ F_{15} &= -\frac{V_{2,19} \cdot F_{19}}{V_{2,15}}. \end{aligned} \tag{6.4}$$

Figure 6.5(a) shows the transfer for actuation at application point 15 and 19 to a sensor at the tip (application point 20). In both $\frac{t_{20}}{F_{15}}$ and $\frac{t_{20}}{F_{19}}$ the flexible mode at 9297 Hz is present. The combination of the actuation, as in Eq. 6.4, removes the second mode from the transfer, while retaining the ability to act on the other modes. In Fig. 6.5(b) the difference is shown between the actuation in the node near the application point 17, and MDA of Eq. 6.4. In both cases, the second mode is rendered uncontrollable. The response in the low frequency region is similar to that of actuation in the node of the mode. In Section 6.2, the mode decoupled actuation is used to reduce the influence of flexible modes and improve the positioning performance of the Slider.

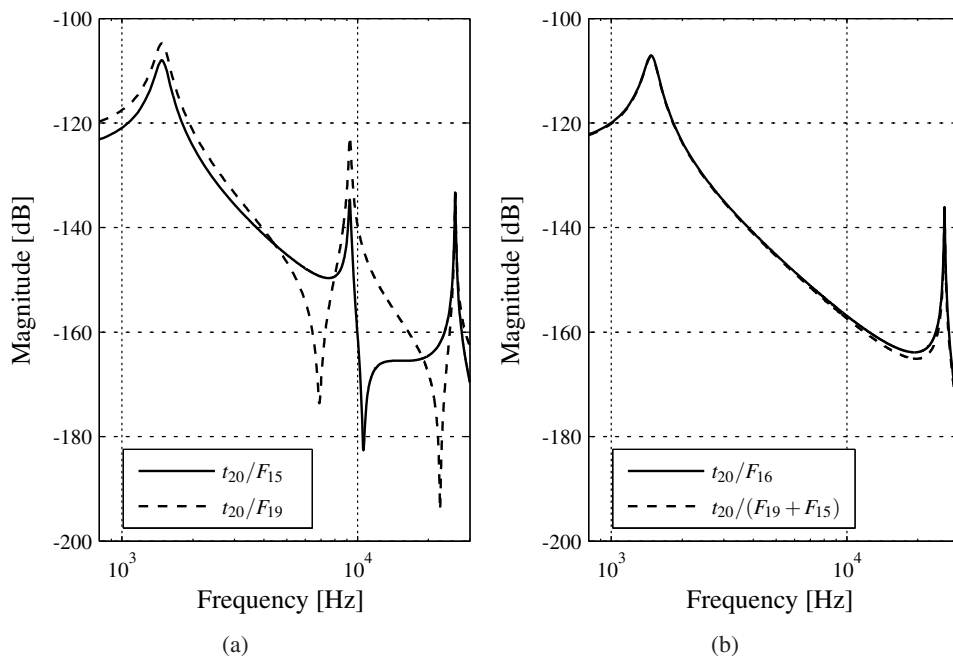


Figure 6.5: Actuation in application point, 15 and 19, to a displacement at the tip of the beam (a), and comparison between actual actuation in the node of the flexible mode near application point 16, and MDA of $F_{15} + F_{19}$, where the total force is $F_{15} + F_{19} = F_{16}$ (b).

6.2 Mode decoupled actuation for the Slider

One of the basic limitations to the performance of the Slider are the resonances originating in the Slider bars of the IU-modules. Figures 6.6 and 6.7 give a graphical overview of the critical mode shapes, in which the Slider bars play a dominant role. The additional degrees of actuation in the IU-modules, allow modal control. In this section an attempt is made, not to excite the flexible modes of the Slider, as was illustrated in Section 6.1. By doing so the flexible modes are rendered uncontrollable.

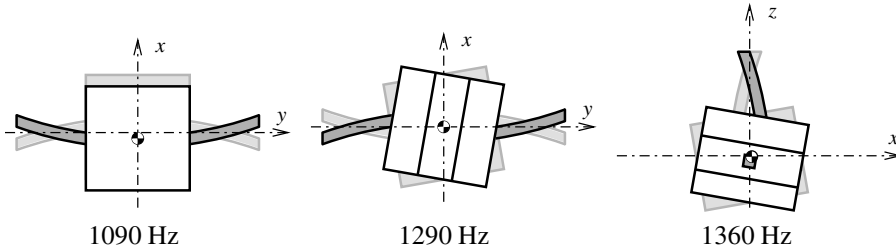


Figure 6.6: Modes visible in propulsion directions.

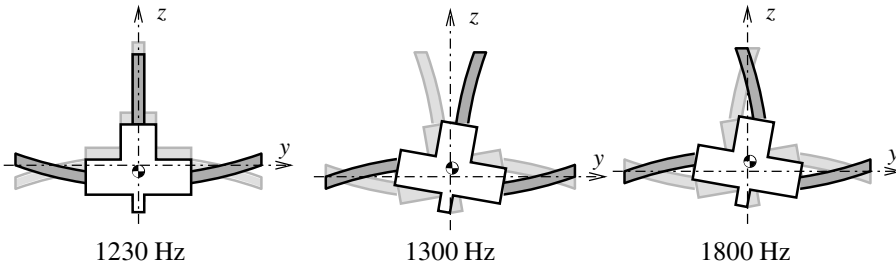


Figure 6.7: Modes visible in suspension directions.

Three types of modal control are distinguished in this thesis, true modal control, modal observation, and mode decoupled actuation. In true modal control the properties of a specific mode, like damping or stiffness, are altered. This type of control is often used to apply damping to the flexible modes of a mechanical structure [61]. An example of modal damping with IU-modules is given in Appendix B.3.

It is deemed beyond the scope of this research to apply true modal control to the Slider. It is possible to use additional sensors and/or observers [23] to separate the flexible modes from the rigid body modes. The sensors are currently not present on the reference frame and will have to be designed in. For implementing an observer, an accurate modal model of the Slider is required. One of the complications for this

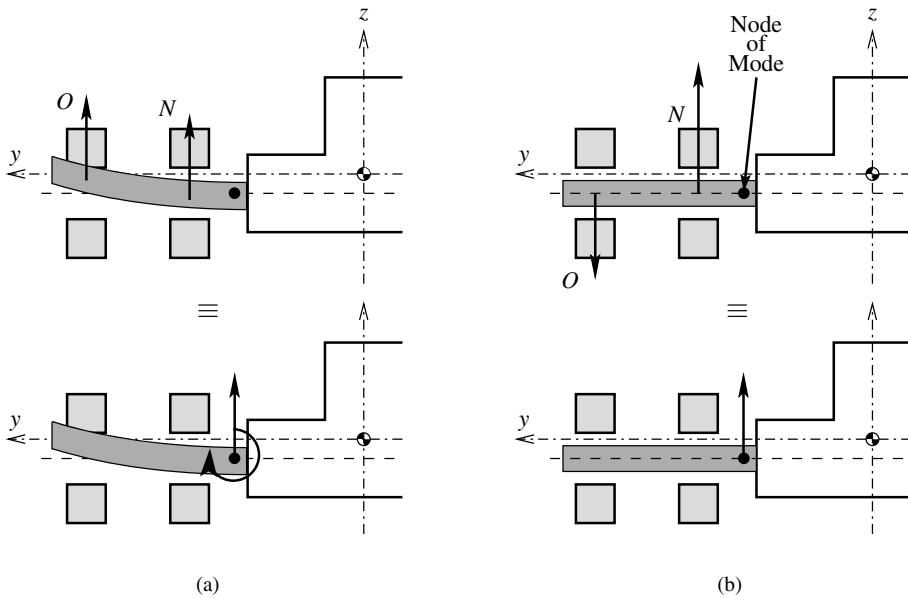


Figure 6.8: Conventional actuation scheme of the Slider, in which the flexible mode is excited (a). Mode Decoupled Actuation, the flexible mode is not excited (b).

model is, that the resonance frequencies of the different Slider bars do not exactly coincide. This is caused by differences in the clamping and glueing of the various Slider bars.

By applying modal observation, rigid body modes can be separately observed from the flexible modes. The control bandwidths of the rigid body modes can then be increased, since the flexible modes are not observable in this control loop. The separation can be performed with additional sensors or with an observer. The risk of not observing a flexible mode is that it is still excited, but not detected in the control loop. When the flexible mode has an influence on the performance of the system, performance is impaired without the control engineer detecting it.

The Mode Decoupled Actuation (MDA) is similar to actuation in the node of the mode, illustrated in Fig. 6.8. The MDA allows a specific mode not to be excited by the control loop. The flexible modes of the Slider are stable by themselves, and do not require stabilisation by a control loop. The flexible modes are even excited by the control loop, hereby deteriorating performance. By applying MDA, the flexible modes are rendered uncontrollable, and control bandwidths can be increased. If due to incorrect implementation of MDA, the flexible modes are excessively excited, frequency content of these modes will be present in the servo-error, and effective measures can be taken to reduce their excitation.

To realise the MDA on the Slider, the full 12×6 plant is measured. The transfer from the “inner”, $N(s)$, and “outer”, $O(s)$, actuator legs, shown in Fig. 6.8, to the CoG coordinates $(x_S, y_S, z_S, \phi_S, \gamma_S, \theta_S)$ contain the contributions of the rigid body modes and the flexible modes. Figure 6.9(a) shows the FRFs for the right actuator leg to x_S . The rigid body modes and flexible modes, present in the FRF are represented in the transfers, $O_{xr}(s)$ and $N_{xr}(s)$, Eq. 6.5-6.6.

$$O_{xr} = \frac{a_1}{m_{q,1} \cdot s^2} + \sum_2^m \frac{a_i}{m_{q,i}s^2 + d_{q,i}s + k_{q,i}}, \quad (6.5)$$

$$N_{xr} = \frac{b_1}{m_{q,1} \cdot s^2} + \sum_2^m \frac{b_i}{m_{q,i}s^2 + d_{q,i}s + k_{q,i}}. \quad (6.6)$$

The modal mass, $m_{q,i}$, modal damping, $d_{q,i}$, and modal stiffness, $k_{q,i}$, are independent of the application point of the force. The contribution factors, a_i and b_i , determine the contribution of a mode, excited by the inner and outer actuator legs, to the CoG-decoupled output. When the contribution factors, a_i and b_i , are scaled to be equal and opposite, the contribution of this mode is eliminated from the full transfer, $G_{xr}(s) = O_{xr}(s) + N_{xr}(s)$. The practical implementation of the MDA on the Slider, is performed along the following steps, and illustrated for the x -direction:

1. The transfer of each actuator leg to the global position error is plotted, as in Fig. 6.9(a). The most critical mode is then identified. In the case for the x -direction, the mode is at 1090 Hz.
2. A linear combination is made between each of the actuator legs to eliminate the first flexible mode from the transfer. At the eigenfrequency, the motion is dominated by the targeted flexible mode. The ratio between the different gains, ξ as depicted in Fig. 6.9(a), is approximately $\xi \approx \frac{a_2}{b_2}$. Because at the resonance frequency, the motion of the flexible mode dominates. The modal parameter $(m_{q,i}, d_{q,i}, k_{q,i})$ and measurement location of the mode are the same for both actuation points.
3. The MDA is formed by a linear combination of the “inner” and “outer” transfer, as given in Eq. 6.7. In Eq. 6.7, η is an added correction ratio to make sure the rigid body mode is actuated by the same amount as in the original CoG-decoupled situation, $(a_1 + b_1) = \eta \left(-\frac{1}{\xi} a_1 + b_1 \right)$.

$$G_{xr,MDA}(s) = \left(-\frac{1}{\xi} O_{xr}(s) + N_{xr}(s) \right) \eta. \quad (6.7)$$

In the MDA FRF of Fig. 6.9(b), the resonance peak at 1090 Hz to x_S is removed.

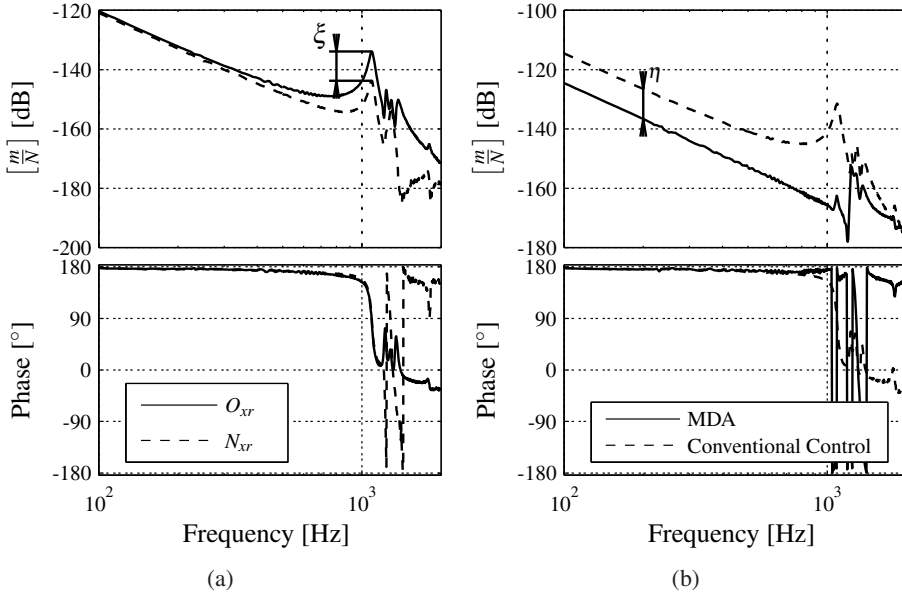


Figure 6.9: The measured transfer for the “inner” N_{xr} and “outer” O_{xr} right actuator leg of the Slider, to the x_S -coordinate (a), ξ is the difference between the gain at the mode. In (b) the transfer from the right leg under conventional control and the MDA is shown. Where, η is the gain difference between mode decoupled actuation and conventional actuation.

4. The previous steps are performed for each Slider leg towards each global coordinate.

To implement the parameters for MDA, the original propulsion actuation matrix, $\mathbf{T}_{act,p}$, and suspension actuation matrix, $\mathbf{T}_{sens,p}$, of Section 5.2.2 are extended towards a 12×6 matrix, by repeating each row. The first row acts on an outer leg, O , while each second repeated row, acts on an inner leg, N . The “inner” and “outer” rows are multiplied with the factors of Eq. 6.7, resulting in a new actuation matrix. This new actuation matrix is uploaded to the controller, when the Slider was already suspended.

Figures 6.10 and 6.11 show the resulting FRF for all global directions. The excitation of the first flexible modes decrease by a factor of at least 20 dB. The decreased influence of the flexible modes, allows the controllers in all directions to be adapted to the new situation, through which positioning performance can be improved. One of the limitations to the current implementation is that next to the intended forces, parasitic torques, disturbing the global actuator decoupling, are

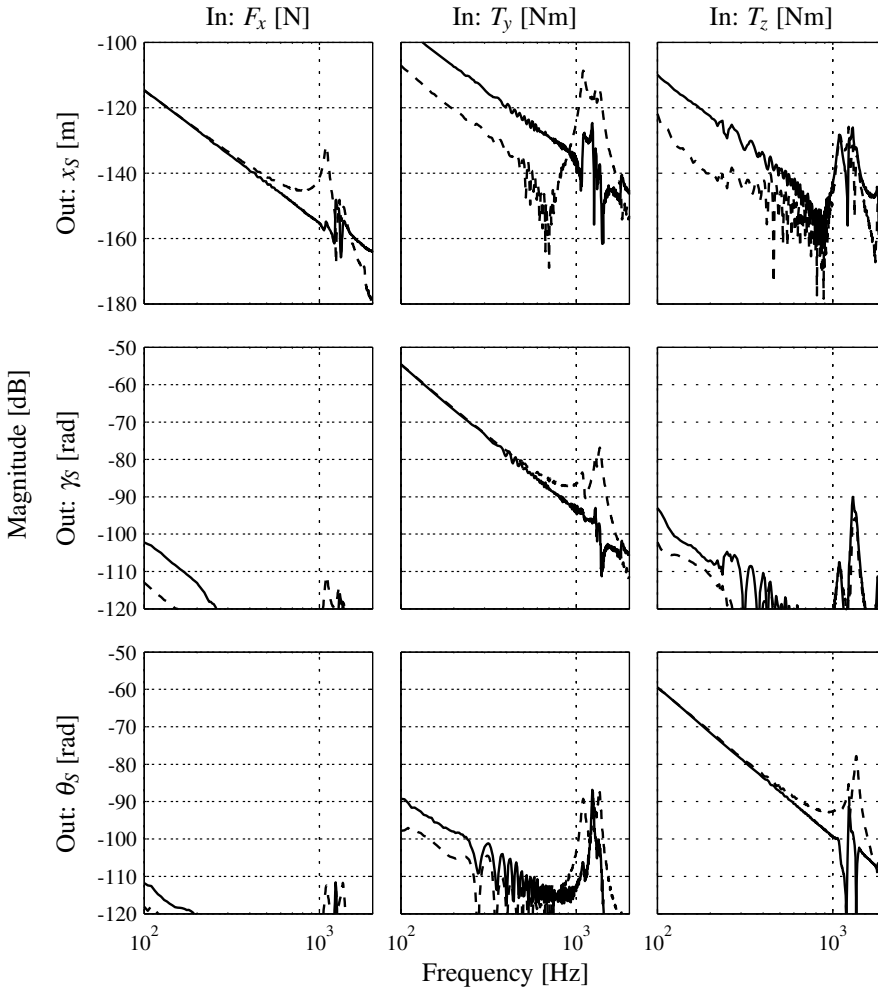


Figure 6.10: Conventional CoG-decoupled plant (---), and mode decoupled actuation (—) for propulsion directions.

introduced. Often these torques are cancelled, because of symmetry. For example, in the x -direction, the moments of the left and right actuator legs cancel. However, this is not the case for the top IU-module. Firstly, the additional torques result in additional coupling, between the geometric directions, where the top IU-module is used. This is visible in the FRF of x_S/T_y in Fig. 6.10. Secondly, the applied actuation scheme greatly reduces the maximum force which can be used to generate accelerations.

The original position controller for the x -direction (Section 5.2.5) has a notch to reduce the excitation of the modal resonance at 1090 Hz. This notch introduces

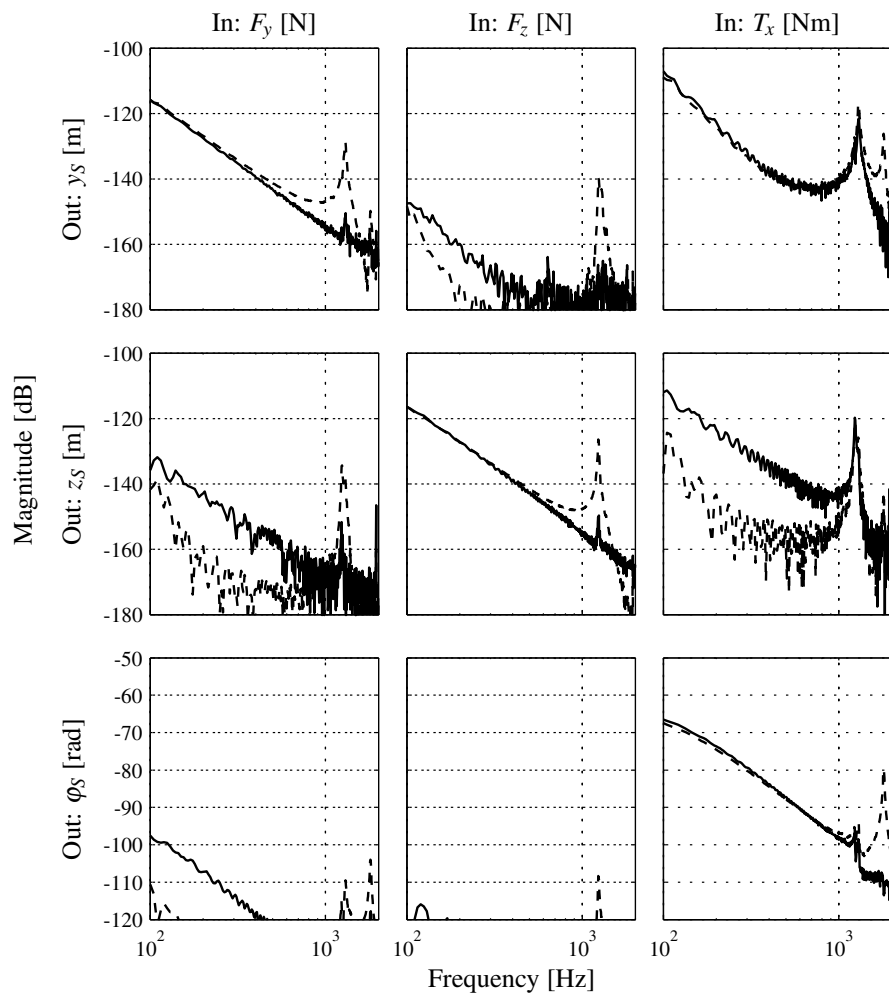


Figure 6.11: Conventional CoG-decoupled plant (---), and mode decoupled actuation (—) for suspension directions.

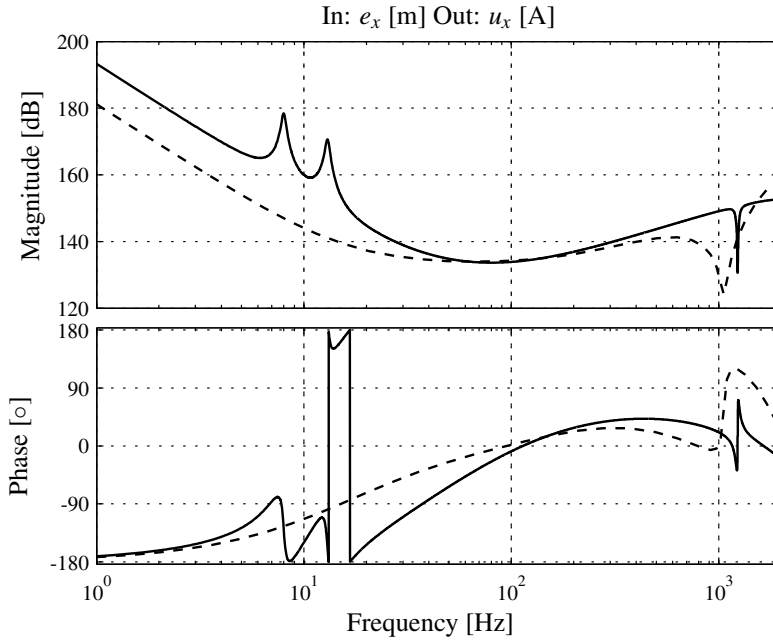


Figure 6.12: The x_S -controller for mode decoupled actuation scheme (—), and controller used for conventional CoG-decoupling (---). The open-loop bandwidth is increased from 400 Hz to 500 Hz.

phase lag in the crossover region at 400 Hz, limiting the phase margins. With these resonances modes decreased, the notch could be removed from the controller. This creates additional phase margin, allowing an increase of low frequency gain. By introducing additional inverse notches at 7 and 11 Hz, the suspension frequencies, of the granite base and the reference frame, are suppressed. Next to this, the open-loop bandwidth can be increased to 500 Hz. Figure 6.12 shows the conventional x_S -controller and the controller applied with MDA. The MDA and newly implemented controller for the x -direction result in a significantly improved performance of 58 pm (σ) at standstill. Figure 6.13 shows the CAS and CPS of e_x , for this controller. The servo-errors, e_y and e_z , remain the same and are not improved. With this result, the Slider is one of the most stable positioning systems, compared to those of Chapter 2.

6.3 Conclusions and remarks

Although many researchers have studied modal control, few experiments are reported where the positioning performance in a high accuracy positioning system is increased. By exploiting over-actuated control on the Slider, a performance improvement of a factor 2 is realised and a position stability of 58 pm is achieved. It

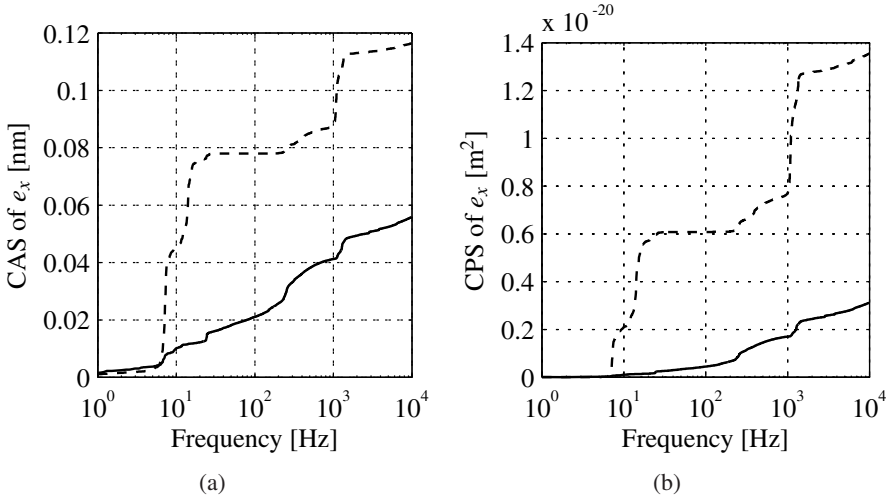


Figure 6.13: Propulsion servo-error, e_x , for the CoG-decoupled controller (---) and the MDA with improved controller (—), CAS of servo-error, e_x (a), CPS of servo-error, e_x . (b).

is clear, that the additional degrees of actuation of the IU-module can be applied to perform modal control. The applied implementation of modal control reduces the excitation of the flexible modes; the flexible modes are rendered uncontrollable. Even though this is only an initial step in modal control, significant performance improvement is achieved. Further study is required to determine the optimal control strategy for the over-actuated Slider. In future designs, using IU-modules, the ability to apply modal control, can be an integral part of the design.

A possible alternative application for modal control, is found in the inverted planar motors, described in Section 2.4, since these systems are heavily over-actuated. Another interesting application of modal control might be found in precision machines with conventional iron-less linear motors. The patent by Philips [1] explains how to use these linear motors as multi-DoF actuators. These motors are widely used, and combining them with modal control has the potential to improve existing positioning systems running in the field.

Chapter 7

Conclusions and recommendations

7.1 Conclusions

The main goal of the research was to determine, whether the IU-module is capable of fulfilling its promise as a modular vacuum compatible actuator for high precision positioning systems. To this end, the IU-module is evaluated separately using various modelling methods and measurements. The main conclusion is that the IU-module can be used as an integrated 4-DoF actuator. The actuator is capable of generating 2 forces and 2 torques. The actuator is only suitable in specific applications, where limited propulsion forces are required.

Next to this, a 6-DoF active electromagnetically suspended linear positioning system, initially using the IU-modules as 2-DoF actuators, is realised. This linear positioning system, the Slider, meets the demands of a linear motion system, applied in modern optical disc mastering equipment. In the propulsion direction a servo-error of 0.15 nm (σ) up to 10 kHz is attained, while the Slider moved at constant velocity. The suspension directions have a position stability of 3 nm (σ) up to 10 kHz. The Slider was designed using the “low stiffness” design concept, where the connection of the individual components to the world is minimised. An active control loop positions the high accuracy components relative to each other. The design was optimised using Dynamic Error Budgeting technique: the most relevant error sources for the suspension directions were the floor vibrations and the AD-conversion noise, while in the propulsion directions the interferometer and current amplifier were the largest contributors.

Since the IU-module is a 4-DoF actuator, the Slider is an over-actuated system. This over-actuation is applied to limit the excitation of flexible modes present in the Slider. In control technical terms, the modes are rendered uncontrollable. The reduced excitation of the flexible modes, allows the position controller to be improved.

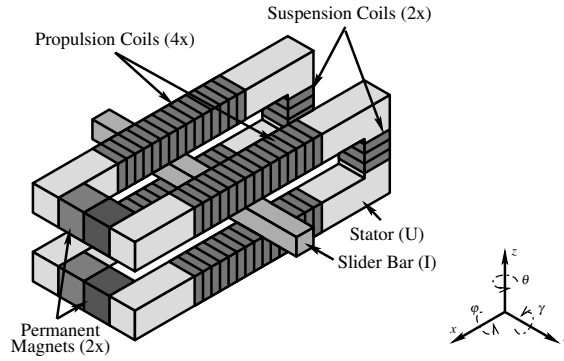


Figure 7.1: The IU-module.

The servo-error in the propulsion direction reduces by a factor of 2 to 58 pm (σ). The positioning results of the Slider show, that the IU-module is suitable as an actuator for a high precision positioning systems.

In the first part of this section, detailed conclusions about the IU-module itself, are summarised. In the second part, the performance of the Slider, using the IU-modules, is discussed.

Conclusions on the IU-module

The IU-module, see Fig. 7.1, is a 4-DoF actuator, capable of creating two forces, F_x and F_z , and two torques, T_x and T_z . The forces and torques can be generated without any wires connected to the moving body. The IU-module is an electromagnetically intricate actuator and is only applicable to situations where limited propulsion forces are required. The actuation of the propulsion, F_x , creates a significant disturbance on the suspension force, F_z . A prototype of the IU-module, the Slider-IU, is realised for integration into the Slider. The following conclusions can be drawn on the general IU-module and the Slider-IU:

Suspension force, F_z

In the suspension direction, a reluctance force is generated by the permanent magnets. This force can be applied to compensate for static loads without energy consumption, by placing the Slider bar in an offset position above the centre of the airgap. The control current, i_z , through the suspension coils allows the force on the Slider bar, F_z , to be manipulated, without crosstalk to the other actuation directions. Both the suspension stiffness, k_{zz} , and suspension actuation constant, h_{zz} , are constant over a considerable range of x and z -positions. This is verified by simulations and measurements. For the Slider-IU prototype the negative stiffness, $k_{zz} = -2.95 \cdot 10^3$ N/m and actuation pa-

parameter, $h_{zz} = 3.13 \text{ N/A}$ were measured. These remain constant (within 5%) over the range of $x = \pm 20 \text{ mm}$, $z = \pm 0.1 \text{ mm}$, and $i_{zz} = \pm 3.5 \text{ A}$.

Propulsion force, F_x

In the propulsion x -direction, the actuation force, F_x , is generated by running a current through the propulsion coils. The propulsion direction uses the “moving iron” concept [50], which ideally has a linear force to current relationship. However, the actuation constant of the Slider-IU, h_{xx} , is only constant up to an actuation current of approximately $\pm 1 \text{ A}$. Above this current, the actuation constant drops, dependent on the direction of the current and the x -position of the Slider bar. For the Slider-IU prototype, the actuation constant even disappears, $h_{xx} = 0$, at a propulsion current of $i_x = 3.5 \text{ A}$ and an x -position close to the permanent magnets. The reason for the drop in the actuation constant, is that the magneto motive force of the propulsion coils counteracts the permanent magnets. The stiffness in the x -direction, k_{xx} , is negligible.

One-way interaction exists from propulsion actuation, i_x , to the suspension force, F_z , when the Slider bar is in the out of centre z -position of the airgap. For extreme positions of the Slider-IU, the ratio between the actuated propulsion and suspension force becomes $|\frac{F_z}{F_x}| \approx 1$. This occurs when the Slider bar is at $z = 0.1 \text{ mm}$ from the centre of the airgap and close to the ends of the propulsion coils. To minimise this crosstalk, the Slider bar should be operated close to the centre z -position of the airgap.

The non-linearity of the actuation parameter, h_{xx} , and the interaction with the suspension direction can be modified by changing the electromagnetic design of the IU-module. It is demonstrated with finite element models, that when the Slider bar is saturated in its centre between the stator legs, the interaction and the non-linearity of propulsion actuation is decreased. The saturation in the centre of the Slider bar, does not degrade the linearity of the suspension force, F_z .

Actuation of torques, T_z and T_x

The IU-module is able to generate two torques, T_z and T_x . These capabilities were established using force measurements on the IU-module. The torques are generated by reversing the direction of the current in the coils on one side of the IU-module, compared to the actuation of propulsion and suspension force. The stiffness in these directions are $k_{\phi\phi} = -8.95 \text{ Nm/rad}$, and $k_{\theta\theta} = 0 \text{ Nm/rad}$. The actuation constants are $h_{\phi\phi} = 57.6 \cdot 10^{-3} \text{ Nm/A}$, and $h_{\theta\theta} = 11.9 \cdot 10^{-3} \text{ Nm/A}$. The actuation of these torques does not interact with the suspension nor the propulsion forces. When these torques can be usefully applied, there is no reason not to actuate them.

Modelling of the IU-module

Three modelling methods are used to predict the performance of the IU-module, a 1st-order model, a magnetic equivalent network model and a finite element model. The applied models are capable of predicting the force in an order of magnitude, but are not able to predict actuation and stiffness parameters exactly. Therefore, force measurements are still required to determine the exact performance of the actuator. Possible reasons for the mismatch between model and reality are the complexity of the non-linear problem and insufficient knowledge of parameter and dimension variations, like: small airgaps caused by the interconnection of the various components, stacking factors of the laminations, and the orientation of the magnetic materials.

Modularity of the IU-module

The IU-module is a complex actuator, where interactions and position dependency play a dominant role on its performance. This is especially true for the propulsion force, F_x . The properties of the actuator can be adapted by changing the electromagnetic design. However, this does not lead to a “simple” modular actuator, which can be easily adapted to each situation.

The IU-module can be best applied in situations, where only a limited propulsion force is required, to avoid introducing non-linearity and interaction. The actuator is generally capable of making larger forces in the suspension direction than in the propulsion direction, due to the nature of the electromagnetic forces. The electromagnetic design of the Slider should attend that the Slider bar operates close to the centre of the airgap to minimise crosstalk between the propulsion force, F_x , and suspension force, F_z .

The positioning performance of the IU-module will generally be better in the propulsion direction. In the propulsion direction, a low to zero stiffness is present minimising the transfer of disturbances. The IU-module has a position dependent crosstalk from propulsion force, F_x , to the suspension force, F_z . This means propulsion actuation forces, will disturb the positioning in the suspension direction. In addition to this, the suspension direction suffers from phase lag between actuation current, i_z , and generated propulsion force, F_z , due to eddy current and hysteresis losses. This phase lag limits the maximum achievable control bandwidth. In the propulsion directions, these eddy current losses are of less influence, and higher bandwidths can be achieved.

Conclusions on 6-DoF electromagnetically suspended Slider using the IU-modules

A magnetically levitated linear Slider, see Fig. 7.2, using IU-modules is realised. The Slider is designed to function as a linear Slider for an optical disc mastering system. A positioning performance of the Slider in the propulsion direction of 0.15 nm

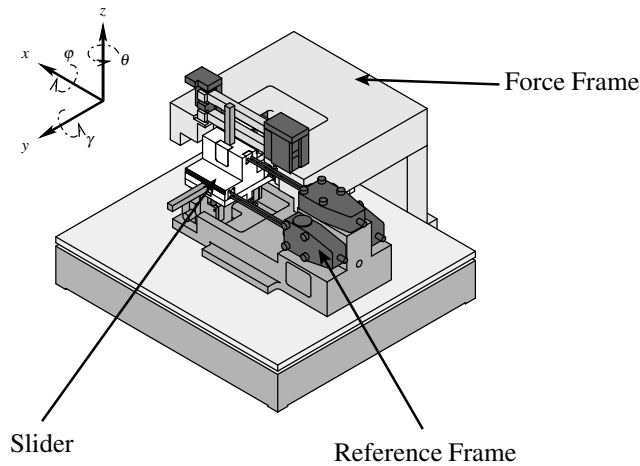


Figure 7.2: Cross-section view of the developed and realised Slider.

(σ) was achieved. The IU-modules are applied as 4-DoF actuators to suppress the excitation of flexible modes by the control loop. This resulted in a position stability in the propulsion x -direction of 58 pm (σ).

Performance of the Slider using a “low stiffness” design concept

Initially, each of the IU-modules generated a suspension and a propulsion force. The required x -position stability in a modern optical disc mastering application is 1 nm (σ) for the Slider to function. In the y and z -suspension directions, an error of 5 nm (σ) is allowed. The Slider has a stroke of 50 mm. The Slider is initially capable of achieving a servo-error in the x -direction of 0.12 nm (σ) at standstill, and 0.15 nm (σ) while moving. The y and z -suspension directions have a servo-error better than 3 nm over all x -positions. These servo-errors are measured between the vibration isolated reference frame and the Slider.

The performance of the Slider is evaluated, using the servo-errors of the system. The actual accuracy of the Slider differs from these servo-errors. In the servo-errors, slowly varying errors are not present, since these are suppressed by the controller. High frequent sensor noise is contained in the servo-error, but is not part of the positioning resolution of the Slider. The optical disc mastering application is tolerant to slowly varying errors. Therefore, it is plausible that the Slider is applicable in a modern optical disc mastering system.

The positioning result is achieved by separating the Slider and the reference frame from disturbance sources, originating in the environment. This is en-

sured by connecting both the Slider and the reference frame to the fixed world with a low stiffness. The Slider and reference frame are kept in relative position to each other, using an active position control loop (with a high stiffness). This overall conceptual design is known as the “low stiffness” design concept. A second advantage of this design concept, is that the actuation forces, generated by the active control loop, are guided to a separate force frame. Since the reference frame is isolated from this force frame, perturbations of the force frame, caused by the actuation forces, do not influence the relative measurement between the reference and the Slider.

The IU-module has a low stiffness connection in the propulsion direction, ideally suited for the “low stiffness” design concept. In the suspension direction the IU-module has a negative stiffness, allowing for the transfer of disturbances to the Slider. To minimise this undesired transfer, a control technical stiffness compensation is performed with respect to the force frame.

Design of the Slider

The Dynamic Error Budgeting design technique [33], facilitated the dynamic design of the magnetically levitated Slider. With this design technique the performance of the closed-loop system was evaluated and the right components were selected. The realised Slider was “first time right” and only minor changes had to be made afterwards. The complete design process of the Slider is illustrated in this thesis, allowing designers to follow the design steps, simplifying integration of the IU-modules in alternative designs.

Effect of the limitations of the IU-modules on performance of the Slider

The limitations of the IU-module fit the requirements of the Slider, when applied in the optical disc mastering application. In the propulsion direction, the IU-module has a non-constant actuation parameter, h_{xx} , as actuation currents increase. For the Slider this is not a significant drawback. The Slider operates at near constant velocity, requiring only limited propulsion forces.

The interaction of propulsion actuation to the suspension force in the IU-module, has limited implications on the Slider. Due to the layout of the Slider, the interaction acts from the accurate x -direction towards the less critical y and z -directions.

The transfer of disturbances, due to the negative stiffness, k_{zz} , of the IU-modules, are aligned with the less critical suspension directions. Next to this, the negative stiffness is compensated using a feedback loop with respect to the force frame, reducing its effects.

Slider performance limits

Currently, the main limits in performance of the Slider are not dominated by

the IU-modules directly. In the suspension and propulsion directions, improvements can be made by reducing the suspension frequency of the reference frame. The active vibrations isolation of the reference frame introduces disturbances at 400 Hz and is therefore currently left inactive.

The most significant contributors to the overall error is the electrical noise of the AD-conversion of the sensor signals. By applying averaging on the signals, the influence of this noise is already reduced, but it still remains one of the most significant error sources.

The suspension directions perform significantly better in the $x = 0$ -position than at the outer x -positions. At the $x = 0$ -position, the servo-error in y -direction is 1.2 nm (σ) and in the z -direction 0.8 nm (σ). At the outer positions of the x -stroke, both are approximately 3 nm (σ). The cause lies in a less effective stiffness compensation at the outer positions. The stiffness, k_{zz} , and actuator constant, h_{xx} , of the IU-modules are constant. However, the gain of the eddy current sensors shows a strong non-linearity. This non-linearity seems to be the cause of the limited performance of the stiffness compensation.

Over-actuated control on the Slider

Using the over-actuated capabilities of the Slider, the positioning performance is significantly improved. In the critical x -direction, the servo-error is reduced to 58 pm (σ). This is realised, by combining the actuation of the left and right actuator legs of the IU-module in such way that the forces acting on a specific flexible mode are cancelled, hereby reducing its excitation. This flexible mode is rendered uncontrollable and is not perturbed by the control loop. This allows the position controller to be improved. High frequency notches, present to suppress the excitation of flexible modes, could be removed. The elimination of the notches creates a better phase margin. This allows the bandwidth and low frequency gain of the controller to be increased, suppressing low frequent disturbances. The bandwidth of the controller is improved to 500 Hz. The drawback of the applied scheme is that the total active propulsion force, and the maximum achievable acceleration is reduced.

7.2 Recommendations

The recommendations are split up in three sections. First, recommendations are made for the improvement of the IU-module itself. In the second part, recommendations for the current Slider and its implementation in an actual optical disc mastering system are given. The third part, gives directions for alternative actuator research.

Recommendations regarding the IU-module

Study on the vacuum compatibility of the applied materials

Principally, the IU-module is a vacuum compatible actuator, since it neither requires lubrication nor a supply of air. The applied materials present in the Slider and IU-module, are not tested for their vacuum compatibility. Points of concern are the glue, with which the bars in the IU-module are glued, and the insulation of the electrical wire. To answer these questions, a study is required to determine which materials and coatings, applied in electromagnetic actuators, are vacuum compatible.

Improved electromagnetic model of the IU-module

There is a significant gap between the modelled forces and measured forces on the IU-module. A basic investigation will have to be performed to explain these differences. The Slider bars of the IU-module are built up from several separate bars. One of the most plausible causes for the difference is small airgaps, between in the interconnection of the different parts. When a better model is available, it will be possible to perform optimisation of the IU-module. One of the main goals of this optimisation can be the reduction of the interaction, while the actuation forces remain unchanged. Lebedev [44] addresses this further.

Recommendations on the Slider

Modal control study

The additional actuation capabilities of the IU-module allow modal control. In this thesis flexible modes are not excited to increase the positioning performance of the Slider. The performance is increased by a factor of 2, showing that a significant improvement can be achieved. The applied scheme, decreases maximum acceleration which can be attained. Next to this, the applied implementation couples the global DoFs. The effect of these drawbacks can be reduced by creating a more accurate model of the Slider and using this model to improve the implementation of the modal control.

Improved negative stiffness compensation

The stiffness compensation scheme, applied to reduce the influence of the negative stiffness in the suspension directions of the IU-modules, is less effective in out of centre x -positions. One of the reasons is the non-linearity present in the eddy current sensors. This can be improved by calibrating the eddy current sensors beforehand and compensating for the non-linearity. However, the ideal situation for the stiffness compensation, is that internal measurements of the Slider are used to determine the negative stiffness on all different positions. Identification techniques, maybe even non-linear tech-

niques as described in [53], might be applied to automatically improve the stiffness compensation.

Improvement of the reference frame vibration isolation

The currently applied vibration isolation reduces the low frequency disturbances, but deteriorates performance at higher frequencies. A redesign of this vibration isolation, making sure performance is improved over the entire spectrum, will improve the performance of the Slider. In this design, one of the aspects that should be addressed is the reduction of electromagnetic noise generated by the current amplifiers of the vibration isolation. Currently, this radiated electromagnetic noise disturbs the capacitive sensors, decreasing the performance of the Slider.

Towards implementation of IU-modules in optical disc mastering machine

Several steps have to be taken before the Slider can be incorporated in an actual optical disc mastering system. The design of the current Slider is mainly focussed on the suppression of dynamic errors. Slowly varying errors due to, for example, thermal effects, and sensor drift, are not considered during the design. Although the optical disc mastering application is relatively tolerant to these errors, they will have to be dealt with in an actual optical disc mastering application.

In the optical disc mastering system, a separate focus actuator has to be integrated. The focus actuator is situated on the Slider, and focusses the laser beam on the glass substrate, on which the pits are written. The focus actuator is an active component and will introduce disturbances, rendering the inclusion of a focus actuator non-trivial. The focus actuator requires a source of power. Since the Slider design is aimed to be fully wireless, it is preferable to use wireless energy transfer.

Alternatives to the IU-module

UO-module

The main limit of the IU-module is the crosstalk from the propulsion to the suspension direction and the non-linear actuation parameter, h_{xx} . An alternative design is the UO-module, see Fig 7.3. The UO-module is a 3-DoF actuator and has the ability to actuate F_x , F_z and T_y . The flux mechanism for the actuation of propulsion force, F_x , in the UO-module, is similar to the actuation of torque, T_z , in the IU-module. The actuation torque, T_z , in the IU-module does not have the crosstalk with the suspension direction and has a constant actuation parameter, $h_{\theta\theta}$. In [77], a proposal is done to integrate 2 UO-modules, placed at an angle, in the design of a Slider.

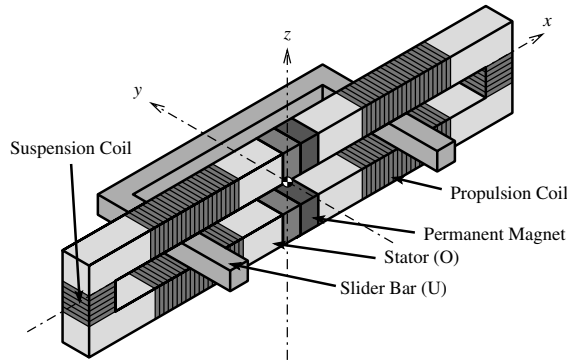


Figure 7.3: UO-module.

Seperate study of “moving iron” actuators

The “moving iron” concept of Molenaar [50], has been studied in this thesis combined with the suspension actuation of the IU-module. The limits of the IU-module, originate in the propulsion actuation using the “moving iron” concept. It will be of great interest, to separately study the “moving iron” concept. An example of a “moving iron” actuator is shown in Fig 7.4. The option of applying multiple short propulsion coils, to minimise crosstalk to F_z , can be incorporated. The separate study of the “moving iron” concept will result in a better understanding to the limitations and capabilities of the IU-module. Secondly, new applications and actuators using the “moving iron” concept might result.

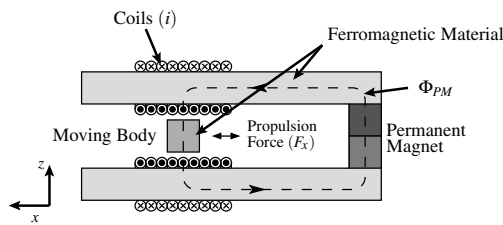


Figure 7.4: Example of a “moving iron” actuator.

Appendix A

Additional design information

In this appendix, additional information about the design of the Slider is summarised. The stiffness compensation is required for the Slider to obtain the desired performance. Since, the stiffness compensation is an active control loop, it will also introduce disturbances. This effect is discussed in appendix A.1. The interfacing of the laser interferometers with the dSPACE controller is illustrated in appendix A.2. In appendix A.3, measurements on the designed current amplifiers are shown.

A.1 Disturbances entering through the negative stiffness compensation

The Slider is based on the “low stiffness” design concept, discussed in Chapter 4. In the “low stiffness” design concept, the connecting stiffness between the environment and the high accuracy components is minimised, to reduce the transfer of disturbances. The IU-module has a significant negative stiffness in the suspension direction. To reduce the transfer of frame perturbations through this negative stiffness, it is compensated using an active feedback loop. Next to compensating the stiffness, the stiffness compensation loop introduces disturbances on the Slider. This appendix discusses these disturbances.

Figure A.1(a) shows the modelled CAS of the position-error, $(z_S - z_R)$, as discussed in Section 4.5. The most significant contributor to the error is the AD-converter noise. The AD-converter noise contains the quantisation noise and the electrical noise of the conversion. The AD-noise enters through the high performance control loop and the stiffness compensation loop. Figure A.1(b) shows the contributions of the AD-noise, of the left eddy current sensor and the left capacitive sensor, to the $(z_S - z_R)$ position error of the Slider. The eddy current sensor contributes through the negative stiffness compensation loop, while the capacitive sensor contributes through the position control loop. One fifth of the total energy of the AD-noise is contributed through the stiffness compensation loop, making this a

significant contributor to the $(z_S - z_R)$ position error.

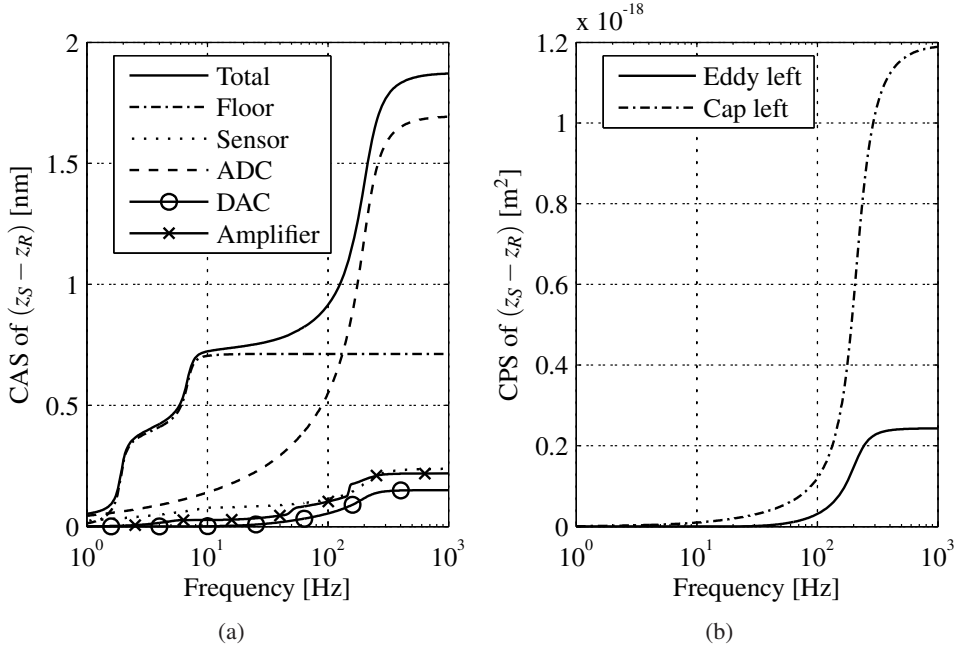


Figure A.1: The CAS of the $(z_S - z_R)$ -position error (a). Contribution of the left eddy current sensor and capacitive sensor to the CPS of $(z_S - z_R)$ (b). Contributions are computed with the model presented in Chapter 4.

When the negative stiffness of the IU-module is 2 times larger, the stiffness compensation loop will have to be improved to obtain the same level of reduction of the floor vibrations. Figure A.2(a) shows the total $(z_S - z_R)$ -error for the Slider system with a 2 times larger negative stiffness of the IU-modules. The negative stiffness is compensated to the same level as in Fig. A.1 to ensure the transfer of floor vibrations is reduced by the same amount. The total error of the system increases by 0.3 nm, for which the AD-noise is still the most significant contributor. In Fig. A.2(b), the origins of the AD-noise are shown. The contribution from the eddy current sensor is now as large as that of the capacitive sensor: the stiffness compensation loop is becoming the main source of error. The contribution to the final position error, $(z_S - z_R)$, of a single eddy current sensors is even larger than the contribution of the floor vibrations.

This shows that the negative stiffness of an actuator, applied in a “low stiffness” design concept, is preferably minimised. A larger actuator stiffness requires an improved stiffness compensation to reduce the transfer of environmental per-

turbations. This improved stiffness compensation increases the transfer of noise sources, present in the stiffness compensation loop, to the final position error. When the negative stiffness is left uncompensated, disturbances from the environment are transferred to the moving body, impairing performance. The negative stiffness, also deteriorates the performance of the position control loop, as it suffers from theoretical control limits for unstable systems, as discussed in [21].

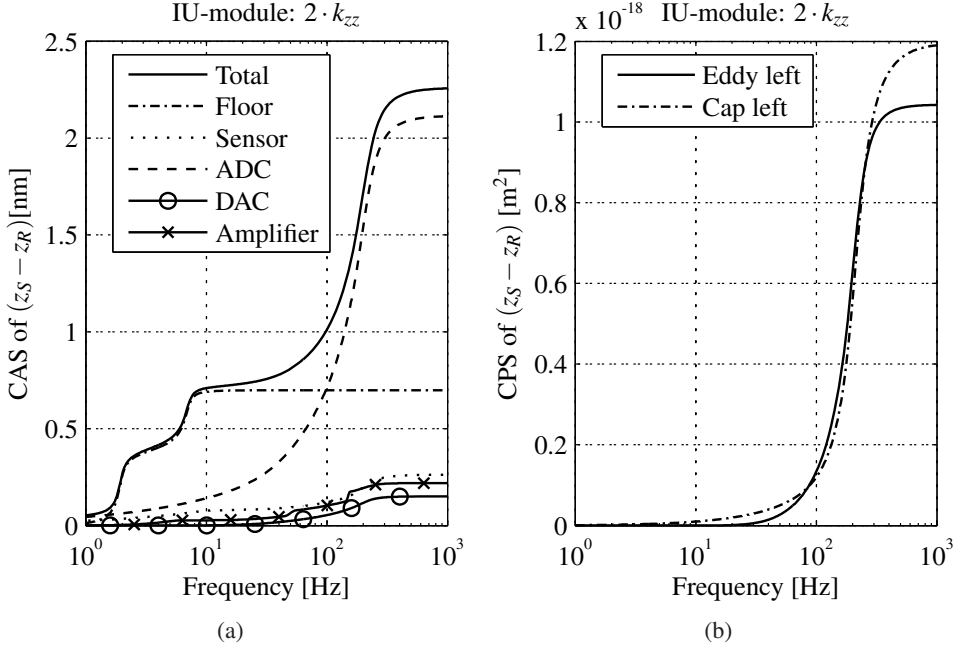


Figure A.2: The CAS of the $(z_S - z_R)$ -position error (a). Contribution of the left eddy current sensor and capacitive sensor to the CPS of $(z_S - z_R)$ (b). The IU-modules have a 2 times increased actuator stiffness, k_{zz} . The stiffness is compensated to the same level as in Fig. A.1.

A.2 Electronic connection of the RPI-20 board

The RPI-20 interpolation board for the Renishaw laser interferometer has a digital parallel 32 bit output. The size of one bit is approximately 38 pm. The boards are designed to be used in conjunction with a VME bus. The VME bus is not available for the dSPACE controller. To read in the position signals, a DS-4003, parallel input board is taken and the VME bus is mimicked, see Fig. A.3. Before the output can be read, several commands have to be send to the RPI-20. The DS-4003 board is much faster in reading signals than sending signals. Therefore, to generate these signals in a fast manner, an ADuC 7024 micro-controller board is placed in between the DS-4003 and the RPI-20. The DS-4003 sends a request for data to the ADuC board through an interrupt line. The ADuC 7024 micro-controller then generates the required sequence for the RPI-20, simulating a VME bus. Finally, the RPI-20 sends the data to the DS-4003 board. It is also possible to let dSPACE generate the sequence for the RPI-20, but this requires significantly more computation time. The freed time, can be used to average the sensor signals.

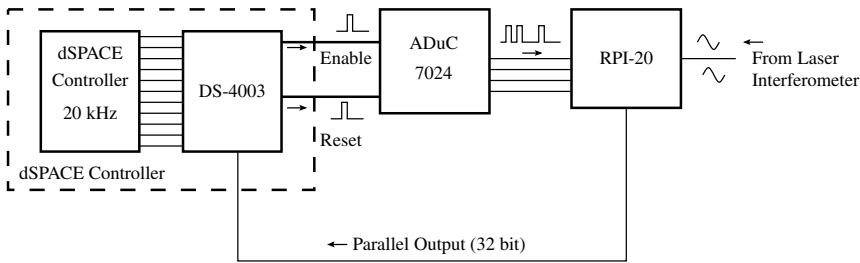


Figure A.3: Schematic of the RPI-20 read-out. The ADuC board mimics the VME bus.

A.3 Amplifier transfers

The FRF of the developed current amplifier, presented in Section 4.4.4, is shown in Fig. A.4. The measurement is performed with the amplifier connected to a propulsion and a suspension coil of the Slider-IU. The measurement is performed with a Tektronix current probe.

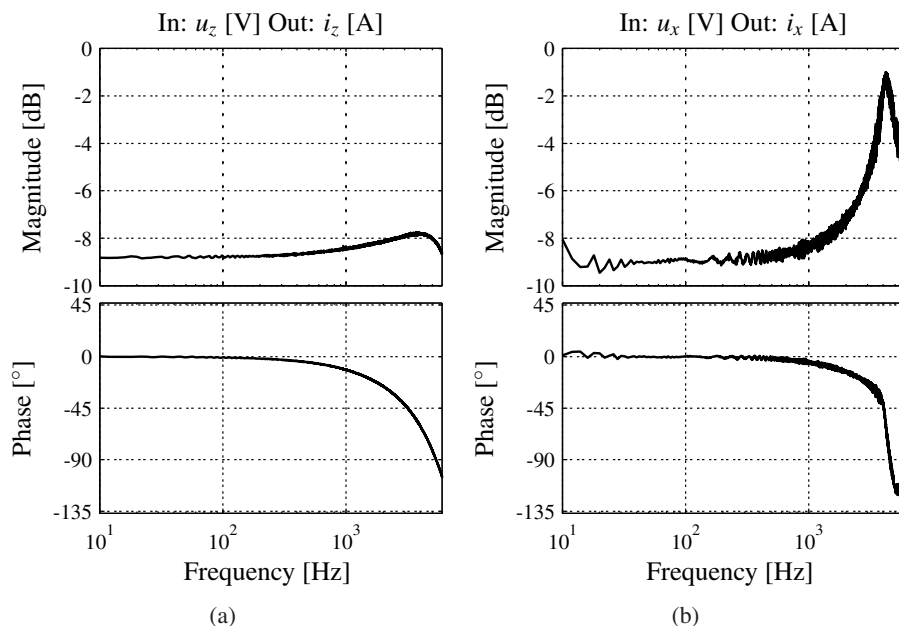


Figure A.4: Measured Bode diagram of the linear current amplifiers from amplifier set-point, u , towards coil current, i . The FRF of the amplifier connected to one of the suspension coils (a), and connected to a series connection of a top and bottom propulsion coil (b). The gain of the amplifier 0.36 A/V.

Appendix B

Additional experimental results of the IU-module

In this appendix, 2 realised test setups of the IU-module are discussed. The first test setup is the IU-demonstrator. The design of this setup is described in [76]. The sizes of the magnetic circuit are similar to that of Molenaars PAMB [50]. The second, is the Baby-IU which has smaller dimensions, and on which the Slider-IU is based.

B.1 The IU-demonstrator

The IU-demonstrator, described in [76], is build to prove the concept of the IU-module. The IU-demonstrator served as the first test platform for further development of the IU-module. The dimensions of the stator and Slider bars are taken to coincide with the PAMB setup [50]. This allowed faster manufacturing time, because equipment, such as the glue mold, could be reused. Testing upon the PAMB was not possible, because it was dysfunctional.

Table B.1 shows the overall dimensions of the IU-demonstrator. The stroke in propulsion x -direction is 100 mm. To facilitate this, the propulsion coils are made 120 mm in length. The stroke in suspension z -direction is 1 mm. The stroke of the IU-demonstrator in z -direction is less than the combined airgaps (2.2 mm), since the propulsion coils occupy a portion of the airgap.

A force measurement setup is added to the IU-demonstrator, to determine the actuation forces in the suspension and propulsion directions. The results of these measurements are discussed in Section B.1.1. An auxiliary bearing is added to realise a dynamic positioning system. The control design and performance of this dynamic setup are discussed in Section B.1.2.

Slider bar	length height width	240 mm 20 mm 20 mm
Stator	length height width clearance	200 mm 20 mm 20 mm 40 mm
Magnet	length height width material supplier	10 mm 63 mm 36 mm NdFeB-BM35 Bakker Magnetics
Suspension coils	turns wire diameter	50 & 100 & 200 0.5 mm
Propulsion coil	turns length wire diameter	211 120 mm 0.5 mm
Airgap	height	1.1 mm
Stroke	x -direction z -direction	100 mm 1 mm
Lamination	thickness material supplier	0.27 mm PowerCore C 130-27 Smit Transformatoren

Table B.1: Properties of the IU-module demonstrator.

B.1.1 Static force measurements on the IU-demonstrator

Static force measurements are performed on the IU-demonstrator to determine the forces acting on the Slider bar. During this measurement, the Slider bar is held by externally mounted strain gage force sensors. The force measurement setup is shown in Fig. B.1. The strain gage force sensors, type S9 supplied by HBM, are available from the research of the PAMB. The IU-demonstrator's stiffness constant, $k_{zz} = -2.8 \cdot 10^5$ N/m, and actuator constant, $h_{zz} = 0.28$ N/(A–turns), are determined using the measurements shown in Fig. B.2. The actuation constant, h_{zz} , of the IU-demonstrator is given in A–turns, because the suspension coils consist of several smaller coils, which can be connected in series.

The static force measurement, shown in Fig. B.2, displays a third order effect. This third order effect can be explained, using the 1st-order analysis of Section 3.1 and expanding the terms in the force equation. However, a reservation on the accuracy of the force measurement should be made. The force measurement setup holds

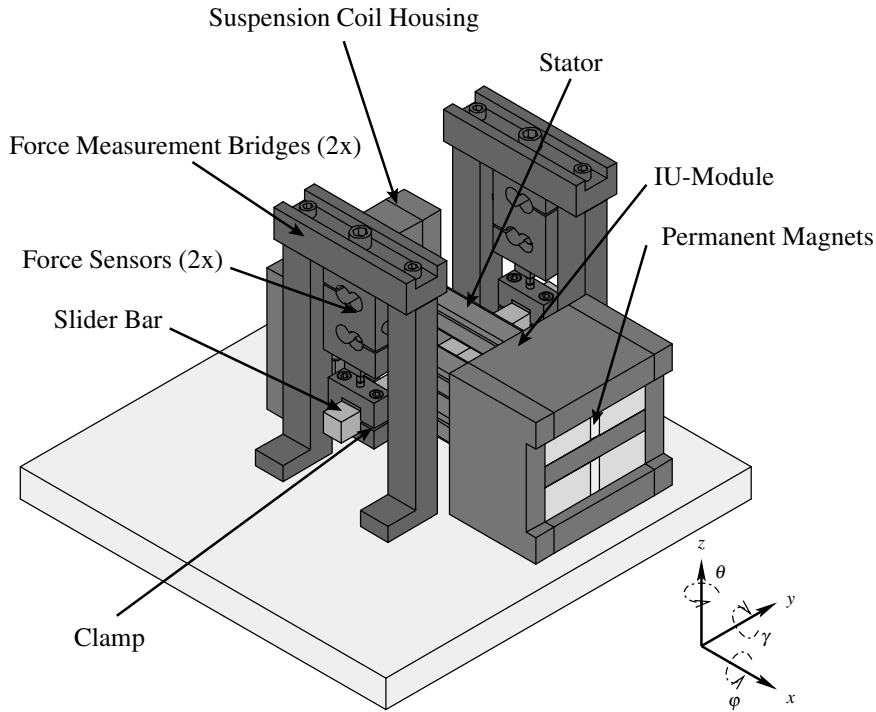


Figure B.1: Force measurement setup for the IU-demonstrator, capable of measuring suspension force, F_z , versus z -displacement and suspension actuation, i_z .

the Slider bar in an over-determined manner. This is clearly not ideal for measuring forces, and makes the measurement result unreliable. The measurement setup of the Baby-IU, presented in Section 3.3, holds the Slider bar in one position, resulting in a more reliable measurement.

The propulsion force, F_x , is measured using a quasi-static force measurement on the dynamic setup of Section B.1.2. The Slider Bar is actively suspended in z -direction, while leaving the propulsion x -direction uncontrolled. A strain gage force sensor is placed next to the Slider bar. By passing current through the propulsion coils, the Slider bar pushes against the strain gage force sensor and the force, F_x , can be measured. The result of the measurement is shown in Fig. B.3.

The crosstalk from propulsion actuation, i_x , to the suspension force, F_z , is also established in [78]. An exact map of the crosstalk for the IU-demonstrator is not made, due to limited capabilities of the force measurement setup.

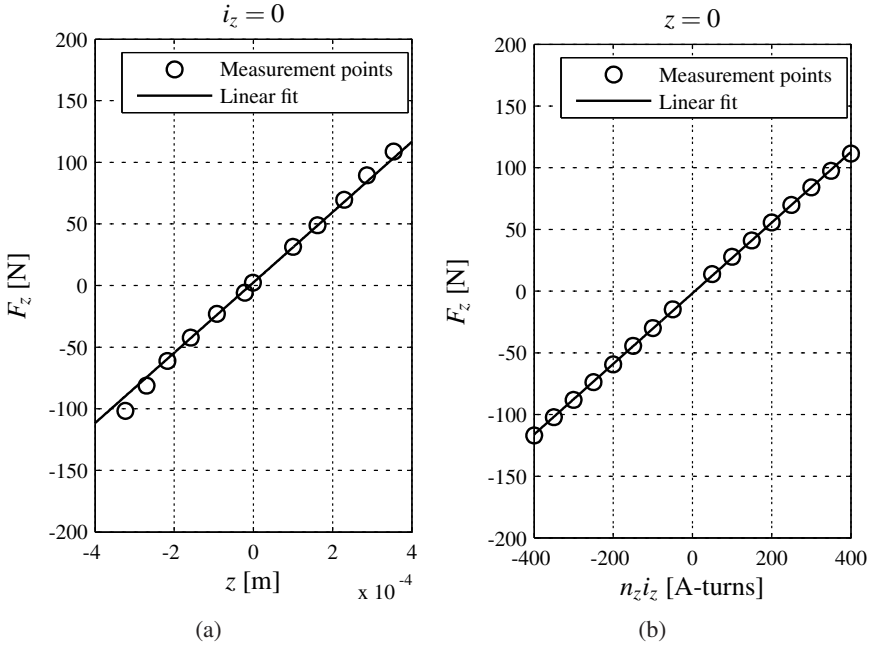


Figure B.2: Force measurements on the IU-demonstrator in the z -direction. Suspension force, F_z , versus z -displacement (a), and suspension force, F_z , versus current, i_z , with n_z is the number of suspension coil turns (b).

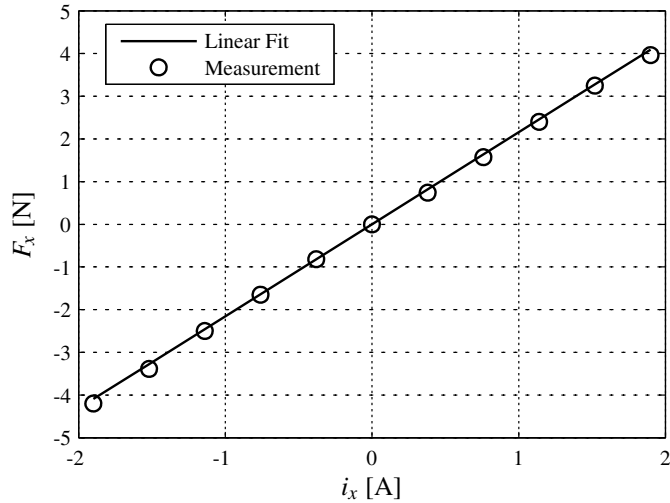


Figure B.3: Measurement of the propulsion force, F_x , versus propulsion current, i_x .

B.1.2 Dynamic results of the IU-demonstrator

An auxiliary bearing is added to the IU-demonstrator, to allow dynamic positioning. The designed setup is shown in Fig. B.4. The air bearings leave the φ and x -DoF unconstrained. Due to the relatively long Slider bar, the φ -DoF allows for a displacement in the z -direction at the location of the IU-demonstrator.

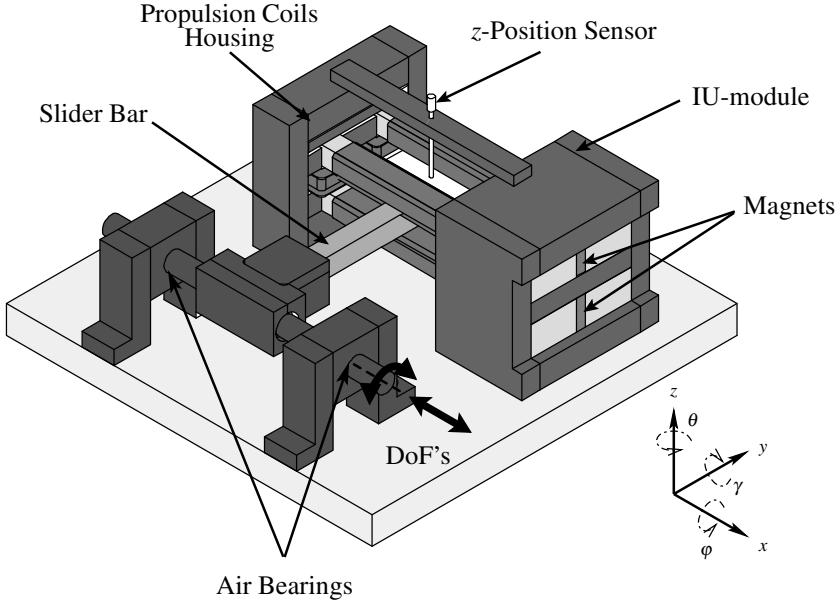


Figure B.4: IU-demonstrator with air bearings, leaving x -direction and φ -angle unconstrained.

To measure the z and x -position of the Slider bar, position sensors are added to the setup. A Philtec photonic sensor measures the z -position. This sensor type sends out light through a fibre, and measures the amount of reflected light. The reflected light is a measure for the distance between the sensor and the reflecting target. As a target for the sensor, a reflecting surface is attached to the Slider bar in between the stator legs. The measurement location is near-coincident with the location of the generated suspension force, F_z . This leads to a simplified controller design, due collocated [47] actuator and sensor placement.

To measure the x -direction, a linear encoder from MicroE, type M3500, is used. The sensor is placed underneath the clamp holding the Slider bar, minimising parasitic z -displacements. The sensor has a mounting tolerance of only ± 0.15 mm in z -direction. The sensors are read in with a dSPACE digital controller (DS-1005).

The current to the coils is supplied using 4 Philips switched mode DCPA50/2 amplifiers, left from the PAMB research. The top and bottom propulsion coils, on

each side of the IU-module, are connected in series, to limit mutual induction with the suspension coils. A suspension coil generates a varying flux path through the propulsion coils, see Fig. B.5. This varying flux induces a voltage in the propulsion coils, which has to be countered by the amplifiers connected to them. If the top and bottom propulsion coils are connected in series, the induced voltages on the top and bottom side cancel. Connecting the top and bottom propulsion coils to separate amplifiers, resulted in a close to unstable system with very poor positioning performance.

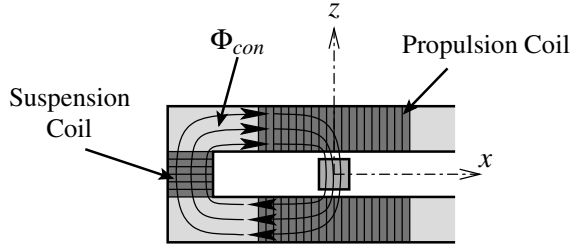


Figure B.5: Flux path of the suspension coils, Φ_{con} , inducing voltages in propulsion coils. This effect is minimised, when the top and bottom propulsion coil are connected in series.

The simplified description of the z -suspension direction, given by Eq. B.1, includes the dynamics of a rigid body. In Eq. B.1, the negative stiffness is k_{zz} , the actuation constant is h_{zz} , the length of the Slider bar is l_{bar} , the mass moment of inertia around the air bearing is $J_{x,b}$, and the rotation angle around the x -axis of the bearing is ϕ_b . The measured, z -displacement, at the location of the IU-demonstrator is equal to $z = \phi_b \cdot l_{bar}$.

$$J_{x,b} \ddot{\phi}_b = -k_{zz} l_{bar}^2 \cdot z + l_{bar} \cdot h_{zz} i_z, \quad (B.1)$$

$$\frac{z(s)}{i_z(s)} = \frac{l_{bar}^2 h_{zz}}{J_{x,b} s^2 + l_{bar}^2 k_{zz}}. \quad (B.2)$$

The IU-module, described by Eq. B.2, can be controlled using a PD controller. However, a significant steady state error can remain, due to the negative stiffness. Integral action can be added to remove this steady state error. Figure B.6 shows the measured open-loop FRF of the IU-module in the suspension and propulsion directions. The open-loop bandwidth in the z -direction is 210 Hz and the bandwidth in the x -direction is 60 Hz. In the propulsion direction, a notch is added to suppress the dynamics, caused by air bearings at 250 Hz.

The achieved servo-error is 1 μm for the suspension direction and 0.3 μm for the propulsion direction. The largest disturbance source in the suspension is the

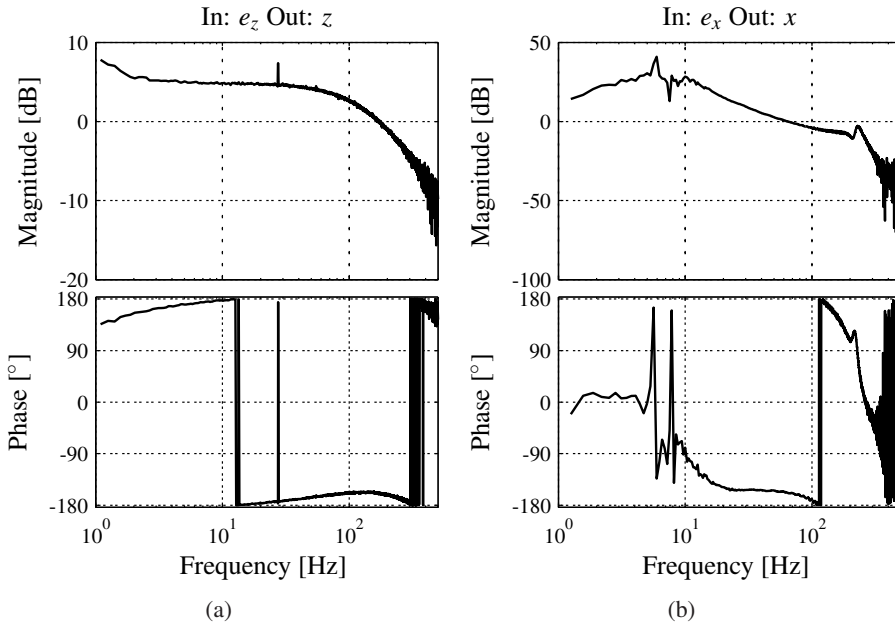


Figure B.6: Bode diagram of the open-loop FRF of the suspension (a), and propulsion (b) of the IU-demonstrator.

photonic sensor, which picks up a relatively large amount of noise from surrounding light sources. The IU-demonstrator is over-sized, in terms of forces and size, for the Slider of Chapter 4. Therefore, the Baby-IU module is developed.

B.2 The Baby-IU setup

The IU-demonstrator of Appendix B.1 is over-sized for the optical disc mastering application of Chapter 4. To this end, the Baby-IU, having less large actuation forces and smaller dimensions, is developed. In Chapter 3, the electromagnetic design and the static force measurements of the Baby-IU setup are discussed.

In Appendix B.2.1, the design of the dynamic Baby-IU setup is presented. In this design, the IU-module is applied as a 2-DoF actuator used to generate a suspension force, F_z , and a propulsion force, F_x . These actuation forces, together with position sensors and the controller, are used realise a dynamic 2-DoF positioning system. In Section B.2.2, the plant and the controller design are discussed. As is demonstrated in Chapter 3, the IU-module has the ability to actuate 2 additional torques. In Chapter 6, these additional DoFs are used reduce excitation of flexible modes. An alternative is to apply active damping to the flexible modes. In Appendix B.3, modal damping is applied to flexible modes present in the Baby-IU setup.

B.2.1 Design of the dynamic Baby-IU setup

A schematic of the Baby-IU setup is shown in Fig. B.7. The Baby-IU setup is primarily developed, to evaluate IU-module as a 2-DoF actuator [42]. Therefore, 4-DoFs are constrained using an auxiliary bearing. The designed bearing is a combination of a Schneeberger linear ball bearing and a plate spring parallel guide. The ball bearing allows for motion in the propulsion x -direction, see Fig. B.7. The plate spring parallel guide allows for motion in the suspension z -direction. The plate spring parallel guide does not have any friction, allowing better investigation of the suspension direction and the behaviour of the reluctance force. To minimise the influence of the positive stiffness of the plate springs on the suspension direction, this z -stiffness is kept below 10% of the negative stiffness of the IU-module.

To measure the z -position an eddy current sensor, the Micro-Epsilon NDCT 3700, is applied. This sensor is applied, because of its high resolution (1.3 nm (σ)) and its large range (1 mm). The eddy current sensor measures the change in inductance, due to eddy currents induced in a conducting target. The eddy current sensor is not placed collocated with the actuation force, but slightly to the side of the Slider bar. This is a realistic position in case of an actual application, where several IU-modules fully support a free floating body, as for example the Slider. The propulsion position is measured using a MicroE linear encoder. The choice for this encoder is made, because it allows a large perpendicular stroke and has relatively large mounting tolerances. The applied linear encoder has interpolated increments of 80 nm. The Baby-IU has the ability to exchange Slider bars, so that different materials can be tested.

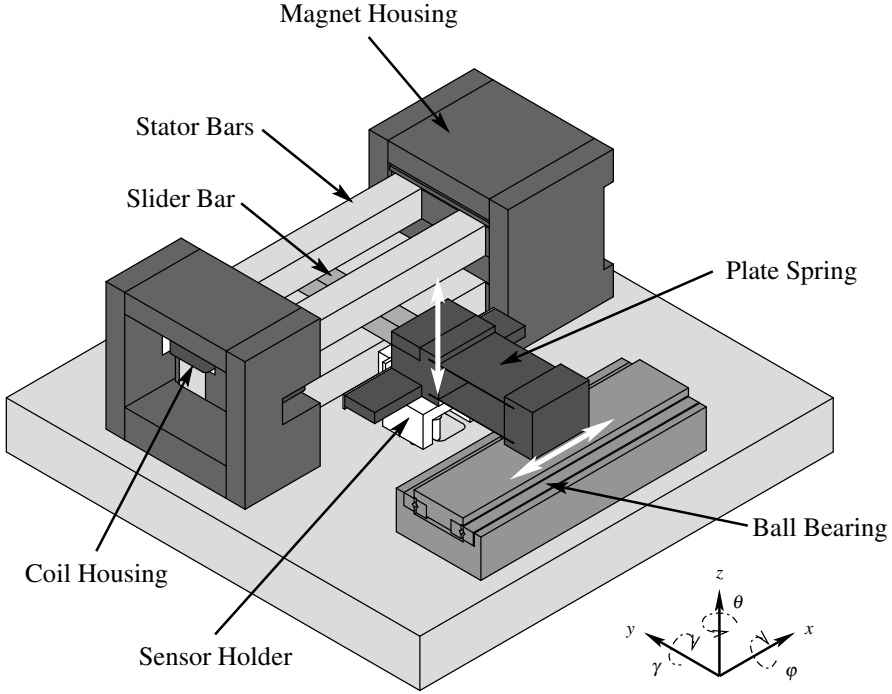


Figure B.7: Baby-IU, dynamic setup.

B.2.2 Dynamic measurement results of the 2-DoF Baby-IU

In first part of this section, the FRF measurements of the Baby-IU are discussed. The second part of this section discusses the positioning performance of the Baby-IU.

Baby-IU plant and controller

Figure B.15 shows the plant transfer, $\mathbf{G}(s)$, together with a mass-spring model of the Baby-IU setup. The model of the IU-module is constructed as a rigid body mass-spring system, $\mathbf{M}_g \ddot{\vec{x}}_g + \mathbf{K}_g \cdot \vec{x}_g = \vec{F}_{act}$, where the stiffness matrix, \mathbf{K}_g , and actuator vector, \vec{F}_{act} , are established using the static measurements of Section 3.3.2.

Since, a magnetic bearing is open-loop unstable, the open-loop FRF can only determined by closed-loop measurements. The open-loop is reconstructed using a measurement of the plant sensitivity, $\mathbf{S}(s)$. The open-loop plant transfer is then computed using $\mathbf{G}(s) = \mathbf{S}(s)^{-1} - \mathbf{I}$. The known controller is then subtracted to obtain the plant, $\mathbf{G}(s)$.

The FRF of the plant, $\mathbf{G}(s)$, and the mass-spring model correspond well on the diagonals. A simplified description of the behaviour in the suspension z -direction is

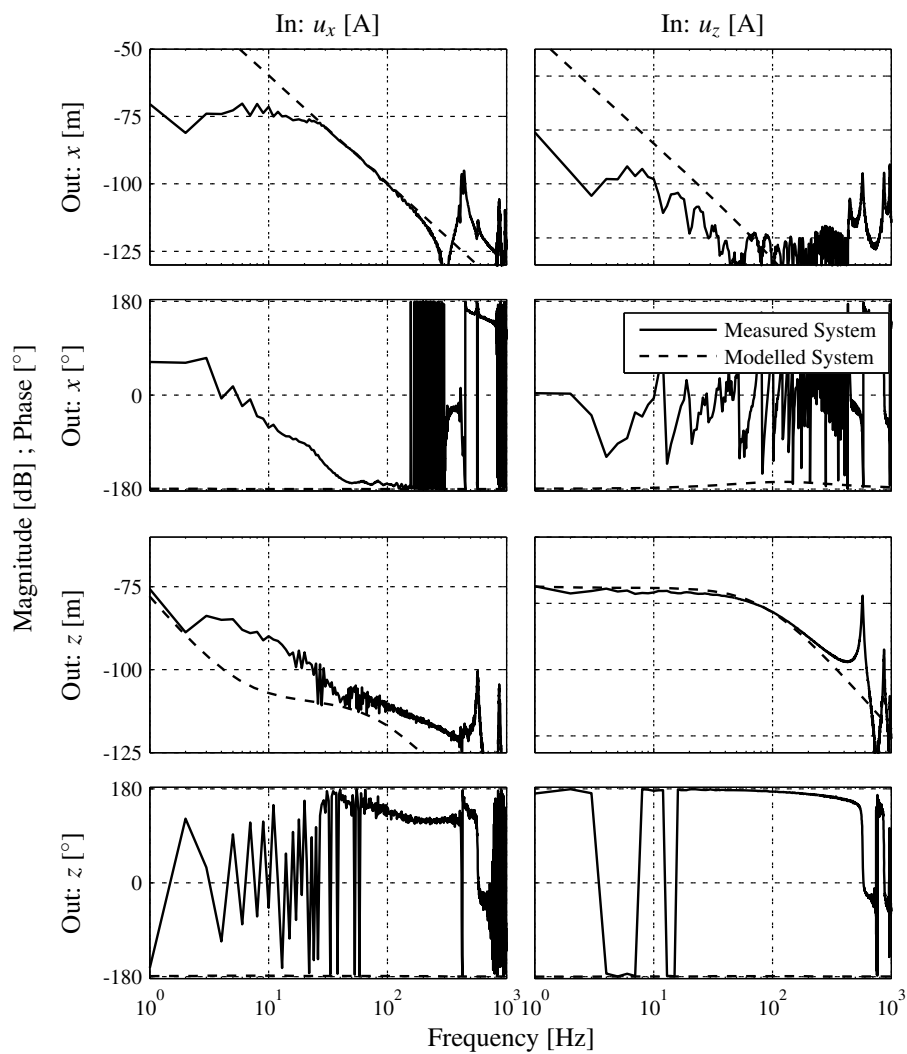


Figure B.8: FRF of Baby-IU plant $G(s)$, from controller output, u_x and u_z (scaled to represent current), to the measured x and z -position.

described by Eq. B.3.

$$\frac{z(s)}{i_z(s)} = \frac{h_{zz}}{m \cdot s^2 + k_{zz}}. \quad (\text{B.3})$$

The transfer function in the suspension z -direction, Eq. B.3, is similar to that of a conventional mass-spring system, except for the spring stiffness, which is negative. The Bode diagram from Fig. B.8 has a flat response up to $f = \frac{1}{2\pi} \sqrt{\frac{k_n}{m}}$ and then rolls off with a -2 slope. The model in x -direction is that of a single mass ($\frac{x(s)}{i_x(s)} = \frac{h_{xx}}{m \cdot s^2}$). The transfer in the propulsion direction differs from the model in the region below 20 Hz, most probably due to stiffness and friction present in the ball bearing guide. The resonances at 450 Hz in propulsion direction and at 560 Hz in suspension direction, are caused by flexible modes of the plate spring bearings. At these resonance frequencies, the interaction between the propulsion and suspension directions increases.

To get a better insight the interaction, the Relative Gain Array [66] defined as: $\text{RGA}(\mathbf{G}) = \mathbf{G} \times (\mathbf{G}^{-1})^T$ of the plant $\mathbf{G}(s)$ is given in Fig. B.9. For a decoupled plant, the RGA is close to the identity matrix. In Fig. B.9, the RGA is close an identity matrix up to 300 Hz. Above this frequency, the flexible modes of the mechanical structure cause interaction. The RGA indicates that the control loops of the Baby-IU can be independently designed for bandwidths below 300 Hz. The designed controllers for the Baby-IU are shown in Fig. B.10.

The static interaction from the propulsion to the suspension direction, present in the IU-module, is static one-way interaction. Such static one-way interaction does not change the pole locations of the system under feedback, compared to the same system without interaction, when a diagonal controller is applied [10]. This means that the suspension and propulsion control loop can be designed independently, without risking instability. However, loss in performance will be present.

Compared to the static model, additional interaction occurs above 600 Hz from suspension force, F_z , to propulsion, x -position. Next to the flexible modes, there might be a problem caused by mutual induction from the suspension to the propulsion coils in combination with non-ideal current amplifiers. The DCPA50/2 amplifiers used in the Baby-IU setup, are later replaced by the linear current amplifiers, discussed in Section 4.4.4.

Positioning performance of the Baby-IU

The Baby-IU realises a servo-error of 136 nm (σ) in z -direction, and of 32 nm (σ) in the x -direction. The Cumulative Amplitude Spectra, defined in Section 4.1.1, for both directions are shown in Fig. B.11. A Dynamic Error Budget of the Baby-IU was made in [12]. This showed that the position error in the propulsion direction, is dominated by the electrical noise in the AD-converter, while the servo-error in

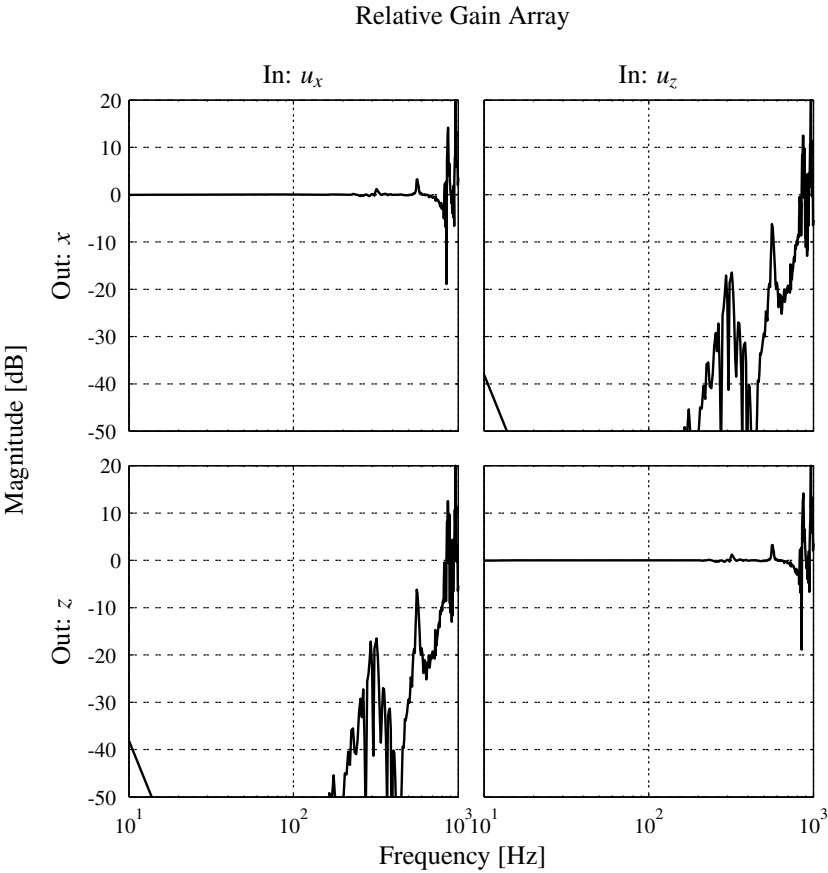


Figure B.9: Relative Gain Array the plant, $G(s)$, of the Baby-IU.

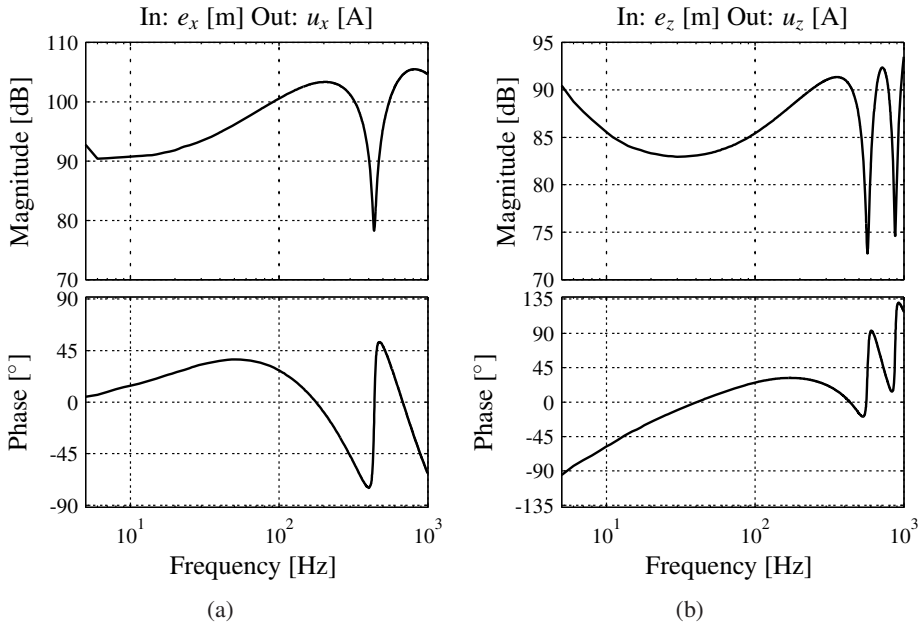


Figure B.10: The controller for the x -direction, realises an open-loop bandwidth of 90 Hz (a). The controller for the z -direction, realises an open-loop bandwidth of 200 Hz (b).

propulsion direction is dominated by quantisation noise originating in the linear encoders.

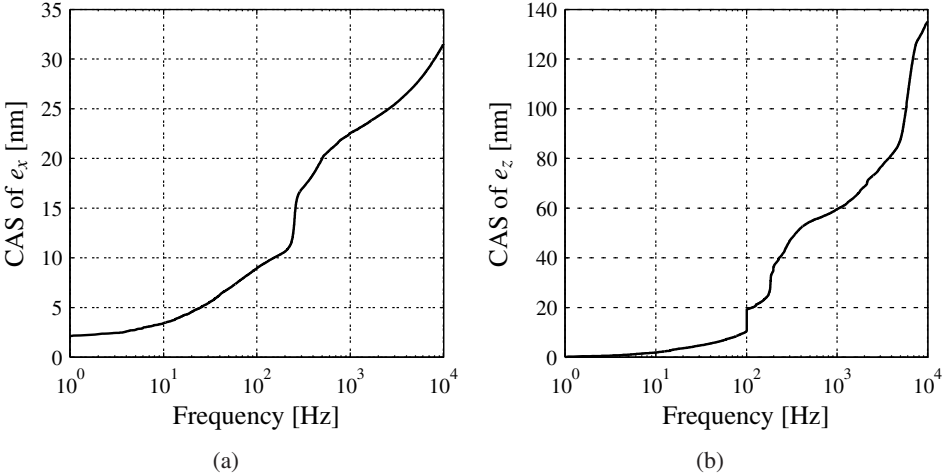


Figure B.11: Cumulative Amplitude Spectra of the propulsion servo-error, e_x (a), and the suspension servo-error, e_z (b), of the Baby-IU.

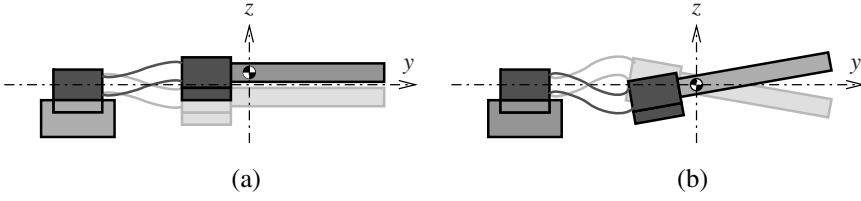


Figure B.12: Modeshapes of the Baby-IU in suspension z -direction, linear mode- q_z (a), rotational mode- q_ϕ (b).

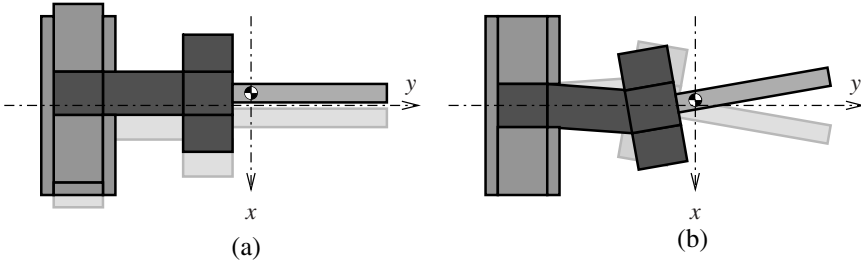


Figure B.13: Modeshapes of the Baby-IU in propulsion, linear mode- q_x (a), rotational mode- q_θ (b).

B.3 Modal control applied to the Baby-IU setup

The Baby-IU setup suffers from flexible modes, caused by the plate spring bearings, see Fig. B.12-B.13. The additional degrees of actuation of the IU-module allow modal control. A study on modal damping of the flexible modes in the Baby-IU, is conducted in [77]. A summary of the results in the suspension z -direction are given in this appendix. The applied method differs from the modal control of Chapter 6. In Chapter 6, the flexible modes are not excited, while here active damping to the flexible modes is applied.

The mode in the suspension direction limits the stability margins, due to the minus -180° phase shift at the resonance mode, see Fig. B.15. To damp this flexible mode, the angular position, q_ϕ , or its velocity is required. The Baby-IU does not have additional sensors, capable of separately measuring this flexible mode. Therefore, a linear observer reconstructs q_ϕ . The observer approximates the modal co-ordinates, q_z and q_ϕ , with estimates \tilde{q}_z and \tilde{q}_ϕ , see Fig. B.14.

The model on which the observer is based, is constructed using a lumped mass-spring approximation. The plate springs are assumed to be a mass-less springs, while the Slider bar and its holder are assumed to be a single rigid body with a translational and a rotational DoF. The actuator constants are taken from the static

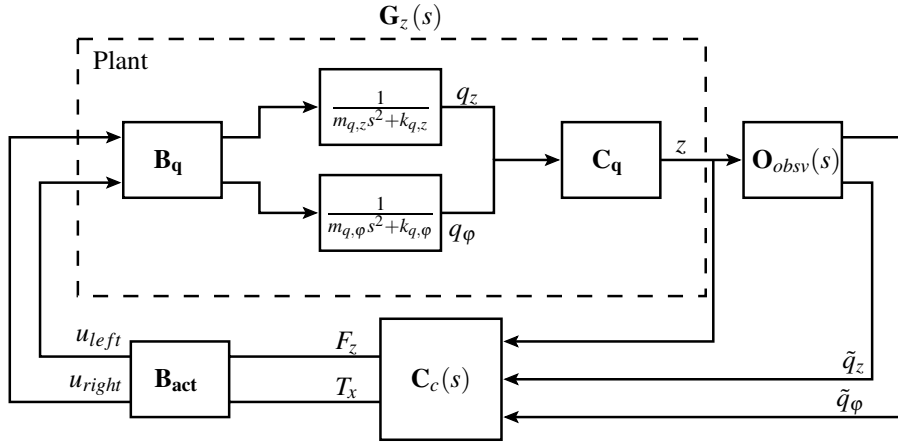


Figure B.14: Modal control scheme of the Baby-IU setup in suspension direction, with observer $O_{obsv}(s)$, controller $C_c(s)$, modal co-ordinates q_z, q_ϕ and estimated modal co-ordinates $\tilde{q}_z, \tilde{q}_\phi$.

force measurements of Section 3.5.1. Figure B.15 shows that the model and the measured FRF of the plant coincide for the first resonance mode¹.

The control strategy is shown in Fig. B.14. The controller, $C_c(s)$, can be used to either control the z -position or the estimated translation mode, \tilde{q}_z . To damp the flexible mode, the velocity \dot{q}_ϕ can be fed back through the controller $C_c(s)$ as well.

Figure B.16 shows the FRFs for four different situations: The conventional propulsion $\frac{z}{F_z}$, the modal observed $\frac{\tilde{q}_z}{F_z}$, modal observed $\frac{\tilde{q}_z}{F_z}$ with \tilde{q}_ϕ damped, and the conventional open-loop $\frac{z}{F_z}$ with \tilde{q}_ϕ damped.

In the modal observed situation the dynamics of the rotational mode, q_ϕ , are separated from the linear mode, q_z using the observer. A PID-controller with a higher gain, can be directly applied to the linear mode q_z , since the destabilising resonance is reduced by 25 dB. With perfect observation, the bandwidth can theoretically be placed above the resonance. However, the dynamics of the rotational mode are not observed in transfer $\frac{\tilde{q}_z}{F_z}$, but still excited. Therefore, it is possible that the mode is still excited and impairs performance.

The flexible mode is damped by applying velocity feedback to $\dot{\tilde{q}}_\phi$. This damping results in a significant reduction of the excitation of the flexible mode, as shown in Fig. B.16. From these experiments, it is clear that the damping of flexible modes can significantly reduce the excitation of a flexible mode. Due to the decreased excitation, the position controller can be improved and positioning performance gained.

¹The damping of the mode was manually fitted.

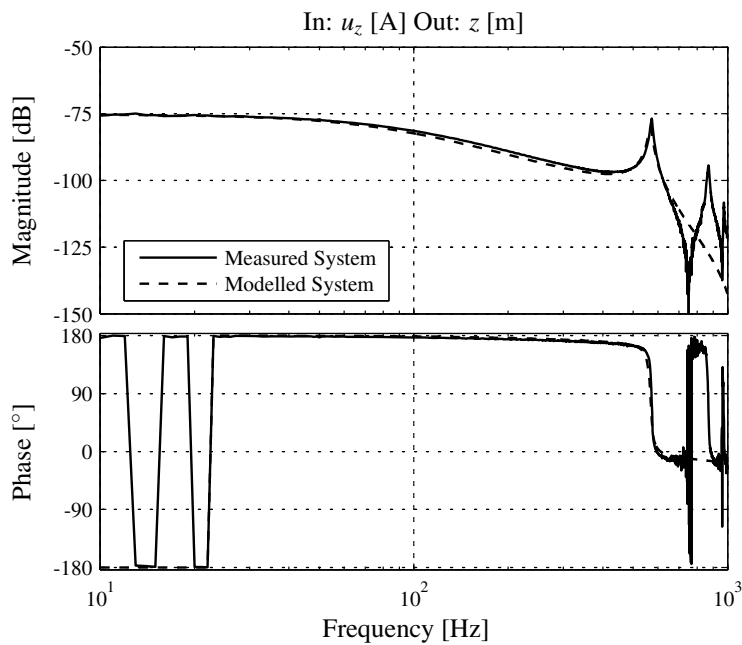


Figure B.15: Measured FRF of the plant, $\mathbf{G}(s)$, and model acting as basis for observer, $\mathbf{O}_{obsv}(s)$.

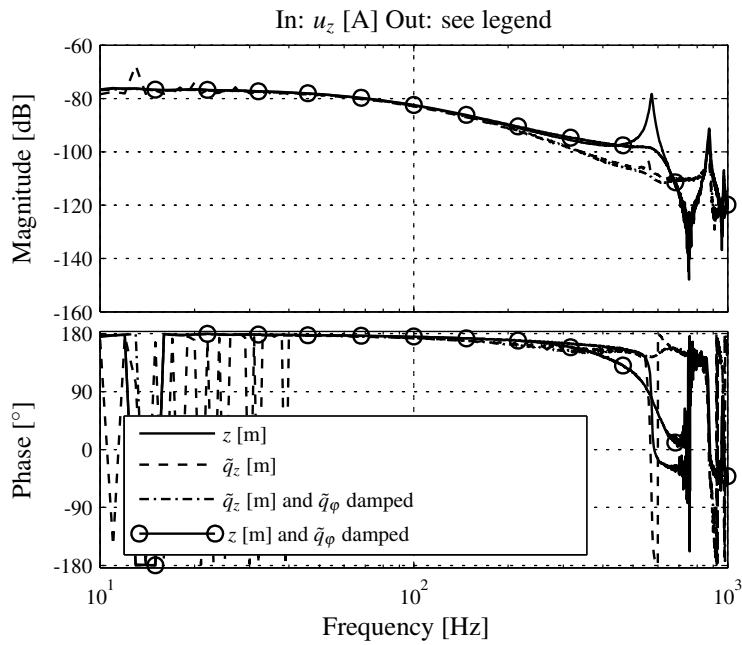


Figure B.16: Results of modal control on Baby-IU setup in suspension direction.

Appendix C

Additional measurement results of the Slider

In this appendix, additional measurements of the Slider are collected. One of the limits on the performance of the stiffness compensation, presented in Chapter 5, might be formed by a non-linearity in the eddy current sensors. This non-linearity is studied in Appendix C.1. A comparison between the modelled and the applied stiffness compensation on the Slider, is given in Appendix C.2. The positioning results, presented in Chapter 5, only show the servo-errors in x , y and z -directions. In Appendix A.2, the servo-errors for the angular directions and the individual sensors are given.

C.1 Position dependency of the eddy current sensor

The stiffness compensation seems to be less effective in the out of centre x -positions, as is discussed in Chapter 5. The static force measurements and simulations, presented in Chapter 3, do not show a varying stiffness, k_{zz} , or actuator constant, h_{zz} , at different x or z -positions of the Slider bar. A possible cause of the decreased performance, might lie in a non-linearity of the eddy current sensors.

To investigate such a non-linearity, the FRFs to the capacitive sensors and the eddy current sensors, are compared. The Slider is placed on different z -positions and FRFs are measured with respect to these sensors. The capacitive sensors have a limited stroke of 100 μm . Therefore, the Slider is first brought to the different z -positions using the eddy current sensors. At these different z -positions, the capacitive sensors are brought in range, using a manual positioning stage on the reference frame. The control loop is then be transferred to the reference frame and the FRFs are measured.

The resulting FRFs, z_S/F_z , with respect to the eddy current sensors on the force frame, and the capacitive sensors on reference frame, are shown in Fig.C.1 and

Fig. C.2. The open-loop FRF of the measurement with respect to capacitive sensors is constant over all z -position, see Fig. C.1. The FRFs with respect to the eddy current sensors vary by 3.5 dB (factor 1.5) in gain. This indicates that the output of the eddy current sensor is non-linear and that its gain depends on the z -position.

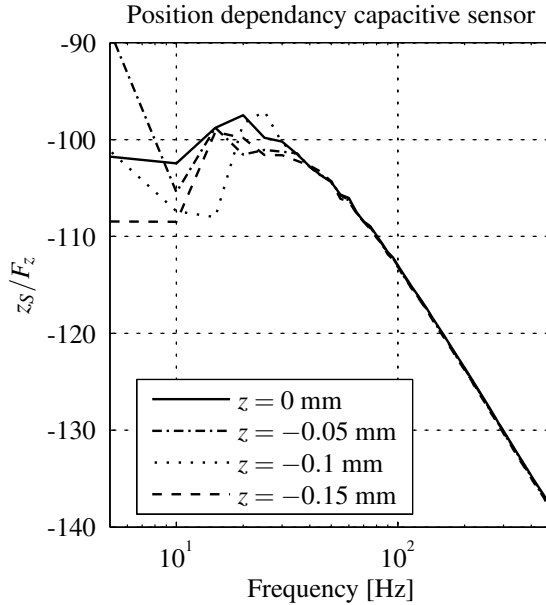


Figure C.1: Capacitive sensor measurement z_s/F_z , showing the same gain on all z -positions.

The applied stiffness compensation, described in Section 5.2.3, assumes that the gain of the sensors is constant. As the Slider translates in x -direction with respect to the reference, it will make small displacements in the suspension directions with respect the force frame, because the reference and force frame are not perfectly aligned. These displacements can cause gain variations, due to non-linear behaviour of the eddy current sensors. These gain variations will decrease the performance of the stiffness compensation.

According to the specifications, the eddy current sensors only have a $\pm 10\%$ linearity deviation over the full range. The measured deviation is clearly much more. The magnetic field of the IU-modules, might influence the linearity of the eddy current sensors. However, additional research is required to establish the exact cause.

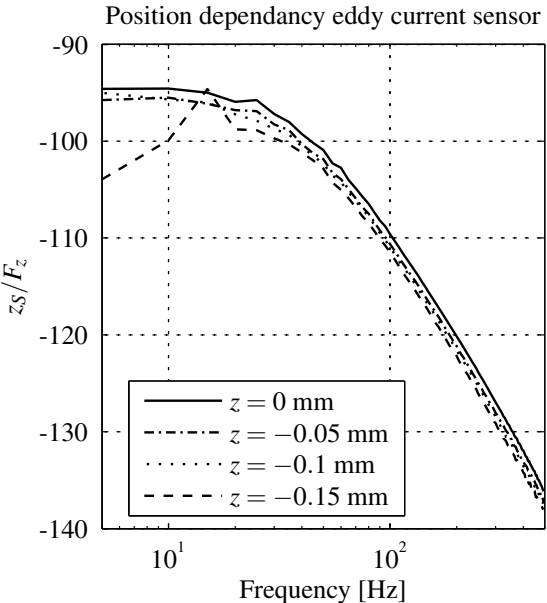


Figure C.2: Eddy current measurement z_S / F_z , showing changes in gain of 3.5 dB over different z -positions.

C.2 Stiffness compensation: model and experiment

In this appendix, the effect of the stiffness compensation on the actual system is compared to the modelled stiffness compensation. The model is constructed using CAD data and stiffness measurements as described in Chapter 3. In the model, the reference frame, the Slider, and the force frame, are modelled as 6-DoF rigid bodies connected with linear springs. More details on the model can be found in Chapter 4.

Figure C.3 shows the FRF in suspension directions of the modelled system and the measured system. The stiffness in the modelled system is compensated by applying a feedback in global co-ordinates using the global stiffness matrix of the Slider, $(a_{comp} \cdot \mathbf{K}_S)$. The stiffness matrix is compensated with a ratio of $a_{comp} = 0.95$.

The measured FRF and 95%-compensated model, both depicted in C.3, compare well. The negative stiffness slightly differs from what was modelled. The reason for this is, that the force measurements are not performed on each individual IU-module of the Slider. Mechanical construction tolerances easily explain small differences in negative stiffness.

An ideal free suspended mass, for a “low stiffness” design concepts, has only -2 slopes on the diagonal. Figure C.4 shows that the Slider approaches the ideal situation as stiffness compensation is improved. However, even with perfect stiffness compensation, the system remains coupled in transfers, $\frac{y_s}{T_x}$ and $\frac{\phi_s}{F_y}$. The origin of this remaining coupling, lies in the force frame. The stiffness measurement of the Slider is not collocated with the stiffness, allowing motions of the force frame to corrupt position measurement of the Slider. The mechanical design of the Slider places the CoG of the Slider and the force frame at a distance of 240 mm. A force, F_y , on the Slider will produce a torque around the x -axis of the force frame, causing the coupling. To decrease couplings through the force frame, the following measures can be taken:

- Use collocated sensors and actuators for the stiffness compensation.
- Design a system where the CoG of the force frame and Slider are at the same position.
- Increase the mass of the force frame.
- Monitor the motions of the force frame separately and compensate for them.

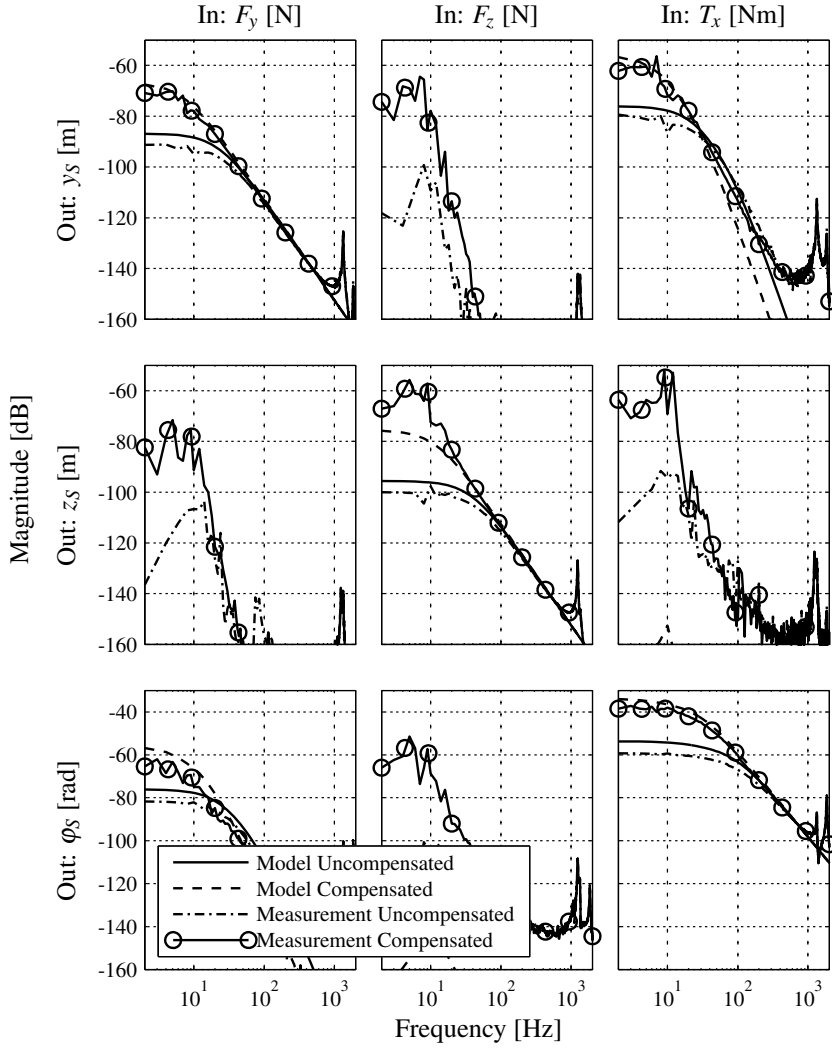


Figure C.3: Modelled system with and without stiffness compensation compared to measured FRF of Slider in suspension directions.

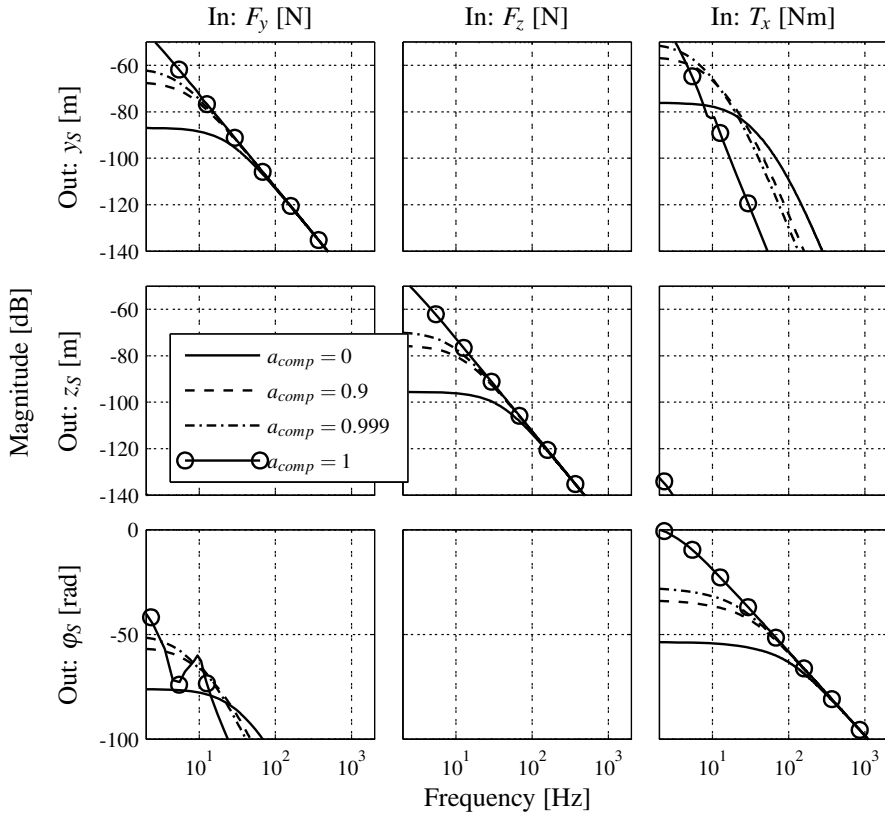


Figure C.4: Modelled FRF between Slider and reference frame for different levels of stiffness compensation.

C.3 Additional servo-errors of the Slider

In this appendix, the CAS, of the angular servo-errors and the sensor errors, are presented. Figure C.5 shows the servo-errors in the angular directions. Less effort is put in optimising the controllers in the angular directions than in the linear directions, presented in Chapter 5. It is likely that performance can be improved in these directions. The servo-error, e_θ , has significant error build-up at 1300 Hz. This may be improved by including a notch at this frequency in the θ_S control loop. The low frequency components in the servo-error, e_ϕ and e_γ , can be optimised by increasing the controller gain at low frequencies.

Figure C.5 shows the CAS of the local sensors without sensor-offset. It is clear that all suspension and the propulsion sensors have errors in the same order of magnitude. Figure C.7 shows the servo-errors, e_x , e_y and e_z belonging to the same measurements as shown in Fig. C.5 and Fig. C.6.

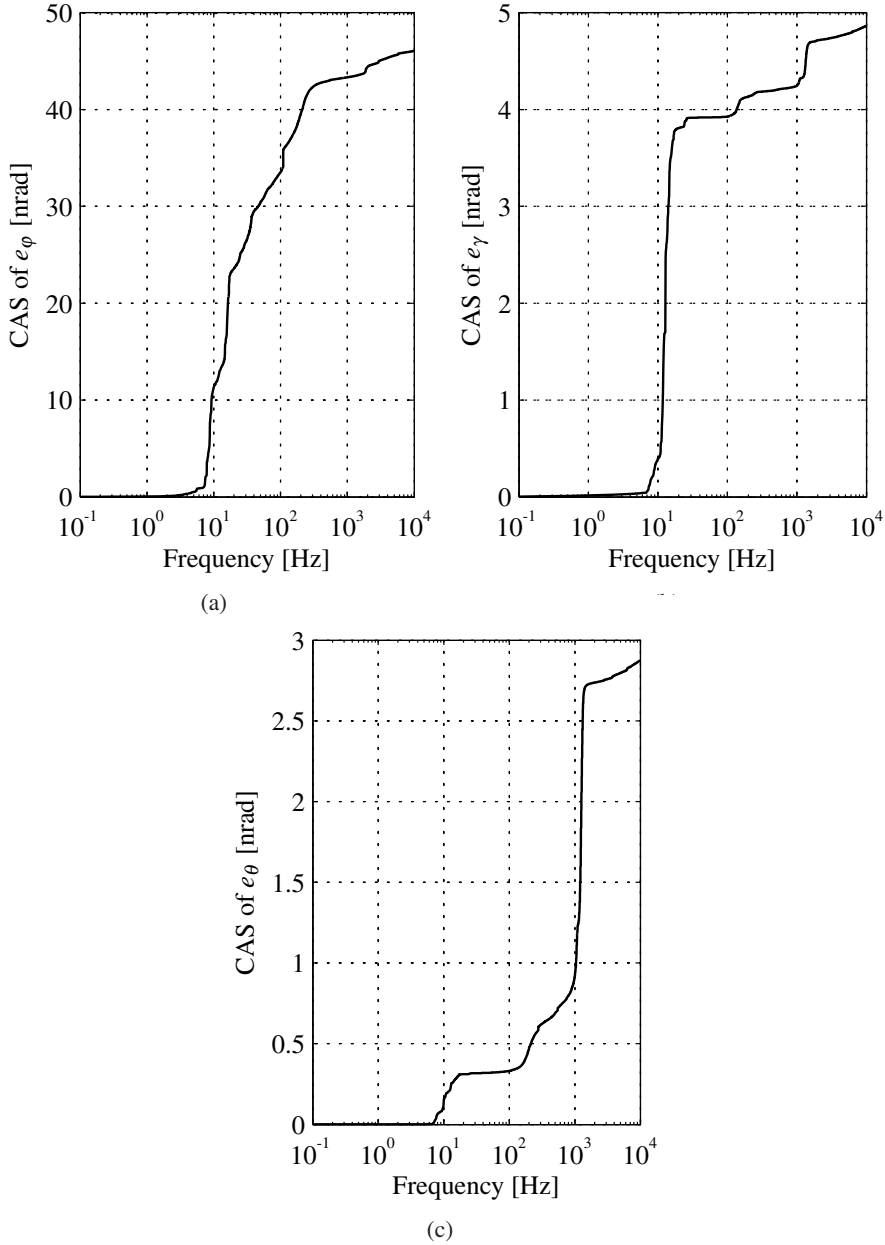
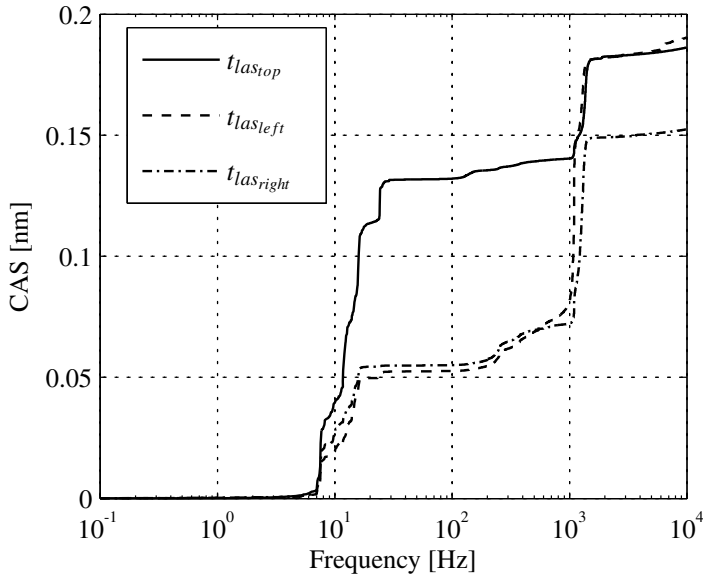
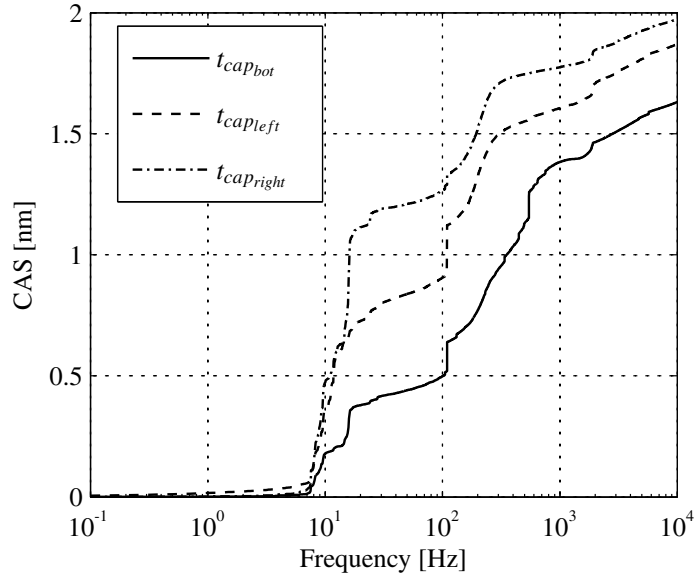


Figure C.5: CAS the angular servo-errors of the Slider at $x_S = 0$ -position, e_ϕ (a), e_γ (b), e_θ (c).



(b)

Figure C.6: CAS of the sensor signals, for the suspension sensors (a), and the propulsion sensors (b). The DC offset has been subtracted.

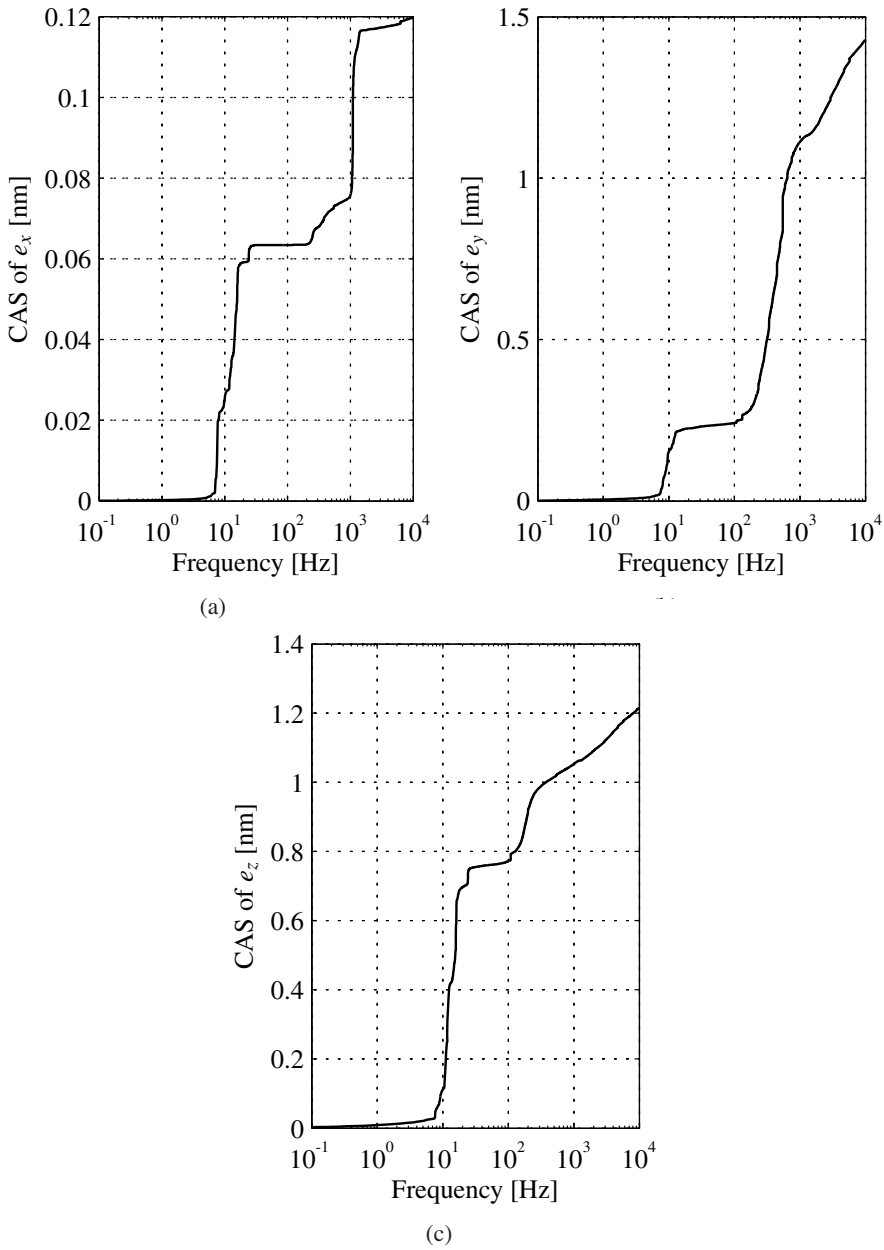


Figure C.7: CAS of the servo-errors of the Slider at $x_S = 0$ -position, e_x (a), e_y (b), e_z (c), belonging to the same measurements as shown in Fig. C.5 and Fig. C.6

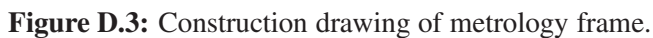
Appendix D

Construction drawings of the Slider

This appendix gives an impression of the construction drawings realised for the Slider.



Figure D.1: Assembly drawing of the full Slider system.



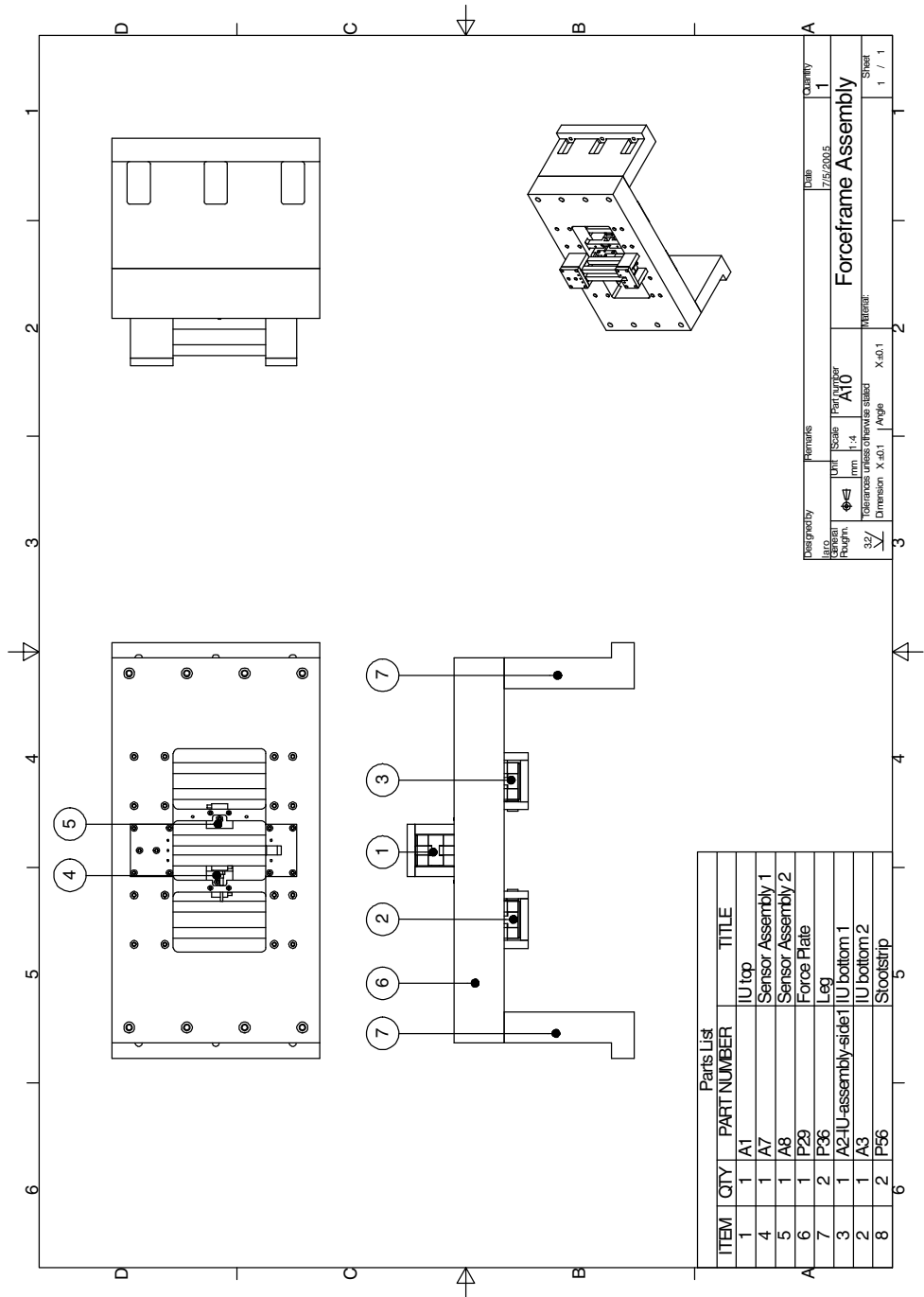


Figure D.4: Force frame assembly drawing

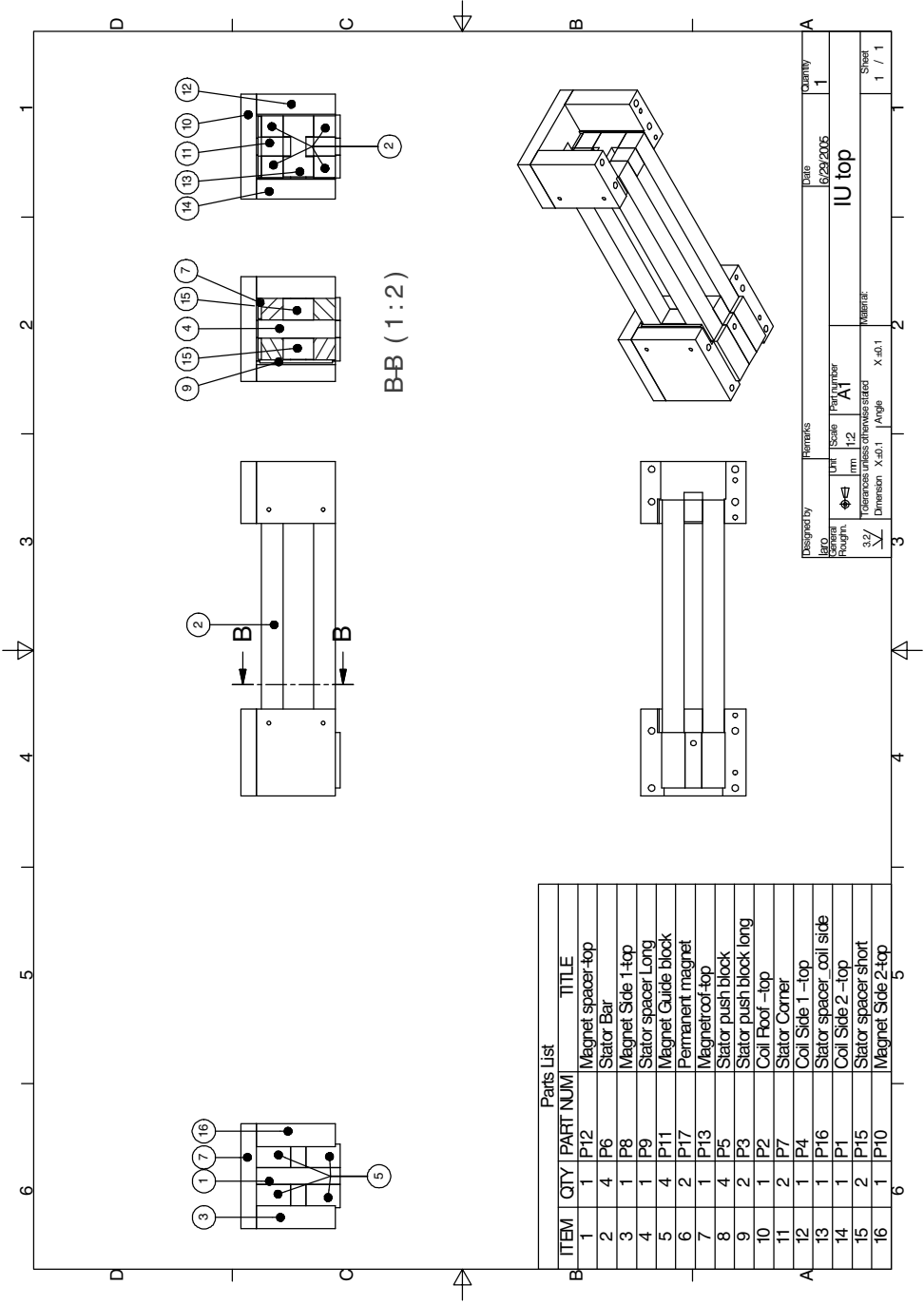


Figure D.6: Assembly drawing of the top IU-module.

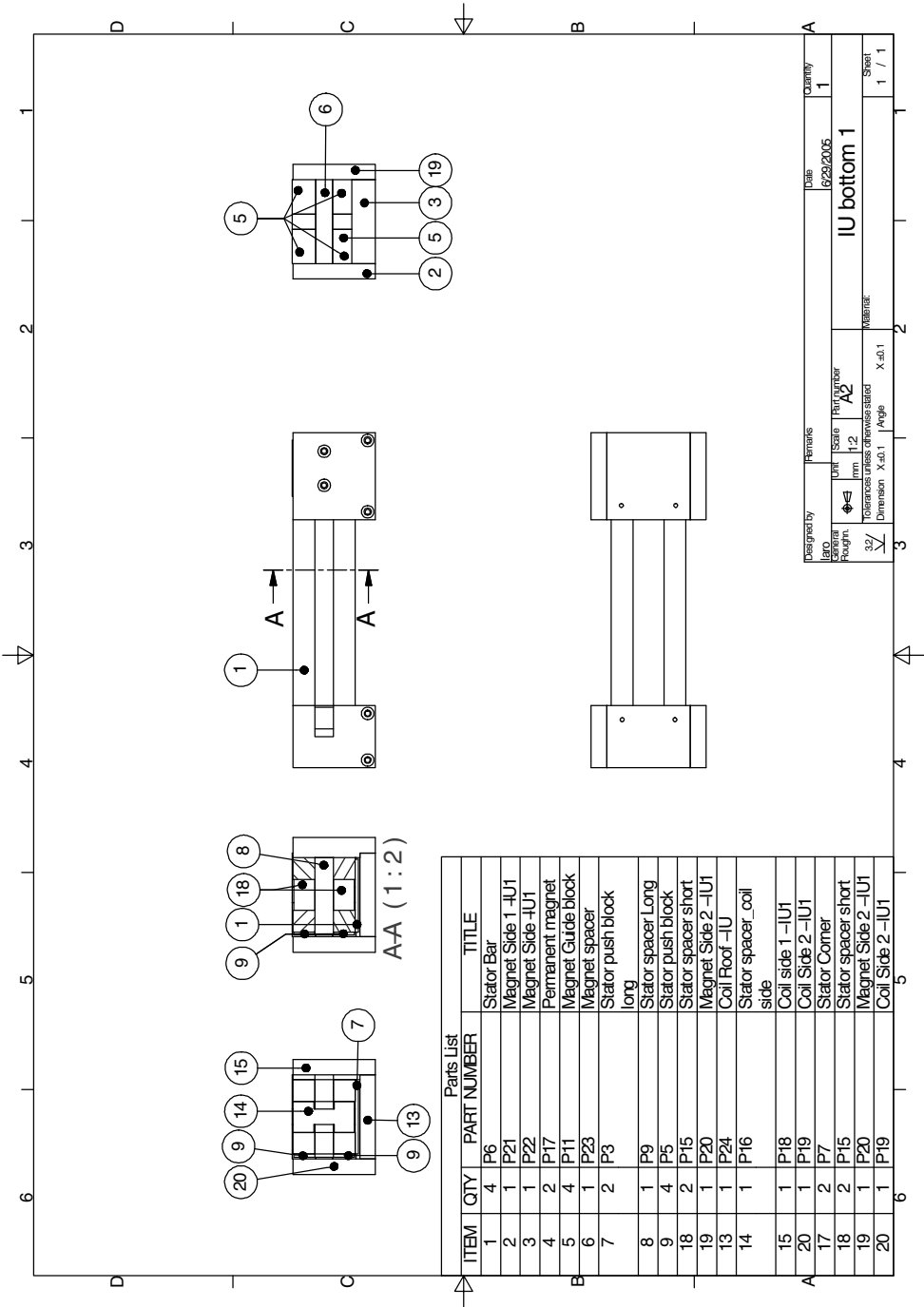


Figure D.7: Assembly drawing of the bottom IU-module.

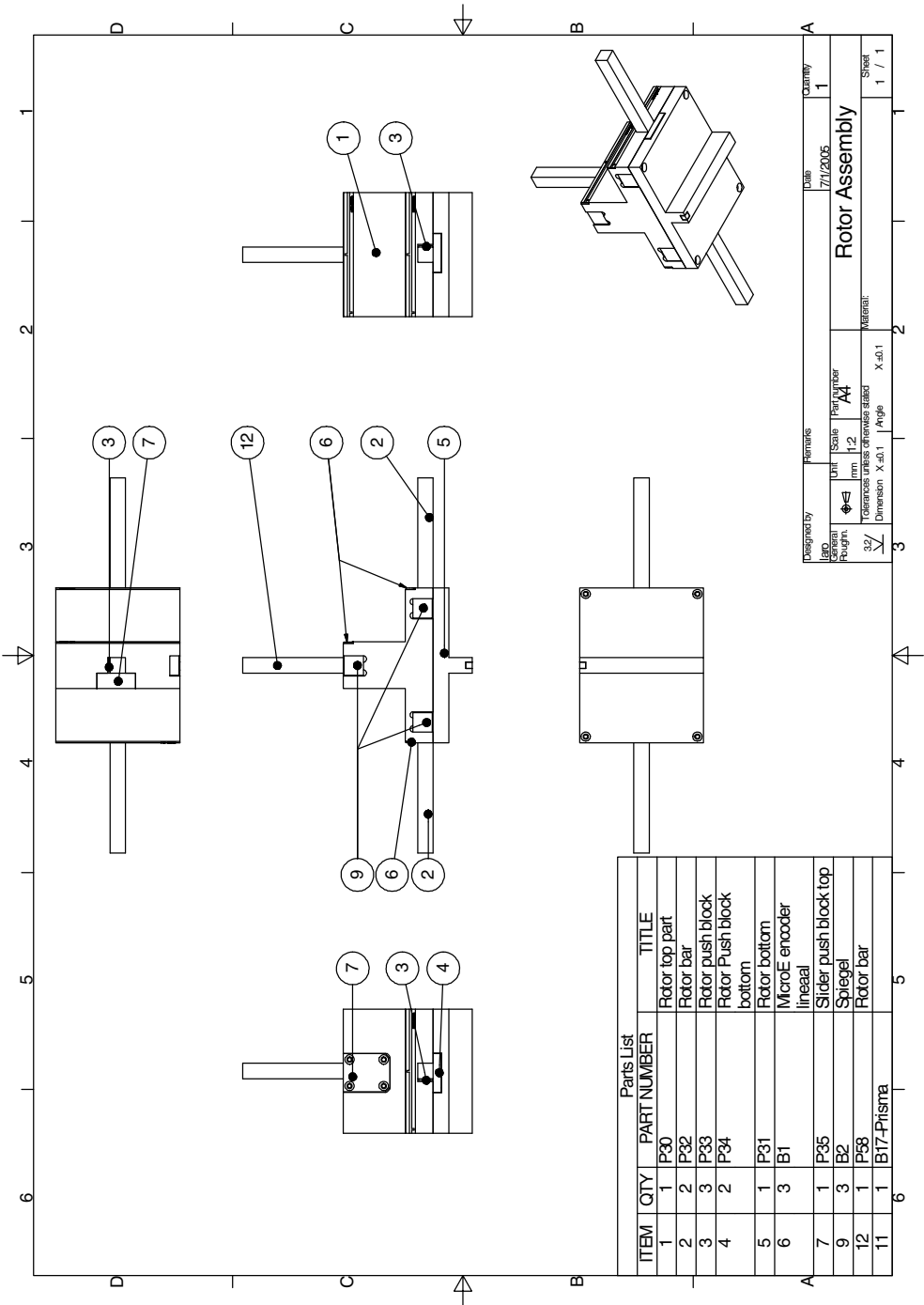


Figure D.8: Construction drawing of the Slider.

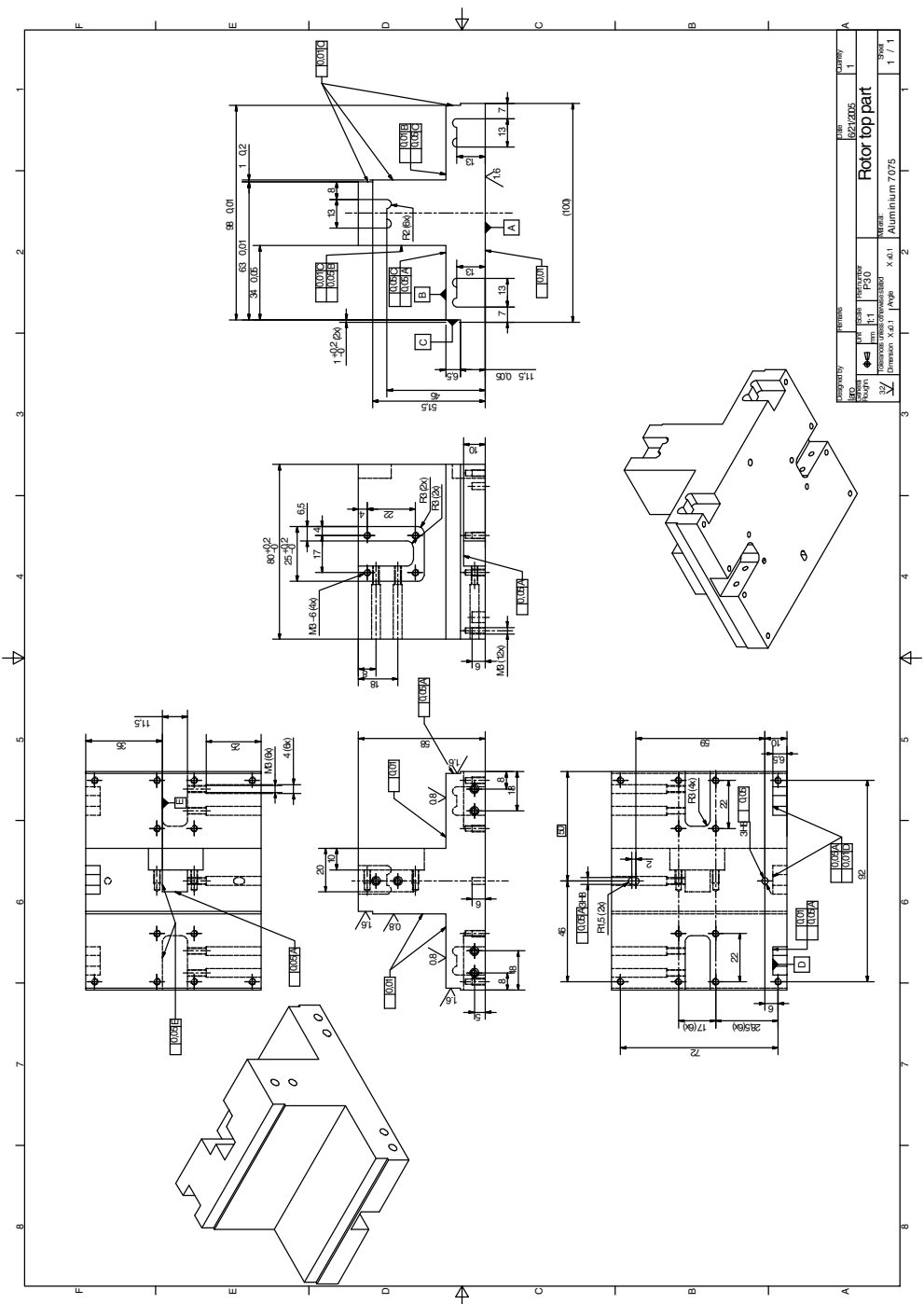
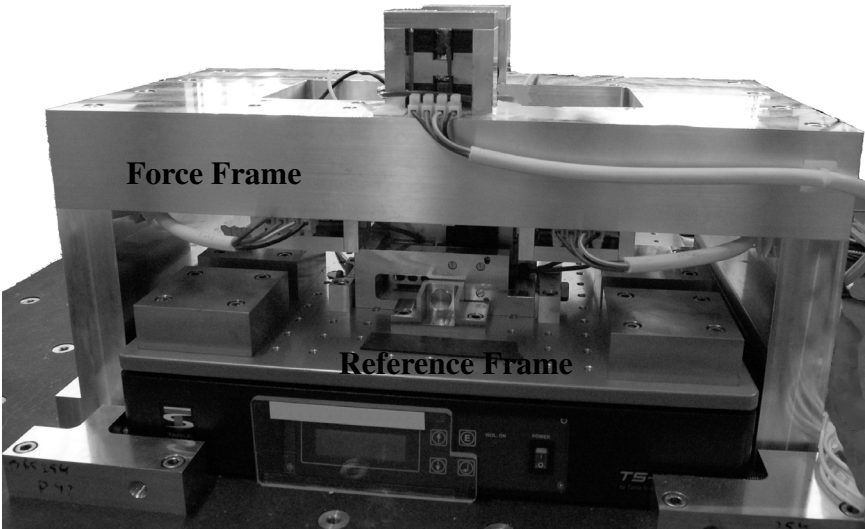


Figure D.10: Construction drawing of the Slider bottom.

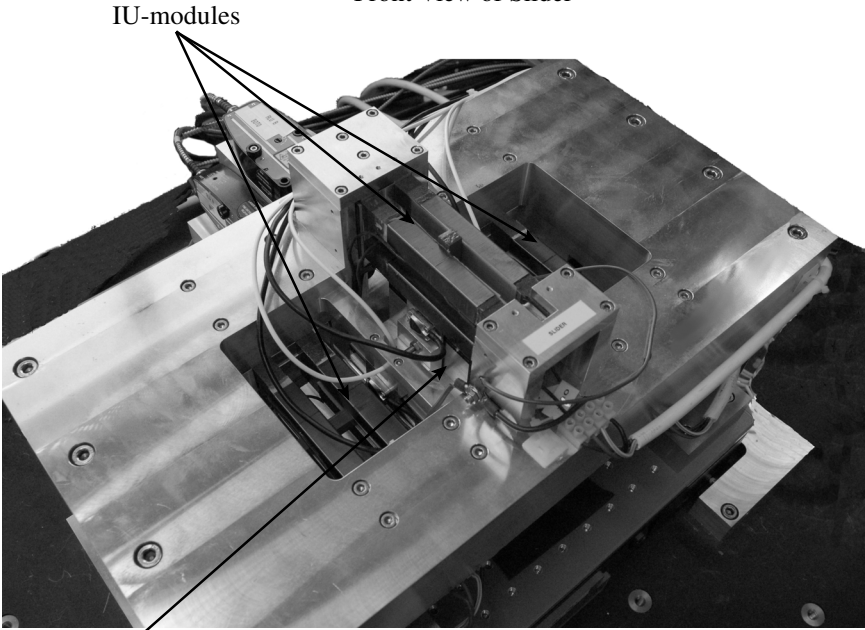
Appendix E

Photographs

The following pages show photographs of the realised setups.

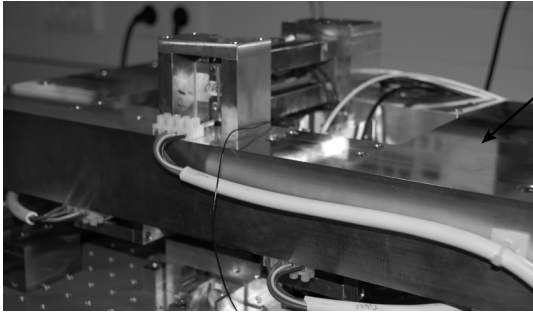


Front View of Slider

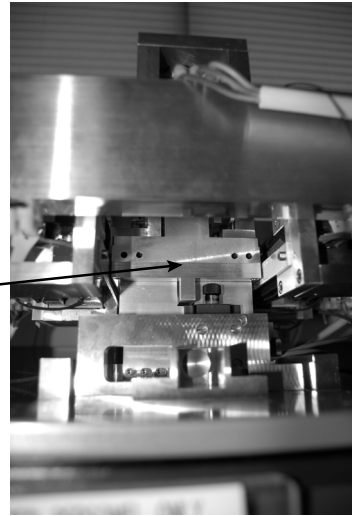


Top View of Slider

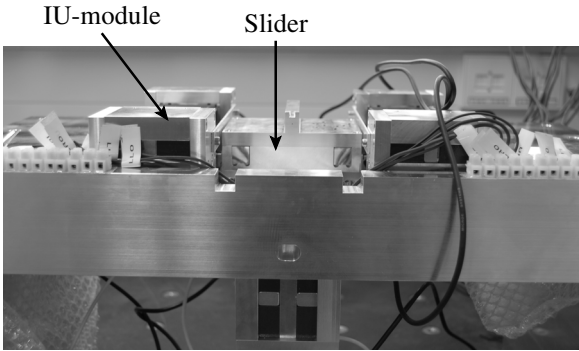
Slider



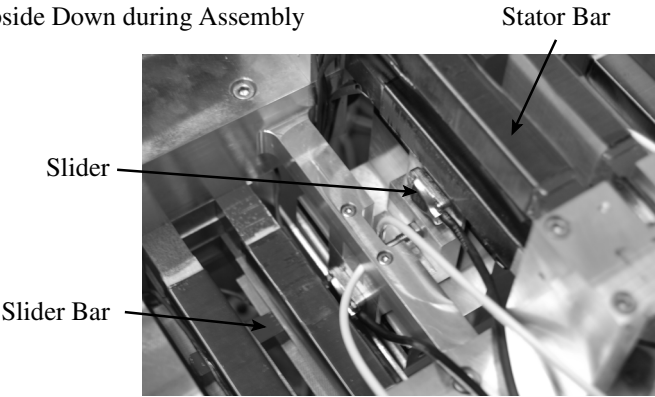
Front View of Slider



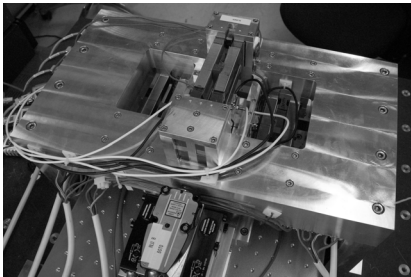
Bottom View of Slider



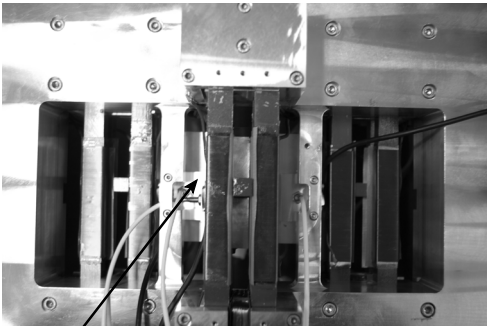
Slider Upside Down during Assembly



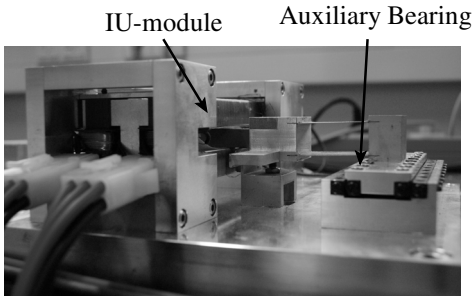
Top view



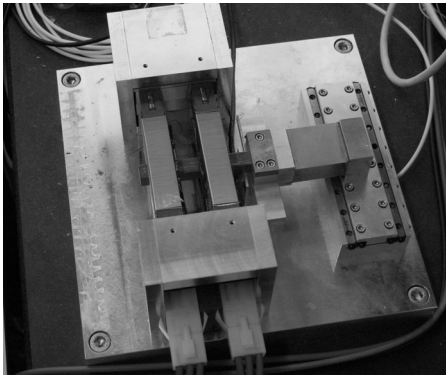
Rear View



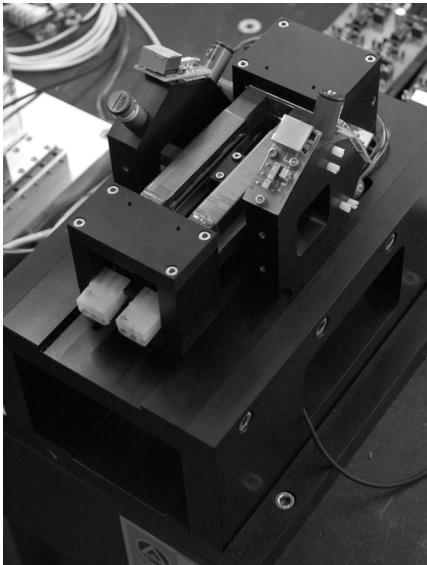
Slider
Top View



Baby-IU



Baby-IU



Force Measurement Setup

Bibliography

- [1] G. Angelis and D. Biloen. Ironless magnetic linear motors having levitating and transversal force capacities. *Patent WO 2007/026270*, 2006. Applicant: Philips.
- [2] J. Anthonis and H. Ramon. Linear mechanical systems and dyadic transfer function matrices. *Automatica*, 39(8):1353–1363, 2003.
- [3] BD Association. White paper blu-ray disc format general. *Available at: <http://www.blu-raydisc.com/>*, 2006.
- [4] F. Auer. *Combined electromagnetic suspension and propulsion for positioning with sub-micrometer accuracy*. PhD thesis, Delft University of Technology, 1995.
- [5] M. Balakrishnan, W. Joines, and T. Wilson. Air-gap reluctance and inductance calculations for magnetic circuits using a schwarzŰchristoffel transformation. *IEEE Transactions on Power Electronics*, 12(4):653–663, 1997.
- [6] M. Balas. Active control of flexible systems. *Journal of Optimization Theory and Applications*, 25(3):415–436, 1978.
- [7] G. Blackwood. *Active vibration isolation for controlled flexible structures*. PhD thesis, Massachusetts Institute of Technology, 1994. ISBN 90-386-2656-8.
- [8] H. Bleuler, D. Vischer, G. Schweitzer, A. Traxler, and D. Zlatnik. New concepts for cost-effective magnetic bearing control. *Automatica*, 30(5), 1994.
- [9] M. Boerlage. *Rejection of disturbances in multivariable motion systems*. PhD thesis, Technical University of Eindhoven, 2008. ISBN 978-90-386-1375-8.
- [10] M. Boerlage, M. van de Molengraft, M. Steinbuch, and G. Angelis. Exploratory study on mimo control for motion systems. *ASPE 2004 Spring Topical Meeting*, 2004.

- [11] H. Cho and K. Jung. Analysis and design of synchronous permanent-magnet planar motors. *IEEE Transaction on Energy Conversion*, 17(4):492– 499, 2002.
- [12] C. Coetsier. Dynamic error budget of the baby-iu. Master's thesis, Delft University of Technology, 2005.
- [13] J. Compter. Electro-dynamic planar motor. *Precision Engineering*, 28(2): 171–180, 2004.
- [14] S. Cosijns. *Displacement laser interferometry with sub-nanometer uncertainty*. PhD thesis, Technical University of Eindhoven, 2004.
- [15] E. Dallago, G. Sassaone, and G. Venchi. High-frequency power transformer model for circuit simulation. *IEEE Transactions on Power Electronics*, 12(4): 664–670, 1997.
- [16] B. Dijkstra. *Iterative learning control*. PhD thesis, Delft University of Technology, 2004. ISBN 90-370-0209-9.
- [17] Ecma. Data interchange on read-only 120 mm optical data disks. *Ecma Document 130*, 1996. Available at: <http://www.ecma-international.org/>.
- [18] Ecma. 120 mm dvd - read-only disk. *Ecma Document 267*, 2001. Available at: <http://www.ecma-international.org/>.
- [19] J. Edmunds and B. Kouvaritakis. Extensions of the frame alignment technique and their use in the characteristic locus design method. *International Journal of Control*, 29(5):787–796, 1979.
- [20] D. Eisenhaure, A. Slocum, and R. Hockney. Magnetic bearings for precision linear slider. *Proceedings of the First International Symposium on Magnetic Bearings*, 1:67–79, 1988.
- [21] J. Freudenberg and D. Looze. Right half plane poles and zeros and design tradeoffs in feedback systems. *IEEE Transactions on Automatic Control*, 30 (6):555–565, 1985.
- [22] P. Frissen, J. Compter, A. Peijnenburg, and E. Loopstra. Displacement device. *WO patent 2001/018944*, 2005. Applicant: ASML and Philips.
- [23] W. Gawronski. *Dynamics and control of structures: a modal approach*. Springer-Verlag, New York, 1998. ISBN 0-387-98527.
- [24] W. Gawronski. Modal actuators and sensors. *Journal of Sound and Vibration*, 229(4):1013–1022, 2000.

- [25] D.J. Griffiths. *Introduction to electrodynamics*. Prentice-Hall, 1999. ISBN 0-13-919960-8.
- [26] P. Grosdidier and M. Morari. Interaction measures for systems under decentralized control. *Automatica*, 22(3):309–320, 1986.
- [27] K. Halbach. Design of permanent multipole magnets with oriented rare earth cobalt material. *Nuclear Instruments and Methods*, 169(1):1–10, 1980.
- [28] A. Hazelton and J. Gery. Planar electric motor and positioning device having transverse magnets. *US patent 6285097*, 2001. Applicant: Nikon Corporation.
- [29] S. Hol, J. van Eijk, A. de Klerk, and H. van der Schoot. Lithographic apparatus and motor for use in the apparatus. *US patent 6717296*, 2004. Applicant: ASML.
- [30] M. Holmes, R. Hocken, and D. Trumper. The long-range scanning stage: a novel platform for scanned-probe microscopy. *Precision Engineering*, 24(3): 191–209, July 2000.
- [31] M. Holmes and D. Trumper. Magnetic/fluid-bearing stage for atomic-scale motion control (the angstrom stage). *Precision Engineering*, 18(1):38–49, 1996.
- [32] D.J. Inman. *Engineering vibration*. Prentice-Hall, 1996. ISBN 0-13-518531-9.
- [33] L. Jabben. *Mechatronic design of a magnetically suspended rotating platform*. PhD thesis, Delft University of Technology, 2007. ISBN 978-90-9022523-4.
- [34] J.W. Jansen. *Magnetically levitated planar actuator with moving magnets: Electromechanical analysis and design*. PhD thesis, Technical University of Eindhoven, 2007. ISBN 978-90-386-1150-1.
- [35] O. Kim, S. Lee, and D. Han. Positioning performance and straightness error compensation of the magnetic levitation stage supported by the linear magnetic bearing. *IEEE transaction on Industrial Electronics*, 50(2):374–378, 2003.
- [36] W. Kim. Method and apparatus for magnetically generating motion with high precision. *US patent 6885536*, 2005. Applicant: The Texas A&M University System.
- [37] W. Kim, D. Trumper, and J. Lang. Modeling and vector control of planar magnetic levitator. *IEEE Transaction on Industrial Applications*, 34(6), 1998.

- [38] A. de Klerk, G. Angelis, and J. van Eijk. Design of a next generation 6 dof stage for scanning application in vacuum with nanometer accuracy and mGauss magnetic stray field. *Proceedings of the 19th ASPE Annual Meeting*, pages 60–63, 2004.
- [39] J. Kokernak and D. Torrey. Magnetic circuit model for the mutually coupled switched-reluctance machine. *IEEE Transactions on Magnetics*, 36(2):500–507, 2000.
- [40] D. Laro, T. Porck, J. Spronck, and J. van Eijk. Control of a magnetically levitated slider with nm-precision. *Proceedings of the 10th International Symposium on Magnetic Bearings*, 2006.
- [41] D. Laro, T. Porck, J. Spronck, J. van Eijk, and A. Lebedev. Design of a magnetically levitated nm-resolution linear slider. *Proceedings of the 6th Euspen International conference*, 2006.
- [42] D. Laro, H. Stoutjesdijk, J. Spronck, and J. van Eijk. Two degree of freedom actuator for suspension and propulsion. *Proceedings of ASPE 2004 spring topical meeting*, 2004.
- [43] D. Laro, J. Wesselingh, D. Thakkar, J. Spronck, J. van Eijk, and A. Lebedev. Mechatronic design of an ultra precision magnetically supported rotor and linear slider for optical disk. *Proceedings of the 7th Euspen International conference*, 2007.
- [44] A. Lebedev. *To be published*. PhD thesis, Technical University of Eindhoven, To be determined.
- [45] A. Lebedev, E. Lomonova, D. Laro, and A. Vandenput. Optimal design strategy for a novel linear electromechanical actuator. *IEEE Transaction Industry Applications*, 126(10):1330–1335, 2006.
- [46] S. Ludwick, D. Trumper, and M. Holmes. Modelling and control of a six degree-of-freedom magnetic/fluidic motion control stage. *IEEE Transactions on Control Systems Technology*, 4(5):553–564, 1996.
- [47] D. MacMartin. Collocated structural control: motivation and methodology. *Control Applications, 1995., Proceedings of the 4th IEEE Conference on*, 4: 1092–1097, 1995.
- [48] D. Markle. Magnetically-positioned x-y stage having six-degrees of freedom. *US patent 5886432*, 1999. Applicant: Ultratech Stepper, Inc.
- [49] E. Maslen, P. Hermann, M. Scott, and R. Humphris. Practical limits to the performance of magnetic bearings: Peak force, slew rate and displacement sensitivity. *Journal of Tribology*, 111(2):331–336, 1989.

- [50] A. Molenaar. *Novel planar magnetic bearing and motor configuration applied in a positioning stage*. PhD thesis, Delft University of Technology, 2000. ISBN 90-6464-737-2.
- [51] H. Na and Y. Park. An adaptive feedforward controller for rejection of periodic disturbances. *Journal of Sound and Vibration*, 201(4):427–435, 1997.
- [52] D.E. Newman. *An Introduction to random vibrations spectral and wavelet analysis*. Dover Publications, New York, 1997. ISBN 0-486-44274-8.
- [53] P. Nuij. *Higher order sinusoidal input describing functions*. PhD thesis, Technical University of Eindhoven, 2007. ISBN 978-90-386-1066-5.
- [54] K. Ogata. *Modern control engineering*. Prentice Hall, London, 1997. ISBN 0-13-261389-1.
- [55] A. Oppenheim, A. Willsky, and H. Nawab. *Signals and systems*. Prentice Hall, United States, second edition, 1996. ISBN 0-13-651175-9.
- [56] P. Overschie. *To be published*. PhD thesis, Delft University of Technology, To be determined.
- [57] D.H. Owens. *Feedback and multivariable systems*. Peter Peregrinus Ltd., Stevenage England, 1978. ISBN 0-906048-03-6.
- [58] A. Peijnenburg, J. Vermeulen, and J. van Eijk. Magnetic levitation systems compared to conventional bearing systems. *Microelectronic Engineering*, 83: 1372–1375, 2006.
- [59] M.A. Plonus. *Applied electromagnetics*. McGraw Hill, New York, 1978. ISBN 0-007-050345-1.
- [60] T. Porck. Controller design for a 6 dof magnetically levitated slider. Master's thesis, Delft University of Technology, 2006.
- [61] A. Preumont. *Vibration control of active structures*. Springer, Netherlands, second edition, 2004. ISBN 978-1-4020-0496-4.
- [62] E. Rivin. Vibration isolation of precision equipment. *Precision Engineering*, 17(1):1372–1375, 1995.
- [63] C. Rojer. System identification of the planar active magnetic bearing. Master's thesis, Delft University of Technology, 2002.
- [64] T. Ruijl. *Ultra precision coordinate measuring machine*. PhD thesis, Delft University of Technology, 2001. ISBN 90-6464-287-7.

- [65] B. Shafai, S. Beale, P. Larocca, and E. Cusson. Magnetic bearing control systems and adaptive forced balancing. *IEEE Control Systems Magazine*, 14(2):4–13, 1994.
- [66] S. Skogestad and I. Postlethwaite. *Multivariable feedback control*. Wiley, New York, 2001. ISBN 0-471-94330-4.
- [67] A.H. Slocum. *Precision machine design*. Prentice-Hall, 1992. ISBN 0-13-690918-3.
- [68] H. Stoutjesdijk. Integrated magnetic sensing for the iu-module. Master's thesis, Delft University of Technology, 2004.
- [69] P. Subrahmanyam. *A model approach to precision motion control*. PhD thesis, Massachusetts Institute of Technology, 1999.
- [70] D. Trumper. *Magnetic suspension techniques for precision motion control*. PhD thesis, Massachusetts Institute of Technology, 1990.
- [71] D. Trumper. Magnetic positioning device. *US patent 5196745*, 1997. Applicant: Massachusetts Institute of Technology.
- [72] D. Trumper, W. Kim, and M. Williams. Magnetic arrays. *US patent 5631618*, 1997. Applicant: Massachusetts Institute of Technology.
- [73] D. Trumper, S. Olsen, and P. Subrahmanyam. Linearizing control of magnetic suspension systems. *IEEE Transactions on Control Systems Technology*, 5(4): 427–438, 1997.
- [74] D. Trumper and M. Williams. Positioner with long travel in two dimensions. *US patent 5699621*, 1997. Applicant: Massachusetts Institute of Technology.
- [75] D. Vaes. *Optimal static decoupling for multivariable control design*. PhD thesis, Katholieke Universiteit Leuven, 2005. ISBN 90-5682-660-3.
- [76] S. van de Ven. Design and realisation of an iu-module. Master's thesis, Delft University of Technology, 2003.
- [77] J. Wesselingh. Characterization and application of a 4 dof iu-module. Master's thesis, Delft University of Technology, 2006.
- [78] E. van West and G. Kusuma. Iu-module, interaction investigation. Master's thesis, Delft University of Technology, 2004.
- [79] H. Woodson and J. Melcher. *Electromechanical dynamics, part I: discrete systems*. John Wiley & Sons, New York, 1968.

Curriculum Vitae

Dick Laro was born on the 4th of November 1978, in Roosendaal en Nispen, the Netherlands. He received his MSc degree in Mechanical Engineering at the Delft University of Technology in 2003. His MSc thesis was the result of research, conducted at Philips ITEC in Nijmegen. The subject was the development of a planar positioning system using plate springs as bearings. In 2003, he started his Ph.D. project at the Advanced Mechatronics group of the Delft University of Technology. The Ph.D. research focussed on the development of a novel electromagnetic multi-DoF actuator to be applied in a nm-resolution linear magnetically levitated positioning system. From 2007 to 2008, he was employed at Singulus Mastering. Here he worked on the development of a commercial magnetically suspended linear positioning system. Since the beginning of 2009, he works as a system developer at MI-Partners in Eindhoven.

Abstract

Future precision machines are expected to operate in a vacuum environment. The vacuum environment isolates the high precision manufacturing process from environmental disturbances, allowing higher accuracies to be reached. The precision engineering industry is therefore investigating vacuum compatible positioning systems and actuators. Active magnetically suspended systems are expected to meet the demands for vacuum compatible high precision positioning systems. In these active magnetically levitated positioning systems, a body is contactlessly suspended and positioned. The position of the body is controlled through an active feedback loop, which generates the required electromagnetic force to achieve the desired position.

The IU-module is a novel contactless electromagnetic actuator, devised by Moleenaar [50]. The IU-module promises to be a modular vacuum compatible actuator for the high precision applications. In this thesis, the potential of the IU-module is studied. The IU-module has a ferromagnetic I-shaped Slider bar, as moving component, and U-shaped stator bars. The actuator is capable of generating 2 forces and 2 torques upon the Slider bar. These actuation forces and torques are generated, with the wires and the permanent magnets situated on the stator. This eliminates the need for moving wires or magnets in a vacuum environment. In the suspension direction, a reluctance force is generated using permanent magnets, and by placing the Slider bar in a non-centred position within the airgap. This reluctance force allows compensation of gravity forces without any actuation current, reducing ohmic losses and heat generation.

Using finite element models and analytical models, an IU-module is developed. The models are verified by performing force measurements on the IU-module. The models and measurements show, that the IU-module is capable of generating a limited propulsion force and that a position dependent interaction exists from propulsion actuation to the suspension force. The actuation of the suspension force and the torques do not have these limitations and have a linear force to current relationship. In the suspension direction, a negative stiffness transfers disturbances to the moving part. The IU-module should generally be applied in applications, where a limited propulsion force is required and the suspension direction is more tolerant to external disturbances.

The potential of the IU-module, to function in a high precision positioning sys-

tem, is researched by integrating it into a linear positioning system, the Slider. To increase the storage capacity of future generations of optical discs, the optical disc mastering (ODM) industry is looking for vacuum compatible positioning systems. Since the ODM machine is a good example of a high precision machine, the specifications for the Slider are taken to coincide with a linear positioning system, present in an ODM system. The Slider requires a position stability in the propulsion direction of 1 nm (σ), to make sure that the optical disc remains within the specifications. In the other directions, a 5 times larger error is allowed. The Slider requires only limited propulsion forces, due the low accelerations needed in the application. These specifications warrant the application of the IU-module. In the design of the Slider, the IU-module is initially applied as a 2-DoF actuator for generating a suspension and a propulsion force.

The Slider design employs a design concept in which the force loop and metrology loop are separated. This is realised by placing the high accuracy sensors on a reference frame, suspended with low stiffness springs, while the actuation forces are guided to a separate force frame. The Slider is held in position with respect to the reference frame by using an active control loop.

The Slider is a mechatronic system consisting of mechanics, electronics, and control. To reach sub nm-resolution, a balanced design over all these disciplines is required. To evaluate this mechatronic design, the Dynamic Error Budgeting (DEB) technique is applied. The DEB technique allows estimation of the closed-loop position error of a system, subjected to several stochastic disturbances. The DEB results in an overview of the total and individual contributions of each disturbance source, to the position error. The DEB forms a design aid to effectively reduce the most significant contributions to the error. Design iterations on the Slider are performed, until the requirements were met.

The 6-DoF electromagnetically levitated Slider was realised. This Slider achieves a servo-error of 0.15 nm (σ) in the most critical direction, while translating at a nominal velocity of 55 $\mu\text{m/s}$. The other directions are well within specifications of the application. The control of the Slider is realised by applying decoupled position control on the rigid body coordinates. To minimise the transfer of disturbances between the Slider and the surrounding world through the stiffness of the IU-module, its stiffness is compensated with a secondary control loop.

One of the limiting factors on the positioning of the Slider are the flexible modes, caused by the Slider bars. The Slider uses 3 IU-modules, each capable of actuating on 4-DoF. This makes the Slider an over-actuated positioning system. The over-actuation can be used to limit the excitation of the flexible modes of the Slider, mimicking actuation in the node of a mode. By doing so, the specific flexible modes are not excited, which is the same as rendering them uncontrollable. This allowed the controller to be improved: Not just in the frequency region, where the flexible modes are active, but also at lower frequencies due to improved stability margins. The servo-error in the propulsion direction reduced to 58 pm (σ), at stand-

still. With these positioning results, the IU-module demonstrates that it is capable of performing within a sub nm-resolution high precision positioning system.

